Using Grazing Incidence Small-Angle X-Ray Scattering (GISAXS) for Semiconductor Nanometrology and Defect Quantification

Dissertation
zur Erlangung des akademischen Grades
doctor rerum naturalium
(Dr. rer. nat.)

im Fach: Physik
Spezialisierung: Experimentalphysik

eingereicht an der
Mathematisch-Naturwissenschaftlichen Fakultät
der Humboldt-Universität zu Berlin

von M. Sc. Mika Hannes Pflüger

Präsidentin der Humboldt-Universität zu Berlin
Prof. Dr.-Ing. habil. Dr. Sabine Kunst

Dekan der Mathematisch-Naturwissenschaftlichen Fakultät
Prof. Dr. Elmar Kulke

Gutachter/innen:	1. Prof. Dr. Kurt Busch
	2. Prof. Dr. Mathias Richter
	3. Professor Hiroshi Okuda
Tag der mündlichen Prüfung:	1.12.2020

Selbständigkeitserklärung

Ich erkläre, dass ich die Dissertation selbständig und nur unter Verwendung der von mir gemäß § 7 Abs. 3 der Promotionsordnung der Mathematisch-Naturwissenschaftlichen Fakultät, veröffentlicht im Amtlichen Mitteilungsblatt der Humboldt-Universität zu Berlin Nr. 42/2018 am 11.07.2018 angegebenen Hilfsmittel angefertigt habe.

Berlin, 11. August 2020

Mika Pflüger

Abstract

Background. The development of nanotechnology such as integrated circuits relies on an understanding of structure and function at the nanoscale, for which reliable and exact measurements are needed. Grazing-incidence small angle X-ray scattering (GISAXS) is a versatile method for the fast, contactless and destruction-free measurement of sizes and shapes of nanostructures on surfaces.

Aims. A goal of this work is to investigate the possibility of precisely measuring the increasingly complex samples produced in science and industry using GISAXS. A second objective is to measure targets used in semiconductor quality control with a size of approx. 40 µm × 40 µm, whose signal is typically not accessible because an area of approx. 1 mm × 20 mm is illuminated at once.

Methods. I take synchrotron-based GISAXS measurements and analyze them using reciprocal space construction, the distorted wave born approximation, and a solver for Maxwell's equations based on finite elements.

Results. I find that the line shape of gratings with a period of 32 nm can be reconstructed from GISAXS measurements and the results deviate less than 2 nm from reference measurements; however, a careful Bayesian uncertainty analysis shows that key dimensional parameters do not agree within the uncertainties. For the measurement of small grating targets, I create a novel sample design where the target is rotated with respect to the surrounding structures and find that this efficiently suppresses parasitic scattering.

Conclusions. I show that GISAXS measurements of complex nanostructures and small targets are possible, and I highlight that further development of GISAXS would benefit tremendously from efficient simulation methods which describe all relevant effects such as roughness and edge effects. Promising theoretical approaches exist, so that GISAXS has the potential to become an additional method in the toolkit of semiconductor quality control.

Zusammenfassung

Hintergrund: Die Entwicklung von Nanotechnologien und insbesondere integrierten Schaltkreisen beruht auf dem Verständnis von Struktur und Funktion auf der Nanoskala, wofür exakte Messungen erforderlich sind. Kleinwinkel-Röntgenstreuung unter streifendem Einfall (GISAXS) ist eine Methode zur schnellen, berührungs- und zerstörungsfreien dimensionellen Messung von nanostrukturierten Oberflächen.

Ziele: Es soll die Möglichkeit untersucht werden, die zunehmend komplexeren Proben aus Wissenschaft und Industrie mit Hilfe von GISAXS präzise zu vermessen. Ein weiteres Ziel ist es, Messtargets aus der Halbleiter-Qualitätskontrolle mit einer Größe von ca. 40 µm × 40 µm zu messen, deren Signal typischerweise nicht zugänglich ist, weil ein Bereich von ca. 1 mm × 20 mm auf einmal beleuchtet wird.

Methoden: Synchrotron-basierte GISAXS-Messungen verschiedener Proben werden mit Hilfe einer Fourier-Konstruktion, der *distorted wave Born approximation* und einem Maxwell-Gleichungs-Löser basierend auf finiten Elementen analysiert.

Ergebnisse: Aus GISAXS-Messungen kann die Linienform von Gittern mit einer Periode von 32 nm rekonstruiert werden und sie weicht weniger als 2 nm von Referenzmessungen ab. Eine sorgfältige Bayes'sche Unsicherheitsanalyse zeigt jedoch, dass wichtige dimensionelle Parameter innerhalb der Unsicherheiten nicht übereinstimmen. Für die Messung von kleinen Gittertargets entwerfe ich ein neuartiges Probendesign, bei dem das Target in Bezug auf die umgebenden Strukturen gedreht wird, und stelle fest, dass dadurch parasitäre Streuung effizient unterdrückt wird.

Fazit: GISAXS-Messungen von komplexen Nanostrukturen und kleinen Targets sind möglich, jedoch würde GISAXS enorm von effizienteren Simulationsmethoden profitieren, die alle relevanten Effekte wie Rauhigkeit und Randeffekte einbeziehen. Hier gibt es vielversprechende theoretische Ansätze, so dass GISAXS eine zusätzliche Methode für die Halbleiter-Qualitätskontrolle werden könnte.

Contents

Abstract 5

Zusammenfassung 7

Acronyms 11

Symbols 13

1 Introduction 17

2 Fundamentals 21
2.1 Interaction of X-rays with matter . . . 21
2.1.1 Photoelectric effect . . . 22
2.1.2 Fluorescence . . . 23
2.1.3 Meitner-Auger decay . . . 24
2.1.4 Scattering . . . 24
2.1.5 Compton scattering . . . 24
2.1.6 Rayleigh scattering at atoms . . . 25
2.1.7 The refractive index . . . 28
2.2 GISAXS . . . 30
2.2.1 Development and related methods . . . 30
2.2.2 Theoretical description . . . 32
2.2.3 Experimental realization . . . 35
2.3 Generation of X-rays . . . 35
2.3.1 Characteristic X-ray emission . . . 36
2.3.2 Bremsstrahlung . . . 37
2.3.3 Synchrotron radiation . . . 37
2.3.4 Undulator radiation . . . 40
2.3.5 Free electron lasers . . . 42
2.4 Detection of X-rays . . . 43
2.4.1 Calorimetric detection . . . 44
2.4.2 Diodes . . . 44
2.4.3 Silicon drift detectors . . . 45
2.4.4 Fluorescent screens . . . 45
2.4.5 Direct illumination solid state cameras . . . 45
2.4.6 Hybrid photon counting detectors . . . 47

3 Methods 49
3.1 Instrumentation . . . 49
3.1.1 BESSY II . . . 49
3.1.2 Four-crystal monochromator beam line . . . 50
3.1.3 Sample alignment . . . 54
3.2 Grating GISAXS . . . 56
3.2.1 Idealized gratings - the Born Approximation . . . 56

3.2.2 Line shapes - the Distorted Wave Born Approximation . . . 62
3.2.3 Solving Maxwell's equations using finite elements . . . 68
3.2.4 Comparing the theoretical approaches . . . 71
3.2.5 Conclusion . . . 74

4 Lithographic Defects in Light Harvesting Nanostructures 75
4.1 Application . . . 75
4.2 Sample description . . . 76
4.3 GISAXS measurements and data analysis . . . 77
4.4 Results . . . 79
4.5 Discussion . . . 80

5 Reconstruction of Complex Line Profiles 83
5.1 Application . . . 83
5.2 Sample description . . . 87
5.3 GISAXS measurements . . . 88
5.4 Simulation of the Diffraction Intensity . . . 90
5.5 Line shape reconstruction . . . 93
5.6 Uncertainties of the line shape reconstruction . . . 95
5.7 Pitchwalk sample series . . . 100
5.8 Pitchwalk reconstruction . . . 102
5.9 Discussion . . . 104

6 Measuring Small Periodic Targets Using Large Beams 107
6.1 Application . . . 107
6.2 Scattering off small measurement targets . . . 108
6.2.1 Sample description . . . 108
6.2.2 GISAXS measurements . . . 108
6.2.3 Results . . . 109
6.2.4 Discussion . . . 113
6.3 Selecting measurement targets in reciprocal space . . . 113
6.4 Small targets in surroundings like logical circuits . . . 114
6.4.1 Sample description . . . 114
6.4.2 Signal separation . . . 116
6.4.3 Comparison of different grating targets . . . 117
6.5 Discussion . . . 118

7 Conclusion and Outlook 119
7.1 Better parameter reconstruction . . . 119
7.2 New applications for GISAXS . . . 121

Acknowledgements 125

Bibliography 127

Acronyms

AFM atomic force microscopy.

BA Born approximation.

CCD charge-coupled device.

DNA deoxyribonucleic acid.
DWBA distorted-wave Born approximation.

EBL electron-beam lithography.
EUV extreme ultraviolet.

FCM four-crystal monochromator.
FEL free electron laser.
FEM finite element method.
finFET finned field-effect transistor.

GISAXS grazing-incidence small angle X-ray scattering.
GTR grating truncation rod.

HZB Helmholtz-Zentrum Berlin.

MC Monte Carlo.
MCMC Markov chain Monte Carlo.

NIL nanoimprint lithography.
NIST National Institute of Standards and Technology.

OCD optical critical dimension.

PSO particle swarm optimization.
PTB Physikalisch-Technische Bundesanstalt.
PV photovoltaics.

SADP self-aligned double patterning.
SAQP self-aligned quadruple patterning.
SAXS small angle X-ray scattering.
SDD silicon drift detector.
SEM scanning electron microscopy.
SI International System of Units.
STM scanning tunneling microscopy.

TEM transmission electron microscopy.

XRD X-ray diffraction.

Symbols

A atomic weight.
$\boldsymbol{a}$ acceleration.
$A^{\pm}_{f,i}$ distorted-wave Born approximation field amplitudes.
A_{ph} geometrical cross section of a photon.
α fine-structure constant, $\alpha = q_{\mathrm{e}}^2/(2c\varepsilon_0 h) = (7.297\,352\,569\,3 \pm 0.000\,000\,001\,1) \cdot 10^{-3}$.
α_c critical angle of total external reflection.
α_f exit angle.
α_i incidence angle.
$\Delta\alpha_{f,\mathbf{fwhm}}$ full width at half maximum of a scattering peak along the exit angle α_f.

$\boldsymbol{B}$ magnetic field.
B magnetic field strength, $B = |\boldsymbol{B}|$.
β absorptive part of the refractive index $\beta = \Im n$.

c speed of light in vacuum, $c = 299\,792\,458$ m/s.

d distance, e.g. between two lines in a grating.
$d\Omega$ solid angle element.
$d\Phi/d\Omega$ photon flux angular density.
δ dispersive part of the refractive index $\delta = 1 - \Re n$.

$\boldsymbol{E}$ electric field.
$\boldsymbol{E}_i$ incident electric field.
E_{c} critical energy.
E_{e} kinetic energy of electrons.
E_{fe} total energy of a free electron.
E_{ph} X-ray photon energy.
ε electric permittivity tensor of a material.
ε_0 electric constant, also known as vacuum electric permittivity,
$\varepsilon_0 = (8.854\,187\,812\,8 \pm 0.000\,000\,001\,3) \cdot 10^{-12}$ F/m.
η diffraction efficiency.

f electronic scattering factor.
f^0 atomic scattering factor, with $f^0 = f_1^0 + if_2^0$.
$\mathscr{F}$ the distorted-wave Born approximation form factor.
F the Fourier transform of a shape, also called the form factor.

G Green function.
γ electronic Lorentz factor $\gamma = E_{\mathrm{ph}}/(m_{\mathrm{e}}c^2)$.

$\mathbf{H}$ Hilbert space.
h Planck's constant, $h = 6.626\,070\,15 \cdot 10^{-34}$ Js $= 4.135\,667\,696 \cdot 10^{-25}$ eV s.
$\hbar$ $\hbar = h/2\pi$.
h_l line height.

I intensity.
I_0 initial intensity.
I_B background intensity.
I_e electron current.

$\boldsymbol{J}$ electronic current density.

K undulator deflection parameter.
k_0 length of the incident and exit wavevectors, $k_0 = |\boldsymbol{k}_f| = |\boldsymbol{k}_i|$.
$\boldsymbol{k}$ X-ray wavevector.
$\boldsymbol{k}_f$ wavevector of the exit X-rays.
$\boldsymbol{k}_i$ wavevector of the incident X-rays.
k_B Boltzmann's constant, $k_\mathrm{B} = 1.380\,649 \cdot 10^{-23}\,\mathrm{J/K} = 8.617\,333\,262\,145 \cdot 10^{-5}\,\mathrm{eV/K}$.

L length.
l loss factor.
λ X-ray wavelength.
λ_u undulator magnetic period.
$\mathscr{L}$ Likelihood.

M a measurement.
m molecular mass of a compound.
$\boldsymbol{m}$ variable parameters of a theoretical model.
m_e resting mass of the electron $m_\mathrm{e} = (9.109\,383\,56 \pm 0.000\,000\,11) \cdot 10^{-31}\,\mathrm{kg}$.
μ magnetic permeability tensor of a material.
μ_0 magnetic constant, also known as vacuum permeability,
$\mu_0 = (1.256\,637\,062\,12 \pm 0.000\,000\,000\,19) \cdot 10^{-6}\,\mathrm{H/m}$.
μ_l linear attenuation coefficient $\mu_l = \rho\mu_m$.
μ_m mass attenuation coefficient.

N number of magnet pairs in a wiggler or undulator.
n complex refractive index $n = 1 - \delta + i\beta$.
NA numerical aperture of an optical system.
N_A Avogadro constant $N_\mathrm{A} = 6.022\,140\,76 \cdot 10^{23}/\mathrm{mol}$.
n_a atomic density.
ν X-ray frequency.

Ω the parameter space, generally a region $\Omega \subseteq \mathbb{R}^n$.

P probability.
p grating diffraction order.
P_beam beam power.
p_dip dipole moment.
P_el power radiated by the electron.
$\boldsymbol{p}_\mathrm{fe}$ momentum of a free electron.
p_fe magnitude of the momentum of a free electron $p_\mathrm{fe} = |\boldsymbol{p}_\mathrm{fe}|$.
$\boldsymbol{p}_\mathrm{ph}$ momentum of a photon.
p_ph magnitude of the momentum of a photon $p_\mathrm{ph} = |\boldsymbol{p}_\mathrm{ph}|$.
P_s power of the scattered electromagnetic wave.
P_sat saturation power of a free electron laser.
p_sur grating diffraction order of the surrounding.
φ azimuthal rotation angle of the sample with respect to the X-ray beam.
$\varphi_\mathbf{target}$ in-plane rotation angle of the target with respect to the rest of the sample.

Ψ vertical emission angle.

$\boldsymbol{q}$ scattering vector.
q_e elementary charge, $q_\mathrm{e} = 1.602\,176\,634 \cdot 10^{-19}$ C.
$\boldsymbol{q}_\parallel$ projection of the scattering vector onto the sample plane.

R radius.
$\boldsymbol{r}$ spatial coordinate $\boldsymbol{r} = (x, y, z)$.
r_e classical electron radius.
ρ density.
ρ_c charge density.
ρ_FEL FEL parameter, also known as Pierce parameter.
$\mathbb{R}$ the set of real numbers.

$\mathcal{S}$ DWBA interference function.
S_i power of the incident electromagnetic wave per unit area, which is the magnitude of the Poynting vector.
σ_a atomic absorption cross section.
$\frac{d\sigma}{d\Omega}$ angular scattering cross section.
σ_R Rayleigh scattering cross section.
σ_r grating line root mean square roughness.

T thermodynamic temperature.
t time.
$\mathcal{T}$ translation operator.
θ scattering angle.
θ_f azimuthal exit angle.

U voltage.
u uncertainty of a simulation or measurement.
u_a linear uncertainty parameter.

V perturbing potential introduced by a sample.
v speed.

ω rotation frequency, $\omega = 2\pi\nu = 2\pi c/\lambda$.
w_l line width, often called the *critical dimension* in the semiconductor manufacturing context.

$\boldsymbol{x}$ position of a particle.
χ^2 measure of the goodness of fit.

Z atomic number.
$\mathbb{Z}$ the set of integer numbers, including the 0 and negative numbers.
ζ roll angle.

1 Introduction

In nature, nanoscopic machines such as proteins fulfill essential functions despite their diminutive size of less than 100 nm. In the last centuries, humans have started to consciously manufacture nanoscopic structures for diverse applications. An early example of such an engineered nanoscopic system is the standard catalyst for nitrogen fixation. Haber and van Oordt (1905) found out that iron surfaces can be used to catalyse the reaction of atmospheric nitrogen to ammonia, which is used in the production of fertilizers and explosives alike (Crookes 1898), but the reaction rate was found to be too low for an industrial application. To enhance the surface area and therefore the reaction rate, Mittasch and Bosch (1912) developed a preparation method for so-called activated iron. They found the best preparation method by screening hundreds of combinations of starting materials and treatments, selecting the method which produced the catalyst with the highest sustained reaction rate. The reasons for the high reaction rate were investigated after the catalyst was already in widespread use. It was found that activated iron has a porous structure with the smallest pores only about 10 nm in diameter, which maximizes the surface area in a given volume while retaining the catalytic properties of the iron surface (Ertl et al. 1983).

This strategy of directed trial and error was successful, because of the relatively simple objective of the ammonia catalyst. For more complex tasks that are fulfilled by modern nanotechnologies, a mechanistic understanding into the structures and processes at the nanoscale is necessary for progress. This is especially evident in the production of computers, which is arguably the most important modern application of nanotechnology. Integrated electronic circuits based on semiconductor technology were invented in 1961 by Noyce and have been developed at a fast pace since then. The number of components in an integrated circuit grew exponentially (G. E. Moore 1965), so that already in the year 2000, highly integrated circuits incorporated about 10^9 components in an area of a few square millimetres (Mack 2011). The smallest structure produced in these circuits was about 70 nm wide, and smaller structures are developed every year (Schor 2020). To produce these integrated circuits, the lithographic production processes consist of multiple steps, with hundreds of parameters in each step; optimizing them all by trial and error just by testing if the final result works better or worse is simply not possible. Instead, it is necessary to observe the intermediate results of production steps and to develop targeted optimizations (Bunday et al. 2018; Orji et al. 2018). This is the case not only for semiconductor technology, but also for other modern nanotechnologies like thin-film solar cells (Green 2007) or nanoparticles for medical applications (Mochalin et al. 2012).

Because nanoscopic systems are too small to observe directly with our senses, we need to rely on measurements in order to understand the workings of nanoscopic systems. For this, it is often necessary to combine measurements of different nanoscopic and macroscopic properties. Combining information obtained from different measurement methods is only possible by tracing back the measurements to a common reference. The most universal common reference is the International System of Units (SI) (Bureau International des Poids et Mesures 2019). By tracing back a measurement to the definition of the corresponding unit in the SI, we can not only link different measurement methods, but also directly compare measurements done in different laboratories. This is the aim of measurement science (metrology) and nanometrology is the application of metrology to nanoscopic systems. My focus is on dimensional nanometrology, i.e. on measurements of the shape and size of nano structures.

The microscopic world was discovered using visible light microscopes (Leeuwenhoek 1677; Lane 2015). However, the resolution of light microscopes using external illumination is limited by the wavelength of the light, which limits such microscopes using visible light to a resolution of about 200 nm (Abbe 1873). Therefore, other methods have been invented to explore the nanoscopic world. The most important methods for exploring the nanoscopic world can be classified into microscopy and scattering methods. Due to the mentioned Abbe's limit, the microscopy methods use probes other than visible light to reach higher resolution. The scattering methods, which do not directly deliver an image of the specimen, are not bound by Abbe's limit.

In microscopy, many different probes have been developed, each with their unique strengths. Due to their finite mass, electrons have a very short de-Broglie wavelength (de Broglie 1924; Davisson and Germer 1928), and consequently transmission electron microscopy (TEM) can reach very good resolution (Alem et al. 2009). TEM works very similarly to visible light microscopy. The entire sample is illuminated at once and electrical fields are used to focus the electron beam onto a sensor surface (Knoll and Ruska 1932). For other microscopy techniques, a beam or other probe is scanned over the sample, collecting the signal point by point. Using an electron beam, the technique is called scanning electron microscopy (SEM) (von Ardenne 1938), but also a cantilever with a sharp tip can be scanned over the surface. When the information is obtained from the deflection of the cantilever, the technique is known as atomic force microscopy (AFM) (Binnig, Quate, and Gerber 1986), and when information is instead obtained from an electrical tunneling current between tip and surface, it is called scanning tunneling microscopy (STM) (Binnig, Rohrer, et al. 1982). While each microscopy technique has different advantages due to the underlying interaction between probe and sample, all of these techniques offer nanometre resolution and detailed insights into the investigated nanostructures, but the field of view is limited to a few μm^2.

Collecting statistical information on large nanostructured surfaces or over many nanoscopic samples spread out in a large volume using microscopy requires collecting many images and is therefore often prohibitively time-consuming. In contrast, scattering methods provide statistical information on the dimensional properties over a large volume, but do not yield a measurement of any individual sample or detail. In my thesis, I will focus on scattering, in particular on X-ray scattering.

Originally, X-ray diffraction (XRD) was used to investigate the arrangement and distances of atoms in crystals. An X-ray beam impinges on the sample under investigation and the scattering of the beam is recorded (Friedrich, Knipping, and Laue 1913). From the recorded scattered pattern, the crystal structure can then be deduced. Due to the interference of the scattered X-rays, there is an inverse relationship between the size of the investigated structure and the scattering angle (Ewald 1913). By recording small angle X-ray scattering (SAXS), nanoscopic structures which are larger than individual atoms can therefore be investigated (Glatter and Kratky 1982). For the investigation of nanostructured surfaces in particular, it is often beneficial to measure in reflection geometry, because spurious signals from bulky samples are avoided while the signal from the surface is enhanced (Levine et al. 1989). The method is then called grazing-incidence small angle X-ray scattering (GISAXS).

Since its introduction in 1989, GISAXS was developed rapidly and is now established as a powerful technique for the investigation of nanostructured surfaces. It offers non-destructive, contact-free measurements of sample structures with feature sizes between about 1 nm and 1 µm, giving statistical information about the whole illuminated volume. GISAXS has been used to investigate the active layer of organic solar cells (Gu, C. Wang, and Russell 2012; Müller-Buschbaum 2014), surface and bulk morphology of polymer films (Müller-Buschbaum 2003; Wernecke, Okuda, et al. 2014), lithographically produced structures (Gollmer et al. 2014; Soccio et al. 2015), and many other

nanostructured surfaces (Renaud, Lazzari, and Leroy 2009; Hexemer and Müller-Buschbaum 2015). However, a method to trace back the measurement results to the SI with a thorough discussion of the measurement uncertainties was so far only presented for measurements of the period of nanoscopic gratings (Wernecke, Krumrey, et al. 2014). As explained above, nanometrology has a crucial role in correlating nanoscopic structure and macroscopic function; therefore, I will develop methods to trace back GISAXS measurements of other key dimensional parameters of nanoscopic systems to the SI and apply GISAXS measurements to additional types of samples.

I will present three studies that I conducted at the synchrotron radiation laboratory of the Physikalisch-Technische Bundesanstalt (PTB), which comprises several beam lines at the electron storage rings BESSY II and MLS I. My work starts in chapter 2 with a review of the physical foundations of X-ray science in general and GISAXS in particular. Then in chapter 3 I will present the methods that I have used in the experiments and the data analysis. Chapter 4 contains a study about the use of GISAXS to quantify defects introduced in nanoimprint lithography (NIL), which harnesses the statistical power of scattering methods. In chapter 5, I will then present the application of GISAXS to the dimensional measurement of complex grating structures produced in high-volume semiconductor manufacturing. For this, I will review the state of the art in GISAXS measurements of lithographically produced gratings, and describe the challenges arising in modern semiconductor metrology. In chapter 6, a method to circumvent the problem of large beam footprints in semiconductor metrology using GISAXS is introduced. Finally, I will conclude in chapter 7 and offer an outlook on future developments which could prove most interesting for the application of GISAXS in the field of dimensional nanometrology.

Electronic supplementary information for my thesis is available at `https://doi.org/10.18452/21660` and `https://doi.org/10.24433/CO.0375205.v1`; links to the supplementary information will be provided where relevant within the text.

2 Fundamentals

In this chapter, I will introduce the physical foundations of grazing-incidence small angle X-ray scattering (GISAXS). In the beginning stands a general introduction into the interaction of X-rays with matter in section 2.1. In section 2.2, the focus will be on the GISAXS method itself. I will close with a discussion of the means to generate (section 2.3) and detect (section 2.4) X-rays for an experimental implementation of GISAXS.

2.1 Interaction of X-rays with matter

X-rays are, like visible and ultra-violet light, electromagnetic radiation, but with a wavelength even shorter than ultra-violet light. The definitions vary, but most scholars agree that X-ray radiation is (at least) radiation with a photon energy E_{ph} higher than 1 keV and lower than 100 keV, corresponding to a wavelength λ shorter than about 1.24 nm and longer than about 12.4 pm.

When Röntgen (1895) discovered the X-rays, he observed that X-rays go through matter without visible refraction and are only weakly attenuated. Röntgen further observed that the transmission of X-rays through matter is generally lower for denser material, and thicker layers of material block more X-rays than thin layers. More quantitatively, the attenuation of X-rays can be described using the Beer-Lambert law:

$$I = I_0 e^{-\mu_l x} \quad , \tag{2.1.1}$$

with the intensity I, the initial intensity I_0, the linear attenuation coefficient μ_l and the path travelled within the absorbing medium x (Meschede 2015a). As Röntgen noticed, μ_l is material dependent and generally small, which is used when X-ray images of otherwise opaque specimens are made for medical or technological purposes.

In a good approximation, the linear attenuation coefficient μ_l of a material depends on its density ρ and its elemental composition

$$\mu_l(E_{\mathrm{ph}}) = \mu_m(E_{\mathrm{ph}})\,\rho \tag{2.1.2}$$

$$\mu_m(E_{\mathrm{ph}}) = \frac{1}{m}\sum_i x_i\,\sigma_{\mathrm{a},i}(E_{\mathrm{ph}}) \tag{2.1.3}$$

$$m = \sum_i x_i A_i \quad . \tag{2.1.4}$$

Here, μ_m is the mass attenuation coefficient of a chemical compound consisting of x_i atoms of type i with atomic mass A_i and the atomic absorption cross section $\sigma_{\mathrm{a},i}$, and the molecular mass of this compound m (Thompson et al. 2009, section 1.6). The reason for this element-specific interaction is that X-rays interact mostly with the electrons in matter; therefore, the most important factor for determining the interaction strength with a material is its electron density, which is determined by its mass density ρ and the ratio of atomic mass to electrons, which is specific for the elements.

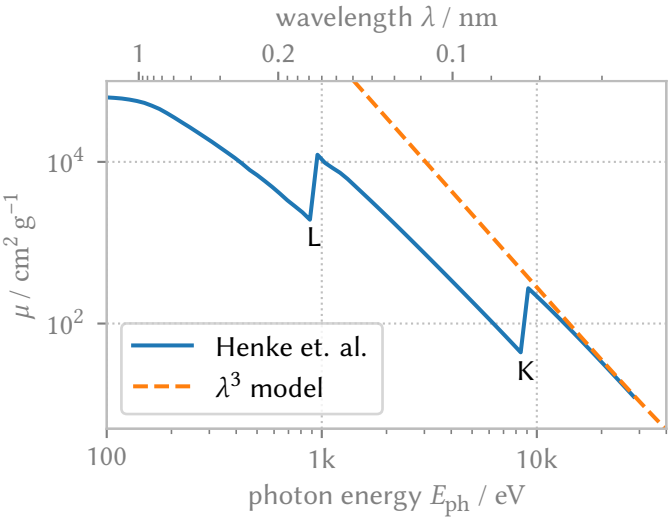

Figure 2.1: X-ray absorption of copper. The solid line shows measured data by Henke, Gullikson, and Davis (1993), the dashed line a λ^3 model by Richtmyer (1921) that is based on an empirical pre-factor and an additive constant. The λ^3 model describes the absorption above the Cu K absorption edge pretty well, but fails at lower photon energies.

To understand X-ray attenuation as well as elastic and inelastic scattering in more detail, I will consider the microscopic processes of interaction between X-ray photons and atoms. Because the electrons in matter are bound in atoms and occupy discrete energy levels, there are fundamentally three different outcomes of an interaction between an X-ray photon and an electron: the electron can transfer into an unbound state and be ejected from the atom, it can transfer to an unoccupied bound state of higher energy, or its energy can be unchanged. I will first discuss the ejection of an electron, which is the main process of X-ray absorption, and then discuss the other two effects, which mainly contribute to X-ray refraction.

2.1.1 Photoelectric effect

If an X-ray photon is absorbed by an atom, an electron can be ejected from the atom if the photon energy E_ph is higher than the binding energy of the electron. Any excess energy is carried away by the photoelectron as kinetic energy, and the atom is left in an ionized state. Because this is one of the fundamental interactions between X-rays and matter, I will derive the qualitative behaviour of the photoelectric absorption cross section with respect to the incident photon energy $\sigma_{\mathrm{a},pe}(E_\mathrm{ph})$, albeit using a very rough semi-classical approximation. I assume that the bound electron can be treated as a Hertz dipole rotating or oscillating with its resonance frequency ν_r. Then the power radiated or absorbed by the electron is

$$P_\mathrm{el} = \frac{8\pi p_\mathrm{dip}^2 \nu_r^4}{3\varepsilon_0 c^3} \propto \nu_r^4 \quad , \tag{2.1.5}$$

with the electronic dipole moment p_dip and the vacuum electric permittivity ε_0 (Larmor 1897; Meschede 2015b). From the power, we can compute the time it takes on average to radiate or absorb one photon with the frequency ν_r

$$t_0 = \frac{E_\mathrm{ph}}{P_\mathrm{el}} = \frac{h\nu_r}{P_\mathrm{el}} \propto \nu_r^{-3} \quad , \tag{2.1.6}$$

with Planck's constant h. I further assume that the radius of the photon is proportional to its wavelength λ, which means that an essentially stationary electron interacts with the photon during a time span $dt \propto c\lambda$, with the speed of light c. Assuming that the electron is vanishingly

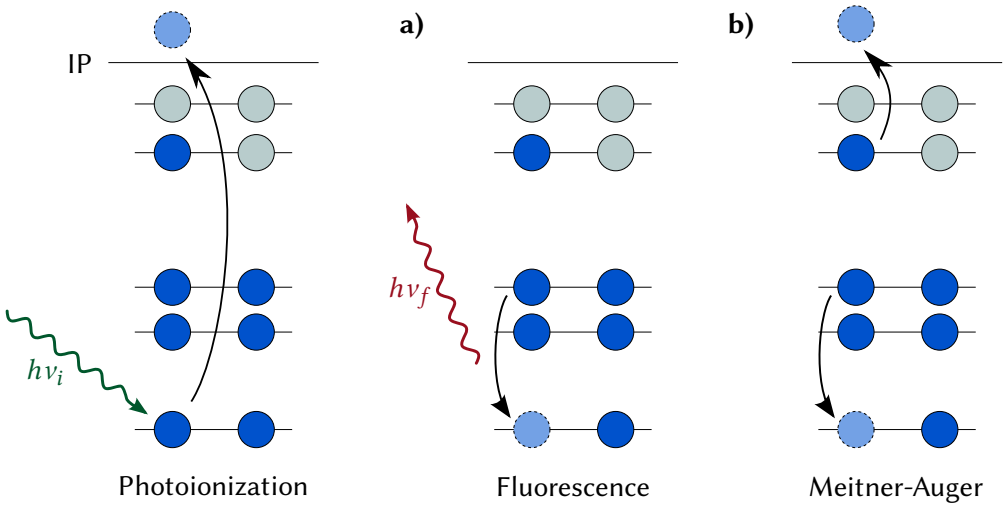

Figure 2.2: Decay mechanisms after X-ray photoionization. The excited state typically produced by X-ray photoionization can decay via different pathways, the two most important are shown here. **a)** In fluorescence, an electron occupying a higher energy level transitions into the empty lower energy level, the energy difference is emitted as a photon of energy $h\nu_f \neq h\nu_i$. **b)** In a Meitner-Auger decay, an electron occupying a higher energy level transitions into the empty lower energy level and another electron occupying a high energy level close to the ionization potential (IP) is ejected. The remaining energy difference is carried away by the ejected electron as kinetic energy.

small and using that the geometrical cross section of the photon is $A_{\mathrm{ph}} \propto \lambda^2$ we arrive at

$$\sigma_{\mathrm{a},pe}(E_{\mathrm{ph}}) = \frac{dt}{t_0} A_{\mathrm{ph}} \propto \frac{\lambda}{\nu_r^{-3}} \lambda^2 \propto \left(\frac{E_r}{E_{\mathrm{ph}}} \right)^3 \quad , \tag{2.1.7}$$

with the resonance energy of the electron E_r (Meschede 2015a, pages 838-839). Even though this description relies on the Bohr model of the atom and some very rough approximations, it reproduces the general features of the photoelectric absorption cross section, namely the existence of absorption edges at the ionization energies of the electrons and the E_{ph}^{-3} behaviour in the rest of the spectrum (see figure 2.1). A proper treatment of the photoelectric absorption cross section needs the full apparatus of quantum mechanics and can in general only be solved numerically, because any atoms heavier than hydrogen present a many-body problem (James 1962, chapters III and IV).

After X-ray photoionization, the ion is generally left in an excited state. This is because at X-ray photon energies, electrons are ejected from lower-lying (core) energy levels, such that a core hole is created, which can be filled by electrons from higher-lying energy levels. The two competing decay processes are fluorescence and Meitner-Auger decay, which I will discuss in the following sections.

2.1.2 Fluorescence

An excited state can decay by filling the core hole left by photoionization with an electron from a higher energy level where the energy difference is emitted as electromagnetic radiation (Barkla 1911), see figure 2.2a. The emitted photon energy $h\nu_f$ is characteristic for the difference between electronic energy levels and therefore characteristic for the element. These energies are tabulated by Thompson et al. (2009). The chemical environment of the involved atom can modify the

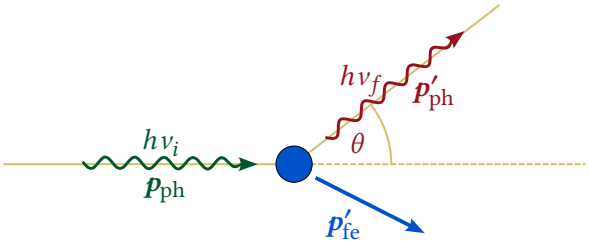

Figure 2.3: Compton scattering. The photon with energy $h\nu_i$ and momentum $\boldsymbol{p}_{\mathrm{ph}}$ scatters off an electron. After the collision, the photon has the momentum $\boldsymbol{p}'_{\mathrm{ph}}$, and the photon is scattered by the angle θ and has the energy $h\nu_f$.

electronic energy levels, in particular the higher energy levels which are involved in chemical bindings. This shifts the energy of the fluorescence, which opens the possibility to discern the chemistry of a sample using X-ray fluorescence spectroscopy. A treatment of the theory and application of X-ray fluorescence can be found in the handbook written by Beckhoff, Kanngießer, et al. (2006).

2.1.3 Meitner-Auger decay

Another decay mechanism of the photoionized state, which is radiation-less, was observed and explained by Meitner (1922) and later independently by Auger (1923). In this process, the energy of the decay is not converted into an X-ray photon. Instead, the energy is transferred to an electron in a high energy level. The energy is partly converted into potential energy by ejecting the electron from the atom, and partly converted into kinetic energy of the electron, see figure 2.2b. Because all of the decay energy is carried away by the expelled electron, no photon is emitted. The kinetic energy of the emitted electron is also related to the electronic energy levels, and thus specific for the element and affected by chemical shifts (Fahlman et al. 1966).

2.1.4 Scattering

If an X-ray photon scatters off an electron without changing its energy, the process is called elastic scattering due to its similarity to elastic scattering in classical mechanics. The other remaining case, where the photon changes energy without being fully absorbed, is called inelastic scattering. Although we are interested in the scattering of photons by bound electrons, I will start with the description of the scattering by a free electron, which is considerably simpler yet still instructive. From there, I will look at different approximations for the treatment of bound electrons.

2.1.5 Compton scattering

The interaction between a photon with energy $E_{\mathrm{ph}} = h\nu_i$ and an electron at rest can be described as a relativistic collision (see figure 2.3). After the collision, the photon has changed energy and direction, with the new energy $E'_{\mathrm{ph}} = h\nu_f$, the new momentum $\boldsymbol{p}'_{\mathrm{ph}}$ and the scattering angle θ, and the electron has the momentum p'_{fe}. From the conservation of energy and momentum Compton (1923a) derived the photon energy after scattering, which is

$$E'_{\mathrm{ph}}(E_{\mathrm{ph}}, \theta) = h\nu_f = \frac{E_{\mathrm{ph}}}{1 + \frac{E_{\mathrm{ph}}}{m_{\mathrm{e}}c^2}(1 - \cos\theta)} \quad . \tag{2.1.8}$$

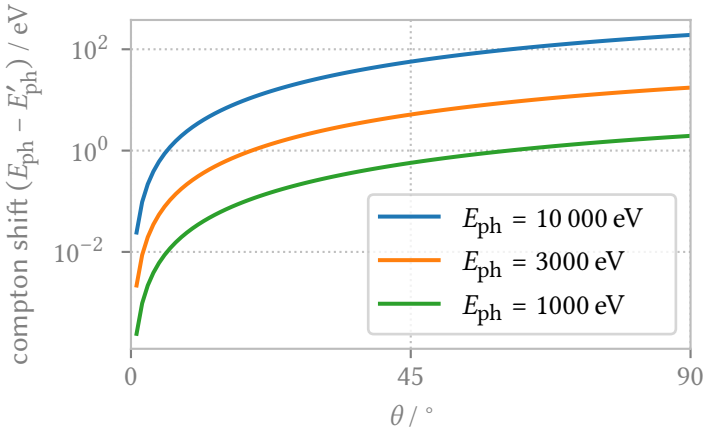

Figure 2.4: Shift in photon energy arising from Compton scattering at a free electron at rest. In the limit of small scattering angles θ or small initial photon energies E_{ph}, the Compton shift vanishes.

The photon energy shift from a Compton scattering event is shown in figure 2.4. In the limit of either small scattering angles or small initial photon energies, the scattering is nearly elastic and coherent. In contrast, at high scattering angles and high photon energies, the shift is considerable.

For a bound electron, two limiting cases can be considered without the need for detailed calculations. In the limit of very high photon energies much larger than the ionization potential of the electron, the electron can be regarded as free and equation (2.1.8) applies. On the other end of the spectrum, in the limit of small photon energies which are smaller than the smallest possible transition of the electron, no energy or momentum can be transferred to the electron alone. Instead, the energy and momentum are transferred to the full atom, and in equation (2.1.8), the electron mass has to be replaced by the atom mass. Because the atom mass is much larger, $E_{ph}/(mc^2)$ vanishes and the scattering can be regarded as elastic. For photon energies which are neither very large nor very small, the inner structure of the atom has to be considered, and Compton scattering does not describe the scattering correctly.

2.1.6 Rayleigh scattering at atoms

In general, the scattering of X-ray photons by an atom is a many-body problem, and can not be solved exactly. However, in a rather rough approximation, we can regard the scattering by an atom as scattering by individual bound electrons and derive the total atomic scattering as a sum over the scattering of all bound electrons. Therefore, I will now derive the scattering cross section of a single bound atom using a semi-classical model. While this approximation is also very rough, we can still learn a lot about the qualitative behavior of scattering of X-rays by matter.

The scattering cross section σ_R is defined by the incident power per unit area S_i and the scattered power P_s

$$\sigma_R = \frac{P_s}{S_i} \quad ; \tag{2.1.9}$$

therefore, I will calculate the incident and scattered power of the electromagnetic waves. For this, I assume that a bound electron exhibits a resonance frequency $\nu_r = \omega_r/2\pi$ and is accelerated in the electric field $\boldsymbol{E}_i$ of the incident electromagnetic wave according to the equations of motion of a damped harmonic oscillator

$$m_e \frac{d^2\boldsymbol{x}}{dt^2} + m_e l \frac{d\boldsymbol{x}}{dt} + m_e \omega_r^2 \boldsymbol{x} = -q_e \boldsymbol{E}_i \quad , \tag{2.1.10}$$

with the position of the electron $\boldsymbol{x}$ and the loss factor $l \ll \omega_r$. The first term in the equations of motion is the acceleration, the second the damping, the third the restoring force of a harmonic oscillator with resonance circular frequency ω_r, and the right hand side is the Lorentz force where the magnetic part is neglected (Attwood 1999, page 42).

With an incident electric field of a photon with frequency $\nu = \omega/2\pi$ the electric field is

$$\boldsymbol{E}_i = \boldsymbol{E}_{i,0} e^{-i\omega t} \quad . \tag{2.1.11}$$

Inserting this into equation (2.1.10), the solutions will then show the same time dependence

$$\boldsymbol{x} \propto e^{-i\omega t} \tag{2.1.12}$$

$$\implies \frac{d\boldsymbol{x}}{dt} = -i\omega\boldsymbol{x} \quad . \tag{2.1.13}$$

Inserting the derivatives into equation (2.1.10) yields

$$-\omega^2 m_\mathrm{e}\boldsymbol{x} - i\omega l m_\mathrm{e}\boldsymbol{x} + \omega_r^2 m_\mathrm{e}\boldsymbol{x} = -q_\mathrm{e}\boldsymbol{E}_i \tag{2.1.14}$$

$$\implies \boldsymbol{x} = \frac{1}{\omega^2 - \omega_r^2 + i\omega l}\frac{q_\mathrm{e}\boldsymbol{E}_i}{m_\mathrm{e}} \tag{2.1.15}$$

$$\implies \frac{d^2\boldsymbol{x}}{dt^2} = \frac{-\omega^2}{\omega^2 - \omega_r^2 + i\omega l}\frac{q_\mathrm{e}\boldsymbol{E}_i}{m_\mathrm{e}} \quad . \tag{2.1.16}$$

The power radiated by an oscillating electron is (Attwood 1999, page 37)

$$P_\mathrm{el} = \frac{8\pi}{3}\frac{q_\mathrm{e}^2}{16\pi^2\varepsilon_0 c^3}\left|\frac{d^2\boldsymbol{x}}{dt^2}\right|^2 \tag{2.1.17}$$

$$\implies P_s = \frac{8\pi}{3}\frac{q_\mathrm{e}^2}{16\pi^2\varepsilon_0 c^3}\left|\frac{\omega^2}{\omega^2 - \omega_r^2 + i\omega l}\right|^2 \frac{q_\mathrm{e}^2|\boldsymbol{E}_i|^2}{m_\mathrm{e}^2} \quad , \tag{2.1.18}$$

and the power per unit area carried by an electromagnetic wave is (Attwood 1999, pages 35f)

$$S = \sqrt{\frac{\varepsilon_0}{\mu_0}}|\boldsymbol{E}|^2 \tag{2.1.19}$$

$$\implies S_i = \sqrt{\frac{\varepsilon_0}{\mu_0}}|\boldsymbol{E}_i|^2 = \varepsilon_0 c|\boldsymbol{E}_i|^2 \quad . \tag{2.1.20}$$

Now, I can calculate the Rayleigh cross section

$$\sigma_\mathrm{R} = \frac{P_s}{S_i} = \frac{8\pi}{3}\frac{q_\mathrm{e}^4}{16\pi^2\varepsilon_0 c^3 m_\mathrm{e}^2}\left|\frac{\omega^2}{\omega^2 - \omega_r^2 + i\omega l}\right|^2 |\boldsymbol{E}_i|^2\frac{1}{\varepsilon_0 c|\boldsymbol{E}_i|^2} \tag{2.1.21}$$

$$= \frac{8\pi}{3}r_\mathrm{e}^2\left|\frac{\omega^2}{\omega^2 - \omega_r^2 + i\omega l}\right|^2 \tag{2.1.22}$$

$$= \frac{8\pi}{3}r_\mathrm{e}^2|f|^2 \tag{2.1.23}$$

$$f := \frac{\omega^2}{\omega^2 - \omega_r^2 + i\omega l} \tag{2.1.24}$$

$$r_\mathrm{e} := \frac{q_\mathrm{e}^2}{4\pi\varepsilon_0 c^2 m_\mathrm{e}} \quad , \tag{2.1.25}$$

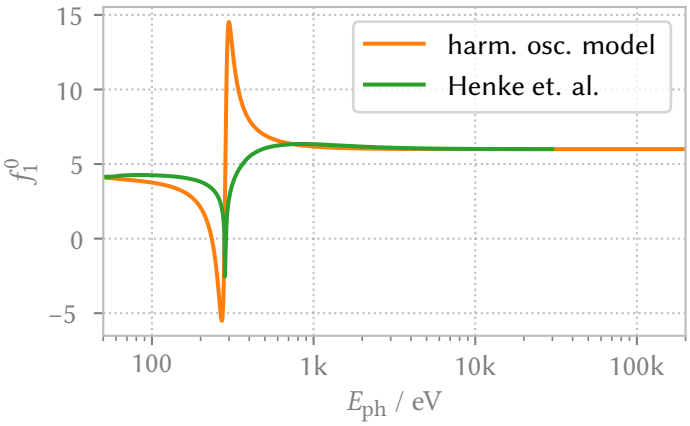

Figure 2.5: The Rayleigh scattering cross section of carbon. Values derived using the semi-classical harmonic oscillator model with a loss factor $l = 0.1\omega_r$ are compared to tabulated values by Henke, Gullikson, and Davis (1993).

with the scattering factor f and the classical electron radius r_e.

Before I turn to the discussion of scattering of whole atoms, I will discuss the limiting cases of small and large photon frequencies. For large photon frequencies $\omega \longrightarrow \infty$, the scattering factor will become unity $f \longrightarrow 1$ and we recover the Thomson cross section

$$\sigma_T = \frac{8\pi}{3} r_e^2 \tag{2.1.26}$$

that describes scattering by a free electron (Attwood 1999, page 43). As already argued, this can be understood from the fact that for very high-energy photons, the bound electrons are essentially free.

Conversely, for small photon frequencies $\omega \ll \omega_r$ the scattering factor reduces to $f \longrightarrow (\omega/\omega_r)^2$ and we recover the Rayleigh cross section for visible light (Strutt 1871)

$$\sigma_R = \frac{8\pi}{3} r_e^2 \left(\frac{\lambda_r}{\lambda}\right)^4 \quad . \tag{2.1.27}$$

From this λ^{-4} behavior, Strutt explained the color of the sky and its changes over the day.

Now, I will get back to the calculation of the scattering factor of a full atom f^0. I calculate it using the scattering factor of an individual bound electron given in equation (2.1.23) by assuming that I can simply sum over all electrons in the atom:

$$f^0 = \sum_i^Z \frac{\omega^2}{(\omega^2 - \omega_{r,i}^2) + \omega l_i} \tag{2.1.28}$$

$$= f_1^0 + i f_2^0 \quad , \tag{2.1.29}$$

with the set of electrons Z in the atom and their resonances $\omega_{r,i}$ and loss factors l_i. The real part of the scattering factor f_1^0, which corresponds to dispersion, is plotted and compared to experimental data in figure 2.5. The model predicts that at photon energies just below the resonance determined by the electronic resonance frequency, f_1^0 will fall steeply, even reversing the sign. Directly above the resonance frequency, it will rise quickly to a peak above the starting value to then slowly settle on a value slightly above the starting value. Qualitatively, this agrees well with the experimental data, with the exception that the experimental data does not show the sharp and high peak just above the resonance which the model predicts. Quantitatively, the model agrees with the experimental data only at considerable distance from the resonance.

Because X-ray energies are frequently close to atomic resonances, the atomic scattering factors have to be measured or calculated properly using relativistic quantum electrodynamics (Kissel, Pratt, and Roy 1980). Tabulated values calculated using a semi-empirical model that incorporates experimental data where available are published by Henke, Gullikson, and Davis (1993) and should be used for practical purposes.

2.1.7 The refractive index

Because it will become useful in the description of GISAXS experiments later on, my next step is to describe elastic X-ray scattering at small angles using the standard wave equation of optics. For this, several additional simplifications are necessary. At small scattering angles, the Compton energy shift vanishes, and Compton scattering can be approximated as elastic scattering, so I will restrict my discussion to Rayleigh scattering. I will follow Attwood (1999, chapter 3), where a more detailed treatment can be found.

I start with the description of X-ray propagation in a homogeneous medium made up of atoms. From Maxwell's equations, the vector wave equation for electromagnetic waves follows directly

$$\left(\frac{\partial^2}{\partial t^2} - c^2\nabla^2\right)\boldsymbol{E}(\boldsymbol{r},t) = \frac{-1}{\varepsilon_0}\left(\frac{\partial \boldsymbol{J}(\boldsymbol{r},t)}{\partial t} + c^2\nabla\rho_\mathrm{c}(\boldsymbol{r},t)\right) \quad , \tag{2.1.30}$$

with the current density $\boldsymbol{J}$, the electric field $\boldsymbol{E}$ and the charge density ρ_c (Attwood 1999, chapter 2, eq. 2.7). For X-rays (and electromagnetic waves in general), the electric field $\boldsymbol{E}$ is perpendicular to the propagation direction $\boldsymbol{E} \perp \boldsymbol{k}$, with wavevector $\boldsymbol{k}$. The vector wave equation can then be reduced to the parts that are perpendicular to $\boldsymbol{k}$

$$\left(\frac{\partial^2}{\partial t^2} - c^2\nabla^2\right)\boldsymbol{E}_\perp(\boldsymbol{r},t) = \frac{-1}{\varepsilon_0}\frac{\partial \boldsymbol{J}_\perp(\boldsymbol{r},t)}{\partial t} \quad . \tag{2.1.31}$$

Because I only consider Rayleigh scattering, I can assume that the X-rays are scattered solely in the forward direction ($\theta = 0$). Then the scattering of all the atoms (and of the individual electrons in the atoms) combines coherently, so that individual positions of the electrons do not matter, and the total current density is simply the sum of the motion of the individual electrons

$$\boldsymbol{J}(\boldsymbol{r},t) = -q_\mathrm{e}\sum_a\sum_i^{Z_a}\frac{\partial \boldsymbol{x}_i(\boldsymbol{r},t)}{\partial t} \tag{2.1.32}$$

$$= -q_\mathrm{e}n_a\sum_i^{Z}\frac{\partial \boldsymbol{x}_i(\boldsymbol{r},t)}{\partial t} \quad \text{for identical atoms} \tag{2.1.33}$$

$$\Rightarrow \frac{\partial \boldsymbol{J}_\perp(\boldsymbol{r},t)}{\partial t} = -q_\mathrm{e}n_a\sum_i^{Z}\frac{\partial^2 \boldsymbol{x}_{i,\perp}(\boldsymbol{r},t)}{\partial t^2} \tag{2.1.34}$$

using the result for individual electrons from equation (2.1.15) it follows

$$\boldsymbol{x}(\boldsymbol{r},t) = \frac{1}{\omega^2 - \omega_r^2 + i\omega l}\frac{q_\mathrm{e}\boldsymbol{E}(\boldsymbol{r},t)}{m_\mathrm{e}} \tag{2.1.35}$$

$$\Rightarrow \frac{\partial \boldsymbol{J}_\perp(\boldsymbol{r},t)}{\partial t} = -\frac{q_\mathrm{e}^2 n_a}{m_\mathrm{e}}\sum_i^{Z}\frac{1}{\omega^2 - \omega_{r,i}^2 + i\omega l_i}\frac{\partial^2 \boldsymbol{E}_\perp(\boldsymbol{r},t)}{\partial t^2} \quad , \tag{2.1.36}$$

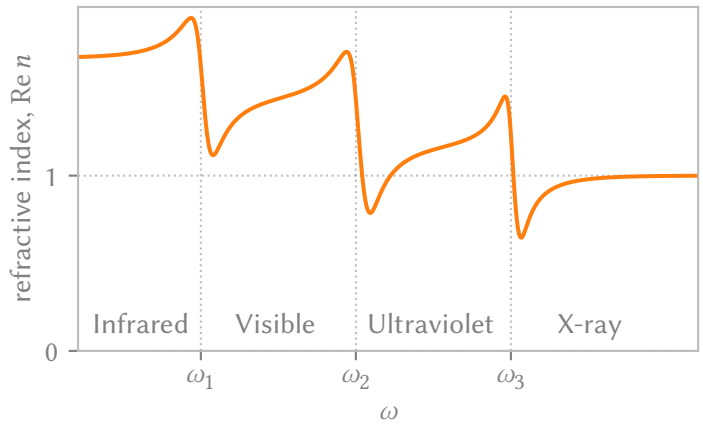

Figure 2.6: Sketch of the real part of the refractive index. The ω_i are atomic resonance frequencies. In the infrared and visible spectral ranges, the refractive index stays above unity, but for X-rays it is generally below unity; in the ultraviolet spectral range, both is possible. Adapted from Attwood (1999, fig. 3.1).

with the set of electrons Z in each atom and their resonances $\omega_{r,i}$ and loss factors l_i and the atomic density n_a. Substituting this into the transverse wave equation (2.1.31) and reordering yields:

$$\left(\frac{\partial^2}{\partial t^2} - c^2\nabla^2\right)\boldsymbol{E}_\perp(\boldsymbol{r},t) = \frac{q_e^2 n_a}{m_e\varepsilon_0}\sum_i^Z \frac{1}{\omega^2 - \omega_{r,i}^2 + i\omega l_i}\frac{\partial^2 \boldsymbol{E}_\perp(\boldsymbol{r},t)}{\partial t^2} \tag{2.1.37}$$

$$\Rightarrow \left(\underbrace{\left(1 - \frac{q_e^2 n_a}{m_e\varepsilon_0}\sum_i^Z \frac{1}{\omega^2 - \omega_{r,i}^2 + i\omega l_i}\right)}_{n^2(\omega)}\frac{\partial^2}{\partial t^2} - c^2\nabla^2\right)\boldsymbol{E}_\perp(\boldsymbol{r},t) = 0 \tag{2.1.38}$$

$$\Rightarrow \left(\frac{\partial^2}{\partial t^2} - \frac{c^2}{n^2(\omega)}\nabla^2\right)\boldsymbol{E}_\perp(\boldsymbol{r},t) = 0 \quad . \tag{2.1.39}$$

This is the standard wave equation of optics, with the frequency dependent refractive index n which can be rewritten in terms of the atomic scattering factor f^0 and the classical electron radius r_e:

$$n(\omega) = \sqrt{1 - \frac{q_e^2 n_a}{m_e\varepsilon_0}\sum_i^Z \frac{1}{\omega^2 - \omega_{r,i}^2 + i\omega l_i}} \tag{2.1.40}$$

$$= \sqrt{1 - \frac{q_e^2 n_a}{m_e\varepsilon_0}\frac{f_0}{\omega^2}} \tag{2.1.41}$$

$$= \sqrt{1 - \frac{n_a r_e \lambda^2}{\pi} f_0} \tag{2.1.42}$$

$$\approx 1 - \frac{n_a r_e \lambda^2}{2\pi} f_0 \quad \text{for } n_a r_e \lambda^2 f^0 \ll 1. \tag{2.1.43}$$

Figure 2.6 shows a sketch of the real part of the refractive index from the infrared to the X-ray spectral ranges. In contrast to the refractive index in standard (visible light) optics, the X-ray refractive index is generally below unity, and the deviations from unity are generally small. Therefore, it is common to express the complex refractive index as

$$n = 1 - \delta + i\beta \quad , \tag{2.1.44}$$

with the dispersion δ and the absorption β. Note that there exist two conventions for the choice of the sign of $i\beta$; the plus sign that I use throughout my work is consistent with the description of

the electromagnetic wave using $\exp(-i(\omega t - \boldsymbol{k} \cdot \boldsymbol{r}))$ and is common in quantum mechanics and optics, while the opposite choice with a minus sign is common in texts on X-ray crystallography. However, β is always defined such that positive values of β correspond to *absorption*, and negative values correspond to luminescence.

2.2 GISAXS

Grazing-incidence small angle X-ray scattering (GISAXS) is a powerful non-destructive technique for the investigation of nanostructured surfaces. In GISAXS, a flat, nanostructured sample of interest is illuminated with X-rays at grazing incidence, and the angular distribution of the reflected and scattered X-rays is measured. This scattering distribution depends on the morphology of the sample, which allows us to obtain statistical information about the nanoscopic structures on the sample surface (Renaud, Lazzari, and Leroy 2009; Hexemer and Müller-Buschbaum 2015).

In this section, I will first give a brief overview of the development of GISAXS and what distinguishes it from related methods; then I will describe the scattering process and discuss what information can be obtained from the GISAXS patterns.

2.2.1 Development and related methods

Friedrich, Knipping, and Laue (1913) discovered that crystals scatter X-rays into sharp diffraction peaks, and that the position of the peaks depends on the crystal lattice. The technique of X-ray diffraction (XRD) quickly became the most important tool to determine the arrangement of atoms within solids, with such important results like elucidating the structure of deoxyribonucleic acid (DNA), the molecule carrying the genome (Watson and Crick 1953; Wilkins, Stokes, and Wilson 1953; Franklin and Gosling 1953) and determining the origins of different properties of amorphous solids like glass (Warren and Biscce 1938).

Because the X-rays that get scattered by the sample interfere, the scattering angles are inversely related to the distances of the scatterers (Ewald 1913). Therefore, the characteristic length scales that can be investigated with X-ray scattering methods depend on the recorded scattering angle. As I will show in subsection 2.2.2, when monochromatic X-rays with wavelength λ are scattered by a series of layers with distance d, diffraction peaks can be seen at the scattering angles θ that fulfill Bragg's law

$$2d \sin\theta = n\lambda \quad , \tag{2.2.1}$$

with the diffraction order $n \in \mathbb{Z}$ (W. H. Bragg and W. L. Bragg 1913). We see that at typical X-ray wavelengths of $\lambda \approx 0.1\,\text{nm}$, simple crystals made of small atoms with $d \approx 0.15\,\text{nm}$ scatter to $\theta \approx 20°$ at $n = 1$. If the scatterers are not the individual atoms in a crystal, but rather nanoscopic structures like nanoparticles, the typical length scales are on the order of $d \approx 100\,\text{nm}$, leading to scattering angles $\theta \approx 0.03°$.

Early in the history of X-ray scattering methods, the development was focused on typical crystals with large scattering angles, and the scattering to small angles was not investigated in detail. However, Krishnamurti (1930) studied colloidal dispersions at small scattering angles, and later small angle X-ray scattering (SAXS) was developed as a separate technique due to the unique experimental and theoretical apparatus needed (Glatter and Kratky 1982). As discussed in subsection 2.1.6, the X-ray scattering cross section is mainly determined by interactions between X-rays and electrons. Therefore, the X-ray contrast is mainly given by the electron density, and a

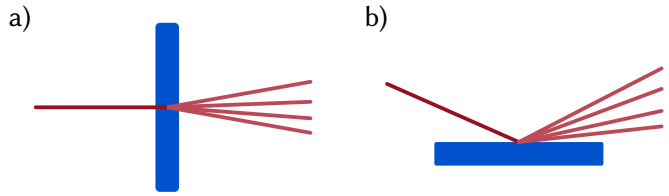

Figure 2.7: SAXS and GISAXS geometry. a) In SAXS, the X-rays are scattered when transmitted through the sample. **b)** In GISAXS, the X-rays are scattered when reflected by the sample.

SAXS signal can always be observed if there is an electron density contrast within the specimen (Glatter and Kratky 1982).

SAXS has been applied in varied fields such as the analysis of proteins and other biomolecules in solution (Koch, Vachette, and Svergun 2003), porous nanoparticles (Sinkó, Torma, and Kovács 2008), and lithographically produced gratings (Jones et al. 2003). An overview of the theoretical methods to analyze SAXS measurements is given by Boldon, Laliberte, and Liu (2015). However, nanostructured surfaces and thin films are often difficult or impossible to measure using SAXS. The scattering of X-rays by matter is weak, and surfaces and thin films provide only a small interaction volume; therefore, SAXS signals can become so small that measurements take unfeasibly long or are impossible due to noise. For these types of samples, Dietrich and Wagner (1983) and Dietrich and Wagner (1984) proposed to measure in reflection geometry close to the critical angle of total external X-ray reflection, and Levine et al. (1989) conducted the first such study and named the method GISAXS.

In GISAXS, the sample is measured in reflection geometry instead of in transmission geometry (see figure 2.7). This enhances the scattered signal, often by several orders of magnitude, due to three main effects. Firstly, for thin films on a substrate, the interaction volume is enhanced geometrically simply by the longer path traveled by the X-rays through the thin film. Secondly, because X-rays are reflected totally at glancing incidence angles below a material-specific angle α_c (Compton 1923b), the reflected beam is almost as intense as the incident beam, and the X-rays travel twice through a specimen on a substrate. Finally, the interference between the incident X-rays and the X-rays reflected by the substrate can form standing waves in a thin film on top of the substrate, enhancing the electric field strengths locally, which leads to a stronger signal as well (Jiang et al. 2011).

Some samples are so thin (or are on top of such a thick substrate) that measurements in transmission geometry are untenable in all circumstances. But increasingly, the high signal intensities attainable in GISAXS geometry are instead used to minimize measurement times of samples that can in principle be measured in transmission geometry. When a measurement of a nanostructured surface is possible in transmission geometry in minutes, the same measurement can sometimes be taken in reflection geometry in a second or less. This enables in-situ measurements to investigate the evolution of a changing sample, for example during thin film growth (Renaud, Ducruet, et al. 2004).

Unfortunately, the GISAXS geometry also has significant downsides compared to measurements in transmission geometry. The most pressing problem is that due to the enhanced interaction between the X-rays and the sample, multiple scattering effects occur with high probability, which complicates the analysis of GISAXS measurements (Lee et al. 2005; Busch et al. 2006). Additionally, the footprint of the incident X-ray beam on the sample is elongated due to the shallow incident angle, which usually limits GISAXS to relatively large and flat samples; I will discuss this particular problem in detail in chapter 6.

The difficulties with the analysis of GISAXS measurements were addressed by Rauscher, Salditt, and Spohn (1995), who introduced the distorted-wave Born approximation (DWBA) into GISAXS

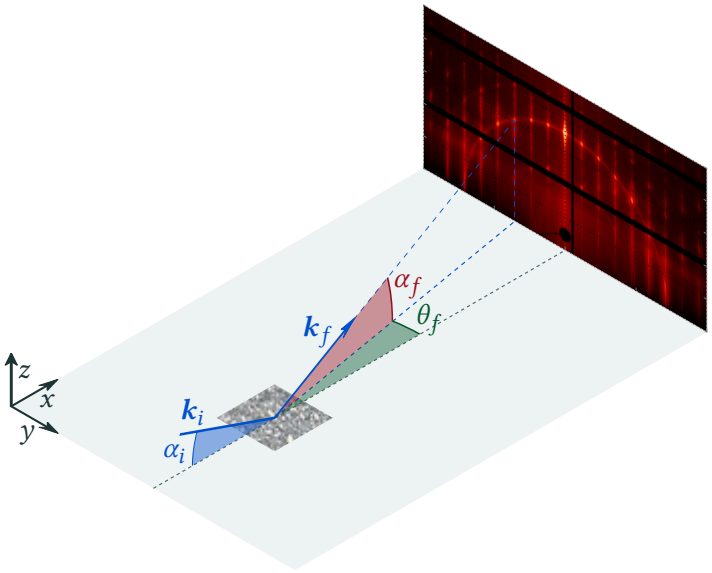

Figure 2.8: Geometry of GISAXS experiments. A monochromatic X-ray beam with a wavevector $\boldsymbol{k}_i$ impinges on the sample surface at a grazing incidence angle α_i. The elastically scattered X-rays with the wavevector $\boldsymbol{k}_f$ propagate along the exit angle α_f and the azimuthal angle θ_f. The intensity distribution of the scattered X-rays is recorded with an angle-resolved detector.

analysis. The DWBA accurately describes a layered system (for GISAXS, often the substrate) and then treats deviations of the actual system from a layered structure (e.g. islands on the substrate) as perturbations (Vineyard 1982; Sinha et al. 1988). The DWBA quickly became the dominant theory for the analysis of the scattering of complex samples, and several software packages were developed for this purpose (Lazzari 2002; Durniak et al. 2014). I will discuss the DWBA in more detail in section 3.2.2.

Nowadays, GISAXS has been established as a powerful technique for the investigation of nanostructured surfaces (Renaud, Lazzari, and Leroy 2009; Hexemer and Müller-Buschbaum 2015). For example, GISAXS is used to investigate the active layer of solar cells ex-situ as well as in-situ (Gu, C. Wang, and Russell 2012; Müller-Buschbaum 2014; Rossander et al. 2014; Pröller et al. 2016), the surface and bulk morphology of polymer films (Müller-Buschbaum 2003; Wernecke, Okuda, et al. 2014), surface roughness and roughness correlations (Holý, Kuběna, et al. 1993; Holý and Baumbach 1994; Babonneau et al. 2009), lithographically produced structures (Gollmer et al. 2014; Soccio et al. 2015), and deposition growth kinetics (Lairson et al. 1995; Renaud, Lazzari, Revenant, et al. 2003).

2.2.2 Theoretical description

The measurement geometry of GISAXS including all relevant angles is shown schematically in figure 2.8. The sample is illuminated under grazing incidence angle α_i, and the resulting reflected and scattered X-rays are collected with an angle-resolved detector at exit angles α_f and θ_f. Throughout my thesis, I use a coordinate system such that the x-y-plane is the sample plane and the x-axis lies in the scattering plane, with the z-axis perpendicular to the sample plane, as shown in figure 2.8.

Because the scattering angles in GISAXS are small, the refractive index $n = 1 - \delta + i\beta$ (see subsection 2.1.7) is used to describe the scattering. Since all interesting samples are not completely homogeneous, the refractive index is in general a function of position $n(\boldsymbol{r})$. Therefore, I will describe a GISAXS experiment as the scattering of a monochromatic incident wave with wavevector $\boldsymbol{k}_i$ from a sample described by the refractive index $n(\boldsymbol{r})$, starting from the wave equation

(2.1.39):

$$\left(\frac{\partial^2}{\partial t^2} - \frac{c^2}{n^2(\boldsymbol{r})}\nabla^2\right)\boldsymbol{E}_\perp(\boldsymbol{r}, t) = 0 \quad . \tag{2.2.2}$$

The full treatment of this vector equation can be found in (Dietrich and Wagner 1984), but qualitatively the same result can be obtained by treating the electric field as a scalar E, which considerably simplifies the treatment. To generate solutions for the wave equation, we separate the scalar field into a time-dependent and a position-dependent part $E(\boldsymbol{r}, t) = E_r(\boldsymbol{r})E_t(t)$,

$$\frac{\partial^2}{\partial t^2}E_r(\boldsymbol{r})E_t(t) = \frac{c^2}{n^2(\boldsymbol{r})}\nabla^2 E_r(\boldsymbol{r})E_t(t) \tag{2.2.3}$$

$$\Rightarrow \frac{1}{c^2 E_t(t)}\frac{\partial^2 E_t(t)}{\partial t^2} = \frac{\nabla^2 E_r(\boldsymbol{r})}{n^2(\boldsymbol{r})\,E_r(\boldsymbol{r})} = -k_0^2 \quad , \tag{2.2.4}$$

where k_0 is a constant, because the left-hand side of the equation depends only on the time and the right-hand side only on the position. While the constant could obviously be chosen differently, we will later see that it is convenient to choose $-k_0^2$ as the constant. We arrive at a second-order differential equation in time and a Helmholtz equation

$$\left(\frac{\partial^2}{\partial t^2} + c^2 k_0^2\right)E_t(t) = 0 \quad \Rightarrow \quad E_t(t) = e^{-i\omega t} \quad \text{with } k_0^2 = \omega^2/c^2 \tag{2.2.5}$$

$$\left(\nabla^2 + k_0^2 n^2(\boldsymbol{r})\right)E_r(\boldsymbol{r}) = 0 \tag{2.2.6}$$

$$\Rightarrow \quad \left(\nabla^2 + k_0^2 - V(\boldsymbol{r})\right)E_r(\boldsymbol{r}) = 0 \quad \text{with } V(\boldsymbol{r}) = k_0^2(1 - n^2(\boldsymbol{r})) \quad , \tag{2.2.7}$$

where V can be interpreted as a potential introduced by an object with $n \neq 1$. In vacuum, where $V = 0$, the solutions are the plane waves $E_r(\boldsymbol{r}) = E_0 \exp(i\boldsymbol{k} \cdot \boldsymbol{r})$ with wave vector $\boldsymbol{k}$ and $|\boldsymbol{k}| = k_0$, but we are interested in solutions with $V \neq 0$.

A first approach to solve equation (2.2.7) is to require that $V(\boldsymbol{r}) = 0$ for large r, i.e. that the sample is limited in size (Daillant and Gibaud 2009, page 54). We can then write the total field as the sum of the incident plane wave $E_{r,i}(\boldsymbol{r}) = E_0 \exp(i\boldsymbol{k}_i \cdot \boldsymbol{r})$ and a scattered field $E_{r,s}$ and transform equation (2.2.7) into an integral equation by introducing the Green function G

$$G(\boldsymbol{r}) = -\frac{1}{4\pi}\frac{e^{ik_0 r}}{r} \tag{2.2.8}$$

$$\Rightarrow E_r(\boldsymbol{r}) = E_{r,i}(\boldsymbol{r}) + E_{r,s}(\boldsymbol{r}) \tag{2.2.9}$$

$$E_{r,s}(\boldsymbol{r}) = \int G(\boldsymbol{r} - \boldsymbol{r'})\, V(\boldsymbol{r'})\, E_r(\boldsymbol{r'})\, d\boldsymbol{r'} \tag{2.2.10}$$

$$= -\frac{1}{4\pi}\int \frac{e^{ik_0|\boldsymbol{r}-\boldsymbol{r'}|}}{|\boldsymbol{r} - \boldsymbol{r'}|}\, V(\boldsymbol{r'})\, E_r(\boldsymbol{r'})\, d\boldsymbol{r'} \quad . \tag{2.2.11}$$

It can be shown that all solutions of this integral equation will be solutions of equation (2.2.7), the proof is provided by Daillant and Gibaud (2009, section 1.2.5). To simplify the integral expression, we first note that $V(\boldsymbol{r'})$ is zero outside of the sample, limiting the integration volume to the sample volume. In addition, we can use the fact that in GISAXS experiments, detectors at $\boldsymbol{r}$ are always placed far away from the sample at $\boldsymbol{r'}$. Using this far-field approximation $r' \ll r$, we can approximate

$$|\boldsymbol{r} - \boldsymbol{r'}| = \sqrt{r^2 + r'^2 - 2\boldsymbol{r}\boldsymbol{r'}} \tag{2.2.12}$$

$$\approx r - \frac{\boldsymbol{r}\cdot\boldsymbol{r'}}{r} \tag{2.2.13}$$

$$\approx r - \frac{\boldsymbol{k}_f\cdot\boldsymbol{r'}}{k_0} \tag{2.2.14}$$

$$\Longrightarrow E_{r,s}(\boldsymbol{r}) \approx -\frac{e^{ik_0 r}}{4\pi r}\int e^{-i\boldsymbol{k}_f\boldsymbol{r'}}\, V(\boldsymbol{r'})\, E_r(\boldsymbol{r'})\, d\boldsymbol{r'} \quad . \tag{2.2.15}$$

Note that here we use the wavevector $\boldsymbol{k}_f$, which points toward the detector at $\boldsymbol{r}$.

An exact solution of equation (2.2.15) is still difficult, because the total scattered field E_r enters in the integral. Using the first-order Born approximation, we can gain an intuitive understanding of the scattered far field. The idea of the Born approximation is to solve equation (2.2.15) iteratively by alternately inserting E_r into equation (2.2.15) to compute $E_{r,s}$ and insert $E_{r,s}$ into equation (2.2.9) to compute E_r, generating a series of approximate solutions $E_r^{(n)}$. To start the approximation, we need a starting point for $E_r^{(0)}$. In the standard Born approximation, we simply insert $E_r^{(0)} = E_{r,i}$, which means that we assume that within the sample, the electric field can be described using the undisturbed incident wave (Daillant and Gibaud 2009, pages 55-56). This yields in first order

$$E_{r,s}(\boldsymbol{r}) \approx -E_0\frac{e^{ik_0 r}}{4\pi r}\int e^{-i\boldsymbol{k}_f\boldsymbol{r'}}\, V(\boldsymbol{r'})\, e^{i\boldsymbol{k}_i\cdot\boldsymbol{r'}}\, d\boldsymbol{r'} \tag{2.2.16}$$

$$= -E_0\frac{e^{ik_0 r}}{4\pi r}\langle f|V|i\rangle \quad , \tag{2.2.17}$$

with $\langle i|$ and $\langle f|$ plane waves with wave vectors $\boldsymbol{k}_i$ and $\boldsymbol{k}_f$. Knowing that the scattered intensity is $I \propto |E|^2$, we see that the result is (up to a prefactor) equivalent to Fermi's golden rule. Fermi's golden rule states that the transition rate from an initial state into a final state is $\propto |\langle f|H|i\rangle|^2$ with H the time-independent Hamiltonian of a quantum mechanical system (Dirac 1927; Fermi 1974). In our case, the initial state $\langle i|$ is the incident plane wave, the final state $\langle f|$ is a plane wave with direction towards $\boldsymbol{r}$, and the potential V can be identified as the Hamiltonian.

While the analogy to Fermi's golden rule is useful in itself, a more graphic understanding of the scattering process can be gained with a further reformulation

$$E_{r,s}(\boldsymbol{r}) \approx -E_0\frac{e^{ik_0 r}}{4\pi r}\langle f|V|i\rangle = -E_0\frac{e^{ik_0 r}}{4\pi r}\int e^{-i(\boldsymbol{k}_f-\boldsymbol{k}_i)\cdot\boldsymbol{r'}}\, V(\boldsymbol{r'})\, d\boldsymbol{r'} \tag{2.2.18}$$

$$= -E_0\frac{e^{ik_0 r}}{4\pi r}\int e^{-i\boldsymbol{q}\cdot\boldsymbol{r'}}\, V(\boldsymbol{r'})\, d\boldsymbol{r'} \tag{2.2.19}$$

$$\propto \hat{V}(\boldsymbol{q}) \quad , \tag{2.2.20}$$

with the Fourier transform $\hat{V}(\boldsymbol{q})$ of the potential V evaluated at the reciprocal scattering vector $\boldsymbol{q} = \boldsymbol{k}_f - \boldsymbol{k}_i$ (Daillant and Gibaud 2009; Burle et al. 2016). This result is very useful when thinking about the scattering of a specific sample for the first time, and I will use it throughout my thesis to qualitatively interpret scattering images. Nevertheless, one has to be aware of the limitations of the first-order Born approximation, especially for GISAXS experiments. This approximation is only valid in the limit of small scattering introduced by V (Daillant and Gibaud 2009, pages 175ff), and the scattering introduced by the sample is certainly not small when total external scattering on a sample surface is involved. In addition, GISAXS samples are often large and thick, so that the approximation of a finite sample, that we had to make in order to arrive at the far-field approximation, is not very useful. For quantitative analyses, other theoretical models have to be used, which I will discuss and compare in section 3.2.

2.2.3 Experimental realization

SAXS experiments in general need a good source of X-rays with a well-collimated beam, a suitable sample holder, and a detector that offers angular resolution. The biggest difference between SAXS and GISAXS experiments is that for grazing-incidence experiments, the sample stage has to offer movement of the sample along and rotation around all three axes for sample alignment. Today, most SAXS setups use monochromatized X-rays for the incident beam; then the detector does not need to be energy dispersive, because the scattering is (nearly) elastic. I will discuss X-ray sources in section 2.3 and X-ray detectors in section 2.4. I will give a general overview, but with a focus on application in GISAXS experiments.

2.3 Generation of X-rays

The easiest way to generate visible light is to simply heat any object until it starts to glow. A perfectly black body in thermal equilibrium emits electromagnetic radiation according to Planck's law,

$$I(E_{\mathrm{ph}}, T) = \frac{2E_{\mathrm{ph}}^3}{h^2c^2} \frac{1}{\exp\left(\frac{E_{\mathrm{ph}}}{k_{\mathrm{B}}T}\right) - 1} \quad , \tag{2.3.1}$$

with the intensity of the emitted light I, the temperature of the black body T, and the Boltzmann constant k_{B} (Planck 1900). The hotter the black body is, the more light is emitted at higher photon energies, so naïvely we could assume we just need to build a hotter incandescent light bulb to get an X-ray source. Unfortunately, this is not feasible. To understand this, I will derive the peak intensity as a function of the temperature T. For this, I use the Wien approximation to Planck's law, which is valid for large E_{ph}, and determine the maximum intensity:

$$I(E_{\mathrm{ph}}, T) \approx \frac{2E_{\mathrm{ph}}^3}{h^2c^2} \exp\left(\frac{-E_{\mathrm{ph}}}{k_{\mathrm{B}}T}\right) \tag{2.3.2}$$

$$\Rightarrow \frac{dI(E_{\mathrm{ph}}, T)}{dE_{\mathrm{ph}}} = 0 = \frac{2E_{\mathrm{ph}}^2}{h^2c^2} \exp\left(\frac{-E_{\mathrm{ph}}}{k_{\mathrm{B}}T}\right)\left(3 - \frac{E_{\mathrm{ph}}}{k_{\mathrm{B}}T}\right) \tag{2.3.3}$$

$$\text{using } E_{\mathrm{ph}} \neq 0 \tag{2.3.4}$$

$$\Rightarrow E_{\mathrm{ph}} = 3k_{\mathrm{B}}T \quad . \tag{2.3.5}$$

In order to obtain visible light with $E_{\mathrm{ph}} = 2\,\mathrm{eV}$, the black body needs to be brought to a temperature of about $T = 7700\,\mathrm{K}$. Because all metals would melt at this temperature, incandescent lightbulbs operate at lower temperatures, and thus have their maximum intensity in the infrared and produce visible light with a relatively low efficiency. Calculating the necessary black body temperature for efficient emission of X-rays, we obtain wholly infeasible temperatures: $T(E_{\mathrm{ph}} = 1000\,\mathrm{eV}) \approx 3.8 \cdot 10^6\,\mathrm{K}$; therefore, we have to rely on other methods to generate X-rays (Meschede 2015e, pages 592ff.). The most important methods to generate X-rays are listed in table 2.1. For a comparison of different X-ray sources, the number of generated photons per unit time is normalized to the product of beam area and divergence and evaluated at a set photon frequency bandwidth; this quantity is known as brightness and used in the table for the comparison. In the following, I will describe each of the listed methods, starting with the older, easier and less bright methods.

Table 2.1: Typical brightness of X-ray sources. Given is the order of magnitude for different X-ray sources (Winick 1998; Schneidmiller and Yurkov 2011; Wansleben et al. 2019). For X-ray tubes, the given values refer to the characteristic X-ray emission, the bremsstrahlung is several orders of magnitude less bright.

X-ray Source		Brightness $\Delta\nu/\nu = 0.1\,\%$ $s^{-1}\,mm^{-2}\,mrad^{-2}$
Tube	rotating anode	10^{8}
	metal jet anode	10^{10}
Synchrotron	bending magnet	10^{12}
	wiggler	10^{15}
	undulator	10^{19}
Free electron laser	average	10^{25}
	peak	10^{34}

2.3.1 Characteristic X-ray emission

In atoms, the electrons occupy discrete energy levels. Due to Pauli's exclusion principle, only two electrons (one spin-up and one spin-down) can occupy the same energy level. Therefore, higher energy levels are occupied even in the ground state of atoms with several electrons. The lowest energy levels are called core levels, and the highest energy levels are called valence levels (Meschede 2015d, pages 718ff.). If an electron occupying a core level is ejected from an atom with several electrons, it leaves the atom in an excited state. This excited state can relax via the transition of a valence electron to the "hole" the core electron left. The energy difference can be released by the emission of a photon, see figure 2.9. Since this energy difference depends on the relative energies of the core and valence levels, the energy of the emitted photon depends on the number of electrons and protons, which means it is characteristic for the element. For elements with an atomic number $Z \geq 11$ (Na), the emission of a transition from the valence level to the lowest core level (called Kα emission line) is X-rays (Zschornack 2006, pages 24ff. Thompson et al. 2009).

In practice, the most popular method to generate the core hole is to throw electrons at the target at high speed. The reason for this is that electrons can easily be accelerated using electric fields and the interaction cross section between a high speed electron and core electrons is reasonably high due to their charge. Technologically, the main limitation of this method is that the conversion efficiency from power of the high speed electrons to emitted X-ray power is still only about 1 % and the rest of the energy is converted to heat, which is deposited in the target. Therefore, the maximum X-ray brightness of an X-ray tube depends on the ability to cool the target. This led to the development of first water-cooled targets, then quickly rotating targets, and most recently liquid metal jet targets (Glatter and Kratky 1982, pages 54-58; Hemberg, Otendal, and Hertz 2003).

For SAXS experiments, characteristic X-ray emission produced by X-ray tubes is routinely used, especially for measurements of static samples that allow long integration times in the range of hours or even days. Here, the higher signal intensities of GISAXS measurements allow to shorten the measurement times. However, there are two main reasons why X-ray tubes can not be used for all kinds of GISAXS experiments. Firstly, in-situ measurements of samples that change over time require shorter measurement times, and even for static samples, thermal drift of the setup can limit the useful measurement time. Secondly, for some GISAXS experiments, it is useful to take advantage of the fact that the refractive index n changes with the photon energy E_{ph}, but characteristic X-ray emission is limited to relatively few photon energies, depending on the anode material. Therefore, methods to generate brighter X-rays and X-rays with a tunable photon energy are needed.

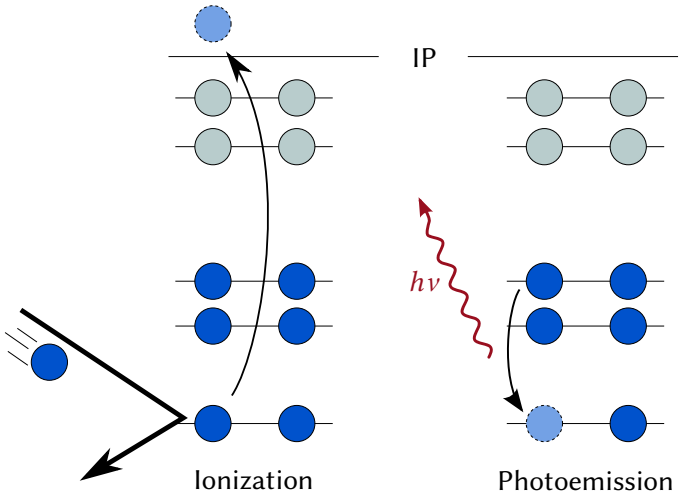

Figure 2.9: Generation of characteristic X-ray emission. *IP* denotes the ionization potential. A fast free electron collides with the atom, ionizing it by ejecting a core electron. Then the excited state decays via the emission of an X-ray photon with $E_{\mathrm{ph}} = h\nu$.

2.3.2 Bremsstrahlung

Accelerating electric charges - in particular electrons - leads to the emission of electromagnetic waves in accordance with Maxwell's equations. Very high accelerations (or, equivalently, decelerations) of electrons can be reached by throwing electrons at matter, as is done in X-ray tubes. Interactions with the electrons in the target material slow down the electrons, which therefore emit electromagnetic radiation, called *bremsstrahlung*. The wave length $\lambda = hc/E_{\mathrm{ph}}$ of the bremsstrahlung is not confined to discrete emission lines like is the case for characteristic emission, but it is spread broadly over the whole spectrum. However, due to the quantized nature of electromagnetic radiation combined with energy conservation, the photon energy E_{ph} is limited to the total energy that was lost by the electron. It follows that in order to create X-ray bremsstrahlung at E_{ph}, we have to use an acceleration voltage $U \geq E_{\mathrm{ph}}/q_{\mathrm{e}}$, with the charge of an electron $-q_{\mathrm{e}}$ (Meschede 2015b, pages 450-452; Meschede 2015a, pages 834-835; Zschornack 2006, pages 92ff.).

Unfortunately, the brightness of the bremsstrahlung obtained in X-ray tubes is several orders of magnitude smaller than the characteristic X-ray emission, and the production of monochromatic bremsstrahlung is therefore even more severely limited by thermal load problems. Therefore, to generate X-rays with a broad spectrum and at high brightness, it is beneficial to accelerate the electrons sideways, which avoids dumping most of the kinetic energy of the electron as heat. This special case of bremsstrahlung is called synchrotron radiation, and I will discuss it in the next section.

2.3.3 Synchrotron radiation

The principle of the generation of synchrotron radiation is to accelerate electrons to relativistic speed and then deflect them with a static magnetic field $\boldsymbol{B}$ produced by a bending magnet. In the magnetic field, the electrons follow a circular path, with radius

$$R = \frac{E_{\mathrm{e}}}{q_{\mathrm{e}} c B} \quad , \tag{2.3.6}$$

with the kinetic energy of the electrons E_{e}, the speed of light c and $B = |\boldsymbol{B}|$. The properties of synchrotron radiation are governed by the fact that the emitted radiation and the emitting electrons move at almost the same speed, such that the radiation emitted over a longer time span

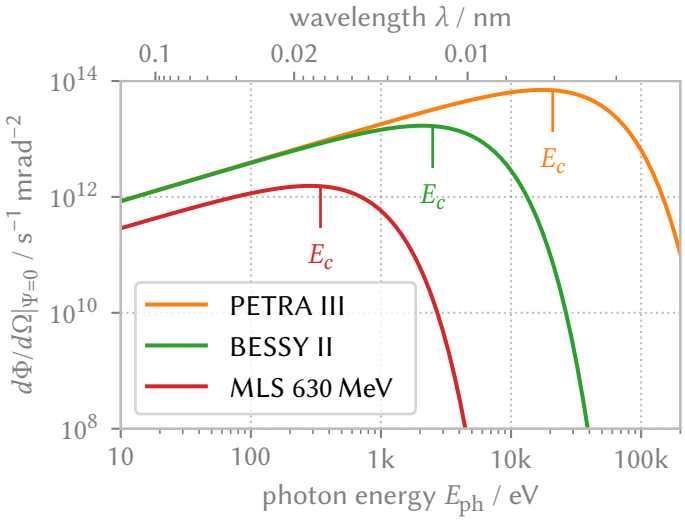

Figure 2.10: In-plane photon flux angular density of bending magnets at selected storage rings. The vertical lines show the critical photon energy E_c. The data was calculated using equation (2.3.11) and the bandwidth was set to 0.1 % for all calculations. Note that for practical applications, $d\Phi/d\Omega$ has to be integrated over $d\Omega$, and the spatial distribution of the electrons in the beam has to be considered in order to compare the usefulness of different sources in a given spectral range (Klein et al. 2008).

reaches the observer at almost the same time (A. Hofmann 2004, pages 3ff.). Quantitatively, the emitted radiation can be calculated from the Maxwell equations using the formalism of retarded and advanced potentials and Lienard-Wiechert potentials. The derivation is presented in detail by A. Hofmann (2004, pages 9-114), but due to its length, I will only review the most important results here. The photon flux angular density $d\Phi/d\Omega(E_{ph}, \Psi)$ emitted at a bending magnet at the vertical angle Ψ into the solid angle element $d\Omega$ with a radiation frequency bandwidth of $\Delta\nu/\nu$ is

$$\frac{d\Phi}{d\Omega}(E_{ph}, \Psi) = \frac{3\alpha}{4\pi^2}\gamma^2 \frac{I_e}{q_e}\frac{\Delta\nu}{\nu}\left(\frac{E_{ph}}{E_c}\right)^2 (1+\gamma^2\Psi^2)\left(\underbrace{K_{2/3}^2(\xi)}_{\text{hor. pol.}} + \underbrace{\frac{\gamma^2\Psi^2}{1+\gamma^2\Psi^2}K_{1/3}^2(\xi)}_{\text{vert. pol.}}\right) \tag{2.3.7}$$

$$\xi = \frac{E_{ph}}{2E_c}(1+\gamma^2\Psi^2)^{3/2} \tag{2.3.8}$$

$$E_c = \frac{3\gamma^3 hc}{4\pi R} \tag{2.3.9}$$

$$\gamma = \frac{E_e}{m_e c^2} \quad , \tag{2.3.10}$$

with the fine-structure constant α, the Lorentz factor γ, the critical photon energy E_c, the resting mass of the electron m_e, and the modified Bessel functions of the second kind K (Schwinger 1946; Schwinger 1949; Thompson et al. 2009). The first part in the braces, labeled "hor. pol." is polarised horizontally, i.e. in the synchrotron plane orthogonal to $\boldsymbol{B}$. The second part, labeled "vert. pol." is polarised vertically. The critical photon energy E_c is defined by the fact that half of the emitted power is at lower photon energies and the other half at higher photon energies.

To understand the main properties of synchrotron radiation, I first consider the special case of emission in the synchrotron plane at $\Psi = 0$. We obtain:

$$\frac{d\Phi}{d\Omega}(E_{ph}, \Psi = 0) = \frac{3\alpha}{4\pi^2}\gamma^2 \frac{I_e}{q_e}\frac{\Delta\nu}{\nu}\left(\frac{E_{ph}}{E_c}\right)^2 K_{2/3}^2(E_{ph}/2E_c) \quad . \tag{2.3.11}$$

We see that the vertically polarised part vanishes, and that, in contrast to the unpolarized emission of X-ray tubes, the emitted radiation is perfectly polarised in the synchrotron plane (Thompson

Storage ring	E_e/GeV	B/T	E_c/eV	I_e/mA
PETRA III	6	0.873	20 900	100
BESSY II	1.7	1.3	2500	300
MLS (max)	0.63	1.3	343	200
MLS (min)	0.105	0.43	3.2	200

Table 2.2: Operating parameters of selected German storage rings. The indicated beam current I_e is the maximum beam current. The MLS can be operated in a range of parameters, shown are the minimal and maximal values.

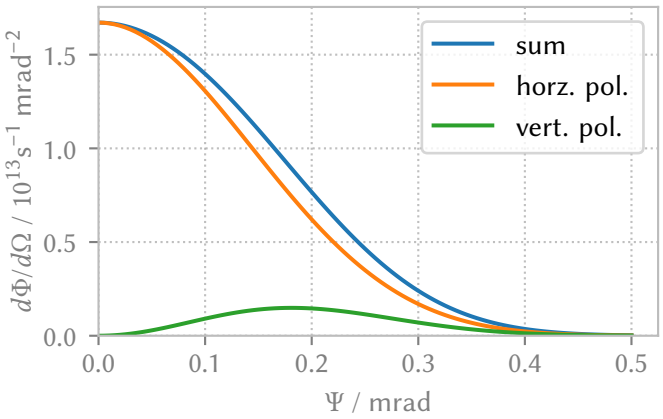

Figure 2.11: Angular distribution of synchrotron radiation emitted by a BESSY II bending magnet. At $\Psi = 0$, the synchrotron radiation is linearly polarized in the synchrotron plane (horizontal). At $\Psi \neq 0$, the radiation is elliptically polarized, with the larger axis in the synchrotron plane. The bandwidth was set to 0.1 % for all calculations.

et al. 2009, section 2; Falta and Möller 2010, pages 94ff.). The spectrum of synchrotron radiation with $\Psi = 0$ is plotted in figure 2.10. The emissions calculated using the properties of the bending magnets of three German storage rings, see table 2.2, are shown. The emission rises steadily with higher photon energy E_{ph}, but reaches a maximum just before E_c and then falls steeply. Because $E_c \propto E_e^2 B$ and B is limited by the available technology, the range of usable photon energies depends strongly on the electron energy E_e. At a given B, higher E_e leads to a larger bending radius, which is why synchrotron radiation sources for X-rays are large facilities with diameters of typically more than 80 m, and larger facilities deliver harder X-rays.

Now we consider $\Psi \neq 0$. In this case, both horizontally and vertically polarized field components are emitted, which leads to the emission of elliptically polarized X-rays (figure 2.11). It can be seen that the horizontally polarized part of the emitted radiation decays towards higher Ψ, and the vertically polarized part rises initially, and then decays as well. Because the vertically polarized part remains much smaller than the horizontally polarized part, the total flux density falls monotonously and the large axis of the elliptical polarization remains horizontal at all Ψ. Usually, the radiation at $\Psi = 0$ is used for experiments, simply because it is the most intense, but it has to be considered that the radiation is always collected at a finite Ψ range, and therefore a small vertically polarized component is always included in the radiation and might need to be considered in the analysis of the results.

The intensity of the X-rays produced by a bending magnet beam line is high enough for fast GISAXS measurements of static samples, and by using proper X-ray optics, monochromatic X-rays with a tunable photon energy can be obtained. However, for very small signals and in-situ measurements with a time resolution in the millisecond range, higher X-ray intensities are still valuable. To obtain more intense radiation than which is emitted at a single bending magnet, other synchrotron radiation devices can be used, a comparison is shown in figure 2.12. A natural idea is to stack multiple bending magnets after another (Winick and Lorant (1975) as cited by Kincaid (1977)). If the magnetic field direction is alternated in the series of magnets, the paths of the electrons are also bent in alternating fashion, i.e. they wiggle left and right around a straight path, which gives this device the name *wiggler* (compare figure 2.12b). In a relatively long and strong magnet such as a bending magnet, the electrons are deflected outside of the cone of emitted

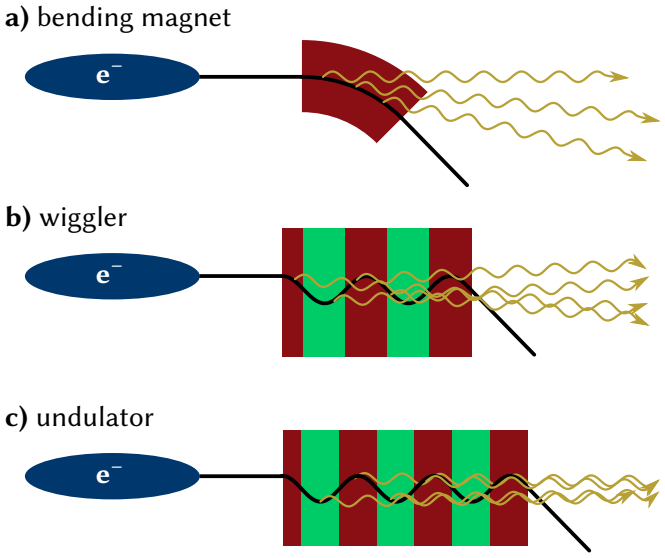

Figure 2.12: Comparison of synchrotron radiation devices.
a) A bending magnet emits polychromatic radiation into a wide angular range.
b) In a wiggler, the radiation of multiple bending magnets combines incoherently.
c) In an undulator, the emitted radiation interferes, leading to emission into a narrower angle and energy bandwidth.
The figure is adapted from (HZB 2020a).

radiation, and interactions between the electrons and the emitted fields can be neglected. This condition is generally fulfilled when the length of the bending magnet $L > 2R/\gamma$ (A. Hofmann 2004, pages 4-6). In this case, the radiation of the bending magnets simply adds up incoherently, and the overall emitted photon flux angular density is:

$$\frac{d\Phi^{\text{wig}}}{d\Omega}(E_{\text{ph}}, \Psi) = 2N \frac{d\Phi^{\text{bm}}}{d\Omega}(E_{\text{ph}}, \Psi) \propto N \quad , \tag{2.3.12}$$

with the number of magnet pairs N and the emission of a single bending magnet $d\Phi^{\text{bm}}/d\Omega(E_{\text{ph}}, \Psi)$ (Thompson et al. 2009, page 2-6). In an electron storage ring, the magnetic field B of the magnets in the wiggler can of course be different than the magnetic field of the bending magnets that keep the electrons on their path. Thus, it is possible to reach higher E_{ph} compared to the emission at the normal bending magnets using wigglers with stronger magnetic fields; these devices are called wavelength shifters (A. Hofmann 2004, page 206).

2.3.4 Undulator radiation

If electrons are deflected by short and weak magnets, with $L < R/\gamma$, the path of the electrons is inside the cone of emitted radiation, and interactions between the emitted radiation and the electrons can not be neglected (A. Hofmann 2004, page 5). This is used in synchrotron radiation devices called undulators (see figure 2.12c) to enhance the intensity of the emitted X-rays even further. In particular, I consider the case of a sinusoidal magnetic field

$$B(x) = B_0 \cos(2\pi x/\lambda_u) \quad , \tag{2.3.13}$$

with the distance along the undulator axis x, the peak magnetic field B_0 and the undulator magnetic period λ_u. The path of the electrons is sinusoidal as well with period λ_u and the radius of the maximal momentary deflection analogous to equation (2.3.6) is

$$R_0 = \frac{E_{\text{e}}}{q_{\text{e}} c B_0} \quad . \tag{2.3.14}$$

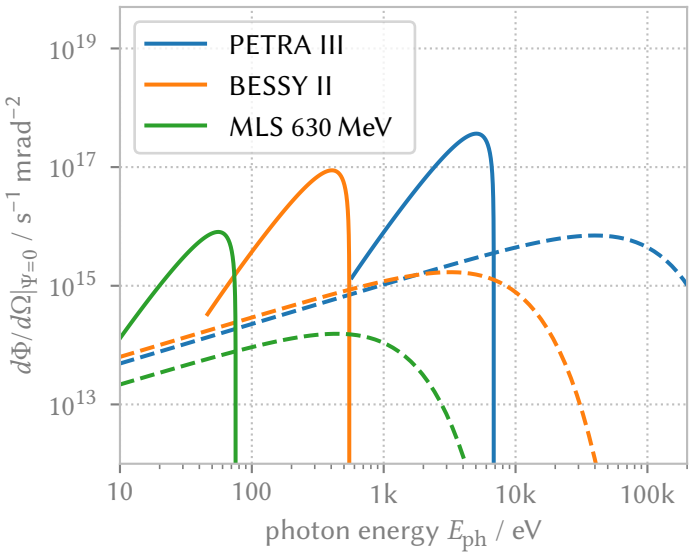

Figure 2.13: Brightness of undulators and wigglers. For the undulators (solid lines), the 1st harmonic is shown, with a magnetic field B_0 from 0 to 1 T and $\lambda_u = 50$ mm. For the wigglers (dashed lines), the magnetic field is fixed at $B = 2$ T. For all spectra, $N = 50$, $\Delta\nu/\nu = 0.1\,\%$ and γ and I_e of the respective storage ring were used.

The radiation emitted at successive periods interferes constructively at the resonance wavelength

$$\lambda_r = \frac{1 + K^2/2}{2\gamma^2}\lambda_u \tag{2.3.15}$$

$$\Longrightarrow E_{\mathrm{ph},r} = hc/\lambda_r = \frac{2hc\gamma^2}{\lambda_u(1 + K^2/2)} \tag{2.3.16}$$

$$K = \frac{q_e B_0 \lambda_u}{2\pi m_e c} = \frac{\gamma}{2\pi R_0}\lambda_u \quad , \tag{2.3.17}$$

with the undulator deflection parameter K (Kim 1986; Thompson et al. 2009, pages 2-6ff). Radiation is emitted at λ_r and at higher harmonics, with the on-axis intensity of the n^{th} harmonic:

$$\frac{d\Phi^{\mathrm{und}}}{d\Omega}(\lambda = n\lambda_r, \Psi = 0) = \begin{cases} \alpha N^2 \gamma^2 \frac{\Delta\nu}{\nu}\frac{I_e}{q_e} G(n,K) & \text{for } n \text{ odd} \\ 0 & \text{for } n \text{ even} \end{cases} \tag{2.3.18}$$

$$\propto N^2 \tag{2.3.19}$$

where

$$G(n,K) = \frac{K^2 n^2}{(1 + K^2/2)^2}\left[J_{(n-1)/2}\left(\frac{nK^2}{4 + 2K^2}\right) - J_{(n+1)/2}\left(\frac{nK^2}{4 + 2K^2}\right)\right]^2 \quad , \tag{2.3.20}$$

with the Bessel functions J_ν (Thompson et al. 2009, pages 2-6ff). Therefore, undulators can reach much higher peak brightness, but the radiation is restricted to discrete wavelengths that are multiples of the resonance wavelength. To be able to tune the photon energy to the experiment at hand, undulators are constructed such that the field strength B_0 is variable, so that the resonance frequency can be shifted. Often, undulators are constructed using permanent magnets and the magnetic field is tuned using the gap between opposing magnets (Bahrdt 2016).

Because the emission of undulators is limited to the resonance frequency and its harmonics, and the resonance frequency grows with smaller magnetic field, we can consider the maximum photon

energy that can be produced by an undulator in the weak magnet limit of $B_0 = 0$

$$E_{\mathrm{ph,max}} = \frac{2hc\gamma^2}{\lambda_u} \quad . \tag{2.3.21}$$

At a given storage ring with typically fixed γ, the only way to reach higher photon energies is to make λ_u smaller, but there are technical limits on λ_u. In figure 2.13, the emission of undulators and wigglers at different storage rings is compared using example parameters. The emission of undulators is up to 2 orders of magnitude more bright than that of the wigglers, but the spectrum of the wigglers is much broader, and in particular also extends to much higher photon energies. Additionally, the brightness of an undulator scales with N^2, while the brightness of a wiggler only scales with N, so that long undulators can reach even higher intensities.

In addition to the basic plane undulators I have discussed in this section, more advanced undulators are in development or already in operation. One example is the helical undulator, in which the magnetic field is structured such that the electrons move on a helical path. In this case, the emitted radiation has circular polarization on-axis, and higher harmonics vanish completely on-axis (Sasaki et al. 1993). An overview of other more advanced undulator designs is given by Falta and Möller (2010, pages 109ff).

The X-rays emitted by undulators are bright enough for all GISAXS experiments, and many synchrotron beam lines that are dedicated to small-angle scattering are therefore installed at undulators.

2.3.5 Free electron lasers

A newer concept to generate even brighter X-ray beams is the X-ray free electron laser (FEL). The principle of an FEL is based on a process called micro-bunching, which happens in a long electron bunch travelling through a sufficiently long undulator given a seeding X-ray wave. If electrons fly with relativistic speeds through an undulator alongside the seeding X-ray beam, the X-rays either loose energy to the electromagnetic field (emitting X-rays) or gain energy from the electromagnetic field, depending on their position relative to the phase of the seeding X-ray beam. This leads to the formation of micro-bunches of electrons, with the distance of bunches equal to the wavelength of the seeding X-ray beam (Schmüser et al. 2014, chapter 4). After formation of the micro-bunches, the X-rays emitted by each micro-bunch interfere coherently if their wavelength is an integer multiple of the seeding wavelength, which leads to coherent amplification of the X-ray beam. The stronger X-ray beam then leads to even stronger micro-bunching of the electrons. The result of this process is that after a short start-up distance in which the micro-bunches form without strong amplification, the amplification of the X-ray beam is exponential with the length of the undulator (Schmüser et al. 2014, pages 57-59):

$$\frac{d\Phi^{\mathrm{FEL}}}{d\Omega} \propto \exp(N) \quad , \tag{2.3.22}$$

thus reaching very high brilliance using long undulators. Eventually, this process saturates and the saturated X-ray beam power is

$$P_{\mathrm{sat}} \approx \rho_{\mathrm{FEL}} P_{\mathrm{beam}} \quad , \tag{2.3.23}$$

with the power of the electron beam P_{beam} and the FEL parameter ρ_{FEL} (Schmüser et al. 2014, pages 71-73). The FEL parameter ρ_{FEL} depends on the properties of the electron beam and the undulator as well as the seeding X-ray wave, and reaches values of approximately 0.1 % (Schmüser

et al. 2014, page 73). With sufficiently high electron beam power, the generated X-ray pulse is very short with a very high peak brilliance (Schneidmiller and Yurkov 2011). Because the electron beam power of storage rings is limited, and the properties of the electron beam are severely altered by an FEL, FELs are not installed in storage rings. Instead, linear electron accelerators are used to generate the high power electron beam and the beam is dumped after one pass through the FEL (Schmüser et al. 2014, chapter 9).

In fact, the X-rays generated by an X-ray FEL are so intense, that samples are generally destroyed after a single X-ray pulse; therefore, GISAXS experiments have not been conducted using an FEL as the X-ray source to date.

2.4 Detection of X-rays

Already Röntgen (1895) describes that X-rays can not be detected by the human eye:

> Die Retina des Auges ist für unsere Strahlen unempfindlich; das dicht an den Entladungsapparat herangebrachte Auge bemerkt nichts,[⋯]
>
> The retina of the eye is not sensitive to our rays; the eye does not notice anything when brought close to the discharge apparatus,[⋯] [1]

Instead, Röntgen used visible fluorescence to detect X-rays and photosensitive image plates to record X-ray intensity distributions. Nowadays, there are many different X-ray detectors in use which rely on a diverse set of detection principles (Falta and Möller 2010, pages 143ff; Beckhoff, Kanngießer, et al. 2006, pages 199ff). When comparing detectors to choose the best detector for a specific experiment, multiple criteria are important. If non-elastic scattering or fluorescence is investigated, it is essential that the detector can resolve photon energies; if, on the other hand, the angular distribution of scattered photons is investigated, as is the case in SAXS, it is highly desirable that the detector can image a large area with good spatial resolution at the same time, so that scanning can be avoided. For SAXS measurements with weak signals in particular, the minimum photon flux density that is detectable is also important. In addition, for metrological applications it is necessary to trace the measurements to the International System of Units (SI). Unfortunately, there is no perfect detector, and while some detectors are excelling at one or

[1] Quoted after (Röntgen 1898, page 5), English translation by myself.

Table 2.3: Properties of selected X-ray detectors. For the commercially available detectors (all but bolometers), typical values for detectors that are commonly in use at synchrotrons in 2020 are listed (Hamamatsu 2014; KETEK 2019; marXperts 2019; Andor 2016; Andor 2019; DECTRIS 2016; Krumrey, Tegeler, et al. 1988). For angle resolved detectors, the photon flux is given per pixel. For angle resolved and energy dispersive detectors, the dynamic range within a single measurement over all channels is given. In special configurations, detectors can often exceed the given numbers.

X-Ray Detector	angle res.	energy disp.	directly traceable	photon energies	photon flux / 1/s	dynamic range
Bolometer	✗	✗	✓	all	-	-
Diodes	✗	✗	✗	all	$> 10^3$	-
Silicon drift	✗	✓	✗	all	$< 10^6$	10^5
Fluorescent screen	✓	✗	✗	all	$> 10^{-1}$	10^4
Direct illumination CCD	✓	✗	✗	$< 10\,\mathrm{keV}$	10^{-2} to 10^4	10^4
Hybrid photon counting	✓	✗	✗	$> 1.7\,\mathrm{keV}$	$< 10^7$	10^6

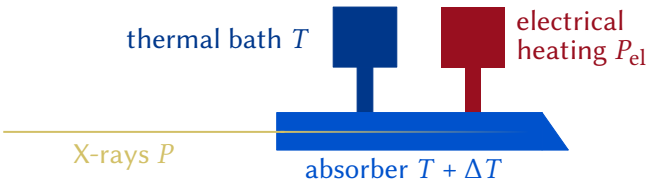

Figure 2.14: Electrical substitution radiometer. The total power of the X-ray beam is P_{beam}, the electrical heating power is P_{el}, the temperature of the thermal bath is T and the temperature of the absorber cavity is $T + \Delta T$.

two of these requirements, compromises have to be made everywhere else. An overview of the properties of some X-ray detection mechanisms commonly in use at synchrotron beamlines is given in table 2.3. In the following sections, I will briefly discuss the detection principle and the properties of each of the detector types.

2.4.1 Calorimetric detection

A conceptually simple detection method which does not rely on a microscopic model of X-ray interactions is calorimetry using bolometers. The idea is that, whatever the underlying mechanisms, the conservation of energy holds and any X-ray photon interacting with enough matter for long enough will eventually end up as heat. Therefore, the energy deposited by an X-ray beam is measured by a change in temperature. In practice, the lowest uncertainties when tracing back the measurement to the definition of the units in the SI can be reached using cryogenic electrical substitution radiometers, see figure 2.14 (Gottwald et al. 2006). In a cryogenic electrical substitution radiometer, the absorber cavity is cooled to a very low temperature and heated electrically to a constant temperature; then the electrical heating power with and without X-ray irradiation is measured, and the electric measurement is traced back to the SI (J. E. Martin, Fox, and Key 1985; Rabus, Persch, and Ulm 1997).

2.4.2 Diodes

In section 2.1.1, I described the external photoelectric effect, where an atom is ionized. While the external photoelectric effect can be used to build X-ray detectors, for example by placing a thin metal mesh in the X-ray beam and measuring the photocurrent, the induced signal is generally low. A very similar interaction with better properties for the detection of X-rays is the internal photoelectric effect, where the energy deposited by a photon is not enough to ionize the atom; instead, the electron is excited into a bound, unoccupied state (an unoccupied molecular orbital in molecules, or a conduction band in solid state matter). This excitation can also happen via intermediate processes. For example, if an X-ray photon is absorbed in the bulk of a solid state material, and ejects a photo electron from an atom, this excited electron can often not escape the material, and will instead excite other electrons into bound, unoccupied states which are lower in energy.

Diodes are detectors which use the internal photoelectric effect to measure the incident light. This works by inducing an internal electric field in a semiconductor. The electrons generated by the incident light are directed by the electric field towards one side, while the unoccupied states which were formerly occupied by the photoelectrons (holes) are directed towards the other side (Meschede 2015c, pages 905ff). When the two sides are connected electrically, an electrical current flows, which is proportional to the flux of an incident X-ray beam. Advantages of diodes as X-ray detectors are their large spectral range and high linearity even at relatively high photon flux densities and of course the relatively low cost (Krumrey, Tegeler, et al. 1988). The efficiency of

a diode is not known *a priori*; therefore, diodes have to be calibrated using calorimetry to enable absolute measurements (Gottwald et al. 2006).

In GISAXS experiments, diodes are often used as beam monitoring devices to measure the intensity of the incident X-rays I_0 and for the adjustment of optics and samples. However, diodes are not useful for the measurement of very small scattered intensities, and angular resolution is only possible with time-consuming scanning; therefore, diodes are not used as primary detectors for the scattered intensity distribution in GISAXS experiments.

2.4.3 Silicon drift detectors

Solid state X-ray detectors use the internal photoelectric effect like diodes, but count individual photons and can also measure the photon energy. The core idea of energy-dispersive solid state X-ray detectors is that the charge generated by an X-ray photon via the internal photoeffect is proportional to the photon energy. Now, if the signal processing electronics is fast enough to detect the individual charges generated by X-ray photons, it is possible to sort the photons by energy and count them, resulting in a histogram of the photon energies. The solid state X-ray detector most commonly in use nowadays is the silicon drift detector (SDD), which is made out of very pure silicon, and has a good energy resolution of approximately 125 eV at a photon energy of 6000 eV (Falta and Möller 2010, pages 148ff). The efficiency of the conversion of photon energy to electrical charge is also not known *a priori*, and SDDs have to be calibrated using calorimetry to enable absolute measurements.

2.4.4 Fluorescent screens

A fluorescent screen[2] emits visible light when it absorbs X-rays. In combination with a digital camera for visible light, which are available in high quality and relatively cheaply, you get a good X-ray detector with spatial resolution. Due to the fact that visible light is easily guided with optics, it is possible to magnify the intensity profile on the fluorescent screen, such that the maximal spatial resolution is given by the fluorescent screen and can reach the single digit micrometer range (Graafsma and T. Martin 2008, pages 277ff). Because the fluorescent screen can be imaged from the side using either an optical mirror or a tilted screen, the camera does not have to be placed in the path of the X-ray beam; therefore, fluorescent screens can be used to image X-ray beams of high intensities, which makes them good detectors for imaging the primary X-ray beam during alignment given their moderate cost.

Fluorescent screens were used in the earliest GISAXS experiments (Levine et al. 1989), and used to be the main GISAXS detector type. However, their dynamic range is limited to about 10^4, and very small photon fluxes can not be measured due to thermal noise of the camera system (compare table 2.3).

2.4.5 Direct illumination solid state cameras

Instead of imaging the visible light generated by a fluorescent screen using a digital camera, the digital camera can be placed directly in the X-ray beam. In this setup, the X-ray photons produce charges just like in an SDD, but the charges are collected in potential wells instead of being detected individually right away. After a given exposure time, the accumulated charge in

[2] In the literature, the terms fluorescence, phosphorescence, luminescence, and scintillation are all used to mean the emission of visible light upon X-ray radiation. I will use the term fluorescence.

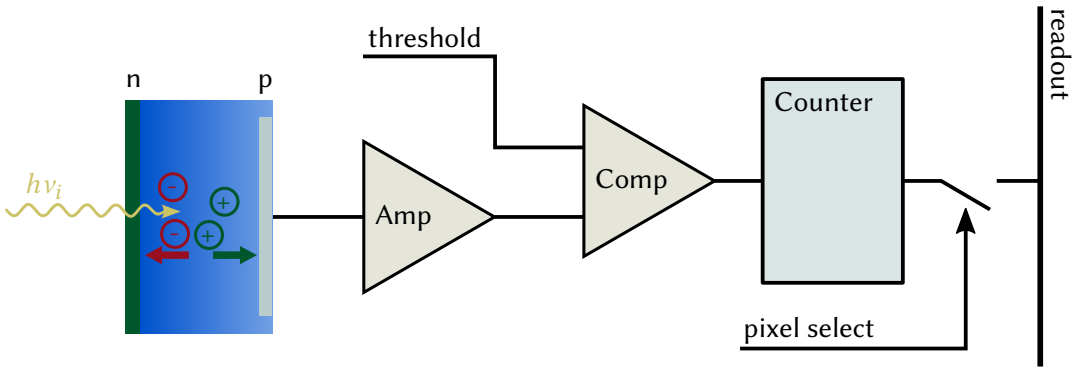

Figure 2.15: Simplified structure of a hybrid photon counting detector. From left to right: in a pn-junction, charges are generated by an X-ray photon $h\nu_i$, separated, and collected by electrodes. The electrical pulse created by the photon is amplified using a charge-sensitive amplifier (Amp) and then compared to a pre-defined threshold (Comp). If the pulse exceeds the threshold, a count is generated and stored in the counter. After exposure, the pixels are read out serially using the pixel select signal and the readout line (Broennimann et al. 2006).

the potential well is read out, and the number of photons detected during the exposure time is proportional to the accumulated charge if the incident X-rays are monochromatic. To form a position-resolved detector, potential wells are arranged as pixels on a two-dimensional grid. The most common technical realization of this concept that is in use today uses a charge-coupled device (CCD) to read out the charges after exposure, and is therefore called a CCD camera (Falta and Möller 2010, pages 148-151).

CCD cameras have some very useful properties. Because the charges are accumulated during the whole exposure time, it is possible to measure weaker X-ray signals simply by using a longer exposure time. Additionally, windowless CCD cameras routinely reach very high efficiencies, so that weaker signals can be detected compared to indirect detection via fluorescent screens. In practice, this is limited on one hand by the limited dynamic range over to whole image and on the other hand by thermal noise. The dynamic range of CCD cameras is limited because the potential wells have a limited capacity, and if more charges are created during the exposure time than fit inside the capacity, the charges start leaking into adjacent potential wells, leading to "blooming" of overexposed signals; therefore, weak signals can not be measured close to strong signals. In GISAXS experiments, the limited dynamic range of CCD cameras due to blooming can be improved by using a beamstop to attenuate or block the specular reflection at $\alpha_i = \alpha_f$, which is usually the most intense scattering feature. On the other end of the intensity scale, thermal noise leads to spontaneous excitation of charges which are also collected by the potential wells, leading to a dark signal that is proportional to the exposure time, deteriorating the signal to noise ratio of weak signals (Stribeck 2007, pages 54f). Another limitation of direct illumination CCD cameras compared to indirect detection via fluorescent screens is that the detection efficiency is small above a certain photon energy, limiting directly illuminated CCD cameras to applications with photon energies smaller than about 10 kev. Because the efficiency of the conversion of X-rays into electrical charges is not known *a priory* either, CCD cameras have to be calibrated for absolute measurements.

2.4.6 Hybrid photon counting detectors

In hybrid photon counting detectors, charges are generated by incident X-ray photons in individual pixels like in a CCD camera, but instead of accumulating the charges during the exposure time, each photon is counted and the total is read digitally after the exposure (see figure 2.15). Single photon counting at high count rates is feasible because the counting circuit can be integrated within the pixel. A main advantage of photon counting detectors is that the height of each pulse can be compared to a pre-defined threshold, and only pulses above the threshold are counted; therefore, thermal excitations which are on the order of $k_\mathrm{B}T \approx 0.02\,\mathrm{eV}$ can be rejected while still counting every X-ray photon. Due to this, photon counting detectors have a very low dark current, which is dominated by background radiation from cosmic particles and radioactive decay. Compared with CCD cameras and fluorescent screens, this yields dramatically better detection of small signals. Additionally, the dynamic range is only limited by the range of the digital counter, which usually exceeds $1 \cdot 10^6$. Because the readout is digital, there is no added noise from readout and the dynamic range can be enhanced simply by taking multiple images with suitably shorter exposure time and adding the images up in the later analysis. However, the maximum count rate of hybrid photon counting detectors is limited by the ability of the comparator to discriminate between two pulses. This limits the count rate of hybrid photon counting detectors, currently to about $1 \cdot 10^7/\mathrm{s}$, but efforts are under way to improve the maximum count rate. Hybrid photon counting detectors have to be calibrated for absolute measurements (Broennimann et al. 2006; Wernecke, Gollwitzer, et al. 2014; Johnson et al. 2014).

Due to the mentioned advantages, hybrid photon counting detectors are the most popular detectors for SAXS and GISAXS today.

3 Methods

In this chapter, I will present the experimental and theoretical methods used in all of my studies. I will start with a description of the experimental setup used for GISAXS measurements in section 3.1. Then the theoretical methods for the simulation of GISAXS measurements of gratings will be presented in section 3.2. Parts of this chapter have already been published in the peer-reviewed paper "Grazing-Incidence Small-Angle X-Ray Scattering (GISAXS) on Small Periodic Targets Using Large Beams" (Pflüger, Soltwisch, Probst, Scholze, and Krumrey, 2017). Additional methods used only in a single study will be introduced in the respective chapter.

The computer programs and scripts that I used for simulation and data analysis together with all measurement data are available in the electronic supplementary information at `https://doi.org/10.24433/CO.0375205.v1`. There, a virtual machine image is provided which contains all necessary software to execute the analysis scripts, reproducing the figures shown throughout the thesis. Not included are sources for figures that I do not have the necessary rights to distribute freely, as well as the commercial *JCMsuite* software package; however, the output of the *JCMsuite* simulations is included and scripts are provided to reproduce these if a *JCMsuite* copy is available.

3.1 Instrumentation

3.1.1 BESSY II

The X-ray source for all measurements presented in this thesis was the *BESSY II* storage ring which is operated by the Helmholtz-Zentrum Berlin (HZB) and located in Berlin, Germany. The BESSY II storage ring is a third-generation synchrotron light source that was commissioned in 1998 (Bakker 1999). Important properties of BESSY II are given in table 3.1, and an overview of BESSY II is shown in figure 3.1. BESSY II comprises a linear accelerator and synchrotron to accelerate electrons to relativistic speed and an evacuated storage ring where the electrons are kept on a closed path and at a constant kinetic energy. In the standard operation mode called top-up mode, electrons are injected regularly into the storage ring, replacing lost electrons and ensuring a nearly constant beam current (Kuske et al. 2008). In normal operation, the storage ring is mainly filled with electron bunches which are about 30 ps long each with a distance between bunches of 2 ns (Müller et al. 2016). For GISAXS purposes, the separation between electron bunches is so small that the emitted X-rays appear continuous.

Storage ring circumference	240 m
Number of bending magnets	32
Number of beam lines	45
Electron energy	1.7 GeV
Electron beam current	300 mA
Duration of light pulses	30 ps
Bending magnet radius	4.2 m
Bending magnet field	1.3 T

Table 3.1: Properties of BESSY II. All data is obtained from HZB (2020b).

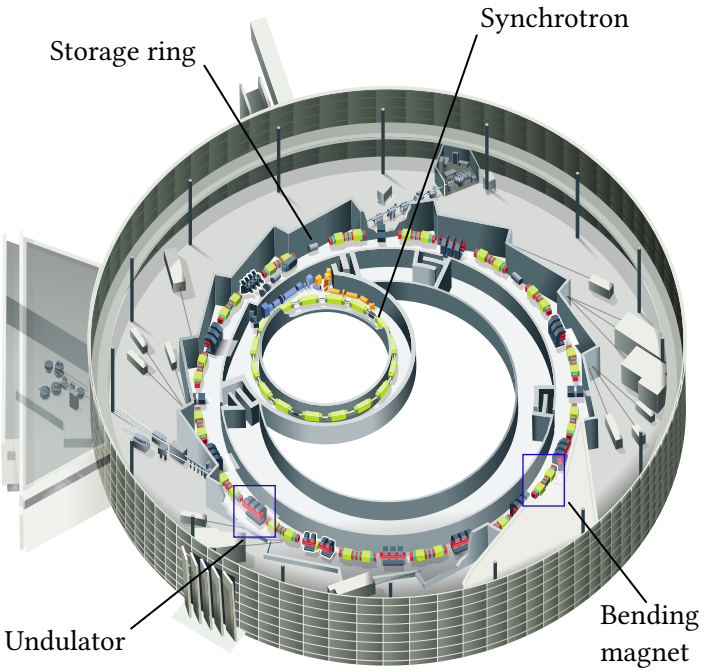

Figure 3.1: Overview of the BESSY II synchrotron light source. Electrons are first accelerated in the inner synchrotron and then stored in the storage ring. Bending magnets keep the electrons in the storage ring on their circular path. In the straight sections between bending magnets, insertion devices such as undulators are installed. Adapted from a graphic by HZB/Ela Strickert.

In the storage ring, the electrons are deflected by bending magnets and in between the bending magnets are straight sections dedicated to house insertion devices such as wigglers and undulators. At the bending magnets as well as at the insertion devices, synchrotron radiation is emitted and passed through ports into beam lines situated in the experimental hall. A section of the experimental hall containing 11 beam lines is dedicated to metrology and operated by Physikalisch-Technische Bundesanstalt (PTB) (Beckhoff, Gottwald, et al. 2009; Richter and Ulm 2019).

3.1.2 Four-crystal monochromator beam line

The beam line that I used to conduct my experiments is the four-crystal monochromator (FCM) beamline in the PTB laboratory at BESSY II. A scheme of the beam line and the end stations for GISAXS experiments is shown in figure 3.2. In the beam line, the X-rays emitted from a bending magnet are passed through the first slit, which defines the acceptance, and reflected by a first mirror. The mirror is made of Si coated with Pt and has radii of curvature of 131 mm and 4.3 km, respectively and focuses the beam in horizontal direction onto the sample site and collimates it in vertical direction. Then, after passing a second slit used as a scatter guard, the X-rays are monochromatized using an eponymous four-crystal monochromator. The advantage of using four crystals for the monochromatization is that it allows to change the selected wavelength while keeping the direction of the monochromatized beam steady. The monochromatic beam is then reflected by a plane mirror which is equipped with a bender. The mirror is made of Zerodur and is coated in one part with Pt and in a second part with MgF_2, allowing to either use the MgF_2 coating for suppression of higher orders or the Pt coating for highest beam line flux. The bender can be used to change the vertical focus. When the bender is not engaged, the beam stays collimated in vertical direction, but when activating the bender, the beam can be focused onto the sample site. Between the last mirror and the sample site, about 150 cm before the sample size, there is a fourth slit and a mount for a first pinhole. Generally, either the fourth slit is used to define the final beam size and a pinhole is not used, or a pinhole is inserted to define the final beam size. After the pinhole mount, the beam passes into the reflectometer sample chamber. In the reflectometer 10 cm before the sample, there is a fifth slit which is used as a final scatter guard. Alternatively,

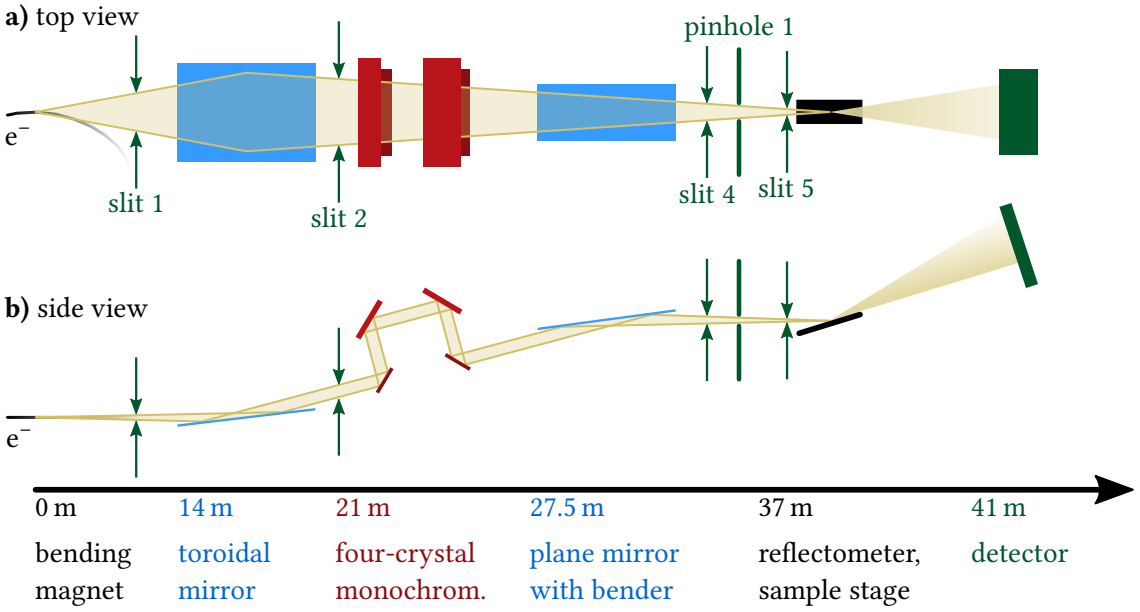

Figure 3.2: Scheme of the four-crystal monochromator beam line and GISAXS setup. Part (a) shows a view from the top, part (b) shows a side view. At the bottom, the distance of the respective element from the source inside the bending magnet is indicated. Slit number 3 is usually not used and therefore not shown here.

the fifth slit can be replaced by a second pinhole, also acting as a scatter guard. Finally, the X-rays scatter at the sample and are collected by a detector (Krumrey and Ulm 2001).

The beam line allows the adjustment of the photon energy in the range from 1.75 keV to 10 keV. For the photon energy range from 1.75 keV to 3.6 keV, InSb crystals are used in the four-crystal monochromator, and in the range from 2.1 keV Si crystals are used. Filters can be used to reduce heat load at the monochromator and to further reduce the intensity of parasitic X-ray wavelengths; in total, five different filters are available, with a thickness of 25 µm or 125 µm Be and 12.5 µm Al, 200 µm Al, or 10 µm Cu.

For GISAXS experiments, I focused the beam onto the sample for highest photon flux. Depending on the requirements of the experiment, in particular the size of the sample under investigation, I used two different optical configurations, one for a smaller size of the focus at the sample and one with a larger focus with a higher flux and minimized scatter. The smaller beam spot size was reached using a Pt pinhole with a diameter of 100 µm (Plano GmbH, Germany) at the position of pinhole 1, and an adjustable slit system with low-scatter blades (XENOCS, France) as a scatter guard at the position of slit 5. The resulting spot had a size of approximately 150 µm × 150 µm full width at half maximum due to strong scattering at pinhole 1. The larger spot size could be obtained by using a SCATEX Ge pinhole selected for minimum scattering with a diameter of 0.52 mm (Incoatec GmbH, Germany) at the first pinhole position and a second low-scatter SCATEX Ge pinhole with a diameter of 1 mm (Incoatec GmbH, Germany) instead of slit 5. The resulting beam spot size was about 0.5 mm × 0.5 mm at the sample position with minimal parasitic scattering.

The setup inside the reflectometer is shown in figure 3.3. The reflectometer is equipped with a goniometer which allows sample movements in all directions with a resolution of 3 µm as well as rotations around all sample axes with an angular resolution of 0.001° (D. Fuchs et al. 1995). A number of additional detectors are placed in the reflectometer. For GISAXS measurements most

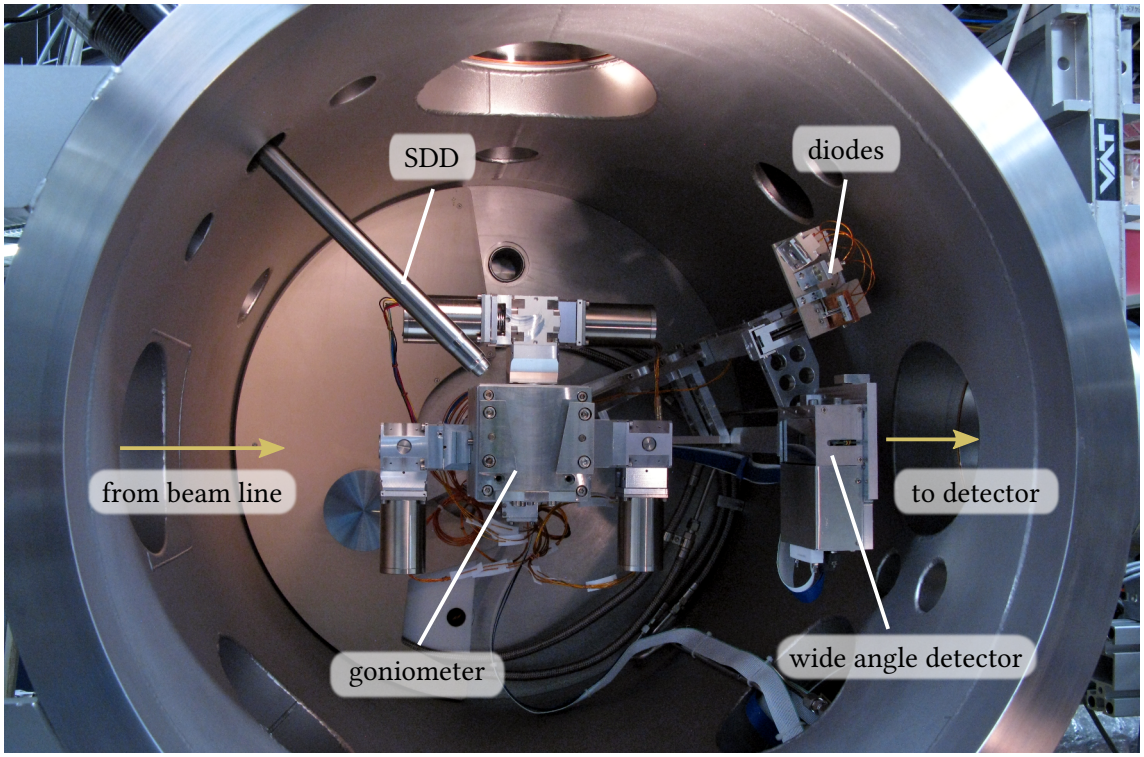

Figure 3.3: Experimental setup inside the reflectometer. Shown is the opened main vacuum chamber of the reflectometer. Samples are fixed on sample holders which can be shuttled into the evacuated chamber from above and mounted on the goniometer; in this image, no sample is mounted. The diodes and the wide angle detector are attached on a rotating arm so that they can be moved into or out of the beam path as required. The holder for slit 5 and pinhole 2 is attached to the door of the vacuum chamber and is therefore not visible in the opened chamber.

importantly, there are several X-ray photodiodes placed on a rotating arm, which are used in sample alignment as detailed below. Auxiliary X-ray fluorescence measurements can be performed with an SDD detector, which can be used to learn about the chemical composition of the specimen under study. Recently, a Pilatus 100K hybrid pixel area detector (Dectris Ltd, Switzerland) was installed on the detector arm (Skroblin, Schavkan, Pflüger, Pilet, Lüthi, and Krumrey, 2020). This allows to perform wide angle scattering measurements for the detection of crystalline structures in the sample or for the measurement of nanostructures with a size under about 5 nm. For GISAXS measurements, the angular resolution of the wide angle detector is not sufficient; instead, the diodes and the wide angle detector are moved outside of the beam path, and the scattered X-rays leave the reflectometer towards the main detector.

The main detector is a Pilatus 1M hybrid pixel area detector (Dectris Ltd, Switzerland) with an active area of 168.7 mm × 179.4 mm containing 981 × 1043 pixels. The detector comprises 10 modules arranged in five rows and two columns, with small inactive gaps between the modules. The gaps show up in measurements as characteristic stripes without information. The detector is mounted on a movable sled on the HZB SAXS setup, which is shown in figure 3.4 (Gleber et al. 2010). By moving the detector on the sled, the distance between the sample and the detector can be changed between 2 m and about 4.5 m and the exit angle can be changed between 0° and 2°. Due to the single-pixel photon detection of the Pilatus detector, the detector angular resolution for both exit angles α_f and θ_f is given by the solid angle covered by an individual pixel, which is between 0.005° for a sample-to-detector distance of 2 m and 0.002° for a sample-to-detector distance of 4.5 m. The quantum efficiency of the detector has been calibrated using a cryo-radiometer as the

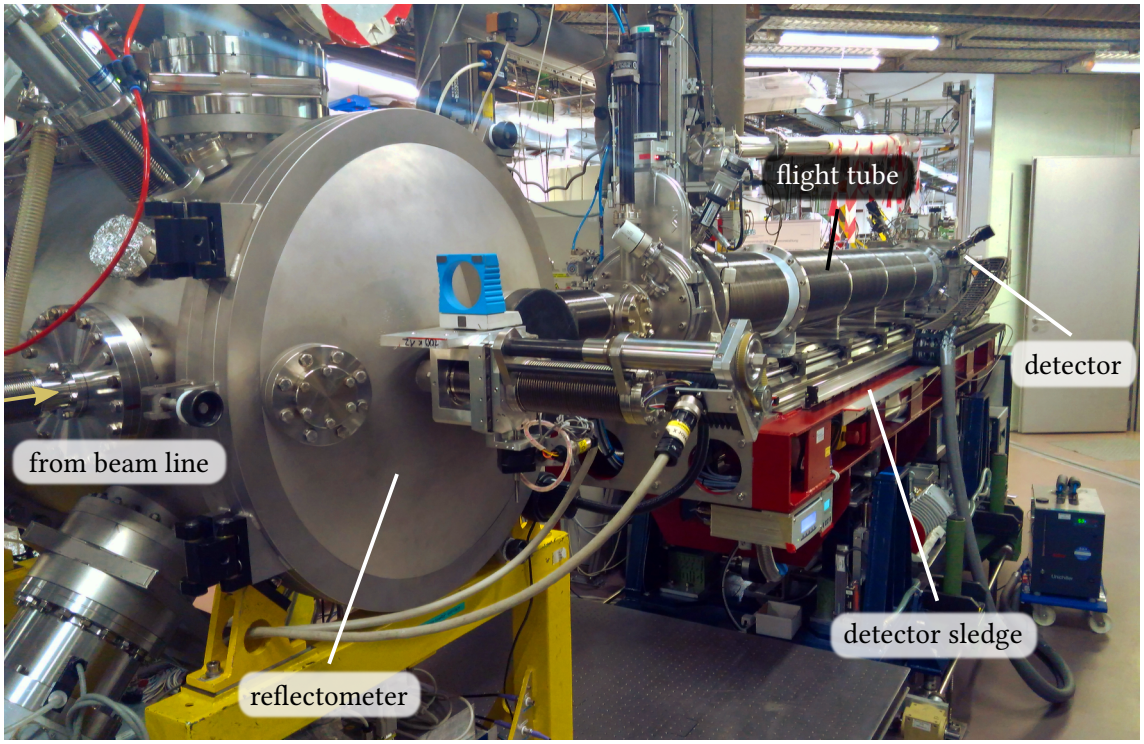

Figure 3.4: Reflectometer, flight tube, and detector sledge. The door of the main vacuum chamber of the reflectometer is closed. To enable movement of the detector on its sledge, the flight tube comprises edge-welded bellows which can expand and contract as needed and can contain a vacuum.

primary standard in the whole photon energy range of the beam line. The resulting uncertainty is 3 % for the average quantum efficiency, and the detector shows an inhomogeneity of about 3 % over the detector surface (Wernecke, Gollwitzer, et al. 2014). Along the whole beam path including the sample site and up to the detector surface, high vacuum (pressure below $1 \cdot 10^{-4}$ mbar) is maintained using differential pumping. Notably, parasitic scattering between sample and detector is virtual absent because there is no optical element or vacuum window between sample and detector.

The photon energy scale of the beam line has been traced back to the SI by back-reflection from a Si crystal, which relates the X-ray wavelength to the Si lattice constant which itself is known with very small uncertainties. Using this calibration, the photon energy of the absorption edge of the Cu filter was measured. This absorption edge is used to calibrate the photon energy in daily operation (Krumrey and Ulm 2001). The resulting relative uncertainties for the photon energy are limited by the resolving power of the monochromator $\Delta E_{\mathrm{ph}}/E_{\mathrm{ph}}$, which is smaller than $2.5 \cdot 10^{-4}$ using the InSb crystals and smaller than $1 \cdot 10^{-4}$ using the Si crystals in the monochromator. The photon flux of the beam line can be measured using a transmission Si diode with a thickness of about 8 µm which is placed directly behind pinhole 1. The transmission Si diode is calibrated using a cryo-radiometer as the primary standard as well, with a relative uncertainty of 1 %. At $E_{\mathrm{ph}} < 3$ keV, the transmission of the Si diode is generally too low for GISAXS measurements, so that measurements have to be taken without a flux detector, so that flux measurements can only be performed before and after the scattering measurements.

The distance between sample and detector is calibrated using triangulation. The detector sled is equipped with calibrated optical encoders (Dr. Johannes Heidenhain GmbH, Germany), so that the relative position of the detector is known with small uncertainties. A silver behenate sample which

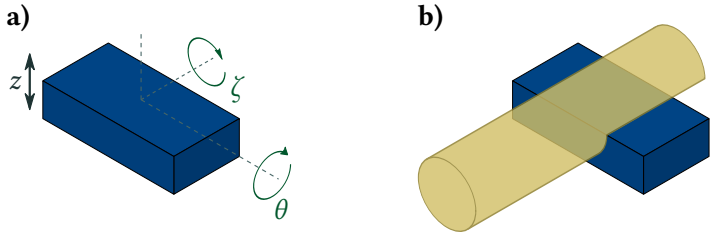

Figure 3.5: Sample alignment. **a)** The position z and two angles need to be adjusted. **b)** The sample is aligned when it cuts the X-ray beam in half and the sample surface is parallel to the beam.

shows well-defined scattering is mounted in transmission geometry, and its scattering is recorded at several detector positions. Then the offset between the relative position of the detector according to the optical encoders and the distance to the sample can be obtained from triangulation without knowledge of the scattering angle of the silver behenate sample. The resulting uncertainty is smaller than 5 mm, so that generally the leading uncertainty for the distance between sample and detector stems from the length of the projection of the X-ray beam on the sample, which generally is longer than 5 mm. The scattering angles can then be calculated from the detector image using the pixel distance of $(172.1 \pm 0.2)\,\mu m$, which was calibrated by translating the detector equipped with optical encoders and observing the position of the unscattered X-ray beam (Wernecke, Gollwitzer, et al. 2014).

3.1.3 Sample alignment

GISAXS measurements rely on very small incidence and exit angles, which means the sample has to be aligned to the X-ray beam carefully. After a perfect alignment, the sample shadows half of the X-ray beam and the sample surface is parallel to the X-ray beam, see figure 3.5. For this, the position of the sample needs to be adjusted in the z direction, and the angle θ needs to be aligned with the X-ray beam. Additionally, to preserve the alignment when measuring at multiple sample positions, it is advantageous to also align the roll angle ζ such that translations of the sample do not change its position in the z direction. Using a real goniometer, it is also important to ensure that the sample is in the center of the θ rotation axis, so that its z position does not change when changing the incidence angle. Since the position of the sample is already determined by the position of the X-ray beam, it is therefore necessary to translate the whole goniometer such that the position of the X-ray beam is at the center of the θ axis.

In the reflectometer that I used at the FCM beam line, the alignment is normally done in this sequence:

1. The X-ray beam is aligned with the goniometer using a thin needle mounted on the goniometer a few centimetres outside the θ axis. Using a diode, the shadow of the thin needle is observed close to $\theta = 0°$ and $\theta = 180°$ and the height of the whole reflectometer is adjusted so that the shadow is observed exactly at 0° and 180°.
2. The sample is mounted on the goniometer, and it is brought into the X-ray beam using translation in z so that it shadows half of the beam according to the photocurrent on the diode.
3. θ is scanned and adjusted to the maximal signal, because when the sample is parallel to the X-ray beam, the shadowing of the sample is minimized.
4. The X-ray beam is again cut in half by adjusting z, and θ is optimized. This is repeated until the values for z and θ are converged.
5. To align ζ, the sample is translated and the beam is cut in half by adjusting z. From the offset in z, the correction in ζ is calculated so that the offset in z is minimized.
6. The alignment in θ is checked by measuring the reflection angle between the direct beam without the sample and the specularly reflected beam using the photo diode, which is

equipped with a rotary encoder as well. If $2\Delta\theta_{\text{diode}} = \Delta\theta_{\text{sample}}$, then the adjustment was successful.

All steps besides the first one have to be repeated for each sample. With some routine, I managed to align a single sample in about 20 min with an accuracy of about 0.01° in θ. However, the manual process is tiring when a large number of samples need to be measured, and my accuracy deteriorated during long measurement campaigns; therefore, I developed a sample alignment program which automatically aligns multiple samples and also checks the alignment of the goniometer.

To develop the program and test it in a safe environment without potentially crashing the sample into detectors in the goniometer due to a sign error, I first developed a virtual reference reflectometer. I used the *PCASpy* library (X. Wang 2020) to mock motors and sensors on the *EPICS* communications bus in use at BESSY II (Dalesio, Kozubal, and Kraimer 1991) and the *quaternion* library (Boyle 2019) for geometrical calculations. To mimic the actual reflectometer as closely as possible, I implemented a simple simulation including finite motor speed and motor acceleration using finite time steps. I also added backlash to the motors, which means that each motor has a preferred direction. When driving to a new location in the preferred direction, the motor directly drives to the location, if driving to a new location in the opposite direction, the motor overshoots the intended location and then retreats in the preferred direction to the target location. In the real reflectometer this is done to ensure that motor positions are accurately repeatable despite mechanical hysteresis; however, it means that small steps in the preferred direction are much faster to execute than small steps in the opposite direction. I also implemented a gaussian X-ray beam and shadowing and reflection at the sample.

Equipped with the virtual reference, I then developed a graphical program for the alignment which executes the above mentioned steps automatically. The algorithm relies on a relatively large number of z scans to cut the X-ray beam in half, because these scans are needed for the alignment of ζ as well as θ and naturally z. Therefore, I optimized these z scans, the best algorithm I found was:

1. Only when cutting the X-ray beam the first time with a sample, engage a flyscan, which means driving the z motor at constant speed while continuously taking measurements of the diode current. When the diode current has crossed half of the current of the direct beam, stop the z motor. Because of delays in the diode current measurement and motor acceleration, this is only useful for searching the approximate sample position.
2. Measure the signal. If it is more than half, move the sample up, if it less than half, move it down. If the movement direction is in the preferred direction of the motor, move by half of the beam height. If it is in the opposite direction, move by ten beam heights. Repeat until the distance between the best known position above the optimum and the best known position below the optimum is smaller than one beam height.
3. Use the *optimize.brentq* implementation of Brent's method (Brent 1973) found in the *SciPy* software package to find the optimum.

For this method, the beam height has to be provided by the user, but I found that it is relatively tolerant to errors in the estimated beam height. With this algorithm, a full automatic alignment of a sample with the same accuracy as a manual alignment takes less than 15 min and the alignment accuracy does not deteriorate anymore in long measurement campaigns.

The uncertainty of $u(\theta) = 0.01°$ reached with this alignment is good enough to take accurate GISAXS measurements, but for the most precise GISAXS simulations, the incidence angle α_i needs to be known with smaller uncertainties. For this, I again used triangulation on the main detector. The distance between the detector and the sample is already known from the SAXS

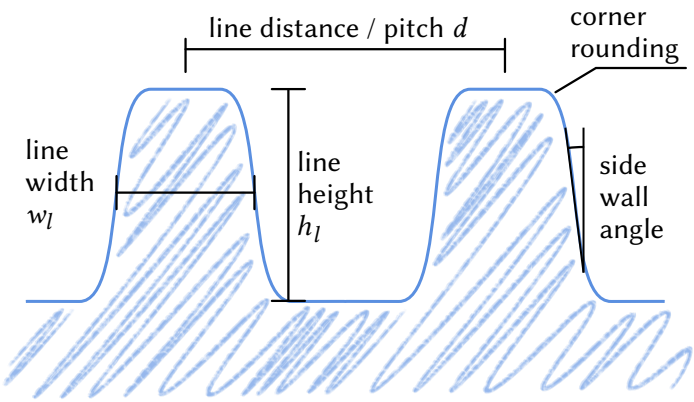

Figure 3.6: Cross section of a grating with important geometric parameters and features. The line distance is also called pitch and the line width is also called critical dimension.

triangulation. Therefore, the incidence angle can be triangulated by measuring the position of the unscattered beam and the specularly reflected beam on the detector. This is safely possible only if the intensity of the X-ray beam is reduced by several orders of magnitude using the available filters in the beam line in combination with a slight misalignment of the last two monochromator crystals with respect to the first two monochromator crystals. The actual GISAXS measurement is then carried out after removing the filters and realigning the monochromator, but without moving the sample or the detector. Using this method, I routinely reached uncertainties of the incidence and exit angles $u(\alpha_i), u(\alpha_f) < 0.002°$.

3.2 Grating GISAXS

Throughout my thesis, line grating measurements using GISAXS will be recurring theme. This is because, on the one hand, line gratings are the fundamental building block in many modern semiconductor production processes (Jung et al. 2006; Natarajan et al. 2014; Seo et al. 2014); therefore, the measurement of the geometrical parameters of gratings (compare figure 3.6) is a central application in semiconductor metrology. On the other hand, many aspects of the scattering of other periodically structured samples can be described using the theory of grating scattering, as well. Therefore, I will introduce and compare different theoretical approaches to describe grating GISAXS in this section.

I will start with introducing the main approaches that so far have been used to describe grating GISAXS in the literature. These are the Born approximation (BA) (subsection 3.2.1), and the distorted-wave Born approximation (DWBA) (subsection 3.2.2). Next, I will introduce a simulation method which has only recently been applied to grating GISAXS, which is the solution of Maxwell's equations using finite elements (subsection 3.2.3). Then I will compare these theoretical approaches in subsection 3.2.4. I will show that the methods that are based on the BA can accurately describe the position of grating diffraction orders, but generally show large deviations when describing their intensity. Based on this, I will argue in subsection 3.2.5 that the right theoretical method has to be chosen depending on the application at hand.

3.2.1 Idealized gratings - the Born Approximation

Several groups have already performed GISAXS measurements on gratings, and the scattering of idealized gratings is well understood. Tolan et al. (1995), Metzger et al. (1997), Jergel et al.

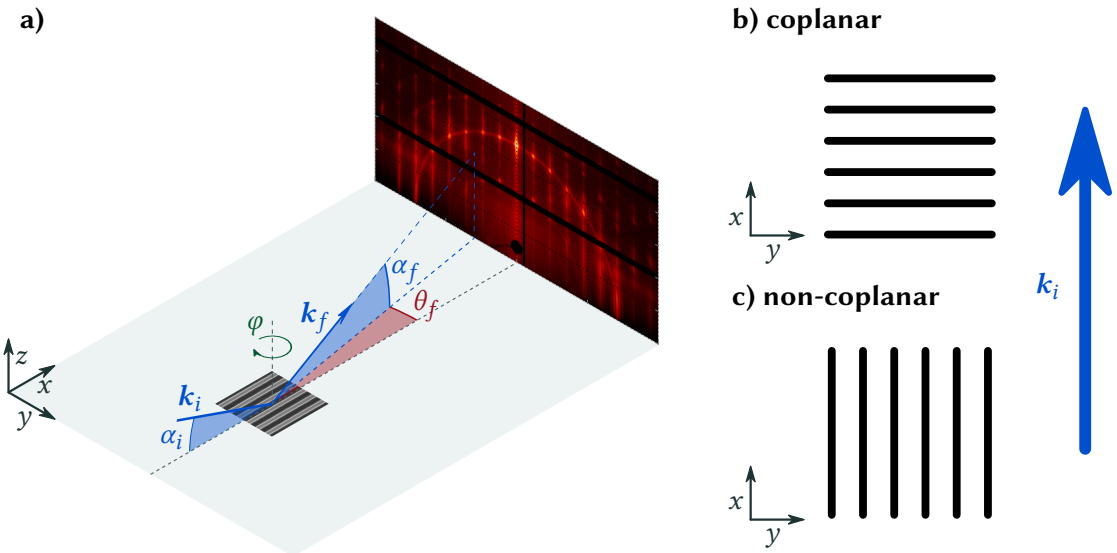

Figure 3.7: Coplanar and non-coplanar grating diffraction. a) Shown is a GISAXS experiment with the grating in non-coplanar geometry. **b)** In coplanar geometry, the grating lines are perpendicular to the incident beam (blue arrow) when viewed from the top. **c)** In non-coplanar geometry, they are parallel.

(1999), and Mikulík and Baumbach (1999) measured gratings using GISAXS with the grating lines perpendicular to the incoming beam (coplanar geometry, compare figure 3.7b).

GISAXS measurements with the grating lines along the incoming beam (so-called non-coplanar geometry, conical mounting or sagittal diffraction geometry, see figure 3.7c) were analysed by Mikulík, Jergel, et al. (2001). They found out that the non-coplanar geometry is superior in GISAXS. While in coplanar geometry the grating diffracts to high exit angles depending on the diffraction order, in non-coplanar geometry all diffraction orders are diffracted to small exit angles. Because the signal intensity rapidly decreases at higher exit angles, more diffraction orders can be imaged in non-coplanar geometry. To quantify this difference and thus understand the advantage of the non-coplanar geometry better, I will derive the positions of the diffraction orders in coplanar and non-coplanar geometry using the Born approximation introduced in subsection 2.2.2. This leads to the reciprocal space construction of the scattering patterns, which was first presented by Mikulík, Jergel, et al. (2001) and laid out in detail by Yan and Gibaud (2007).

My derivation closely follows the derivation of Yan and Gibaud (2007), but instead of the laboratory coordinate system, I will use the more prevalent sample coordinate system (see figure 3.7a). The k-space is the reciprocal of the real space, with the corresponding axes in the same direction as the real axes. In this space, the wavevectors of the incoming beam $\boldsymbol{k}_i$ and the scattered beam $\boldsymbol{k}_f$ are

$$\boldsymbol{k}_i = k_0 \begin{pmatrix} \cos\alpha_i \\ 0 \\ -\sin\alpha_i \end{pmatrix} \tag{3.2.1}$$

$$\boldsymbol{k}_f = k_0 \begin{pmatrix} \cos\alpha_f \cos\theta_f \\ \cos\alpha_f \sin\theta_f \\ \sin\alpha_f \end{pmatrix} \tag{3.2.2}$$

$$k_0 = |\boldsymbol{k}_i| = |\boldsymbol{k}_f| = \frac{2\pi}{\lambda} \tag{3.2.3}$$

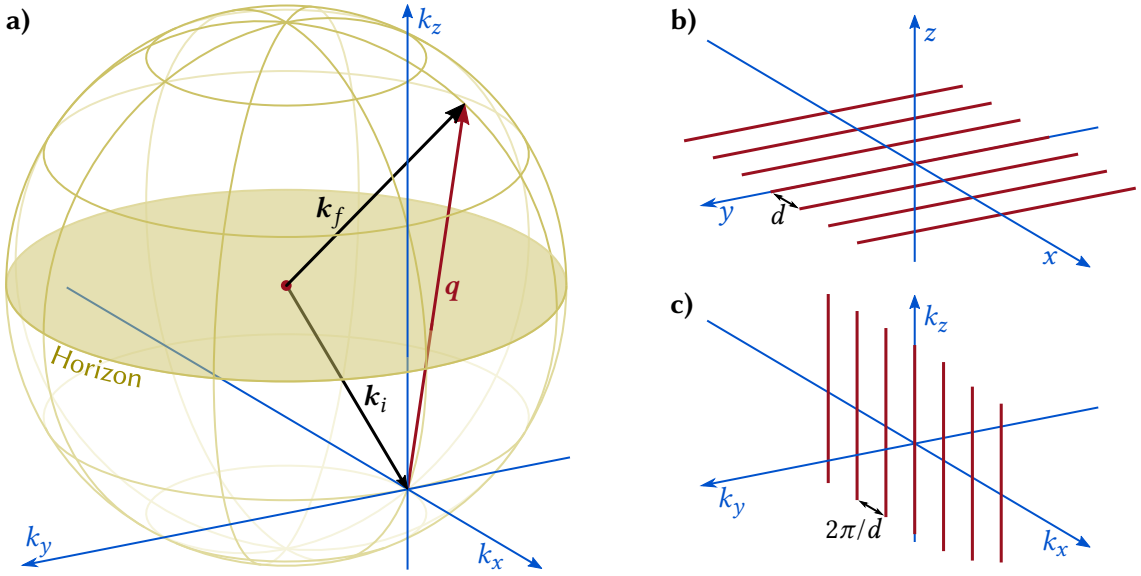

Figure 3.8: The Ewald sphere and gratings in reciprocal space. a) The Ewald sphere has its center at $-\boldsymbol{k}_i$ and is spanned by $\boldsymbol{k}_f$. $\boldsymbol{k}_f$ rotates freely, but has fixed length k_0. The scattering vector $\boldsymbol{q} = \boldsymbol{k}_f - \boldsymbol{k}_i$ reaches to any point on the surface of the sphere, but only scattering above the horizon is visible in GISAXS. Note that in GISAXS, the incidence angle is usually much smaller than shown in the sketch. **b)** A grating in coplanar geometry consists of lines parallel to the y-axis, lying in the y-x-plane, with distance d. **c)** The Fourier transform of this grating consists of lines parallel to the k_z-axis in the k_z-k_x-plane, with reciprocal distance $2\pi/d$.

with the incident angle α_i, the angle between the sample plane and the scattered beam α_f and the angle between the projection of the scattered beam on the sample plane and the x-axis θ_f as well as the incident wavelength λ.

From subsection 2.2.2 we know that in Born approximation, the scattering is proportional to the Fourier transform $\hat{V}(\boldsymbol{q})$ of the sample evaluated at $\boldsymbol{q} = \boldsymbol{k}_f - \boldsymbol{k}_i$. $\boldsymbol{q}$ expressed in angle coordinates is

$$\boldsymbol{q} = k_0 \begin{pmatrix} \cos\alpha_f \cos\theta_f - \cos\alpha_i \\ \cos\alpha_f \sin\theta_f \\ \sin\alpha_f + \sin\alpha_i \end{pmatrix}. \tag{3.2.4}$$

Using the interpretation of Ewald (1913), we can visualize $\hat{V}(\boldsymbol{q})$ as the intersection of $\hat{V}$ with the Ewald sphere of elastic scattering. With equations (3.2.3) and (3.2.4) we obtain the equation for the Ewald sphere of elastic scattering

$$k_0 = |\boldsymbol{k}_f| = |\boldsymbol{q} + \boldsymbol{k}_i| \tag{3.2.5}$$

$$\begin{aligned} \Longrightarrow k_0^2 &= |\boldsymbol{q} + \boldsymbol{k}_i|^2 = (q_x + k_{i,x})^2 + (q_y + k_{i,y})^2 + (q_z + k_{i,z})^2 \\ &= (q_x + k_0 \cos\alpha_i)^2 + q_y^2 + (q_z - k_0 \sin\alpha_i)^2 \quad . \end{aligned} \tag{3.2.6}$$

The Ewald sphere thus has radius k_0 and center $-\boldsymbol{k}_i$, see figure 3.8a).

Perfectly aligned coplanar mounting An idealized grating in coplanar mounting consists of infinite grating lines parallel to the y-axis, which lie in the sample plane and are separated by the pitch d (see figure 3.8b). The Fourier transform $\hat{V}$ of the grating in coplanar mounting comprises

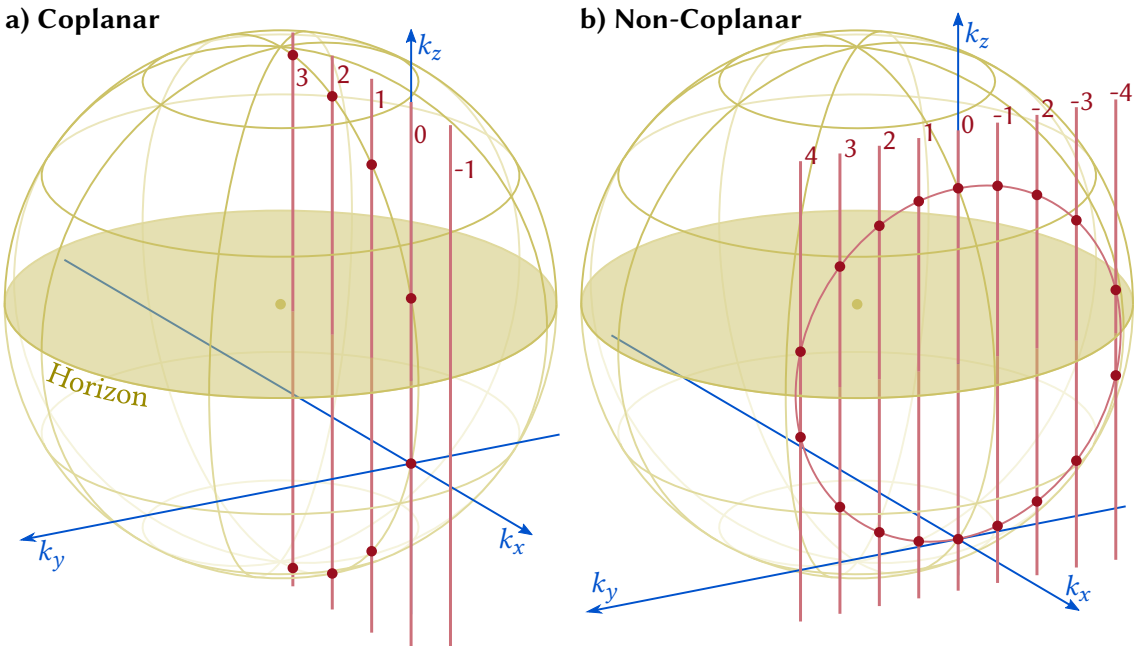

Figure 3.9: The reciprocal space construction of grating scattering. Grating truncation rods are shown in red, the Ewald sphere in yellow. Red dots mark the points of intersection, i.e. the diffraction orders. The diffraction order p is indicated at the truncation rods. **a)** In coplanar geometry, the grating truncation rods intersect the Ewald sphere in the k_z-k_x plane. **b)** In non-coplanar geometry, the diffraction orders lie on a circle, of which a semi-circle is visible above the horizon. For clarity, a higher incident angle is shown in non-coplanar geometry.

grating truncation rods (GTRs), which are parallel to the k_z-axis in the k_z-k_x-plane and separated by $2\pi/d$ in k_x:

$$k_{g,x} = -p\,2\pi/d = -k_0\,p\lambda/d \tag{3.2.7}$$

$$k_{g,y} = 0 \quad , \tag{3.2.8}$$

with the grating diffraction order $p \in \mathbb{Z}$ (see figure 3.8c). To obtain the resulting scattering, we intersect the Ewald sphere with the reciprocal space representation of the grating, so that $\boldsymbol{q} = \boldsymbol{k}_g$. The intersection is shown in figure 3.9a. As can be seen, the GTR intersect the Ewald sphere in the k_z-k_x plane once above and once below the scattering horizon. Using equation (3.2.4), we can directly express the scattering in angular coordinates:

$$q_y = k_{g,y}: \qquad k_0\,\cos\alpha_f \sin\theta_f = 0 \tag{3.2.9}$$

$$\Rightarrow \sin\theta_f = \theta_f = 0 \quad \text{for } \alpha_f \neq \pi/2 \tag{3.2.10}$$

$$q_x = k_{g,x}: \qquad k_0\,(\cos\alpha_f \cos\theta_f - \cos\alpha_i) = -k_0\,p\lambda/d \tag{3.2.11}$$

$$\Rightarrow \cos\alpha_f = \cos\alpha_i - p\lambda/d \tag{3.2.12}$$

$$\Rightarrow \alpha_f = \pm\arccos(\cos\alpha_i - p\lambda/d) \quad . \tag{3.2.13}$$

The solutions with the minus can be discarded, because they lie below the sample horizon.

Perfectly aligned non-coplanar mounting A perfectly aligned grating in non-coplanar mounting has the infinite grating lines parallel to the x-axis. Thus, the GTRs are parallel to

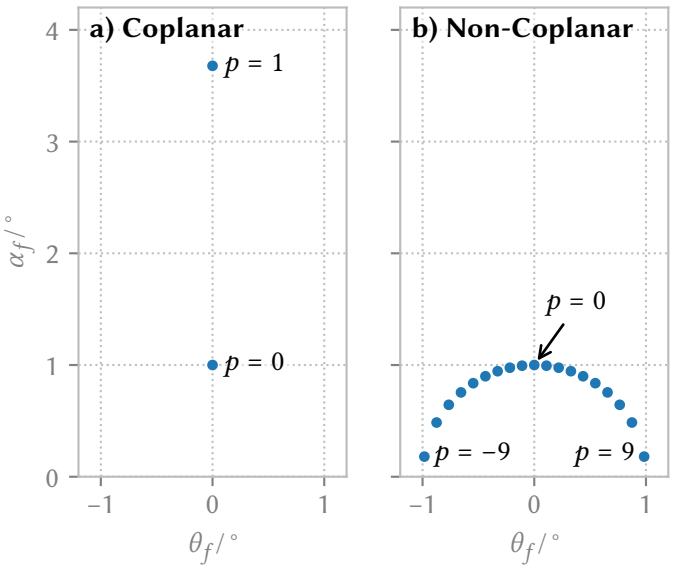

Figure 3.10: Comparison between coplanar and non-coplanar scattering.
a) At a given wavelength, grating pitch, and incident angle, the diffraction orders are widely separated in coplanar geometry. **b)** In contrast, in non-coplanar geometry the diffraction orders are all at small α_f.

the k_z-axis in the k_z-k_y-plane and separated by $2\pi/d$ in k_y:

$$k_{g,x} = 0 \tag{3.2.14}$$

$$k_{g,y} = p\,2\pi/d = k_0\,p\lambda/d \quad . \tag{3.2.15}$$

Again, we obtain the scattering by intersection with the Ewald sphere $\boldsymbol{q} = \boldsymbol{k}_g$, shown in figure 3.9b. The scattering now lies on a circle in the k_z-k_y-plane. To express $\boldsymbol{q}$ in angle coordinates, we need to calculate q_z. To obtain an expression for q_z, we use equation (3.2.6) and insert $q_x = k_{g,x}$ and $q_y = k_{g,y}$, yielding

$$k_0^2 = (0 + k_0 \cos\alpha_i)^2 + (p\,k_0\,\lambda/d)^2 + (q_z - k_0 \sin\alpha_i)^2 \quad . \tag{3.2.16}$$

Solving this for q_z yields

$$\begin{aligned}(q_z - k_0 \sin\alpha_i)^2 &= k_0^2(1 - \cos^2\alpha_i) - (p\,k_0\,\lambda/d)^2 \\ &= k_0^2\left(\sin^2\alpha_i - (p\,\lambda/d)^2\right) \qquad (3.2.17)\\ \Rightarrow q_z &= k_0\left(\sin\alpha_i \pm \sqrt{\sin^2\alpha_i - (p\,\lambda/d)^2}\right) \qquad (3.2.18)\end{aligned}$$

Now, we discard the solution with the minus as it corresponds to reflections below the sample horizon, arriving at

$$q_z = k_0\left(\sin\alpha_i + \sqrt{\sin^2\alpha_i - (p\lambda/d)^2}\right) \tag{3.2.19}$$

$$\boldsymbol{q} = k_0\begin{pmatrix} 0 \\ p\lambda/d \\ \sin\alpha_i + \sqrt{\sin^2\alpha_i - (p\lambda/d)^2}\end{pmatrix} \quad . \tag{3.2.20}$$

To express the scattering in angle coordinates, we use equations (3.2.4), (3.2.14), (3.2.15) and

(3.2.19), giving

$$q_z: \quad \sin\alpha_f + \sin\alpha_i = \sin\alpha_i\left(1+\sqrt{1-\left(\frac{p\lambda}{d\sin\alpha_i}\right)^2}\right)$$

$$\Rightarrow \alpha_f = \arcsin\left(\sqrt{\sin^2\alpha_i - \left(\frac{p\lambda}{d}\right)^2}\right) \tag{3.2.21}$$

$$q_y: \quad \cos\alpha_f \sin\theta_f = p\lambda/d$$

$$\Rightarrow \sin\theta_f = \frac{p\lambda/d}{\cos\alpha_f} \tag{3.2.22}$$

$$q_x: \quad \cos\alpha_f\cos\theta_f - \cos\alpha_i = 0$$

$$\Rightarrow \cos\theta_f = \frac{\cos\alpha_i}{\cos\alpha_f} \tag{3.2.23}$$

$$\frac{q_y}{q_x}: \quad \tan\theta_f = \frac{\sin\theta_f}{\cos\theta_f} = \frac{p\lambda/d}{\cos\alpha_f}\frac{\cos\alpha_f}{\cos\alpha_i}$$

$$\Rightarrow \theta_f = \arctan\left(\frac{p\lambda}{d\cos\alpha_i}\right) \quad . \tag{3.2.24}$$

As an example, the position of the grating diffraction orders of a grating with $d = 65\,\text{nm}$ measured at a photon energy of $E_{\text{ph}} = 10\,\text{keV}$ in coplanar and non-coplanar geometry with an incident angle of $\alpha_i = 1^\circ$ is shown in figure 3.10. The main advantage of non-coplanar geometry in comparison to coplanar geometry is that all diffraction orders are at $\alpha_f < \alpha_i$ and thus close to the regime of total external reflection. Therefore, the scattering cross section of diffraction orders with higher p is much higher in non-coplanar mounting (Mikulík, Jergel, et al. 2001), and all subsequent GISAXS studies of gratings used conical mounting.

Misaligned gratings In practice, the alignment is generally not perfect, and a misaligned grating scatters to different angles. For the misaligned grating, the grating lines are rotated around the z-axis by φ, with $\varphi = 0$ corresponding to perfect conical alignment (see figure 3.11). The GTRs are also rotated around the k_z-axis by φ, giving the conditions

$$q_x = k_0 \sin\varphi\, p\lambda/d \tag{3.2.25}$$

$$q_y = k_0 \cos\varphi\, p\lambda/d \quad . \tag{3.2.26}$$

The intersection with the Ewald sphere equation (3.2.6) now yields

$$\begin{aligned} k_0^2 &= (k_0 \sin\varphi\, p\lambda/d + k_0\cos\alpha_i)^2 + (k_0\cos\varphi\, p\lambda/d)^2 + (q_z - k_0\sin\alpha_i)^2 \\ &= k_0^2\left((\sin^2\varphi + \cos^2\varphi)(p\lambda/d)^2 + 2\sin\varphi\cos\alpha_i\, p\lambda/d + \cos^2\alpha_i\right) + (q_z - k_0\sin\alpha_i)^2 \end{aligned} \tag{3.2.27}$$

solving for q_z and discarding the reflections below the sample horizon yields

$$q_z = k_0\left(\sin\alpha_i + \sqrt{\sin^2\alpha_i - (p\lambda/d)^2 - 2\sin\varphi\cos\alpha_i\, p\lambda/d}\right) \quad . \tag{3.2.28}$$

To express the scattering in angle coordinates, we use equations (3.2.4), (3.2.25), (3.2.26) and (3.2.28), giving

$$\alpha_f = \arcsin\left(\sqrt{\sin^2\alpha_i - (p\lambda/d)^2 - 2\sin\varphi\cos\alpha_i\, p\lambda/d}\right) \tag{3.2.29}$$

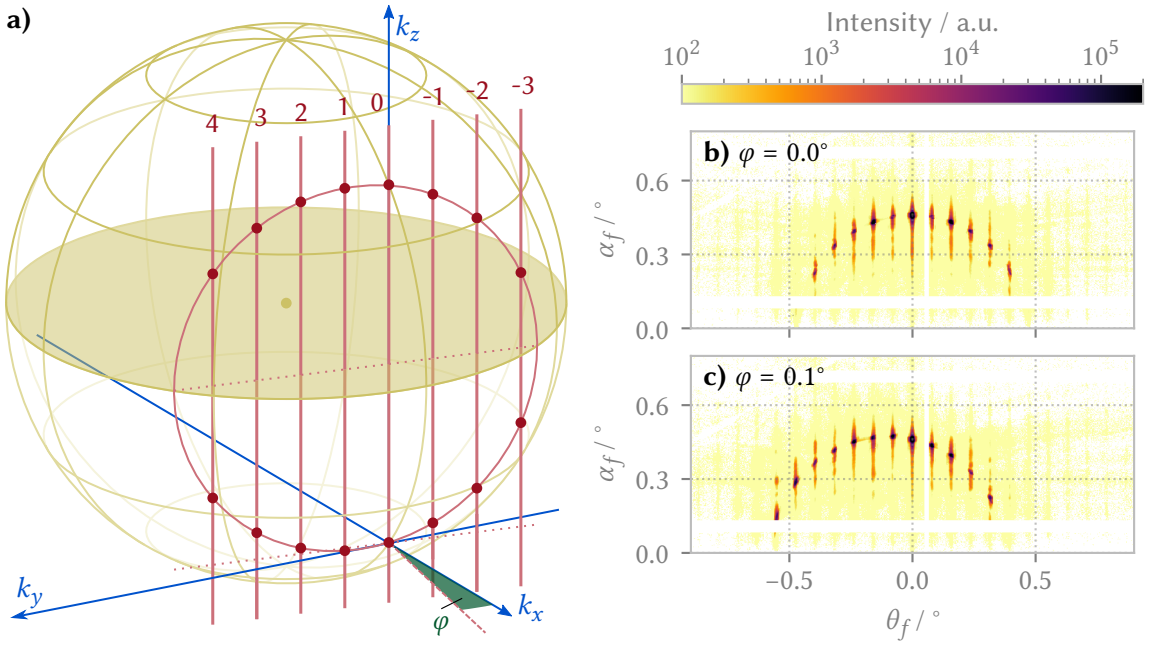

Figure 3.11: Scattering of a misaligned grating. a) Shown is the reciprocal space construction of the scattering of a misaligned grating. Grating truncation rods are shown in red, the Ewald sphere in yellow, red dots and numbers mark the diffraction orders. When the grating is misaligned, i.e. rotated around the z-axis by the angle φ, the GTRs are also rotated by φ around the k_z-axis. **b,c)** Shown are measurements of gratings with $\varphi = 0°$ (**a**) and $\varphi = 0.1°$ (**b**). Even small misalignments lead to asymmetric scattering images.

$$\theta_f = \arctan\left(\frac{\cos\varphi\, p\lambda/d}{\sin\varphi\, p\lambda/d + \cos\alpha_i}\right) \quad . \tag{3.2.30}$$

The reciprocal space construction of grating scattering I presented here delivers results for the position of grating diffraction orders, but does not give results for their scattering intensity. This is because the theory only considers the position of the grating lines, but neglects their form. I will consider the form of the grating lines in the next two sections.

3.2.2 Line shapes - the Distorted Wave Born Approximation

The most widely employed theoretical framework for the description of GISAXS experiments in general and GISAXS of gratings in particular has been the DWBA. In the DWBA, multiple scattering at the surface and, if applicable, layered structures below the grating is considered in addition to single scattering at the grating lines (Vineyard 1982; Sinha et al. 1988; Renaud, Lazzari, and Leroy 2009). I will first review the existing literature on grating line shape analysis using GISAXS with a focus on studies that used the theoretical framework of the BA and the DWBA. Then I will discuss the mathematical basis and results of the DWBA.

In an early quantitative grating GISAXS study, T. Hofmann, Dobisz, and Ocko (2009) reconstructed a simple grating line profile from the measured intensity of the grating diffraction orders using the DWBA combined with least-squares fitting. They also compared results obtained from the DWBA and the BA, and found that the BA suffers from large errors in GISAXS. Accepting these large errors in exchange for a simpler data analysis, Hlaing et al. (2011) use the BA to derive analytical expressions for the relationship between the intensity oscillation along q_z and the side-wall angle

of a grating. Using this, they examine the production of gratings by nanoimprinting and extract the side-wall angle of the grating profile directly from the measured diffraction efficiencies at different q_z without the need for fitting.

The DWBA allows to incorporate roughness into the modelling of the grating. Here, roughness leads not only to reduced intensity of the diffraction orders, but also to diffuse scattering outside of the diffraction orders. Meier et al. (2012) studied very rough polymer gratings, where the diffraction efficiencies are so low that the scattering into the diffraction orders could not be used for the analysis. They could still extract the line profile including the side-wall angle and line width by comparing DWBA calculations incorporating roughness with the measured diffuse scattering. Measuring rough polymer gratings as well, Rueda et al. (2012) use the DWBA formalism with grating lines of different length to model gratings with varying roughness, albeit with little theoretical justification.

Using the BA, Wernecke, Scholze, and Krumrey (2012) and Wernecke, Krumrey, et al. (2014) extracted line and groove width as well as the line height of gratings by means of a Fourier analysis. As long as scattering at the surface and multiple scattering can be neglected, their approach offers a simple method to determine not only the parameter values, but also associated uncertainties. Suh et al. (2016) measured rough polymer gratings and extracted the average line profile as well as the magnitude of deviations from the average line profile using the DWBA and nonlinear optimization to fit the calculated scattering to the measurements. Notably, they also showed that the difference between measurement and calculation did not decline further when using a more complex line profile model, thus demonstrating that a relatively simple line shape already describes the X-ray scattering of their grating. Using very similar theory, more detailed line shapes with a top and bottom corner rounding were extracted from GISAXS measurements by Yamanaka et al. (2016) using the DWBA.

To understand the advantages and limitations of the DWBA for the description of grating GISAXS, I will give an overview of the most important results for the DWBA. The full derivation can be found in the works of Burle et al. (2016) and Daillant and Gibaud (2009, pages 145ff).

In subsection 2.2.2 I discussed the BA, and arrived at equation (2.2.17), which is very similar to Fermi's golden rule. The result was that the time-independent part of the scattered field $E_{r,s}$ can be expressed as:

$$E_{r,s}(\boldsymbol{r}) \approx -E_0 \frac{e^{ik_0 r}}{4\pi r} \langle f|V|i\rangle \quad , \tag{3.2.31}$$

with the amplitude of the incident X-rays E_0, the magnitude of the incident wave vector k_0, the sample potential V, and the initial and final states $|i\rangle$ and $|f\rangle$, respectively. In the BA, the initial and final states are plane waves propagating in vacuum, and V is the deviation of the optical density from the vacuum, which is introduced by the sample. In the DWBA, instead of using vacuum as the reference state, a more appropriate reference state is chosen. The initial and final states are then solutions of the reference state, and V is the deviation of the optical density of the sample from the reference state. Because the solutions of the reference state are not in general plane waves, the initial and final states are called *distorted*, which leads to the name distorted-wave Born approximation (DWBA). For the GISAXS geometry, appropriate reference states are layered systems, which are homogeneous in the x- and the y-direction, i.e. their refractive index is $n(\boldsymbol{r}) = n(z)$, and $n(z)$ is a stepwise function.

For layered systems, the initial and final states can be obtained using the matrix method, which is described in detail by Daillant and Gibaud (2009, pages 99ff). The solutions that are obtained are the sum of a downwards travelling wave and an upwards travelling wave $E_l^{\pm} = A_l^{\pm} e^{i\boldsymbol{k}\boldsymbol{r}}$, with the

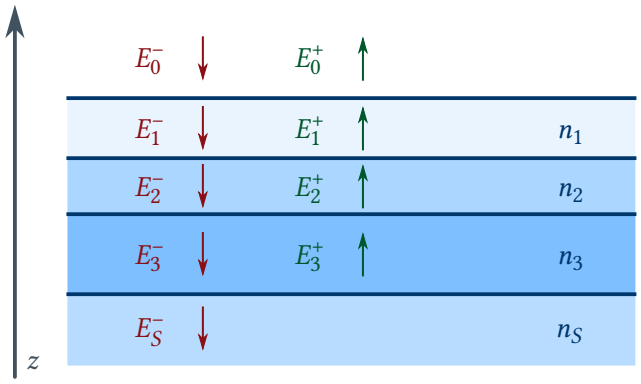

Figure 3.12: The electric field in a layered system. Each layer has the refractive index n_l, and the substrate has the refractive index n_S. The electric field is described as the sum of the downwards travelling wave E^- (red) and the upwards travelling wave E^+ (green). In the substrate, nothing is reflected so that $E_S^+ = 0$.

field amplitudes $A_l^\pm$ (see figure 3.12). Accordingly, the initial and final states can be written as sums as well, $|i\rangle = |i^+ + i^-\rangle$ and $|f\rangle = |f^+ + f^-\rangle$. This leads to

$$\langle f|V|i\rangle = \langle f^+ + f^-|V|i^+ + i^-\rangle \tag{3.2.32}$$
$$= \langle f^+|V|i^+\rangle + \langle f^-|V|i^+\rangle + \langle f^+|V|i^-\rangle + \langle f^-|V|i^-\rangle \quad . \tag{3.2.33}$$

We can again express each of the summands as a fourier transform by using the wave vector representation (for simplicity, I elide the layer index l):

$$\langle f^\pm|V|i^\pm\rangle = \int A_f^\pm e^{-i\boldsymbol{k}_f^\pm\cdot\boldsymbol{r}'} V(\boldsymbol{r}') A_i^\pm e^{i\boldsymbol{k}_i^\pm\cdot\boldsymbol{r}'}\, d\boldsymbol{r}' \tag{3.2.34}$$
$$= A_f^\pm A_i^\pm \hat{V}(\boldsymbol{k}_f^\pm - \boldsymbol{k}_i^\pm) \tag{3.2.35}$$
$$\Longrightarrow \langle f|V|i\rangle = \mathscr{F} = A_f^+A_i^+\,\hat{V}(k_f^+ - k_i^+) + A_f^+A_i^-\,\hat{V}(k_f^+ - k_i^-)$$
$$+ A_f^-A_i^+\,\hat{V}(k_f^- - k_i^+) + A_f^-A_i^-\,\hat{V}(k_f^- - k_i^-) \tag{3.2.36}$$
$$= \sum_{i^\pm, f^\pm} A_f^\pm A_i^\pm\,\hat{V}(k_f^\pm - k_i^\pm) \quad . \tag{3.2.37}$$

As shown, $\langle f|V|i\rangle$ is also called the DWBA form factor $\mathscr{F}$. Its four components are then called the DWBA components, and can be interpreted as four different scattering channels with and without reflection at the layered system before or after scattering at V.

At this point, the main difference between the DWBA and the BA can be seen clearly. In the BA (see figure 3.13a), only single scattering at the whole sample is considered, and only direct scattering from the incident wave into the exit wave. In contrast, in the DWBA (see figure 3.13b) refraction and multiple scattering at all interfaces in the layered system is considered. Then single scattering at the remaining deviation of the sample from the layered approximation is considered, with scattering between the upwards and downwards travelling components of the electric field. Due to the small incidence angles in GISAXS, multiple scattering at the interfaces of layered systems is often a dominant interaction, so that the DWBA delivers much better results (T. Hofmann, Dobisz, and Ocko 2009).

To describe gratings, which are collections of similar grating lines, it is useful to consider the effect of translating the scattering potential V. A translation $\mathscr{T}_{\boldsymbol{r}_V}$ by $\boldsymbol{r}_V$ leads to a phase shift after Fourier transformation:

$$\widehat{\mathscr{T}_{\boldsymbol{r}_V} V}(\boldsymbol{q}) = e^{i\boldsymbol{q}\boldsymbol{r}_V}\,\hat{V} \quad . \tag{3.2.38}$$

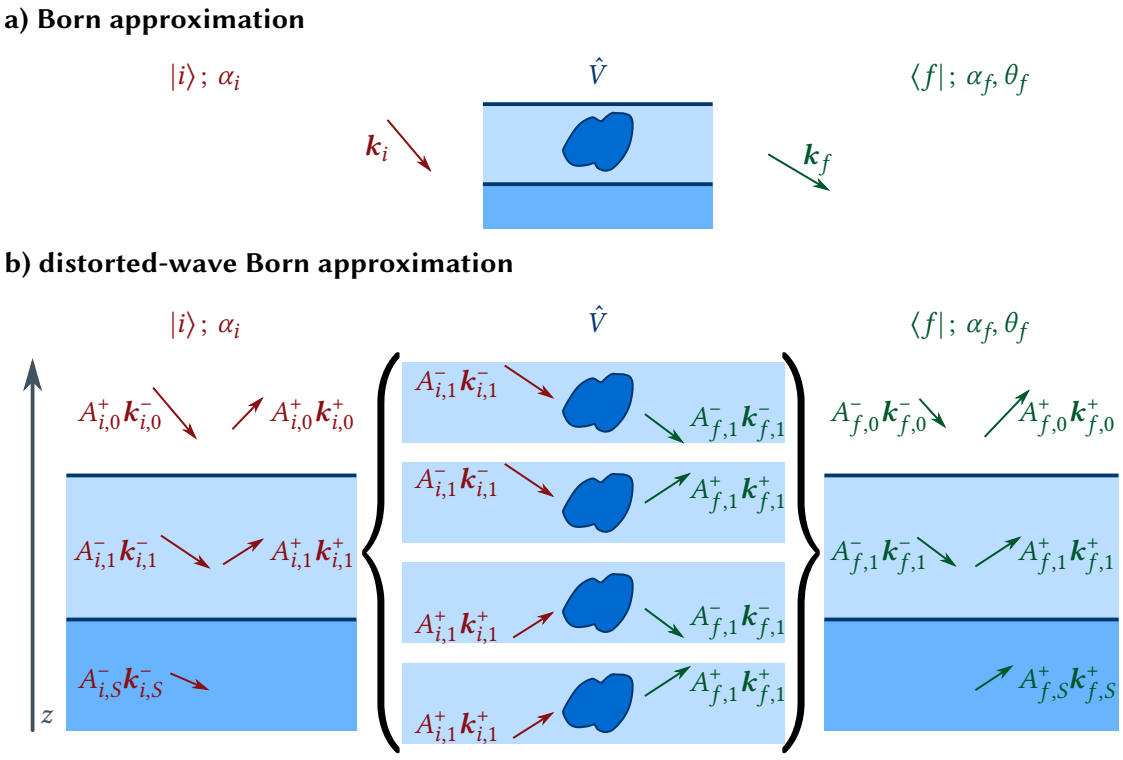

Figure 3.13: Comparison between the Born approximation and the distorted-wave Born approximation. a) In the Born approximation, the initial and final states are plane waves in vacuum. Only single scattering at the whole sample (here, a particle in a layer on a substrate) is considered. **b)** In the distorted-wave Born approximation, the initial and final states are solutions for the layered system. The calculation for the layered system is fully dynamical and considers multiple scattering. Single scattering at the deviation from the layered system (here, a particle in the middle layer) is considered, with the four components arising from scattering between up- and downwards components of the initial and the final state.

For the next step, I note that the DWBA form factor $\mathcal{F}$ is a sum of fourier transformations and that $\boldsymbol{k}^+$ and $\boldsymbol{k}^-$ only differ in the z component for s-polarized light. Then I can reduce translations in the sample plane $\mathcal{T}_{\boldsymbol{r}_{V,\parallel}}$ to phase shifts also for the DWBA form factor

$$\mathcal{T}_{\boldsymbol{r}_{V,\parallel}}\mathcal{F} = \sum_{i^\pm,f^\pm} A^\pm_f A^\pm_i \widehat{\mathcal{T}_{\boldsymbol{r}_{V,\parallel}} V}(k^\pm_f - k^\pm_i) = \sum_{i^\pm,f^\pm} A^\pm_f A^\pm_i\, e^{i\boldsymbol{q}_\parallel \boldsymbol{r}_{V,\parallel}}\, \hat{V}(k^\pm_f - k^\pm_i) \tag{3.2.39}$$

$$= e^{i\boldsymbol{q}_\parallel \boldsymbol{r}_{V,\parallel}}\,\mathcal{F} \quad , \tag{3.2.40}$$

where $\boldsymbol{q}_\parallel$ is the in-plane component of the scattering vector $\boldsymbol{q}$.

Now, I consider a grating consisting of lines, where the jth line has the DWBA from factor $\mathcal{F}_j$ and is shifted from the origin by $\boldsymbol{r}_j$. The lines all lie at the same z position, so that the resulting expression for the angular scattering cross section is

$$\frac{d\sigma}{d\Omega} \propto \left| \sum_j e^{i\boldsymbol{q}\boldsymbol{r}_j}\,\mathcal{F}_j \right|^2 \quad . \tag{3.2.41}$$

A further simplification can be gained using the *decoupling approximation* (Burle et al. 2016, section 3.3). I assume that all grating lines have the same DWBA form factor $\mathcal{F}_j = \mathcal{F}$, which

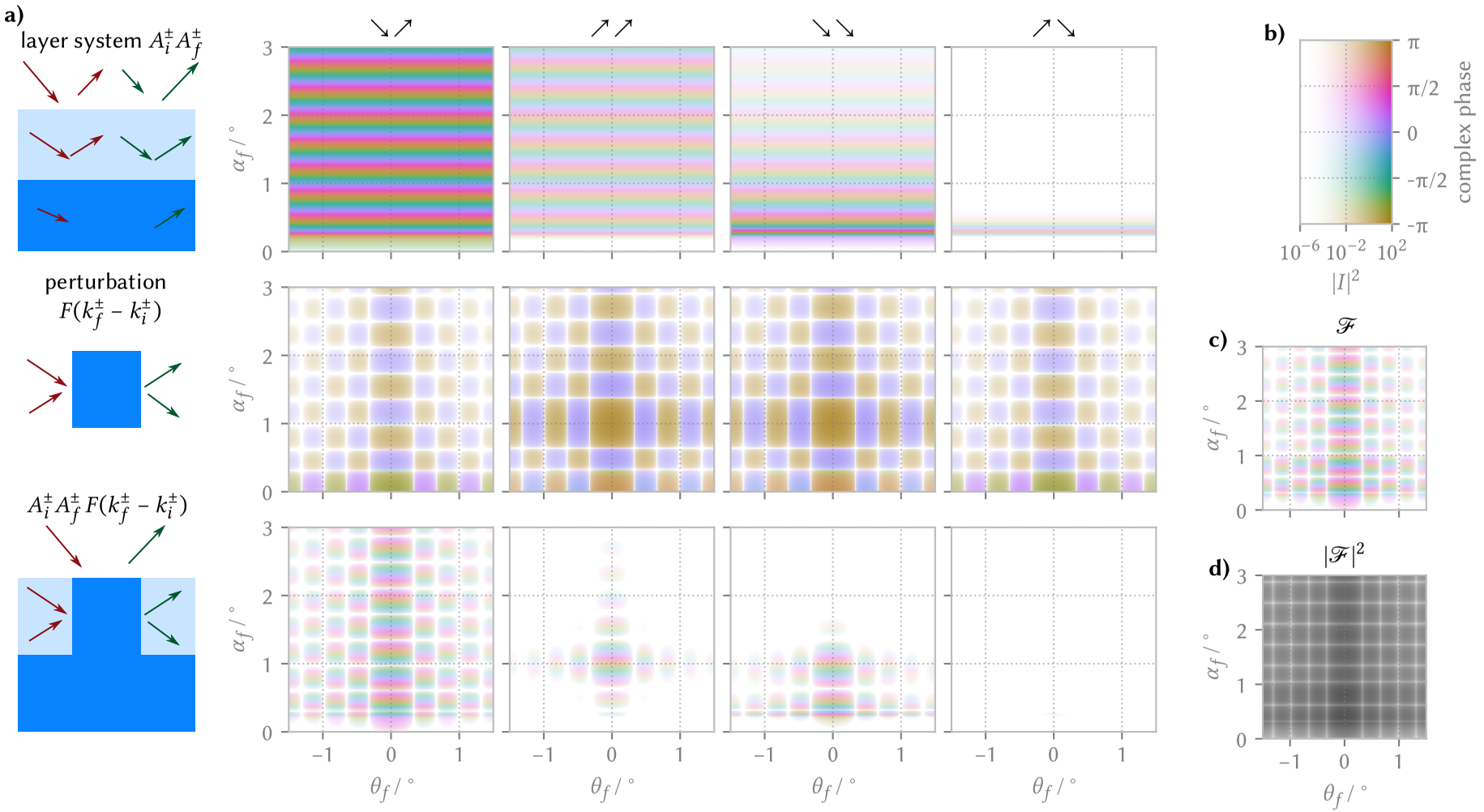

Figure 3.14: Individual components of the DWBA form factor. a) The plots show the individual components. The rows show the field amplitudes $A_i^{\pm} A_f^{\pm}$, the form factor $F(k_f^{\pm} - k_i^{\pm})$, and their product (from top to bottom, see the graphics at the left). The columns show the scattering channels indicated by the arrows on top. All plots use the color code shown in **(b)**, where the hue indicates the complex phase and the saturation shows the absolute value. **c)** Shown is the sum of all four products, the DWBA form factor. **d)** During measurement, the phase is lost, and only the intensity can be measured.

allows me to separate the form factor and introduce the interference function $\mathcal{S}$:

$$\frac{d\sigma}{d\Omega} \propto \left| \sum_j e^{i\boldsymbol{q}\boldsymbol{r}_j} \right|^2 |\mathcal{F}|^2 = \mathcal{S}(\boldsymbol{q}) |\mathcal{F}|^2 \quad . \tag{3.2.42}$$

The interference function of a grating, which is a one-dimensional periodic lattice, is

$$\mathcal{S}(\boldsymbol{q}) = \frac{2\pi}{d} \sum_{p \in \mathbb{Z}} \delta\left(q_x - \frac{2\pi p}{d} \right) \quad , \tag{3.2.43}$$

with the grating line distance d and the Dirac delta function δ (Burle et al. 2016, page 37).

With a trivial DWBA form factor $\mathcal{F} = 1$, the scattering cross section naturally reduces to the reciprocal space construction result given in equation 3.2.8. But in the framework of the DWBA, we can now introduce better form factors $\mathcal{F}$. Because the scattering cross section is the product of interference function and form factor, the position of grating diffraction orders will not be affected by the introduction of non-trivial form factors, but the intensity of the grating diffraction orders is modified. To calculate the DWBA form factor $\mathcal{F}$, the Fourier transform, often called the form factor F, of the grating line shape needs to be calculated. This can of course be done by solving the integrals involved in the Fourier transform, but this is laborious for lots of shapes, and the results are not necessarily numerically stable close to specific points like $\boldsymbol{q} = 0$. A general algorithm for the numerically stable and efficient computation of two- and three-dimensional form factors of polygons and polyhedrons is presented by Wuttke (2017).

To understand the results of DWBA calculations, it is useful to consider the four DWBA scattering channels separately. Each scattering channel is the product of the corresponding field amplitudes $A_f^{\pm} A_i^{\pm}$ and the form factors $F(k_f^{\pm} - k_i^{\pm})$. There are several publicly available implementations for the simulation of GISAXS experiments using the DWBA. In particular, *BornAgain* (Durniak et al. 2014) is a high-quality open-source software package with a graphical user interface and a large library of available three-dimensional form factors. However, it does not output the scattering channels separately, and it is relatively complex to implement custom form factors and interference functions. Therefore, I developed an implementation of the DWBA using the *numpy* package for the *Python* programming language, and optimized it for fast evaluation using the *numba* just-in-time compiler (Virtanen et al. 2020; Millman and Aivazis 2011; Lam, Pitrou, and Seibert 2015). Using this implementation, I will now consider a relatively simple system as an example. A single grating line, consisting of a rectangle with width w_l and height h_l, is located in a layer on top of a substrate. The form factor of a rectangle is

$$F_{\text{rect}}(\boldsymbol{q}) = w_l h_l \, \text{sinc}(q_y w_l/2) \, \text{sinc}(q_z h_l/2) \quad . \tag{3.2.44}$$

The geometry, the individual DWBA components as well as the overall result are presented in figure 3.14.

It can be seen that while the scattering at the rectangle governs the intensity oscillations in the scattering pattern, the field amplitudes that result from the scattering in the layer system determine the relative strength of scattering channels and the intensity profile along α_f. In this example, the incidence angle $\alpha_i = 1°$ is much larger than the angle of total external reflection $\alpha_c \approx 0.3°$, and therefore reflections at the substrate are relatively weak. Therefore, the strongest contribution comes from the first scattering channel that contains all scattering events with an even number (including zero) of reflections in the layer system before and after scattering at the grating line. The next two scattering channels have an odd number (i.e. at least one) of reflections before or after scattering at the grating line, respectively. Even though the scattering at the grating line is strongest in these two channels, the product of scattering at the grating line and reflections

in the layer system is smaller for these scattering channels. Finally, in the last scattering channel with an odd number of reflections before and after scattering at the grating line, the reflections in the layer system are so weak that its contribution is negligible. For other geometries, with resonant scattering in the layer system or with $\alpha_i \approx \alpha_c$, the contributions of other scattering channels besides the first can become dominant. During the measurement, the intensity of the electric field is measured, which means that the phase information is lost (see figure 3.14d), and the individual scattering channels can no longer be discerned easily.

The principal limitation of the DWBA lies in the fact that while the calculation of the layered system is fully dynamical and therefore considers multiple reflections at interfaces, only single scattering is considered at the potential V. Therefore, the DWBA should work best for the simulation of systems where the deviations from the layered system, and therefore V, are small, and multiple scattering at V is unlikely. The DWBA has been used very successfully to describe such systems, like nanoparticles embedded in a layer, or island growth on top of a substrate (Renaud, Lazzari, and Leroy 2009). However, in grating samples, the X-ray contrast is often very high, and the lines are densely packed. Therefore, it is not *a priori* obvious that this approximation is appropriate for GISAXS measurements of grating samples.

3.2.3 Solving Maxwell's equations using finite elements

While the DWBA is well established for the simulation of GISAXS measurements, the scattering of electrodynamic radiation at gratings has also been studied extensively in other applications. Solving Maxwell's equations for grating geometries analytically is in the general case intractable; therefore, many different approximation methods have been developed. A good overview can be found in the book by Popov (2014).

Not all approaches are applicable for the simulation of typical grating GISAXS experiments. In particular, typical grating measurements are made in the non-coplanar diffraction geometry, which is less common in other application areas, and the method needs to be able to describe arbitrary line shapes. One approach which is usable in this scenario is the finite element method (FEM) to directly solve Maxwell's equations numerically. I will give a short overview of the method itself and its application to grating scattering, with a focus on the specific techniques that are used in the commercial *JCMsuite* software package which I used in my thesis (Pomplun et al. 2007).

To describe electromagnetic radiation, I will limit myself to the description of the electric field $\boldsymbol{E}$. Because I describe elastic scattering, the electric fields are time-harmonic, i.e. they have an $\exp(-i\omega t)$ time dependence and are time-independent otherwise. In this case, Maxwell's equations can be reduced to yield

$$\nabla \times \mu^{-1} \nabla \times \boldsymbol{E} - \varepsilon \omega^2 \boldsymbol{E} = 0 \quad , \tag{3.2.45}$$

with the material- and position-dependant electric permittivity tensor ε and magnetic permeability tensor μ (Pomplun et al. 2007). After multiplication with a test function $\boldsymbol{\Phi}$ and partial integration over the domain Ω with boundary Γ, equation (3.2.45) is reformulated in weak form:

$$\int_\Omega (\nabla \times \boldsymbol{\Phi})^* \cdot (\mu^{-1} \nabla \times \boldsymbol{E}) - \omega^2 \boldsymbol{\Phi}^* \cdot \boldsymbol{E} \, dr^3 = \int_\Gamma \boldsymbol{\Phi}^* \cdot \boldsymbol{F} \, dr^2 \quad \forall \boldsymbol{\Phi} \quad ,$$
$$\text{with } (\mu^{-1} \nabla \times \boldsymbol{E}) \times \boldsymbol{n} = \boldsymbol{F} \quad \text{on } \Gamma, \tag{3.2.46}$$

where $\boldsymbol{n}$ is the normal vector of Γ, and the star denotes the complex conjugate (Pomplun et al. 2007). For the finite element method, equation (3.2.46) is not approximated. Instead, the space of solutions on which $\boldsymbol{E}$ is defined is approximated.

The full space of solutions for $\boldsymbol{E}$ is the Hilbert-space H, with the condition that $\nabla \times \boldsymbol{E} \in H$ (Monk and Zhang 2019). For the FEM, this infinitely-dimensional solution space is approximated by a finite-dimensional polynomial solution space. This is achieved by subdividing the geometrical space into finite elements. On these elements, suitable ansatz functions $\boldsymbol{\phi}_i$ are defined, such that

$$\boldsymbol{E} = \sum_i a_i \boldsymbol{\phi}_i \quad . \tag{3.2.47}$$

The problem then reduces to finding the right weights a_i (Pomplun et al. 2007).

For the quality of the approximation, the choice of finite-dimensional subspace, i.e. the choice of discretization of the geometrical space and the choice of the ansatz functions are critical. In *JCMsuite*, the ansatz functions are generated by first considering a basis for scalar functions defined on a single element, and then constructing vectorial functions with desired properties. For the scalar basis, nodal basis functions are used, where each function assumes the value of unity on one node and zero on all other nodes. The vectorial basis is then constructed by considering that both the ansatz functions and their curl should be Lebesgue integrable and thus $\in H$. This ensures that the subspace preserves the mathematical structure of equation (3.2.45) (Nedelec 1980; Pomplun et al. 2007, section 8).

The geometry of a grating GISAXS experiment presents additional challenges, which all relate to the boundary conditions that have to be imposed, which differ for the three directions of space. In the direction along the grating lines (in perfect non-conical mounting, the x-direction), the grating extends into infinity. Assuming that the grating lines are smooth and uniform in this direction, the geometry can be reduced to a two-dimensional geometry and can be described in the y-z-plane, with $H = L^2$ (Popov 2014, chapter 5). In the perpendicular direction (in perfect non-conical mounting, the y-direction), the grating is made up of grating lines repeating into infinity. Using the decoupling approximation, all grating lines are assumed to be identical, so that periodic boundary conditions can be used in the y-direction. The periodic boundary conditions can then be treated by describing only the unit cell explicitly and imposing a Bloch condition on the solutions (Popov 2014, chapter 5). In the z-direction, there is a substrate below the grating and the vacuum above the grating. Both are uniform and therefore no reflections occur within the substrate or vacuum, so that transparent boundary conditions have to be enforced on the upper and lower boundary. Here, *JCMsuite* uses adaptive perfectly matched layers to describe the substrate and vacuum. The core idea of perfectly matched layers is to find finite elements which have the desired transparency (Pomplun et al. 2007). Perfectly matched layers can be understood as a complex stretch of the coordinate along which the electric field must decay, which changes the effective permittivity and permeability tensors of the matched layer while ensuring that no spurious reflections can occur (Popov 2014, pages 161ff).

Taking into account the boundary conditions, the remaining unit cell is of finite size, with its width equal to the grating period d and the height equal to roughly $1.2\, h_l$ (see figure 3.15). After discretization, the scattering problem then reduces to the solution of a large set of linear equations, with relatively sparse matrices. Therefore, the computational effort scales only slightly worse than linearly with the number of unknowns in the set of linear equations, and the number of unknowns corresponds roughly to the product of the number of finite elements used to discretize the unit cell and the number of degrees of freedom of the polynomials used as basis functions (Pomplun et al. 2007).

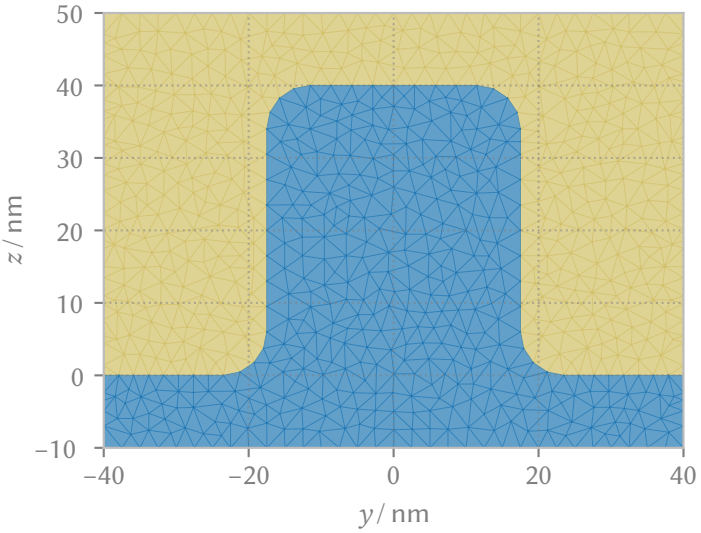

Figure 3.15: A simple grating line discretized using finite elements. The unit cell is divided into finite elements. Here, each finite element is composed of homogeneous material. The edges of the finite elements are shown with thin lines, their composition is indicated by the color.

The result of the calculation is the electric field within the unit cell, and the intensity of the grating diffraction orders is obtained by a Fourier transformation. We have used this approach to simulate the scattering of gratings with complex line profiles, including a top and bottom corner rounding as well as the side-wall angle, the line width, and line height (Soltwisch, Fernández Herrero, Pflüger, Haase, Probst, Laubis, Krumrey, and Scholze, 2017).

A key consideration for the applicability of the FEM for X-ray scattering is the finite element size that is necessary for a good approximation. Typically, the sides of the finite elements have to be smaller than the wavelength λ of the used light. A quick estimation of the number of finite elements necessary to describe even small unit cells at X-ray wavelengths shows why the FEM is not generally applicable for X-rays. Given a unit cell of 100 nm × 100 nm area and the area of a single finite element $A_{\mathrm{FE}} < \lambda \times \lambda = 0.1\,\mathrm{nm} \times 0.1\,\mathrm{nm}$, we have to use more than 1 000 000 finite elements. While it is possible to solve a set of linear equations with millions of unknowns on modern computer systems, this is generally not fast enough for fitting algorithms with many variable parameters where the evaluation of hundreds of thousands of line shapes is necessary. Fortunately, the electric fields arising in GISAXS measurements of line gratings that I need to simulate can be described using much larger finite elements, because they are measurements in non-coplanar geometry at small incident and exit angles. Intuitively, this can be understood from the fact that the initial and final wave vectors have a large component in the x-direction along the lines and only a small component in the y-z-plane in which the unit cell lies, which implies that the associated fields vary slowly in the y-z-plane. This can also be seen in an example simulation that I carried out, the results are shown in figure 3.16. The simulation is done at three different incidence angles. The smaller the incidence angle is, the larger is the wavelength of the standing waves in the y-z-plane, which means the field can be approximated with larger finite elements. Therefore, the performance of FEM simulations of grating GISAXS measurements is acceptable for many applications.

The main advantage of this method is that if the accuracy of the approximation is not good enough for the given sample geometry, a better approximation is conceptually easy to accomplish. A single geometry can be computed with increasing polynomial degree of the *ansatz* functions and/or decreasing size of the finite element side length until the computation is converged, i.e. there is no appreciable change in the results. For this purpose, *JCMsuite* offers adaptive mesh refinement, where the size of finite elements is reduced at the points in space where the gradient of the electric field is highest, enabling fast convergence to a quasi-exact result.

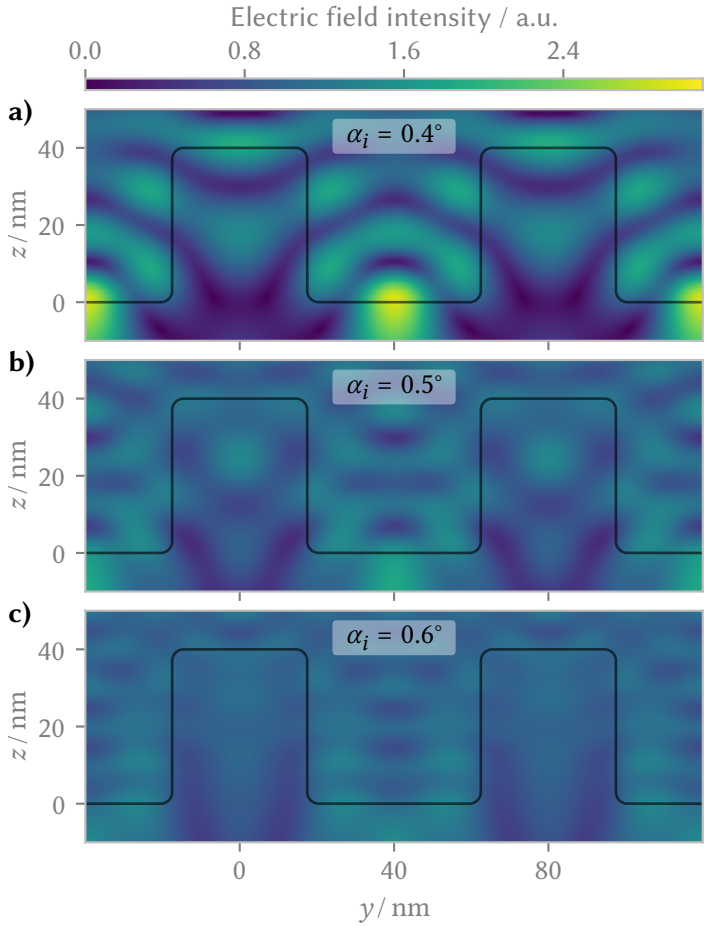

Figure 3.16: Near field in a simple line grating illuminated at different incident angles. Three different incident angles are shown: $\alpha_i = 0.4°$ **(a)**, $\alpha_i = 0.5°$ **(b)**, and $\alpha_i = 0.6°$ **(c)**. The black line shows the outline of the grating, two unit cells are shown. At all incident angles, standing waves form in the trench and, with a smaller amplitude, also within the grating lines. The photon energy is $E_{ph} = 6000\,\text{eV}$, corresponding to a wavelength of about $\lambda \approx 0.2\,\text{nm}$, but the length of the standing waves is much larger. At $\alpha_i = 0.4°$, the wavelength of the standing waves is about 10 nm, at higher incidence angles the wavelength and the amplitude are smaller. The simulations were carried out in perfectly aligned non-coplanar geometry.

3.2.4 Comparing the theoretical approaches

For metrological applications, where a rigorous analysis of the sources of measurement uncertainty is necessary, the errors introduced by approximations in simulations have to be considered. The most thorough comparison of theoretical approaches found in the literature was carried out by T. Hofmann, Dobisz, and Ocko (2009), who fitted measurement data of a single grating with a model based on the DWBA and the BA. They found that only the DWBA model could fit the measurement adequately, and yielded qualitatively the same result as a scanning electron microscopy (SEM) investigation. Consequently, the DWBA is the method that has seen the most use in the simulation of GISAXS experiments in general and GISAXS measurements of gratings in particular (see also section 3.2.2). However, the accuracy of results of the DWBA has not been investigated quantitatively and systematically, so far. Therefore, I have carried out the simulation of three different DWBA models of the same sample and have compared the results with the results from a well-converged finite-element solution of Maxwell's equations.

I used a very simple grating model, consisting of rectangular silicon lines on top of a silicon substrate, see figure 3.17a. The period of the grating is $d = 100\,\text{nm}$, the height of the grating lines is $h_l = 60\,\text{nm}$, the incident angle is $\alpha_i = 0.5°$, the photon energy is $E_{ph} = 6\,\text{keV}$, and the refractive index of silicon at that photon energy was taken from the work of Henke, Gullikson, and Davis (1993). The grating lines are all identical, there is no roughness or corner rounding and the side walls are perfectly perpendicular to the substrate. Because it is one of the most critical parameters of gratings, I left the line width w_l as a variable in the model.

For the solution of Maxwell's equations using finite elements, I used a maximum side length of

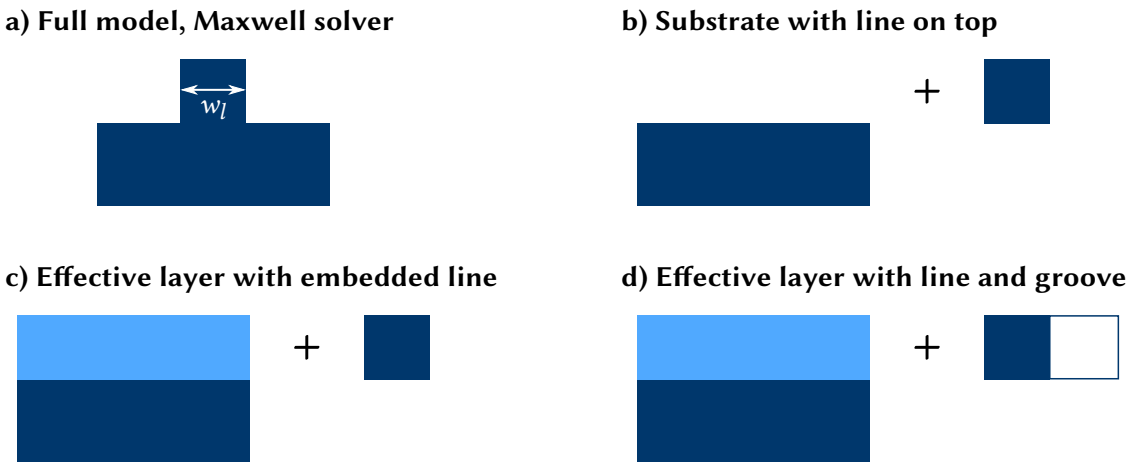

Figure 3.17: Simulation models used for the comparison. a) The full model consists of a rectangular silicon line on a silicon substrate. **b-d)** For the DWBA, the model needs to be split into a layered part and a perturbation. In the simplest model **(b)**, the layer system consists of the silicon substrate and the vacuum, and the perturbation is a silicon rectangle. In the more complex models, a layer with effective density is introduced between substrate and vacuum. The perturbation is then either represented as a silicon rectangle embedded in the layer **(c)** or as a silicon rectangle (the line) and an empty rectangle (the groove) embedded in the layer **(d)**.

1 nm and a polynomial degree of 3. With these settings, well-converged solutions for a single geometry and all diffraction orders were obtained in about 24 s on an *Intel Xeon E3-1246 v3* CPU. I calculated solutions for all w_l in the range between 0 nm and 100 nm with a step size of 1 nm.

To calculate the grating using the DWBA, I used three different approaches to split the model into a layered part that I solved fully dynamically, and a perturbation which will only contribute via single scattering, see figure 3.17b-d. The calculation of the intensity of a single diffraction order of a single geometry then took about 0.6 ms for the model that consists of a perturbing rectangle directly on top the substrate (figure 3.17b), about 0.7 ms for the model that places the perturbing silicon rectangle in a layer with an effective density (figure 3.17c), and about 1 ms for the model which additionally places a perturbing vacuum rectangle in the effective layer (figure 3.17d). To compare the run times to the finite element simulation, all computations were carried out on the same CPU and only a single thread was used. All DWBA models were more than 4 orders of magnitude faster than solving the full model.

Independent of the DWBA model for the form factor, the DWBA interference function yields the exact same exit angles for all diffraction orders within machine precision when compared to the solution obtained using the finite element method. The DWBA interference function for gratings is mathematically equivalent to the position of grating diffraction orders that follow from reciprocal space construction in the BA. Therefore, both the BA and the DWBA reproduce the position of grating diffraction orders correctly.

The results of the calculations of the intensity of the diffraction orders as a function of the line width are compared in figure 3.18. For the second diffraction order shown in figure 3.18a, the calculation of the full model yields a large peak at 25 nm, a shoulder at about 60 nm, a smaller peak at about 85 nm, and a very small peak at about 95 nm. At $w_l = 0$ nm and $w_l = 100$ nm, which both correspond to a bare substrate without a grating, the diffraction vanishes. The absolute scattering intensity is not reproduced properly in the DWBA calculations, which is why I show

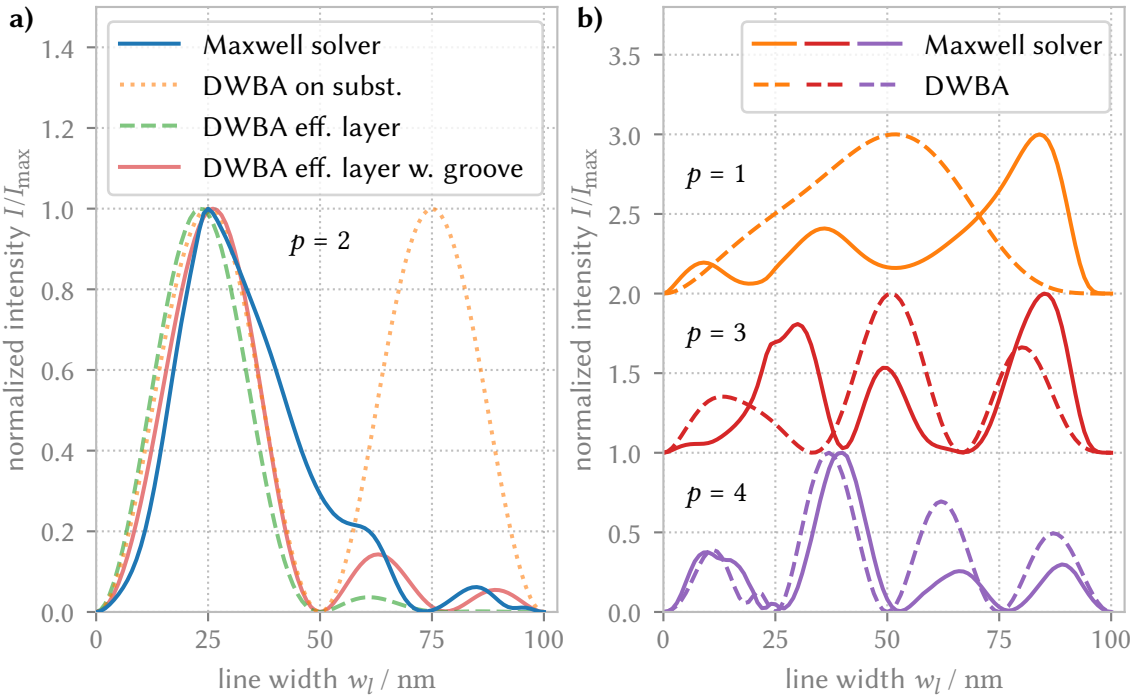

Figure 3.18: Comparison of grating diffraction calculated using different methods.
a) Shown is the normalized intensity of the second diffraction order ($p = 2$) for all simulation models at different line widths w_l. **b)** For all other diffraction orders, I have shown the comparison between the result of the Maxwell solver (solid lines) and the DWBA calculation that includes line and groove (dashed lines). The orders are shifted for visibility.

the normalized intensity

$$I_{\text{norm}}(w_l, p) = \frac{I(w_l, p)}{\max\limits_{w_l} I(w_l, p)} \quad . \tag{3.2.48}$$

This is acceptable for the analysis of most GISAXS measurements, because the absolute scattering intensities are not experimentally accessible anyway. After normalization, all DWBA models reproduce the main peak at 25 nm relatively well. However, the other features are not reproduced faithfully. The simplest DWBA model, which consists of a perturbing rectangle on top of the substrate, has no similarity to the correct result at $w_l > 35\,\text{nm}$. The results of the two models that include a layer with an effective density are better, but still not accurate. Both reproduce the shoulder as a second peak, and the most complex DWBA model even reproduces the third peak and its relative intensity, but the peak positions are not accurate at $w_l > 50\,\text{nm}$. While the most complex DWBA model is the best approximation, all DWBA models fail drastically close to $w_l = 50\,\text{nm} = d/2$. Due to symmetry reasons, the intensity of the second diffraction order always vanishes at $w_l = d/2$ for the DWBA models. Unfortunately, this is not correct.

The other diffraction orders with $p = 1$, 3, and 4 are shown in figure 3.18b. Here, the correct solution is compared to the calculation using the best DWBA model. For $p = 3$ and $p = 4$, the number of peaks is reproduced correctly, but there are large deviations in peak position and relative intensity for some of the peaks. For $p = 1$, the DWBA calculation fails completely, predicting only a single broad peak while the correct solution yields three peaks.

3.2.5 Conclusion

Simulations of GISAXS measurements of gratings based on the BA and DWBA can often be expressed mathematically in a closed form such as the formula for the position of grating diffraction orders that I derived in section 3.2.1. I found that the position of grating diffraction orders predicted by the BA treatment is exact.

Even the more complex expressions that follow from a DWBA description of the intensity of the diffraction orders can be calculated very quickly on modern computers. However, the intensities of the grating diffraction orders are not predicted correctly using the DWBA. Even for the very simple sample model I analysed, the deviations of DWBA calculations from the correct result obtained using the Maxwell solver are not acceptable in metrology applications.

Unfortunately, not every grating sample can be described adequately using the finite element method presented in section 3.2.3. For example, Meier et al. (2012) measured very rough gratings, and in their experiments the grating diffraction orders vanished almost completely. They are able to extract qualitative information using the diffuse scattering, which they describe with the DWBA. Here, the finite element method would not be applicable because as described it can not incorporate roughness in the model itself, and therefore will not yield the diffuse scattering intensities.

In summary, for every simulation of a GISAXS measurement of gratings, the appropriate method has to be chosen. For the description of the position of grating diffraction peaks, the results of the reciprocal space reconstruction using the BA are exact and fast to calculate, but from this only the pitch and orientation of a grating can be reconstructed. Of all methods which have been used for the simulation of GISAXS measurements of gratings in the literature so far, only the computationally expensive Maxwell solver based on the finite element method yields the intensity of diffraction orders correctly. For the analysis of the diffuse scattering, which is necessary for example for very rough samples, the best method currently available remains the DWBA.

4 Lithographic Defects in Light Harvesting Nanostructures

In this chapter, I will present a study about the application of GISAXS for quality control of lithographically produced nanostructures intended for light harvesting purposes. In this application, the statistical nature of GISAXS can be used to full effect, because defects on the nanoscale can be evaluated statistically on square millimeter areas with high precision.

Light harvesting naturally happens on large areas, so that the lithographic methods used for structuring need to scale to square meters of surface area. Therefore, lithographic methods have been developed that can be used to quickly and cheaply structure large areas; however, these methods introduce defects and distortions into the structures. I will use GISAXS to quantify lattice distortions on a 20 mm × 15 mm sample area for samples produced with traditional electron-beam lithography (EBL) and compare it with samples produced with cost-effective nanoimprint lithography (NIL).

Most of what I will present in this chapter has already been published in the peer-reviewed paper "Distortion Analysis of Crystalline and Locally Quasicrystalline 2D Photonic Structures with Grazing-Incidence Small-Angle X-Ray Scattering" (Pflüger, Soltwisch, Xavier, Probst, Scholze, Becker, and Krumrey, 2019).

4.1 Application

To satisfy the primary energy demand by renewable sources, a mix of different technologies is optimal. Due to the high total power radiated by the sun onto the earth, solar energy will be an essential part of this mix (Quaschning 2010, chapter 4). The most important current technology to harvest solar energy is crystalline silicon photovoltaics (PV) (Burger et al. 2019), but due to the indirect band-gap and thus low absorption of silicon, active films in standard silicon PV need to be comparatively thick. This leads to high energy consumption in the production of standard silicon PV cells, which in turn leads to a longer energy payback time of about 3 years for polycrystalline silicon modules in middle europe (Bhandari et al. 2015). To minimize the resource and energy usage of silicon PV, it is desirable to use thin active silicon films.

One approach to maintain high efficiency in thin-film devices is to structure the active film over the whole device surface with a structure size ranging from about 100 nm to 10 µm, enhancing the absorbance using light trapping or wave-optics effects (Becker et al. 2013; Priolo et al. 2014). Crystalline, i.e. periodic nanostructuring of solar cells provides enhanced absorption only at specific wavelengths. Therefore, quasicrystalline structuring is investigated as well, because it leads to broadband high absorption (Xavier, Probst, Back, et al. 2014). The broader absorption is attributed to the fact that quasiperiodic lattices show a dense Fourier spectrum with more Fourier components than periodic lattices (Suck, Schreiber, and Häussler 2002).

However, quasiperiodic lattices are not periodic and therefore manufacturing them using standard lithographic techniques is very difficult. To solve this problem, locally quasicrystalline lattices

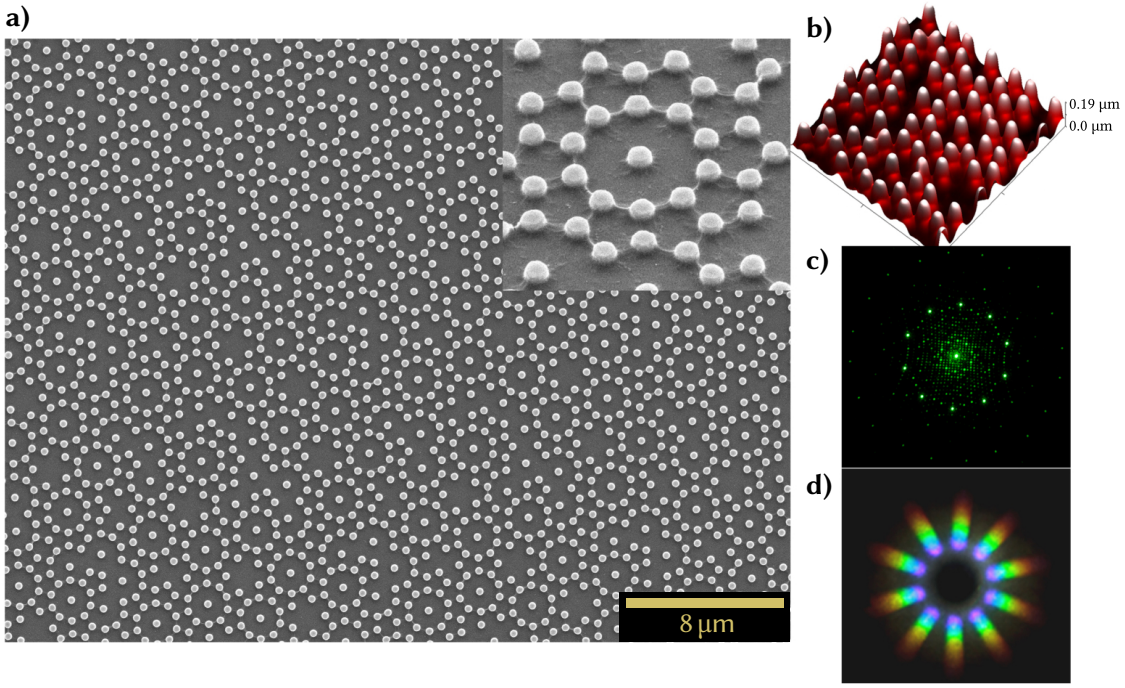

Figure 4.1: Ten-fold symmetric locally quasicrystalline photonic lattice. **a)** Shown is a SEM top-view of nanopillars arranged on a quasicrystalline lattice. The inset shows a tilted closeup. **b)** Shown is an atomic force microscopy (AFM) measurement of the same sample. **c)** When illuminated with green laser light, the sample shows a ten-fold rotationally symmetric diffraction pattern with essentially sharp diffraction orders. **d)** White light is dispersed when passing through the photonic crystal.
Adapted with permission from Xavier, Probst, Back, et al. (2014) (© The Optical Society).

have been proposed, see figure 4.1 (Xavier, Probst, Back, et al. 2014; Xavier, Probst, and Becker 2016). Locally quasicrystalline lattices exhibit an essentially sharp diffraction pattern with a non-crystallographic rotational symmetry like quasicrystals (Shechtman et al. 1984; IUCr 2018), but are nevertheless periodic with a large unit cell. Thus, they combine the optical properties of quasicrystals with periodicity, which solves the manufacturing problem (Xavier, Probst, Back, et al. 2014).

Regardless of the structuring approach, the structured interface is buried under other layers like the active film, the front contact, or coating layers in the finished device (Eisenhauer et al. 2015), which makes it difficult to measure. Here, GISAXS provides an attractive measurement technique due to the possibility to vary the depth sensitivity using different incident angles and incident photon energies (Jiang et al. 2011; Wernecke, Okuda, et al. 2014). As a first step towards the characterization of complex buried interfaces found in modern solar-cell devices, I will report on GISAXS measurements of light harvesting surface structures comprising crystalline and locally quasicrystalline lattices.

4.2 Sample description

The light harvesting nanostructures I investigated are silicon oxide samples consisting of 275 nm high pillars forming a crystalline or locally quasicrystalline (Xavier, Boguslawski, et al. 2010) structure produced by NIL (Verschuuren and Sprang 2007). For reference, I also measured a comparable silicon sample with 370 nm high pillars forming a crystalline structure manufactured

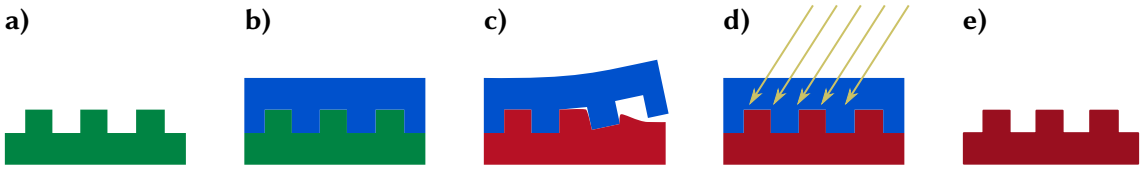

Figure 4.2: The nanoimprint lithography method. **a)** A master (green) is prepared using standard lithography. **b)** A stamp (blue) is produced as a negative of the master. **c)** The stamp is pressed into a flexible target layer (red), transferring the structure. **d)** The target layer is cured (e.g., using ultraviolet light), becoming rigid. **e)** The stamp is peeled off, yielding a replica of the master structure.

Table 4.1: Samples investigated in this study.

Sample	Lithography	Periodicity	Rotational symmetry of diffraction pattern
EBL	E-beam	periodic	4-fold
NIL hexagonal	NIL	periodic	6-fold
NIL 10-fold quasi	NIL	locally quasiperiodic	10-fold
NIL 12-fold quasi	NIL	locally quasiperiodic	12-fold

using EBL (see table 4.1). For all samples, the pillars had a diameter of 200 nm to 300 nm, with nearest neighbor distances of 400 nm to 800 nm.

To be economically and ecologically viable, structuring approaches for PV applications need to be inexpensive and applicable at large scale (Priolo et al. 2014). Therefore, rapid, large-area structuring methods such as (directed) self-assembly or NIL (Chou, Krauss, and Renstrom 1996) are more suited for PV applications than more precise but prohibitively laborious E-beam or optical lithography. For NIL, a stamp is used to transfer the structures onto the sample. In the production of the samples I investigated in this study, a master structure is produced using traditional e-beam lithography, and a stamp is prepared as a negative of this master structure. Then the stamp is used to transfer the structure into a flexible target layer, which is subsequently cured (see figure 4.2). The stamp can be used multiple times, and multiple stamps can be prepared from a single master structure, which reduces the overall effort.

The *EBL* sample as well as the master templates for the production of the *NIL* samples was produced by Jürgen Probst at HZB. The *NIL* samples were designed and produced by Jolly Xavier, also at HZB. Details of all the used ingredients and procedures for NIL and EBL are described by Xavier, Probst, and Becker (2016). The production process was not particularly optimized for the highest reproduction quality, since my study aimed at the quantification of inhomogeneities.

4.3 GISAXS measurements and data analysis

I took GISAXS measurements of all four samples using the setup at the FCM beamline described in section 3.1.2. Since the elongated beam footprint of the approximately 0.5 mm × 0.5 mm large beam is longer than the samples, each GISAXS measurement collects information on an approximately 0.5 mm wide, full-length strip of the 20 mm × 20 mm large sample. In order to gain spatially resolved data, I took GISAXS measurements in a scan along the y-direction. The GISAXS measurements of the *EBL* and *NIL hexagonal* samples were conducted at a photon energy of 6 keV,

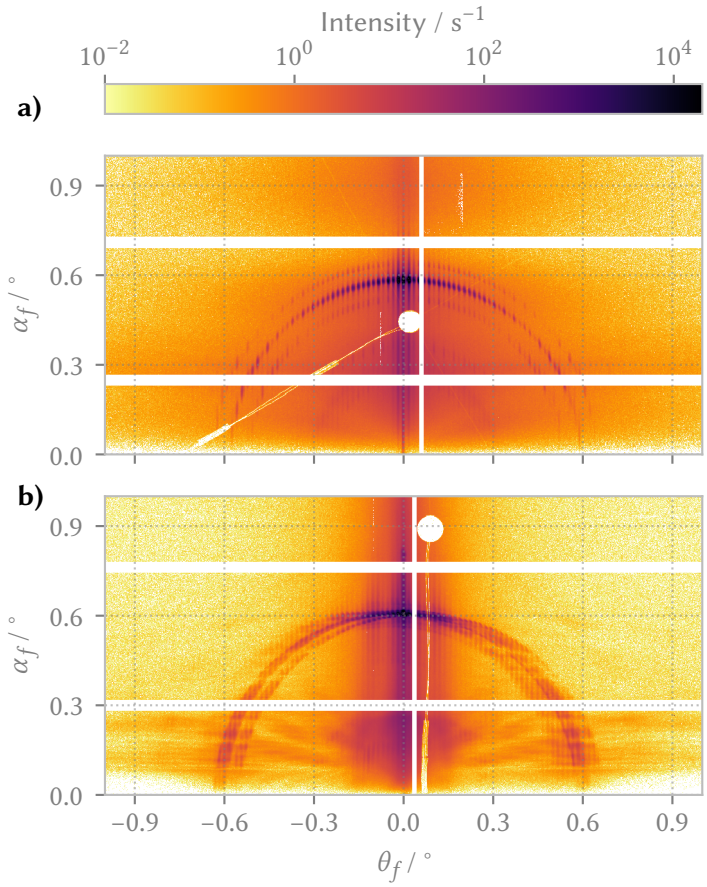

Figure 4.3: Example GISAXS patterns of structures produced using EBL and NIL.
a) Shown is a GISAXS pattern of the *EBL* sample with a clearly visible and relatively sharp semi-circle of diffraction orders.
b) In a pattern of the *NIL hexagonal* sample, the semi-circle is visible, but not clearly defined due to distortions in the crystal lattice. Both measurements were taken at a photon energy of 6 keV and at nominally $\alpha_i = 0.6°$.

the measurements of the *NIL 10-fold quasi* and the *NIL 12-fold quasi* sample were conducted at a photon energy of 3 keV.

Example patterns of the *EBL* sample and one sample produced by NIL are shown in figure 4.3. As can be seen, both samples show a semi-circle characteristic of structures which are periodic in the x-direction. This periodicity in the x-direction is given for all samples. For the periodic samples, this is obviously true when the projection of the X-ray beam onto the surface plane is parallel to a symmetry axis, and for the locally quasiperiodic samples this is given by the periodic tiling of the locally quasiperiodic unit cells. Therefore, the scattering of the samples can be modeled using the theory of grating scattering. To describe the position of the diffraction orders, the reciprocal space theory on the level of the BA that I described in section 3.2.1 is therefore adequate.

However, the diffraction orders of the sample produced by NIL are stretched along α_f. I attribute this to inhomogeneities introduced by the production process. To model this disturbed order, I assume that the nanostructures are locally well ordered, but due to the manufacturing, several domains exist which have a slightly different direction and therefore, different azimuthal orientation φ_{target} (see figure 4.4a). I assume the domains to be large compared to the coherence length of the incident X-rays, so that the measured signal is the incoherent superposition of the signals of the domains illuminated by the X-ray beam. The resulting scattering pattern can be seen in a DWBA simulation I did for the *NIL 12-fold quasi* sample assuming that three domains with differing φ_{target} are illuminated (see figure 4.4b).

Using equations (3.2.26) and (3.2.28) from section 3.2.1, the scattering image can then be cut into slices with differing φ_{target} (see figure 4.4c). To arrive at the φ_{target} distribution in the illuminated area, I integrate the intensity in each slice. For the slicing of the scattering image, a trade-off between signal intensity and resolution needs to be made. For high signal intensities, the slices

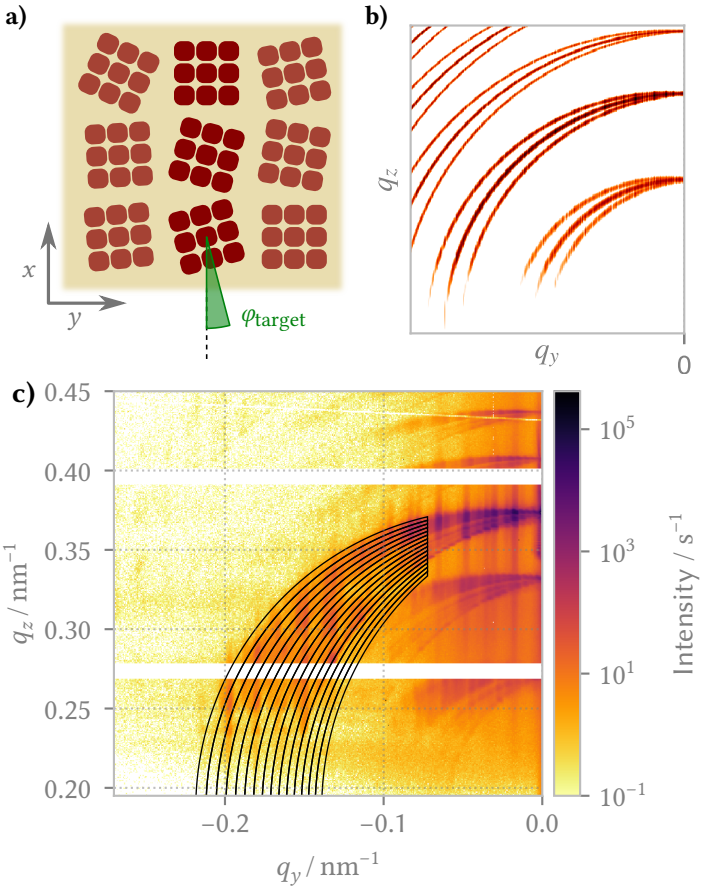

Figure 4.4: Model of the distorted periodicity and data evaluation.
a) Shown is a top view of my sample model. I model the sample using domains of perfectly ordered lattices of supercells, each having a slightly different azimuthal orientation φ_{target}.
b) As can be seen from the DWBA simulation, each domain leads to scattering into tilted semicircles, and the signals combine incoherently.
c) This example shows a measurement of the φ_{target} distribution of the *NIL 12-fold quasi* sample. For the measurement of φ_{target} variations, the GISAXS image is cut into slices corresponding to a φ_{target} range, and the intensity in each slice is integrated. In the analysis, the slices are twice as dense as shown here.

need to be continued towards $q_y = 0$, because scattering at smaller $\boldsymbol{q}$ is generally more intense due to roughness. On the other hand, the height of the slices decreases towards $q_y = 0$. Given a constant resolution in q_z due to divergence or pixel size, extending the slices towards smaller q_y will decrease the φ_{target} resolution. With the resolution in the exit angle α_f of the setup of 0.005° and my slicing range of $q_y < -0.072$/nm, I have a φ_{target} resolution of about 0.015° with an acceptable signal-to-noise ratio.

4.4 Results

The results of the φ_{target} evaluation for all measured samples are given in figure 4.5 and show the statistical inhomogeneities of each sample in an area of about 15 mm × 20 mm. The *EBL* reference sample shows a very narrow φ_{target} distribution close to the resolution limit of 0.015°, with no changes over y. Apart from demonstrating the high quality of the EBL production process, the absence of any measurable drift also shows the angular stability of the measurement setup for sample movements. In contrast, the nanoimprinted samples all display larger inhomogeneities. Two (*NIL hexagonal* and *NIL 10-fold quasi*) show only slightly wider φ_{target} distributions, which however drift along y. The *NIL 12-fold quasi* sample shows the largest inhomogeneities, both as wider φ_{target} distributions at each y position and as a high shift along y. This shows a loss of homogeneity for all samples produced by NIL due to the additional processing steps after the production of the master structure by EBL. All three *NIL* samples were simultaneously manufactured on one substrate using one template, but they show differing φ_{target} homogeneity. The differences in φ_{target} homogeneity cannot be explained by the different lattice design, since each *NIL* sample shows large spatial variations in φ_{target} homogeneity in the scan in the y-direction.

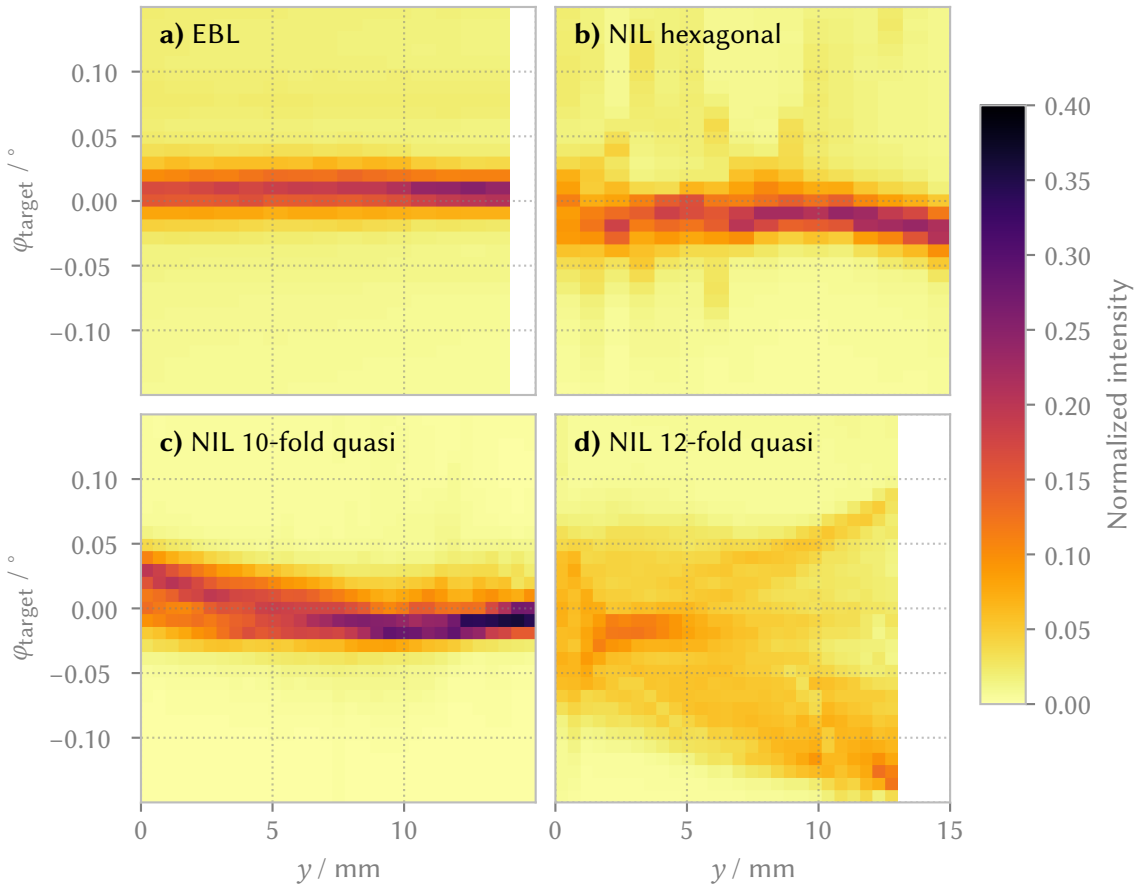

Figure 4.5: Results of the spatially resolved φ_{target} evaluation. The *EBL* sample (**a**) shows a narrow, homogeneous φ_{target} distribution with a width close to the resolution limit. The *NIL* samples all show larger inhomogeneities. While the *NIL hexagonal* and *NIL 10-fold quasi* samples (**b**, **c**) have a rather narrow distribution, they display a drift of the central φ_{target} along y. Finally, the *NIL 12-fold quasi* sample (**d**) shows a comparatively wide and inhomogeneous φ_{target} distribution. An interactive animation presenting diffraction patterns for the selected y position on the *NIL 12-fold quasi* sample is available as Figure S1 in the electronic supplementary material at `https://doi.org/10.18452/21660`.

I conclude that inhomogeneities were introduced in the nanoimprinting process, which can be explained with the flexible NIL template, which leads to small variations in the imprint. The absolute magnitude of the largest φ_{target} variations is still relatively small with $\varphi_{target} \leq \pm 0.15°$. As explained earlier, the nanoimprinting process was not optimized for the highest homogeneity.

4.5 Discussion

To describe samples comprising multiple misaligned domains, I used the theoretical framework of misaligned gratings to describe lattices rotated in the sample plane. With this description, I was able to extract the distribution of the azimuthal lattice orientations of the locally quasicrystalline samples as well as the periodic samples. I extracted the lattice distortions on a 15 mm × 20 mm area spatially resolved in the y-direction, showing the statistical power of GISAXS for the investigation of average properties of comparatively large nano-structured areas. Because GISAXS is very sensitive to misalignments of the local lattice direction, distortions down to 0.015° could be resolved.

As expected, the *EBL* sample shows minimal lattice misalignments over the whole sample, demonstrating the high quality achievable using EBL. Likewise, I find only small lattice misalignments in the nanoimprinted samples considering their intended use in the solar spectrum. However, in comparison to the *EBL* sample, the variations in homogeneity are considerably larger, with lattice misalignments up to ±0.15°. In an optimized nanoimprinting process, the homogeneity of the nanoimprinted samples could likely be increased further, if necessary.

I have shown that GISAXS is a suitable method to investigate complex surface designs intended for use in solar cells, and an extension to buried interfaces is desirable. Using a relatively simple theoretical description, I was able to extract a structural parameter of interest from the GISAXS measurements without the need for parameter fitting. However, to extract additional structure parameters of the investigated samples, a more quantitative theoretical description coupled with an appropriate fitting procedure would be needed. In particular, I neglected the form of the individual pillars, focusing on the positions of the pillars, but the average form of the pillars is also of interest for the intended application. This would be a worthwhile target of future studies.

5 Reconstruction of Complex Line Profiles

In this chapter, I will present a study about the application of GISAXS to answer metrology questions relevant to the production of integrated circuits by the semiconductor industry. I will start with an introduction about the semiconductor industry and the intended metrology applications in general and GISAXS in particular. Then I will present the reconstruction of the line shape of a complex grating sample using GISAXS. To determine the uncertainties of the reconstruction as well, I will introduce and apply Markov chain Monte Carlo (MCMC) methods. Finally, I will investigate a series of six grating samples with intentionally introduced defects, and reconstruct the magnitude of the defects from the GISAXS measurements. The samples in this study were produced using a modern semiconductor process, so that the measurements can serve as a benchmark for the usage of GISAXS in semiconductor metrology.

Most of what I will present in this chapter has already been published in the peer-reviewed paper "Extracting Dimensional Parameters of Gratings Produced with Self-Aligned Multiple Patterning Using Grazing-Incidence Small-Angle x-Ray Scattering" (Pflüger, Kline, Fernández Herrero, Hammerschmidt, Soltwisch, and Krumrey, 2020).

5.1 Application

The development of integrated electronic circuits based on semiconductor technology (Noyce 1961) and the subsequent development of ever cheaper devices with more integrated components (G. E. Moore 1965) has enabled a multitude of applications. From huge business and research mainframe computers to today's smartphones and electronic home appliances, the fields of application are so diverse, that the integrated circuit is considered a *general-purpose technology*, i.e. a technology which enables other technologies and innovations (Khan, Hounshell, and E. R. H. Fuchs 2018).

The technology was developed from 1959 until 1975 at a fast pace, such that the maximum economically viable number of components in an integrated circuit roughly doubled every year, from only one single component in 1959 to about 32 000 components in 1975. This development has been named "Moore's law" because G. E. Moore spotted and predicted it already in 1965. After 1975, Moore's law slowed down somewhat, to a doubling *only* about every 18 months. Nevertheless, this exponential growth has led to highly integrated circuits, which incorporated about 10^9 components already in the year 2000 (Mack 2011).

A main driver for the integration of more components in a single circuit was the miniaturization of components (see table 5.1). While in 1979 a typical memory cell occupied 1740 μm^2, it only occupies 0.0312 μm^2 in the most recent "10 nm" process node (Minato et al. 1982; Seo et al. 2014). Today, functional units such as memory cells are most commonly build from finned field-effect transistors (finFETs), which are fins forming the source and drain of the transistor, surrounded on three sides by the gate. A cut through two fins produced in a modern semiconductor process is shown in figure 5.1. It can be seen that the dimensions are well under 100 nm, which means that today's semiconductor technology is a nanotechnology.

Table 5.1: Selected semiconductor device fabrication nodes. Indicated is the year of introduction into high-volume manufacturing and the wavelength used for optical lithography. Before 2001, the process node name was based on the logic gate length; since 2001, the name is not based on a device characteristic anymore. In 2011, finFETs were introduced, and the distance of fins is a more useful measure of feature sizes than the logic gate length. Source: Schor (2020) and Blumenstock et al. (2005).

Year	Process node name	Logic gate length	Fin pitch	Light wavelength
1972	10 µm	10 µm		N/A
1979	2 µm	2 µm		436 nm
1989	800 nm	800 nm		436 nm
1995	350 nm	350 nm		365 nm
1999	250 nm	250 nm		248 nm
2001	130 nm	70 nm		248 nm
2005	65 nm	35 nm		193 nm
2009	32 nm	30 nm		193 nm
2011	22 nm	26 nm	60 nm	193 nm
2014	14 nm	20 nm	42 nm	193 nm
2019	10 nm	18 nm	34 nm	193 nm

In most semiconductor production processes, the structures are etched into a surface using photolithography. The process starts by coating the substrate with a light-sensitive photoresist, which is then exposed to patterned light, selectively degrading (or hardening) the photoresist. Then the pattern inscribed by the light into the photoresist is transferred into the substrate by etching. One limit for the resolution of photolithography is the optical exposure of the photoresist. Just like in microscopy, the Abbe limit (Abbe 1873) states for the distance of two lines d:

$$d \geq \frac{\lambda}{2\mathrm{NA}} \quad , \tag{5.1.1}$$

with the wavelength of the used light λ and the numerical aperture NA. Because NA is usually smaller than 1, the Abbe limit has been the dominant limit for the size of semiconductor structures in high-volume manufacturing since about 1995 (Blumenstock et al. 2005). As can be seen from table 5.1, at first the resolution was enhanced by introducing light sources with smaller wavelength, but no appropriate light source was available for wavelengths smaller than 193 nm. While extreme ultraviolet (EUV) lithography employing light sources with λ = 13.5 nm is in development and has been introduced into high-volume manufacturing recently (S. K. Moore 2019), most of the high-volume production today is still using light with a wavelength of 193 nm.

To manufacture structures with dimensions much smaller despite the Abbe limit for λ = 193 nm, multi-patterning methods have been developed (Hazelton et al. 2009). Multi-patterning works by introducing additional processing steps, most often either additional exposure/etch cycles that have to be carefully aligned (Lim et al. 2006) or a combination of uniform layer deposition and anisotropic etching (Jung et al. 2006). Because there is no need to align multiple photoexposures, the latter methods are called self-aligned multiple patterning. Self-aligned double patterning (SADP) as well as self-aligned quadruple patterning (SAQP) have already been introduced into high volume manufacturing for the "14 nm" node (Natarajan et al. 2014) and for the "10 nm" node (Yeoh et al. 2018), respectively. Due to the additional processing steps, errors early in the process can be propagated in later steps and lead to additional defects. Therefore, the availability of metrology tools that are suited for the measurement of dimensional parameters of semiconductor devices is critical (Orji et al. 2018).

On one hand, the average properties over a large surface area need to be measured. If, for example, the width of the lines produced by photolithography is too high, later etching of the trenches will not reach the required depth, leading to non-functional devices (Chao et al. 2016). On the other hand, also individual deviations from the mean need to be characterized. The number of defects needs to be kept very low to arrive at an acceptable overall yield of fully functional

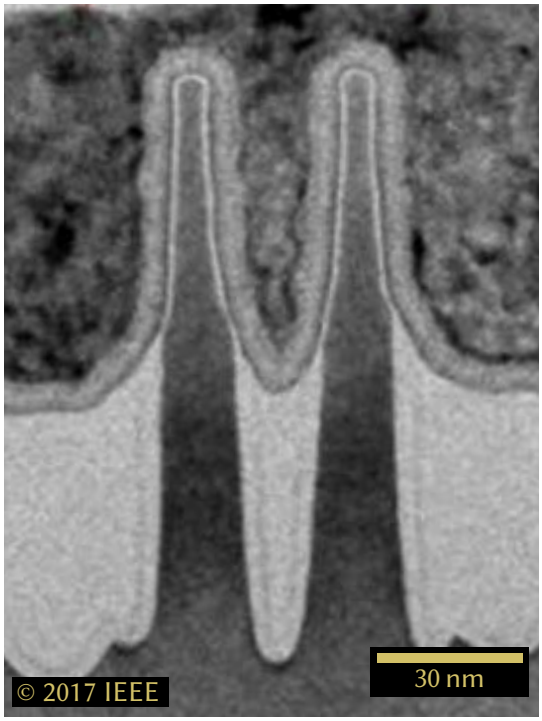

Figure 5.1: Cut through two fins produced in a "10 nm" finFET process. The distance between the fins is only 34 nm, and the width of the upper part of the fins is under 10 nm. The tolerance for deviations from the optimal fin width is very small to avoid contact of neighboring fins as well as breaking of the fins. The image is adapted from Auth et al. (2017).

integrated devices (Kumar et al. 2006). Because no method can address these metrology needs alone, imaging methods which excel in the study of small areas and individual features have to be developed as well as statistical methods with a large field of view (Bunday et al. 2018). For imaging applications, SEM, transmission electron microscopy (TEM), and AFM are widely employed in the industry and there is active research to further develop them for future metrology needs. Additionally, other probes for microscopy are investigated, including helium ion microscopy and proton microscopy (Bunday et al. 2018). For statistical, non-imaging applications, the industrially established method is scatterometry including optical critical dimension (OCD) metrology. In OCD metrology, visible or ultra-violet light is reflected by the nanostructured surface under study, and the specularly reflected light is measured. Relevant dimensional parameters of the sample are then concluded from the strength and polarization of the reflection at different incidence angles and wavelengths using optical modeling. Current research is focused on extensions such as Mueller-matrix spectroscopic ellipsometry (Novikova et al. 2006; Dixit et al. 2015; Diebold, Antonelli, and Keller 2018) and virtual reference OCD (Vaid et al. 2015; Bunday et al. 2018). However, new methods with high statistical power are also investigated and the most important is SAXS (Jones et al. 2003; Bunday et al. 2018).

For applications in semiconductor metrology, SAXS has distinct advantages, but there are also several challenges which have so far hindered wide-spread usage (see table 5.2). Like OCD, X-ray scattering probes the average structure with nm precision over a relatively large (μm^2) area (Sunday et al. 2015). Also like in optical scatterometry, modeling has to be used to determine relevant structural parameters from a SAXS measurement, but there are two key advantages compared to optical measurements. Firstly, because the employed wavelength is much smaller than the feature sizes, multiple diffraction orders can be measured; the additional information aids the reconstruction, such that complex models with more than 12 parameters can be reconstructed, parameter correlations can be reduced, and unique solutions can be determined more easily (Sunday et al. 2015; Bunday et al. 2018). Secondly, as shown in section 2.1.7, the refractive index of X-rays far from the elements' absorption edges only depends on the elemental composition and the refractive indices are well known (Henke, Gullikson, and Davis 1993). This enables reference-

Table 5.2: Selected advantages and disadvantages of SAXS and GISAXS for applications in semiconductor metrology. The table is adapted from Bunday et al. (2018, page 15), the emphasis is in the original.

Advantages	Disadvantages
• SAXS: High confidence measurement of average profile up to 12+ parameters of 3D structures (very important) • Averages over many features (statistical validity) • Parameter cross-correlations are expected to be rare • Refractive indices are well-known • GISAXS: Measurement speed approaching acceptable level	• **GISAXS: Spot size too large for many applications** • GISAXS: Insensitive at large depths, cannot measure high aspect-ratio samples • **SAXS: Currently too slow for high-volume manufacturing** • SAXS: Must transmit through wafer, so that buried patterned layers may provide interference • The inverse problem is ill posed, meaning that the solution is not necessarily unique

free modeling of the SAXS measurements and consequently the evaluation of uncertainties and traceability of the measurement results to the SI without the need for reference measurements (Sunday et al. 2016). The main limitation of transmission SAXS are the small signal intensities and consequently long measurement times. Ideally, quality control measurements are done during manufacturing between two production steps to spot and hopefully correct problems as soon as possible; In practice, in-process metrology should therefore be done in approximately 1 s (Bunday et al. 2018). Unfortunately, SAXS signal intensities are small because X-rays are attenuated during transmission through the wafer, and the scattering cross section of X-rays with matter is small. Even when using a synchrotron as an X-ray source, data collection at a single scattering angle therefore takes on the order of 10 s for SAXS measurements. For successful reconstructions, many scattering angles are needed and measurements using laboratory X-ray sources take considerably longer than synchrotron measurements (Sunday et al. 2016).

The signal intensities can be enhanced significantly in the GISAXS geometry, and measurements in reflection geometry approach acceptable measurement speed (Bunday et al. 2018). Some additional challenges arise from the GISAXS geometry. Because the small incidence angle leads to an elongation of the X-ray beam on the sample, very large (mm^2) areas are probed at the same time. While this is acceptable or even desirable in applications with large homogeneous sample structures such as memory manufacturing (Hagihara, Taniguchi, Yamanaka, Omote, et al. 2017; Hagihara, Taniguchi, Yamanaka, Hirano, et al. 2019), other applications rely on the measurement of small metrology targets (approximately 40 µm × 40 µm) (Thony 2003). I will discuss this footprint problem and possible solutions in chapter 6.

Compared to transmission SAXS measurements, the data evaluation in GISAXS experiments also presents additional challenges. As discussed in sections 2.2 and 3.2, multiple scattering processes are common in GISAXS, so that the BA, which is common in SAXS modeling and simplifies the simulation of SAXS measurements considerably, is not applicable in GISAXS (Sinha et al. 1988). Instead, more complex modeling methods (see section 3.2) have to be employed, which complicates the analysis considerably.

Despite these challenges, GISAXS has already been shown to be a suitable method for several applications in semiconductor metrology, in particular for determining line grating pitches (Yan

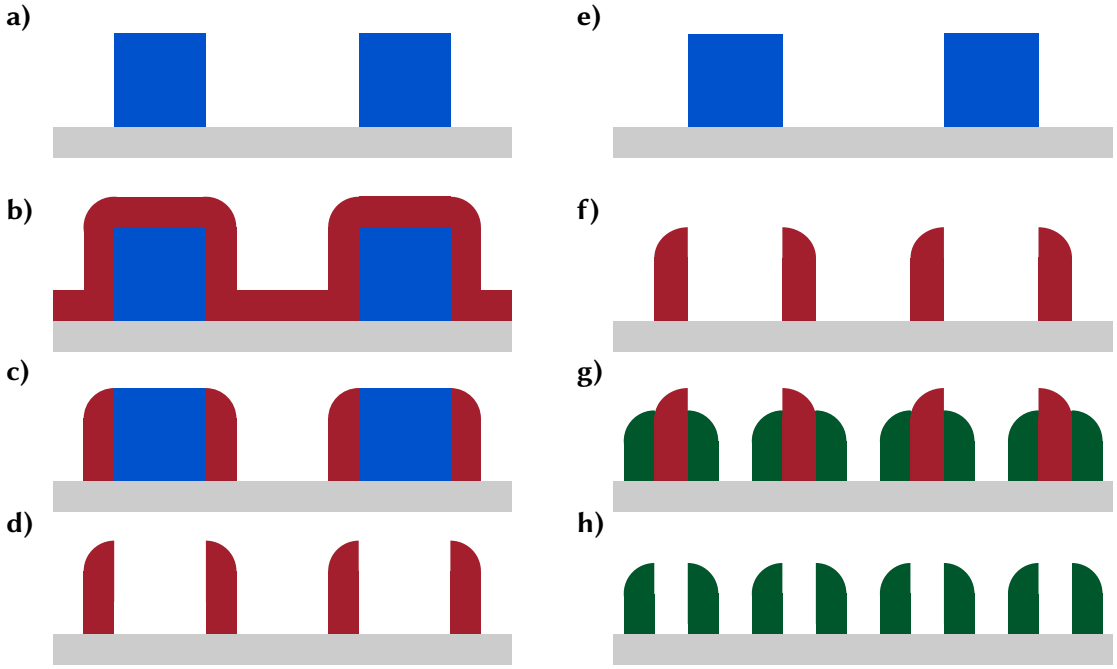

Figure 5.2: Principle of self-aligned multiple patterning.
a-d) Self-aligned double patterning. The processing steps are: a) conventional lithography, b) atomic layer deposition, c) anisotropic etching of the deposited layer, leaving only the deposited side walls, and d) chemically selective etching to remove the original line.
e-h) Self-aligned quadruple patterning. The processing steps are: e) conventional lithography, f) first pitch doubling, and g) the second pitch doubling, leading to h) the final feature.

and Gibaud 2007; Wernecke, Krumrey, et al. 2014) and line profiles (T. Hofmann, Dobisz, and Ocko, 2009; Soltwisch, Fernández Herrero, Pflüger, Haase, Probst, Laubis, Krumrey, and Scholze, 2017; Yamanaka et al., 2016) as well as line-edge roughness (Suh et al., 2016; Fernández Herrero, Pflüger, Probst, Scholze, and Soltwisch, 2019). It has also been used to reconstruct the average profile of contact holes (Hagihara, Taniguchi, Yamanaka, Omote, et al. 2017), and to unravel complex hierarchical nanostructures (Khaira et al. 2017). However, GISAXS reconstructions have been limited to structures with relatively large (> 50 nm) pitches. Additionally, measurements of grating structures produced by modern multi-patterning methods have not been reported to date. These gratings have more complex line profiles and layer stacks, and defects typically introduced by multi-patterning need to be characterized.

I will therefore investigate the capabilities of GISAXS for the measurement of complex structures with many parameters using a series of grating sample with 32 nm pitch produced using a process comparable to the “10 nm” high-volume manufacturing node.

5.2 Sample description

The sample that I investigated consists of a silicon wafer with grating measurement targets, and was obtained from collaborators at the National Institute of Standards and Technology (NIST). Each measurement target covers an area of 1 mm × 9 mm and other structures are surrounding the measurement targets. The sample was structured in a process that consisted of coating and lithographic exposure followed by etching to produce a line grating with a 128 nm pitch

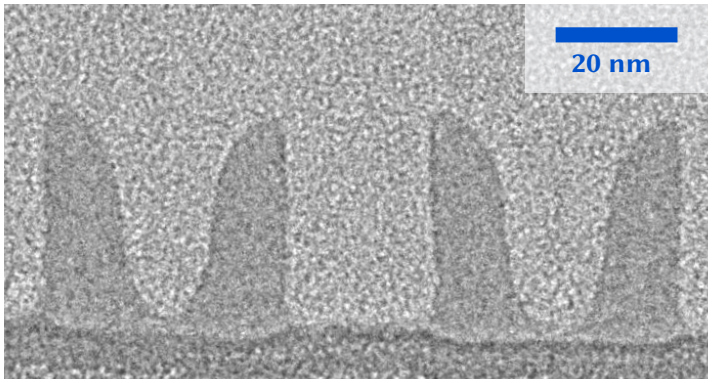

Figure 5.3: SEM cross section of a grating produced by SAQP. Each grating line is asymmetric, but each pair is axially symmetric around the middle. Adapted from (Sunday et al. 2015).

and subsequent pitch quartering for a final grating pitch of 32 nm using self-aligned quadruple patterning (SAQP) (van Veenhuizen et al. 2012; Chawla et al. 2014). In self-aligned multiple patterning, existing lines are coated uniformly using atomic layer deposition (see figure 5.2a,b). Then the material on top of the lines and in the trench is removed by anisotropic etching, leaving the material on the sidewalls (see figure 5.2c). Finally, chemically selective etching removes the original lines, leaving the material on the former sidewalls as a grating with a half pitch compared to the original grating (figure 5.2d). For SAQP, this process is performed twice to reach quarter pitch (figure 5.2e-h). A section through a sample produced using the same SAQP process like the grating targets I investigated is shown in figure 5.3. The asymmetrical line shape resulting from the etching processes is clearly visible.

The grating lines are made of silicon oxide. Due to the multi-step production process, the grating lines rest on top of a layer structure consisting of 30 nm of silicon nitride on top of 25 nm of titanium nitride on top of 100 nm of silicon oxide, on the silicon wafer. Further details of the sample production are published by Sunday et al. (2015) and Villarrubia et al. (2015).

There is one measurement target produced with an optimized process, and five measurement targets were produced with an intentionally introduced defect. I will first report on measurements of the optimized target, and introduce the intentionally defective targets later in section 5.7.

SAXS measurements of all measurement targets (Sunday et al. 2015; Sunday et al. 2016) and electron microscopy measurements of a similar measurement target produced using the same process (Villarrubia et al. 2015) have already been reported in the literature. I will use the results of SAXS measurements by Sunday et al. (2015) as a comparison for my GISAXS measurements.

5.3 GISAXS measurements

I performed the measurements at the FCM beam line, which is described in detail in subsection 3.1.2. For the measurements presented here, I used the smaller beam-defining pinhole, resulting in a beam spot size of about 150 µm × 150 µm full width at half maximum. At the selected incident angle of approximately $\alpha_i = 1°$ for the GISAXS experiments, this results in a size of the projected footprint of about 9 mm full width at half maximum. The GISAXS measurements were taken from targets directly next to the targets measured by Sunday et al. (2015) using SAXS. Because the production conditions were identical for both rows of targets, the measurements are fully comparable.

I took GISAXS measurements for each measurement target over a range of X-ray photon energies E_{ph} and sample rotations φ. $\varphi = 0°$ was aligned by tuning the sample rotation until the recorded scattering was symmetric along the specular axis, yielding $|\varphi| < 0.005°$. The incident angle was

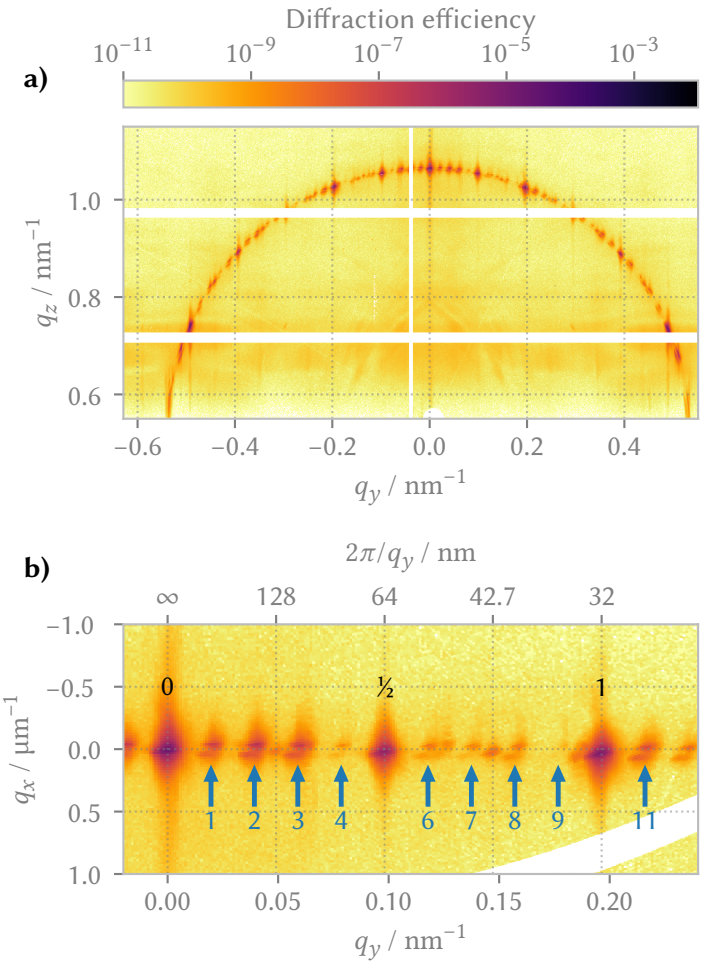

Figure 5.4: GISAXS pattern example.
a) Shown is a scattering pattern taken at $\varphi = 0°$ and $E_{ph} = 6000$ eV. Due to the high quality of the grating, scattering is confined almost exclusively to a semi-circle. **b)** The first few diffraction orders are shown in detail, converted to a q_y-q_x map. The diffraction orders of the target grating are marked with black numbers above the diffraction orders; the $p = 0, ½, 1$ diffraction orders are visible. The parasitic diffraction orders stemming from the surroundings are additionally marked with blue arrows and numbers below the diffraction orders.

set to approximately $\alpha_i = 1°$ and the exact value for α_i was determined from the collected GISAXS patterns and the calibrated sample-to-detector distance. Using the signal of the calibrated monitor diode, the scattering images obtained were normalized to the incident flux and the exposure time. Due to the detector's counting limit of approx. 1 000 000 counts per pixel, I enhanced the dynamic range of the images by combining two images, one long-exposure image with $t > 150$ s and a short-exposure image with $t = 1$ s. For this combination, I used an intensity threshold corresponding to about 1 000 000 counts per pixel in the long exposure time image, and took all pixels above this threshold from the corresponding $t = 1$ s image.

A representative scattering pattern is shown in figure 5.4a. Due to the small grating pitch and despite the relatively large incidence angle of 1°, only diffraction orders with $p \leq 2.5$ are visible above the horizon. To collect more data points for the reconstruction, I therefore took measurements at $\varphi = 0°$ for a range of photon energies from 5750 eV to 6250 eV in steps of 50 eV, using $t = 300$ s as the long exposure time. Additionally, at $E_{ph} = 5900$ eV, $E_{ph} = 6000$ eV, and $E_{ph} = 6100$ eV, measurements were taken for a range of sample rotations from $\varphi = 0.1°$ to $\varphi = 0.5°$ in steps of 0.1° using $t = 180$ s as the long exposure time (see figure 5.5). In total, measurements at 26 different (E_{ph}, φ) sets were taken.

From the scattering patterns, I extracted the intensity of the diffraction orders by integrating over each diffraction order. I estimated the background noise (mainly from diffuse scattering) and subtracted it from the diffraction orders. Because the projection of the incident beam onto the sample was about 9 mm full-width at half maximum, weak tails of the approximately gaussian incident beam also illuminated the area outside of the measurement targets. Therefore, an

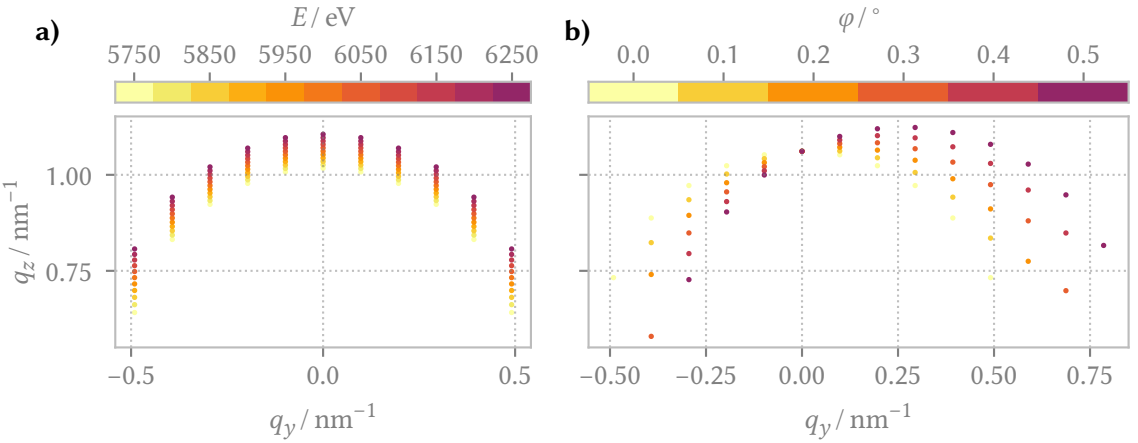

Figure 5.5: Reciprocal space map of GISAXS measurement points. a) By varying the photon energy E_{ph}, the diffraction orders are translated in q_z. **b)** Variations of the azimuthal angle φ change the q_z of the higher diffraction orders much more than that of the lower diffraction orders, yielding complementary information.

additional signal due to scattering of the surroundings of the measurement target is also visible in the scattering patterns. In the surroundings is a structure with a period of about 320 nm, which means the 10th diffraction order of the surrounding structure $p_{sur} = 10$ coincides with the $p = 1$ diffraction order of our target with a period of 32 nm, see figure 5.4b. Fortunately, the scattering of the surrounding structure is strong only for small p_{sur}, meaning that their contribution to the total scattered intensity does not bury the target signal (note the logarithmic color scale). To account for these parasitic signals, the intensities of the diffraction orders of the surrounding structure that do not coincide with a diffraction order of our target are extracted for $p_{sur} \geq 4$. The effect of the parasitic signals on the diffraction orders is then estimated as the mean intensity of the parasitic diffraction orders, which is $1.8 \cdot 10^{-7}$. I then subtracted this from the diffraction intensity of the target where the diffraction orders coincide. Experimental uncertainties of the target diffraction orders are estimated conservatively as the maximum intensity of the parasitic diffraction orders, which is $2.2 \cdot 10^{-6}$.

5.4 Simulation of the Diffraction Intensity

For the quantitative reconstruction of grating line shape from the GISAXS measurements, an accurate theoretical description that yields the diffraction efficiencies η of a given grating line model is needed. As I have shown in section 3.2, from the methods that have been used to simulate grating GISAXS so far, only the Maxwell solver based on the finite element approximation is suitable for this purpose. To use the finite element method, it is necessary to define a geometrical model, and choose the computational precision parameters for finite element sizes and the polynomial degree.

To find out what computational precision is actually needed for the targeted accuracy, we have carried out a convergence study with varying polynomial degrees and finite element side length constraints in a previous study (Soltwisch, Fernández Herrero, Pflüger, Haase, Probst, Laubis, Krumrey, and Scholze, 2017). For a single sample geometry, a well converged solution is obtained by successive computation with higher computational accuracy (higher polynomial degree and/or smaller finite element side length), until there is no appreciable change in the resulting diffraction intensities. We assume that the well-converged solution is a quasi-exact result, and compare

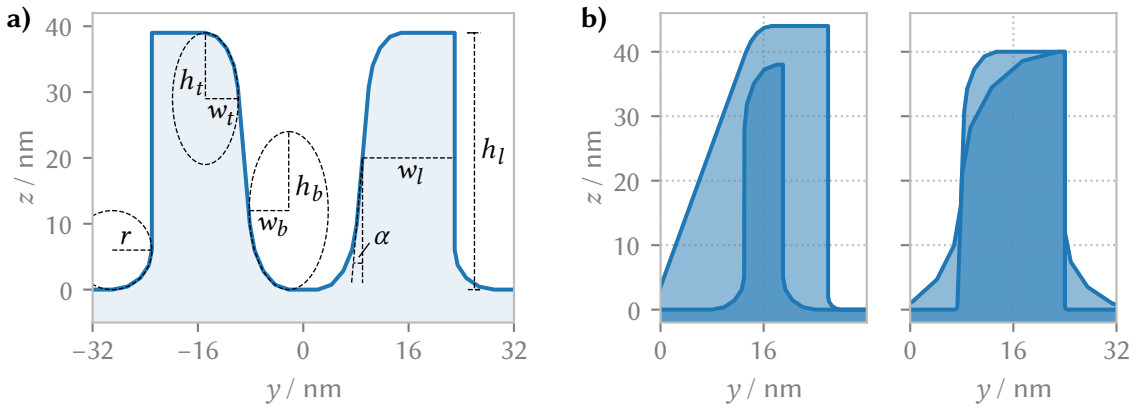

Figure 5.6: Geometrical model used for the simulation. **a)** Shown is an overview of the model. Dashed lines show the geometrical parameters. Here, r, h_t, w_t, h_b, and w_b are parameters for the corner rounding, α is the side wall angle, w_l is the line width, and h_l is the line height. **b)** Shown is the maximum variability of the model. The boundaries of line width, line height, and side wall angle are shown to the left. To the right, the boundaries of the corner rounding are shown.

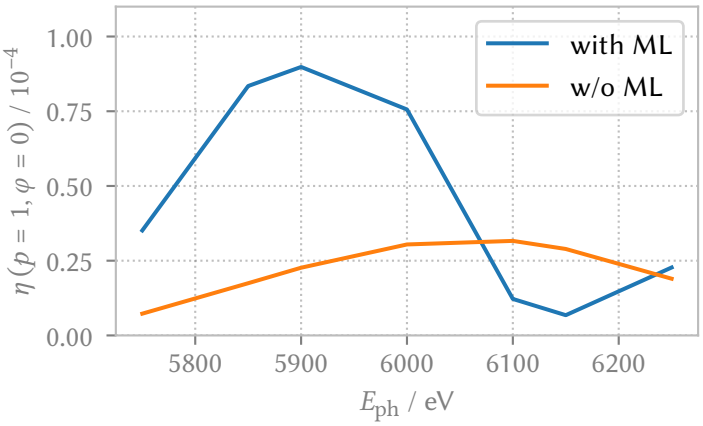

Figure 5.7: Comparison of a simulation with and without the multi layer (ML) structure. Shown is the diffraction efficiency η into the first diffraction order at $\varphi = 0$.

the less precise calculations against the quasi-exact result. This was repeated for many sample geometries that were generated at random. We found that to reach a relative numerical precision of about $1 \cdot 10^{-2}$ at $\alpha_i = 1°$ and $E_{\mathrm{ph}} = 6\,\mathrm{keV}$ (corresponding to $\lambda \approx 0.21\,\mathrm{nm}$), it is necessary to discretize with a maximum finite element side length of about 4 nm with a polynomial degree of 4.

For the geometrical model, I used prior knowledge about the production process and electron microscopic images of sections of samples produced in a similar way (compare figure 5.3) to construct a model with enough variability to cover a wide range of line shapes. From the prior knowledge it is evident that the grating lines can not be described as repeating with the pitch. Instead, I model the grating using a unit cell with a width of twice the pitch $2d = 64\,\mathrm{nm}$, and place an axially symmetric pair of lines in the unit cell (see figure 5.6a). I describe the individual lines using the line width, the line height, elliptic rounding of two of the four corners, circular rounding of one corner, and a side wall angle of one of the sides. An additional parameter describes the distance between the mirrored lines. The parameters are varied within predefined limits; the extent of these boundaries is shown in figure 5.6b. After discretizing the line profile with finite elements, Maxwell's equations are then solved for a monochromatic incident plane wave at a given incident angle as described in subsection 3.2.3.

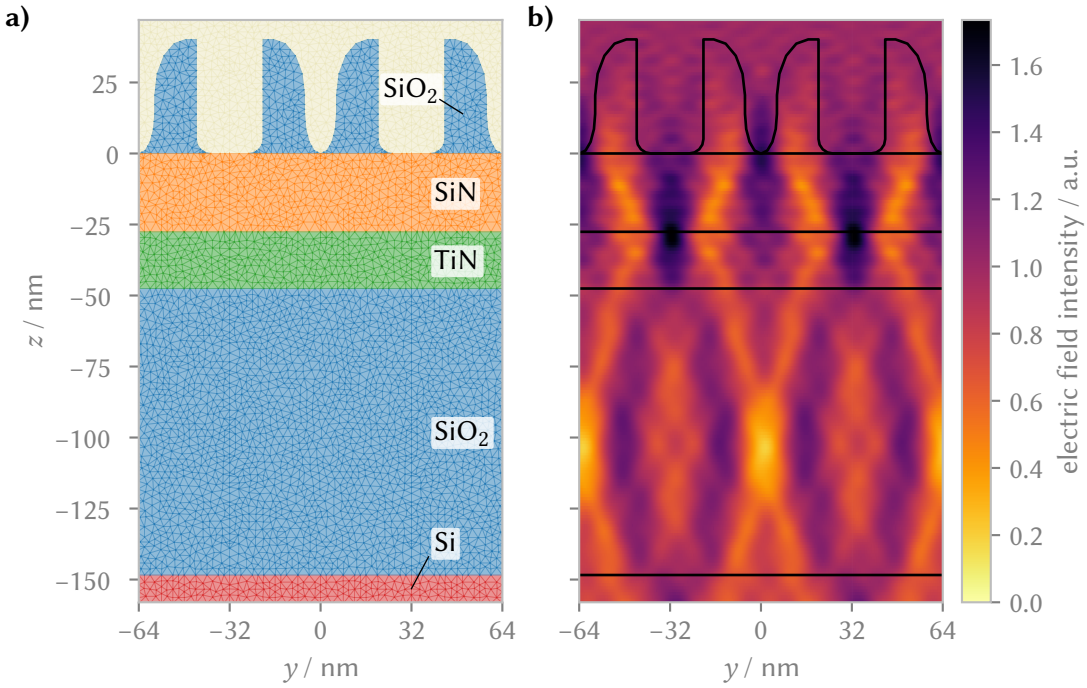

Figure 5.8: Layer stack and simulated electric field. a) Shown is the elemental composition of the layer stack underneath the grating. Thin lines show the discretization for the simulation. **b)** In the resulting electric field, standing waves form within the layer stack. Black lines show the sample geometry. In both parts, two unit cells are shown.

For production reasons, there are several additional layers underneath the grating. Unfortunately, their simulation is time-consuming due to their large height, which contributes considerably to the total size of the computational domain. Given that the layers are homogeneous and not structured in the x-y-plane, it could be expected that their influence on the grating diffraction orders can be neglected. Then the grating can be placed directly on top of the silicon substrate in the computational model. However, comparing the results from otherwise identical calculations with and without the multi layer (see figure 5.7), I found that the results differ greatly. The reason for this is that the incidence angle used $\alpha_i \approx 1°$ is higher than the critical angle of total external reflection $\alpha_c \approx 0.3°$; thus, the X-rays penetrate the layer stack and form standing waves (see figure 5.8). I therefore included the multi layer in my model, with the thicknesses of the individual layers as additional parameters.

The calculation yields diffraction efficiencies η for each diffraction order, assuming a perfect grating. However, the grating lines generally show variations in the width and position of the lines along the lines and this roughness can not be neglected. Roughness can not be introduced into the calculation using finite elements, because we have to assume perfectly periodic boundary conditions in the y-direction and can not calculate a larger or three-dimensional unit cell for performance reasons. Therefore, a Debye-Waller like factor (Mikulík and Baumbach 1999) is introduced to describe the roughness. The derivation of this factor can be found in a previous paper by Fernández Herrero, Pflüger, Probst, Scholze, and Soltwisch (2019). There, we showed the applicability of this approach to line roughnesses with small roughness amplitudes or gaussian roughness distribution. The result is a factor of

$$e^{-q_y^2 \sigma_r^2} \quad , \tag{5.4.1}$$

with the root-mean-square roughness σ_r. Additionally, to account for the X-ray intensity lost because only a part of the incident beam illuminates the target, a loss factor $l < 1$ is introduced, yielding a final intensity I of:

$$I = \eta\, l\, e^{-q_y^2 \sigma_r^2} \quad . \tag{5.4.2}$$

l and σ_r are additional free parameters of the model. With this setup, the simulation of a single measurement geometry took about 3 s on a single CPU core.

5.5 Line shape reconstruction

To recover the line shape from the GISAXS measurements, the model parameters needed to be fitted to the data by minimizing the difference between the measured and simulated intensities. More quantitatively, I minimized the goodness-of-fit parameter χ^2 by varying the parameters $\boldsymbol{m}$ of the theoretical model. Using the principle of maximum likelihood, the goodness-of-fit parameter is

$$\chi^2(\boldsymbol{m}) = \sum_k \frac{-(I_{s,k}(\boldsymbol{m}) - I_{m,k})^2}{2w_k^2} \quad , \tag{5.5.1}$$

with the product over all measured diffraction orders k, the simulated intensity of the kth diffraction order $I_{s,k}$, the measured intensity of the kth diffraction order $I_{m,k}$, and the weight of the kth diffraction order w_k. As the weight of the kth diffraction order, I use the measurement uncertainty u_k. For the simulation of the intensity, I also consider a misalignment of the sample rotation angle φ, which I introduce into the model using an offset φ_0, such that the sample rotation used for the simulation is $\varphi_{s,k} = \varphi_{m,k} + \varphi_0$. Therefore, I obtain as the goodness of fit

$$\chi^2(\boldsymbol{m}) = \sum_k \frac{-(I_{s,k}(\boldsymbol{m}) - I_{m,k})^2}{2u_k^2} \tag{5.5.2}$$

$$\text{with} \quad I_{s,k}(\boldsymbol{m}) = \eta(E_{\mathrm{ph},k}, \varphi_{m,k} + \varphi_0, p_k, \boldsymbol{m}_g)\, l\, e^{-q_{y,k}^2 \sigma_r^2} \tag{5.5.3}$$

$$\boldsymbol{m} = (\boldsymbol{m}_g, l, \sigma_r, \varphi_0) \quad , \tag{5.5.4}$$

where $\boldsymbol{m}$ are the adjustable parameters of the model including the geometrical parameters $\boldsymbol{m}_g$.

Because fitting requires a relatively large number of evaluations of χ^2 for different $\boldsymbol{m}$, it is useful to discuss the relative computational cost of computing different parts of χ^2. To evaluate $\eta(E_{\mathrm{ph}}, \varphi, p, \boldsymbol{m}_g)$, a geometrical model needs to be built according to $\boldsymbol{m}_g$, this model needs to be discretized, and then the Maxwell equations need to be solved for the given E_{ph} and φ. Of these tasks, the last one takes by far the most effort, because the solution is obtained in an iterative fashion and contains many degrees of freedom due to the large number of finite elements. The solution η for all grating diffraction orders p is then obtained in one calculation. When η is obtained, the other steps to calculate χ^2 are comparatively fast. Here, only a few elementary calculations and the evaluation of an exponential are needed. This is several orders of magnitude faster. Therefore, it makes sense to "make the most" out of each evaluation of η.

The first measure towards this goal is to use all grating diffraction orders p at each $(\varphi, E_{\mathrm{ph}})$ setup, since they are all calculated at once. I therefore used all measured diffraction orders ranging from $p = -2$ to $p = 3$ with $2p \in \mathbb{Z}$, with different diffraction orders visible depending on φ. The second method I used to avoid evaluation of η is to fit the two parameters which can be changed without re-evaluating η, namely the loss factor l and the roughness σ_r. For this I modify the goodness of

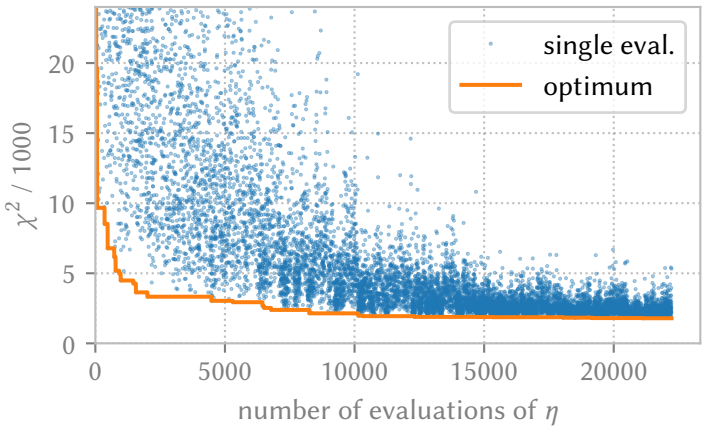

Figure 5.9: Convergence of the line shape fit. At first, the differential evolution algorithm explores a large parameter space as evidenced by the wide χ^2 distribution before about 5000 evaluations. Later, all evaluations are concentrating close to the minimum.

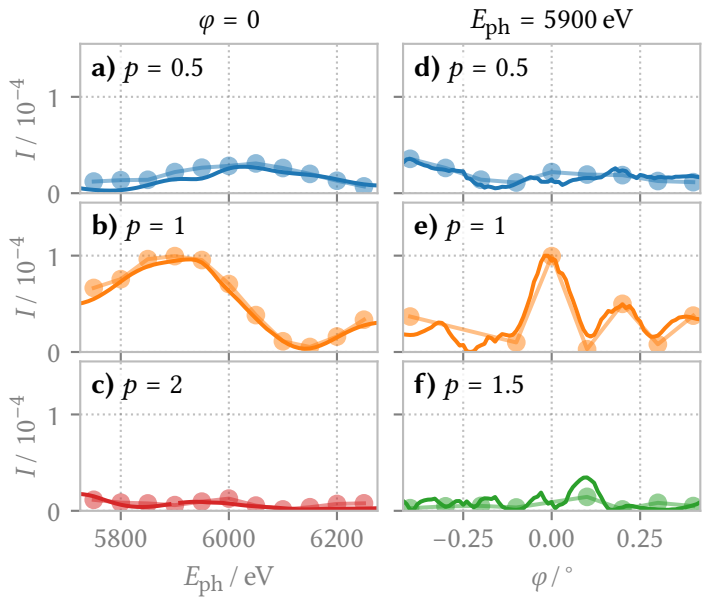

Figure 5.10: Comparison between best simulation and measurement. For clarity, only a representative subset of the data is shown. Measured intensity I_m is shown with connected circles, the simulation I_s with a solid line.
a-c) Scans with a variable E_{ph} use a constant φ. The diffraction orders with (a) p = 0.5, (b) p = 1.0, and (c) p = 2.0 are shown.
d-f) Scans with a variable φ use a constant E_{ph}. The diffraction orders with (d) p = 0.5, (e) p = 1.0, and (f) p = 1.5 are shown.

fit so that it reads

$$\chi^{2\prime}(\boldsymbol{m}_g, \varphi_0) = \min_{l,\sigma_r} \chi^2(\boldsymbol{m}_g, \varphi_0, l, \sigma_r) \quad . \tag{5.5.5}$$

The variation of l and σ_r leads to relatively well-behaved changes in χ^2, so that I can use the standard `optimize.minimize` function from the SciPy software package, which is a general-purpose gradient-based local optimization method (Virtanen et al. 2020).

To minimize $\chi^{2\prime}$, a local optimization method cannot be used due to local minima in the parameter space (Fernández Herrero, Pflüger, Probst, Scholze, and Soltwisch, 2019). Instead, I use the differential evolution fitting algorithm (Storn and Price 1997; Wormington et al. 1999; Hannon et al. 2016), also from the SciPy software package. The fit converged after about 15 000 evaluations of η and was terminated after about 22 000 function evaluations (see figure 5.9). A comparison between the best fit and the measurement data is shown in figure 5.10. The fit reproduces the relative intensity of the diffraction orders as well as the intensity oscillations of the p = 0.5 and p = 1 diffraction orders well. The reconstructed line profile is shown in figure 5.11.

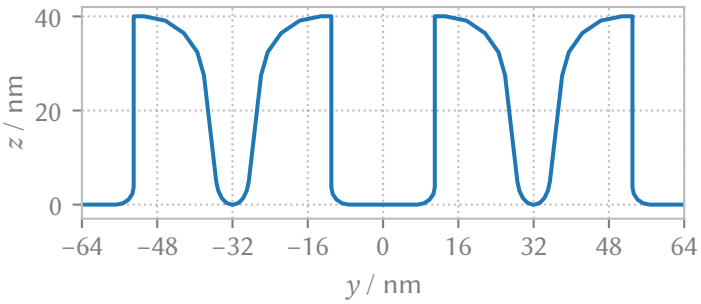

Figure 5.11: Reconstructed line profile. Two unit cells of the line profile corresponding to the best fit are shown.

5.6 Uncertainties of the line shape reconstruction

To evaluate the quality of the reconstruction and to compare the reconstruction to the SAXS results, it is necessary to obtain uncertainties for the reconstructed parameters. Because the reconstruction is obtained by fitting and not using a direct measurement formula, linear uncertainty propagation (JCGM 2008) cannot be used. Instead, I evaluated the uncertainties in the framework of Bayesian statistics using Monte Carlo (MC) sampling.

A generalized concept of parameter uncertainty is a probability distribution $P(g)$ of a general parameter g. In our case, we want to know the probability distribution of the set of model parameters. In particular, we want to know this probability distribution given the measurement M, which I denote as $P(\boldsymbol{m}|M)$. To obtain this, we use Bayes' theorem (Bayes 1763), which states

$$P(\boldsymbol{m}|M) = \frac{P(\boldsymbol{m})\,P(M|\boldsymbol{m})}{P(M)} \quad , \tag{5.6.1}$$

with the probability distribution $P(\boldsymbol{m})$ that we assume before obtaining the data, the probability of obtaining the measurement given the model parameters $P(M|\boldsymbol{m})$, and the probability of obtaining the measurement under any model parameters $P(M)$ (Downey 2013, pages 5-6). If we assume the measurement M as constant, $P(M|\boldsymbol{m})$ reduces to the likelihood function $\mathscr{L}$ with

$$P(M|\boldsymbol{m}) =: \mathscr{L}(\boldsymbol{m}) \tag{5.6.2}$$

$$P(M) = \int_\Omega \mathscr{L}(\boldsymbol{m})\,d\boldsymbol{m} = \text{const.} \quad , \tag{5.6.3}$$

with the parameter space Ω. To evaluate parameter uncertainties, it will be sufficient to obtain the probability distribution $P(\boldsymbol{m}|M)$ up to a constant, so that we can write Bayes' theorem as

$$P(\boldsymbol{m}|M) \propto P(\boldsymbol{m})\,\mathscr{L}(\boldsymbol{m}) \quad . \tag{5.6.4}$$

This equation is so fundamental that its terms have own names. Because $P(\boldsymbol{m})$ captures what we believe about the parameters before the measurement, it is called the *prior* distribution; accordingly, $P(\boldsymbol{m}|M)$ is called the *posterior* distribution; and $\mathscr{L}$ is the *likelihood*.

To arrive at the likelihood function for the reconstruction problem, I assumed that at each measurement point, the obtained measurement scatters around the true value following a normal distribution with width $u_{m,k}$ as estimated in section 5.3. Additionally, I also assumed that because not all aspects of the measurement can be simulated, the simulation scatters around the true value following a normal distribution, with width $u_{s,k}$. I estimated $u_{s,k}$ using a linear error model as $u_{s,k} = u_a\,I_{s,k}$ with the simulation error parameter u_a. Then the likelihood to obtain the single

measurement $I_{m,k}$ for the diffraction order k given the parameters $\boldsymbol{m}$ is

$$\mathscr{L}_k(\boldsymbol{m}, u_a) = \frac{1}{\sqrt{2\pi(u_{m,k}^2 + u_a^2 I_{s,k}^2(\boldsymbol{m}))}} \exp\left(\frac{-(I_{s,k}(\boldsymbol{m}) - I_{m,k})^2}{2(u_{m,k}^2 + u_a^2 I_{s,k}^2(\boldsymbol{m}))}\right) \tag{5.6.5}$$

$$\text{and } \mathscr{L}(\boldsymbol{m}, u_a) = \prod_k \mathscr{L}_k(\boldsymbol{m}, u_a) \quad . \tag{5.6.6}$$

In the following, I will include the simulation error parameter u_a in the model parameters $\boldsymbol{m}$.

For the prior distribution $P(\boldsymbol{m})$, I assumed normal distributions centered around estimated parameter values with large variances. Additionally, I truncated the priors at unreasonable or unphysical values, enforcing for example that the loss parameter $0 < l < 1$ and that the side wall angle stays between 70° and 89.9°. The resulting variability of the geometrical model is the same as in the fit (see figure 5.6b).

Now, equation (5.6.4) can be evaluated for any $\boldsymbol{m}$, but it is still unfeasible to compute $P(\boldsymbol{m}|M)$ in the whole parameter space $\Omega \subset \mathbb{R}^{16}$ at reasonable resolution. Even computing only 100 data points in every dimension, the computation takes about $3 \cdot 10^{24}$ years - a brute force approach was therefore not possible within the time frame of my thesis.

A more efficient method to evaluate $P(\boldsymbol{m}|M)$ is Markov chain Monte Carlo (MCMC) sampling. Using MCMC sampling it is possible to draw a representative set of samples from the posterior distribution, and the effort to do so scales linearly with the dimension of the parameter space if the posterior distribution is sufficiently well-behaved (Metropolis et al. 1953; Hastings 1970). Like differential evolution, MCMC algorithms can be understood using the picture of a collection of particles moving in the parameter space. Given a set of particles distributed in parameter space with a probability proportional to the posterior distribution, an updated candidate position is generated for each particle. If the function that generates candidate positions satisfies a set of conditions known as *detailed balance*, then a new set of particles whose distribution conforms to $P(\boldsymbol{m}|M)$ is obtained if the candidate position for each particle is accepted with a probability

$$p(\boldsymbol{m}_c, \boldsymbol{m}_0) \propto \frac{P(\boldsymbol{m}_c|M)}{P(\boldsymbol{m}_0|M)} \quad , \tag{5.6.7}$$

with the candidate position $\boldsymbol{m}_c$ and the current position $\boldsymbol{m}_0$ (MacKay 2005, pages 365ff). If the candidate is accepted, the particle moves to $\boldsymbol{m}_c$; otherwise, it stays at $\boldsymbol{m}_0$. By performing multiple consecutive steps, independent samples can be drawn from $P(\boldsymbol{m}|M)$ (MacKay 2005, pages 365ff). To obtain a set of particles conforming to $P(\boldsymbol{m}|M)$ in the first hand, a second property following from detailed balance is used. It can be shown that any set of particles which is updated according to detailed balance for N successive steps will eventually converge to conform to $P(\boldsymbol{m}|M)$ if $N \longrightarrow \infty$ (MacKay 2005, page 366).

In practice, convergence is reached in a finite number of steps, and the speed of convergence depends on the exact form of $P(\boldsymbol{m}|M)$ and the function that generates candidate positions. The most well-known method to generate candidate positions is the Metropolis-Hastings method (Hastings 1970). In this method, the candidate is generated by performing a Gaussian random step. For this, a variance has to be given for each parameter dimension to determine the average length of the random step in this dimension. If these variances, also called hyper parameters, are not chosen optimally with respect to the form of $P(\boldsymbol{m}|M)$, convergence is poor. Unfortunately, the hyper parameters can not be chosen optimally without at least partial knowledge of the form of $P(\boldsymbol{m}|M)$. In this situation, the hyper parameters have to be estimated from experience, and often the convergence is sub-optimal. Hyper parameters can be avoided completely by using an affine-invariant function to generate candidate positions. In the affine-invariant method I use, the

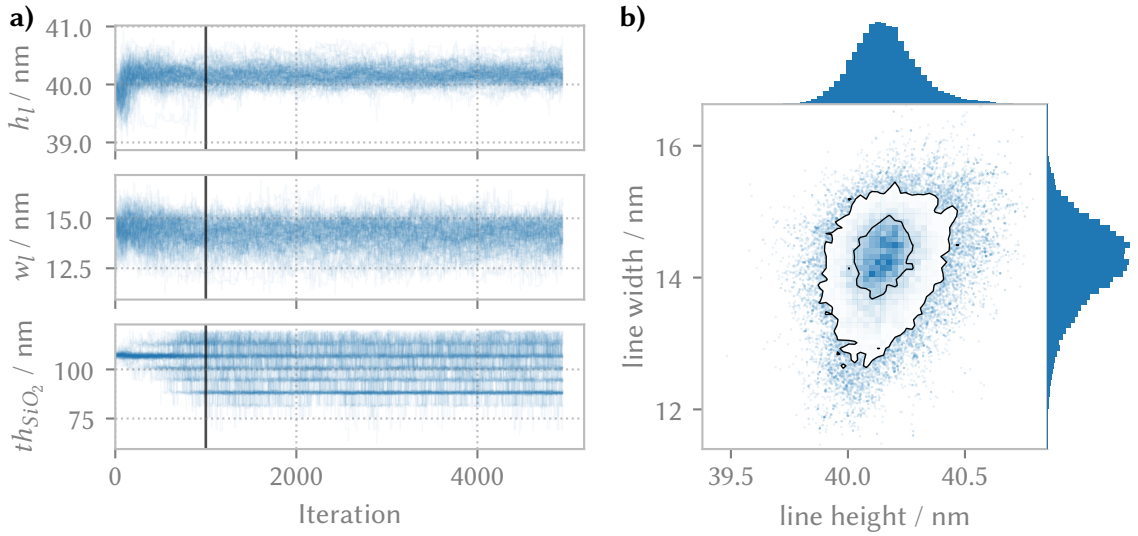

Figure 5.12: Markov-Chain Monte Carlo convergence and results. a) Shown is the convergence of the MCMC run for selected parameters. From top to bottom, traces of the line height h_l, line width w_l, and the thickness of the SiO_2 layer th_{SiO_2} are shown. Each trace shows the movement of one particle. The black line indicates where the run converged. **b)** The histograms at the axes show the results for the line width and the line height individually, and the main plot shows the result for their cross-correlation. The black contours show the parameter regions that contain the 1σ and 2σ confidence interval. The color shows the relative density of samples, corresponding to the posterior probability density. Outside of the 2σ contour, individual samples are shown instead.

candidate for a particle is generated by randomly selecting another particle, and performing a random jump along the straight line connecting both particles. Since the direction and average length of the random step are determined by the other particles, no prior knowledge is needed to select optimal jumping parameters. Instead, good jumping parameters are found automatically when converging, which leads to fast convergence (Goodman and Weare 2010). Therefore, I used the *emcee* python package (Foreman-Mackey et al. 2013) which implements parallel affine-invariant MCMC sampling.

Even though I used these comparatively efficient MCMC sampling methods, a large number of function evaluations was necessary to reach convergence, and then another large number of function evaluations was necessary to sample the posterior adequately. To minimize the number of costly evaluations of η, I again vary the parameters which do not require an evaluation of η independently using the SciPy gradient optimizer `optmize.minimize`:

$$\mathscr{L}'(\boldsymbol{m}_g, \varphi_0, l) = \max_{\sigma_r, u_a} \mathscr{L}(\boldsymbol{m}_g, \varphi_0, l, \sigma_r, u_a) \quad . \tag{5.6.8}$$

Note that I did not optimize l using the gradient optimizer because I wanted to evaluate an uncertainty for l. Additionally, I thinned the measurement points that I included in the evaluation, since I assumed that the measurement was oversampling, so that not much accuracy is lost by excluding some measurement points (Sunday et al. 2016). Specifically, I excluded all measurements at 5800 eV, 5950 eV, 6050 eV, and 6200 eV photon energy. I then used 150 particles and used slightly disturbed positions around the best fit from the differential evolution algorithm as the starting positions.[1]

[1]While I used slightly disturbed positions around the fit result initially, I initialized the starting positions to the result of a previous run when restarting calculations because this led to faster convergence. I restarted calculations several times due to errors or enhancements like the introduction of the error parameter u_a.

Table 5.3: Reconstructed parameter values with standard 1σ uncertainties. The parameters σ_r and u_a were locally optimized with the gradient method, and therefore no uncertainties could be obtained. For these two parameters, the value of the sample with the highest posterior probability obtained in the MCMC run is given.

Parameter	Result	Unit
line height	40.14 ± 0.13	nm
line width	14.3 ± 0.6	nm
side wall angle	81.7 ± 1.9	°
line distance	26.2 ± 0.4	nm
top rounding width	9.8 ± 1.2	nm
top rounding height	14.9 ± 2.6	nm
bottom rounding width	3.9 ± 1.0	nm
bottom rounding height	10 ± 5	nm
bottom outer rounding	4.9 ± 0.6	nm
thickness SiN layer	27.67 ± 0.13	nm
thickness TiN layer	19.90 ± 0.11	nm
thickness SiO_2 layer	100 ± 12	nm
φ_0	0.0054 ± 0.0018	°
loss factor	0.418 ± 0.031	
σ_r	2.139	nm
u_a	0.386	

The movement of the particles during the MCMC run is shown in figure 5.12a. Initially, the ensemble position shifts and the distribution of the particles widens, but after about 1000 iterations, the run is converged and the posterior $P(\boldsymbol{m}|M)$ is sampled. To obtain the final posterior distribution, I therefore discarded the first 1000 iterations and ran the MCMC for more than 3500 further iterations, with 500 000 evaluations of $\mathscr{L}$. The total computational time required is therefore on the order of one year. Utilizing the highly parallel nature of the problem and distributing the computation over several workstations, I was able to finish the MCMC computation in about one week.

Because the positions of the particles are drawn from the posterior, the posterior distribution is obtained from the positions of the particles without regard to the computed value $P(\boldsymbol{m})\mathscr{L}(\boldsymbol{m})$. In the resulting posterior, the line height and the line width show a pronounced maximum, but the thickness of the SiO_2 layer shows multiple local maxima. In figure 5.12b, the posterior distribution is projected onto the line width and the line height. Here, we see that the two parameters are not correlated significantly, and both are approximately normally distributed.

For every parameter m_i, the central value and the uncertainty was then obtained from the projected (i.e. marginalized) distributions $P(m_i|M)$ using the cumulative distribution function

$$CDF(m_i) = \int_{-\infty}^{m_i} P(m_i'|M)\,dm_i' \quad . \tag{5.6.9}$$

The central value $m_{i,0}$ and the standard 1σ uncertainty u_{m_i} were then obtained using

$$CDF(m_{i,0}) = 0.5 \tag{5.6.10}$$

$$CDF(m_{i,m}) = 0.16 \tag{5.6.11}$$

$$CDF(m_{i,p}) = 0.84 \tag{5.6.12}$$

$$u_{m_i} = m_{i,m} - m_{i,p} \quad . \tag{5.6.13}$$

The results are shown in table 5.3. For some parameters like the line height, the uncertainties are relatively small, while for other parameters like the bottom rounding height the uncertainties are relatively large. Notably, the fitted error parameter for the linear error of the simulation

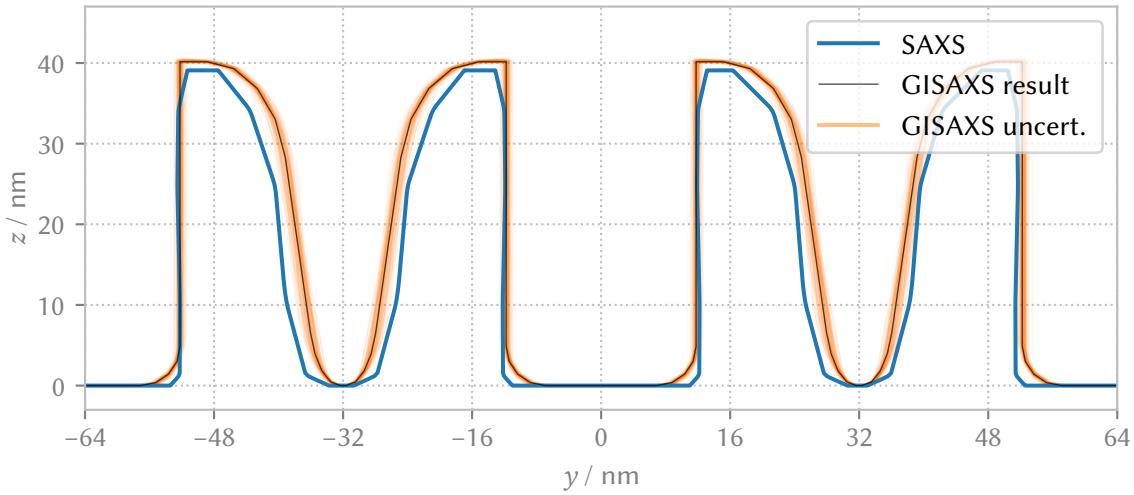

Figure 5.13: Reconstructed profile with uncertainties. The reconstructed profile from SAXS measurements (Sunday et al. 2015) of the same sample is shown for comparison. Two unit cells of the GISAXS model are shown. This equals one unit cell of the SAXS evaluation, which included two different line widths for the two pairs of lines. Uncertainties of the SAXS evaluation are not shown because they are generally much smaller than the GISAXS uncertainties.

Parameter	GISAXS result / nm	SAXS result / nm
Line height	40.1 ± 0.3	39.1 ± 0.3
Line width A	14.4 ± 1.3	12.4 ± 0.2
Line width B	N/A	12.5 ± 0.2

Table 5.4: Comparison of parameters reconstructed from GISAXS and SAXS (Sunday et al. 2015) measurements. Shown are the expanded 2σ uncertainties, because those were reported for the SAXS measurements.

is $u_a \approx 39\,\%$. Compared to the linear error that we obtained in an earlier study of $u_a \leq 15\,\%$ (Fernández Herrero, Pflüger, Probst, Scholze, and Soltwisch, 2019), the fitted error is relatively high. In this study we found that beam divergence had a significant effect on the simulated diffraction intensities. Due to the high computational cost of evaluating beam divergence, I did not include it in my model, which at least partly explains the relatively high linear error parameter.

The reconstructed geometry with uncertainties is shown in figure 5.13. For comparison, the reconstructed profile from SAXS measurements (Sunday et al. 2015) is shown as well. Note that in the SAXS reconstruction, a model with two different line widths for adjacent pairs of lines was used. As can be seen, the GISAXS and SAXS reconstructions agree remarkably well on the general form of the lines, including the corner rounding and the slope of the walls. However, the width and height of the lines do not agree between the reconstructions. To quantitatively compare the GISAXS measurements with the SAXS measurements, the expanded 2σ uncertainties are calculated from the *CDF* at 0.023 and 0.977 and compared to those reported for the SAXS measurements. Due to different parameterization of the GISAXS and SAXS line shape models, only the line height and the line width are directly comparable, the results are shown in table 5.4.

Considering the large uncertainty of the simulation, the uncertainty of the line height as reconstructed from GISAXS is remarkably small. However, the results of SAXS and GISAXS reconstructions do not agree within their uncertainties, with a difference of (1.0 ± 0.4) nm (expanded 2σ uncertainty). For the line width, the uncertainty of the GISAXS reconstruction is much larger than the uncertainty of the SAXS reconstruction, and GISAXS yields a larger line width, with a difference of (2.0 ± 1.3) nm (expanded 2σ uncertainty) compared to the average of the two

line widths measured by SAXS.

Notably, the GISAXS evaluation results in thicker and higher lines, i.e. in more material in the lines. While I could neither determine the reason for this discrepancy nor which of the results is closer to the truth, I would like to discuss two possible reasons for the differences. The first possibility is that the roughness of the interfaces in the multi layer under the grating is significant. In the FEM model, it was not possible to include interface roughness, so I simulated perfectly flat interfaces. However, the model also showed that standing waves formed inside the multi layer, and the multi layer reflected a significant fraction of the incident X-rays back into the grating. By not including roughness into the simulation, the amount of X-rays reflected by the multi layer was likely overstated. It is conceivable that the fit would compensate this by adding more absorbing material in the grating lines, resulting in a larger line height and line width. Note that while the SAXS evaluation did not include the multi layer at all, this likely has almost no effect on the SAXS results because in transmission mode, the multi layer only results in a weak and broad diffuse background and does not change the intensities of the diffraction orders.

Another possibility is that the refractive indices that I used for the SiO_2 grating lines are not correct. While the atomic scattering factors of silicon and oxygen are well-known for photon energies around 6000 keV, the stoichiometry and density of the material of the grating lines is not actually known precisely. Because silicon scatters much stronger than oxygen at the used photon energies, I would not expect the stoichiometry to matter much, but the dispersion and absorption scale linearly with the density of the grating lines. For the density, I used the density of amorphous bulk silica, which is 2.2 g/cm^3, but crystalline silica can reach densities of up to 2.65 g/cm^3. If the material in the grating lines is (partly) crystalline, it is possible that I underestimated its density, which was compensated for in the fit by adding more material.

5.7 Pitchwalk sample series

After reconstructing the grating line profile of the measurement target which was produced with minimal defects, I will now discuss the grating targets with a deliberately introduced defect. A defect which is commonly introduced in SAQP is pitchwalk. When pitchwalk is present due to alignment errors, the distance between two lines in a grating alternates between a higher and a lower value, such that the average pitch stays the same. Unfortunately, even small changes in the distances between lines can lead to large deviations after further processing steps. A relatively small pitchwalk introduced in the first line doubling leads to severe distortions in the line distances after the second line doubling (see figure 5.14). Even worse, if the lines manufactured by multi-patterning are then used as an etch mask for the production of fin structures, small variations in distances can lead to large variations in etch depth (Chao et al. 2016). Due to this defect amplification, it is vital to measure the pitchwalk during processing, so that corrections can be made before additional costly processing steps. Therefore, I have also investigated five additional grating targets with an intentionally introduced pitchwalk.

All measurement targets were produced on the same wafer and in the same process as the sample that I reconstructed in the previous sections and which I described in section 5.2. To introduce a pitchwalk gradient, the wafer was produced with a different lithographic focus and exposure along one axis, resulting in six targets with differing fill ratio and therefore different pitchwalk δp. I label the rows PQ 1 – PQ 6 from left to right, where the δp grows from negative values at PQ 1 to positive values at PQ 6, crossing nominally zero pitchwalk at PQ 4. The grating target PQ 4 with nominally zero pitchwalk is the grating target I measured and reconstructed in the previous sections.

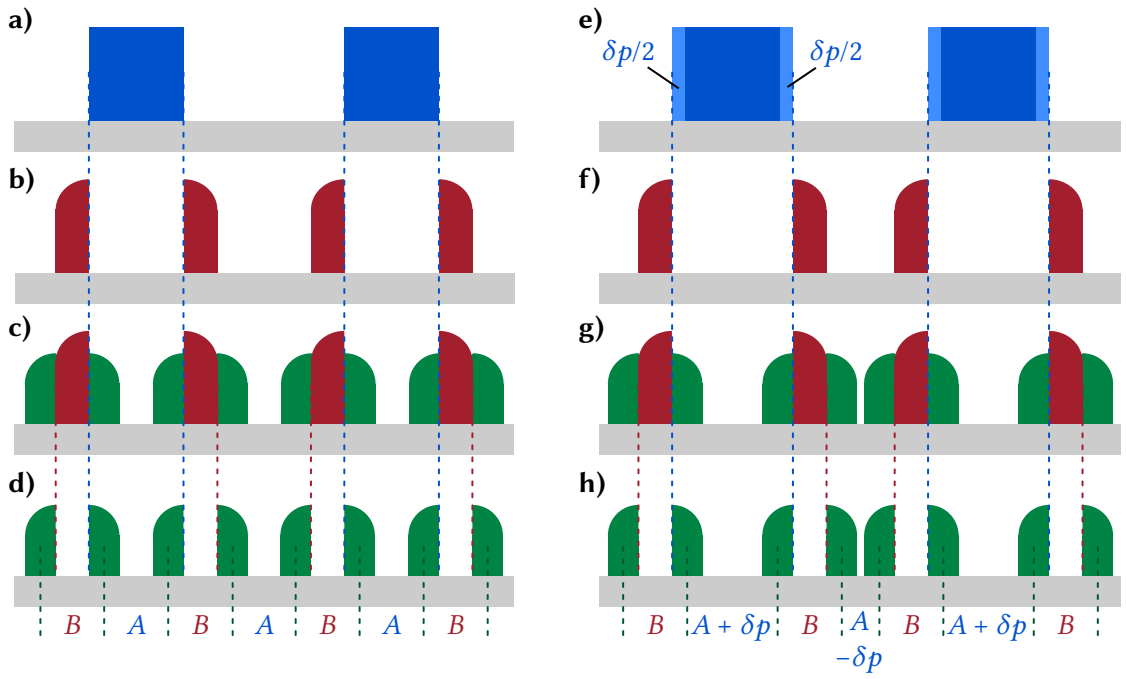

Figure 5.14: Propagation of defects in SAQP. a-d) In a properly aligned SAQP process, the distances between grating lines are uniform. **e-h)** If the original line is δp wider than it should be (e), a pitchwalk is introduced in the first line doubling (f). After the second line doubling (g), the distances between grating lines are severely disturbed (h). In this example a relatively small defect in the original lines leads to a large defect in the final grating, where some grating lines are barely separated at all.

I measured all targets at multiple photon energies E_{ph} and sample rotations φ, as described in section 5.3. A comparison of measurement results of target PQ 4 without pitchwalk and target PQ 6 with a relatively high pitchwalk is shown in figure 5.15. The main difference seen in the diffraction images of samples with a non-zero pitchwalk is the emergence of additional diffraction peaks halfway between the grating diffraction peaks. These additional diffraction orders show that the 64 nm-periodicity is broken, and the targets with non-zero pitchwalk show a periodicity of 128 nm, instead. This is consistent with the expectation that we have from the production process. The defect is introduced already in the original lithography (see figure 5.14e), and then propagated to the final feature (figure 5.14h), so that the final feature shows the same periodicity as the original lithography, which is 128 nm.

I extracted the diffraction intensities of all diffraction orders from all measurements. For the diffraction orders with $p = n/2$ with n integer, I evaluated the experimental uncertainties from the intensities of the parasitic signals stemming from the surrounding as described in section 5.3. The newly arising quartered diffraction orders with $p = n/4$ with n odd do not coincide with any of the diffraction orders of the surroundings, because the surroundings have a periodicity of 320 nm, and 128 nm is not a divisor of 320 nm. Therefore, I estimate the experimental uncertainties of the quartered diffraction orders from the background noise, which is smaller than $5 \cdot 10^{-8}$ for all orders. The resulting diffraction intensities are shown in figure 5.16. The intensity of all quartered diffraction orders is very small for the PQ 4 target with nominally zero pitchwalk, and is much higher for the other measurement targets. In comparison, the intensity of the $p = 1/2$ and $p = 1$ diffraction orders changes much less for the different measurement targets.

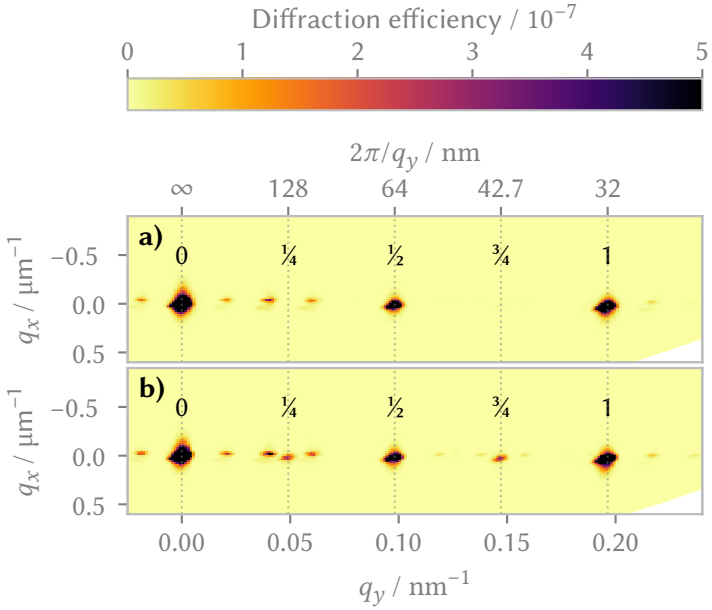

Figure 5.15: GISAXS scattering patterns of targets with and without pitchwalk. The measurement of target PQ 4 with nominally zero pitchwalk (**a**) shows no scattering intensity at the $p = 0.25$ and $p = 0.75$ diffraction orders. In contrast, in the measurement of target PQ 6 (**b**) the $p = 0.25$ and $p = 0.75$ peaks emerge.

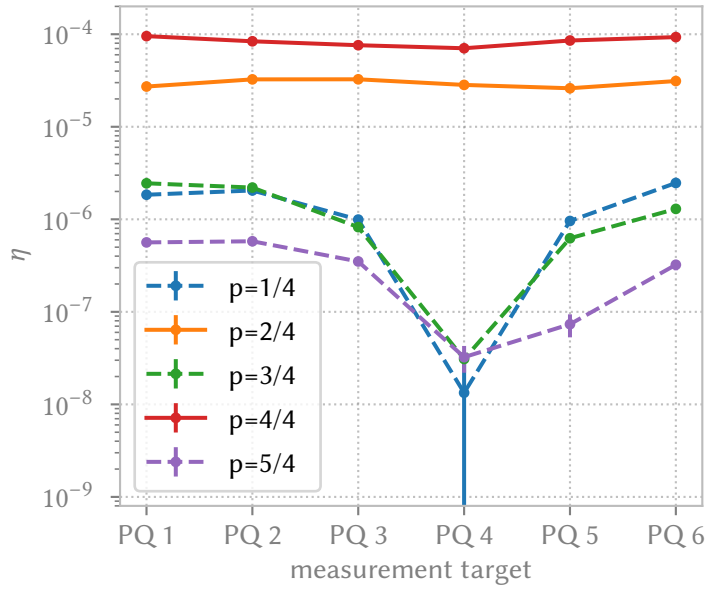

Figure 5.16: Measured diffraction efficiencies of grating targets with different pitchwalk. Quartered diffraction orders are shown with dashed lines, the other diffraction orders are shown with solid lines. Vertical bars indicate the measurement uncertainty. Shown are only the intensities measured at $E_{\mathrm{ph}} = 6000\,\mathrm{eV}$ and $\varphi = 0°$.

5.8 Pitchwalk reconstruction

To introduce the pitchwalk δp into my computational model, it is necessary to simulate a unit cell with a width of quadruple pitch $4p = 128\,\mathrm{nm}$. The pitchwalk was then described by alternating the distance between pairs of lines, see figure 5.17a. Due to the high computational demand of a full line shape reconstruction, it was not feasible to do a full reconstruction for every measurement target. Instead, I assumed that the shape of the lines was not affected by the pitchwalk, and that I am therefore able to reuse the line shape reconstructed for target PQ 4, thus leaving the pitchwalk as the only geometrical parameter. I calculated the diffraction order intensities for $|\delta p| \in [0, 10]\mathrm{nm}$, in steps of 0.1 nm, yielding a library of results, see figure 5.17b. Because much less function evaluations are necessary than in the reconstruction, I chose the FEM approximation parameters for a higher accuracy and used a maximum side length of the finite elements of 2 nm and set the degree of the *ansatz* polynomials to 5. Due to the axially symmetric nature of the problem, negative and positive pitchwalks yielded the same result, so I restricted my calculation

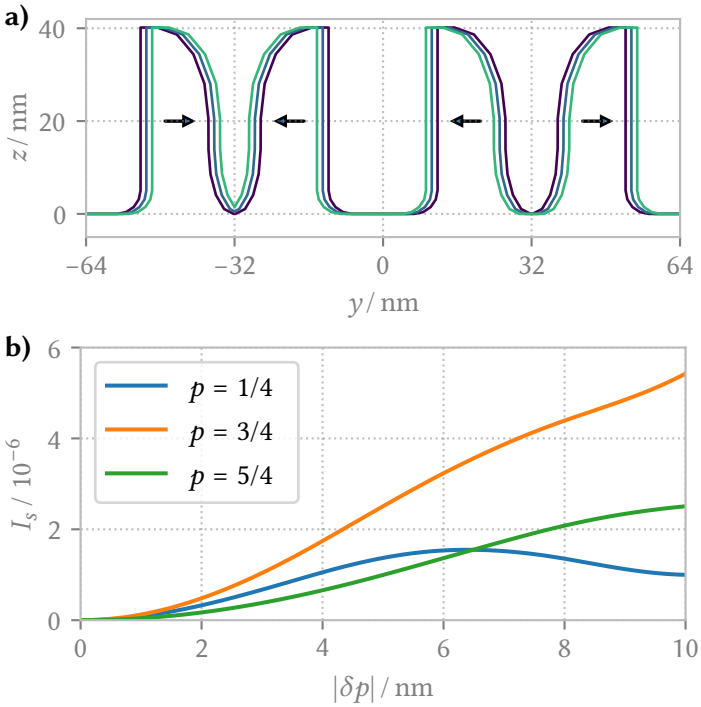

Figure 5.17: Pitchwalk simulation model and results.
a) For the pitchwalk simulation, the unit cell is 128 nm wide and one pair of lines is moved closer while the other pair is moved further apart.
b) The simulated scattering efficiencies of the quartered diffraction orders for E_{ph} = 6000 eV and φ = 0° are shown.

to the magnitude of the pitchwalk $|\delta p|$.

Because mostly the intensities of the quartered diffraction orders are differing between the different grating targets, I compared the intensities of the p = 1/4, p = 3/4, and p = 5/4 diffraction orders between the simulation and the measurement to determine the pitchwalk from the measurements. For each quartered diffraction order measured at a specific E_{ph} and φ, the result from the simulation library which was closest was chosen, yielding a value for $|\delta p|$. In some cases, there is more than one $|\delta p|$ value which minimizes the difference, because the intensity of a diffraction order is not strictly rising with $|\delta p|$ as is the case for p = 1/4 in figure 5.17b. In these cases, I chose the smaller $|\delta p|$. Since each target was measured at many different E_{ph} and φ, this yields a total of $N > 40$ measurements of $|\delta p|$ per target. I then estimated $|\delta p|$ and its type A uncertainty (JCGM 2008) $u(|\delta p|)$ from the arithmetic mean and the experimental standard deviation, respectively.

The results are shown and compared to SAXS measurements in figure 5.18. Qualitatively, the results agree, with maximum deviations between the measurements of about 2 $u(|\delta p|)$. This shows that, using a library approach based on a sample known to be good, pitchwalk excursions can be quantified with GISAXS measurements without the need for a time-consuming full line shape reconstruction, albeit with large uncertainties compared to SAXS . However, there are also further effects that can be seen in the data.

First, the GISAXS results show a clear bias towards higher values of $|\delta p|$. This can be explained by the secondary effects of the pitchwalk introduced that I neglected in my model due to the computational constraints. For the SAXS measurements, a full reconstruction of the line profile was performed for all targets, which was possible because the computation of the SAXS models required much fewer resources. In this reconstruction, it was found that the introduced pitchwalk also changed the heights and in particular the widths of the different lines in the unit cell (Sunday et al. 2015). The change in line widths also breaks the 64 nm periodicity and therefore contributes to the intensity of the quartered diffraction orders in addition to the contribution of the pitchwalk. Since I only considered the direct effect of the pitchwalk in the GISAXS model and neglected the change in line profile, my model consistently overestimates the pitchwalk to fit the observed higher intensities.

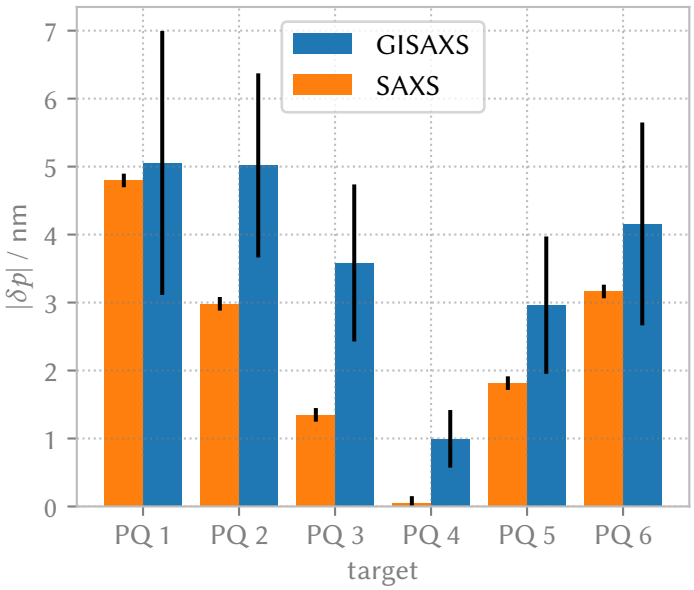

Figure 5.18: Comparison between measurements of pitchwalk using SAXS and GISAXS. The black bars indicate the standard 1σ uncertainties. Both measurement techniques qualitatively measure the same behavior. The GISAXS measurements show consistently higher pitchwalk, but are compatible with the SAXS measurements due to the relatively large GISAXS uncertainties.

Second, at the highest $|\delta p|$ values (for sample PQ 1), the relative uncertainty of the GISAXS measurement increases considerably and the $|\delta p|$ measured is not higher than that of sample PQ 2, contrary to the trend. This is likely also due to the rather large changes in the line profile introduced by the highest pitchwalks. According to the SAXS measurements, the line height of the PQ 1 sample is circa 1 nm greater than the line height of the PQ 4 sample I used as a reference. As the GISAXS measurements are very sensitive to changes in the line height, this deviation from my assumption of an undisturbed line shape disturbs the $|\delta p|$ determination based on the library approach, leading to diverging measurements and consequently high uncertainties.

5.9 Discussion

Gratings manufactured using current semiconductor production techniques exhibit complex line profiles and material compositions, and perturbations such as pitchwalk might be introduced during the production process. In this chapter, I have shown that complex line profiles can be reconstructed using GISAXS measurements, and uncertainties for the geometrical parameters can be calculated using a Bayesian approach and an MCMC evaluation. Using the reconstructed line profile as the basis, I then determined the pitchwalk of a series of disturbed samples and the corresponding uncertainty using a library of simulation results, but a number of additional challenges in both the measurement and the analysis have to be overcome compared to earlier measurements of well-defined gratings with larger pitch (Soltwisch, Fernández Herrero, Pflüger, Haase, Probst, Laubis, Krumrey, and Scholze, 2017).

The measured grating targets were surrounded by other structures, and the scattering of the surroundings contributed to the total signal. Therefore, I suppressed the parasitic signals by using a small beam and relatively high incident angles, and included the residual parasitic signals as an additional measurement uncertainty in my further analysis. However, this was only feasible because the measurement targets were comparatively large, with a size of 1 mm × 7 mm. I will discuss how to measure smaller measurement targets surrounded by disturbing structures in the next chapter.

The data acquisition and the reconstruction of the grating profile were complicated by the small pitch $d = 32\,\text{nm}$. The small pitch leads to relatively few grating orders ($|p| \leq 2$) being scattered

above the horizon even at the relatively high incident angles ($\alpha_i \approx 1^\circ$) I used. Nevertheless, using measurements at a range of photon energies and sample rotations allowed me to collect enough data points to successfully reconstruct the grating line profile. The reconstructed grating profile is compatible with reconstructions from SAXS measurements within the uncertainties in the general shape, side-wall angle and corner rounding measurements, but the line widths and heights measured do not agree. This reconstruction shows the usefulness and limitations of GISAXS as a metrology tool for small-pitch line gratings with complex line profiles. However, the reconstruction required significant computational resources due to the larger unit cell and the multi layer under the grating, both leading to a large computational domain. Due to limited computational resources, beam divergence could not be simulated accurately, which leads to high simulation uncertainties and consequently higher uncertainties in the geometrical parameters.

To enable fast analysis of the pitchwalk for multiple samples despite the considerable computational resources required, I took a library approach. By calculating a library of diffraction efficiencies from grating profiles disturbed only by pitchwalk, I could efficiently analyze a series of measurements of 6 measurement targets with varying pitchwalk. The analysis yielded uncertainties $u(|\delta p|) < 0.5\,\text{nm}$ for the smallest pitchwalk, and higher uncertainties up to $u(|\delta p|) \approx 2\,\text{nm}$ for the highest pitchwalk. I compared the results of my analysis with SAXS measurements, and found that the differences were $< 2.5\, u(|\delta p|)$ for all measurement targets. I also identified a bias towards systematically higher pitchwalks, and attributed this together with the higher uncertainties at high pitchwalks to additional changes in the line profile due to the introduced pitchwalk. To improve the accuracy of the pitchwalk measurements, a more comprehensive library would be required, not only with differing pitchwalk, but also with differing line height and line widths. Unfortunately, even including a moderate amount of additional parameters (such as two line heights and two line widths) leads to an unfeasibly large number of geometries that have to be calculated for a full library; for the example of five parameters in total, a brute force library approach needs $100^5 = 10\,000\,000\,000$ evaluations. Therefore, the development of more efficient simulation methods geared specifically to GISAXS measurements of periodic structures would be most welcome.

6 Measuring Small Periodic Targets Using Large Beams

One problem I had to deal with in the last chapter was the GISAXS signal of the structures surrounding the actual measurement target. The small incidence angle used in GISAXS leads to an elongation of the X-ray beam footprint on the sample, so that very large (mm^2) areas are probed at the same time, leading to parasitic signals from surface areas around the measurement target; this is known as the footprint problem. Due to the long footprints, GISAXS has so far been routinely used only on samples which are at least several millimetres long. However, for many applications including semiconductor metrology, the measurement of very small target areas down to a few micrometres in length is necessary, and the use of laboratory X-ray sources with comparably large beams is desirable. This chapter describes a method to measure small metrology targets using large X-ray beams that I developed.

I will start with an introduction into the footprint problem of GISAXS in general, and the resulting challenges for semiconductor metrology in particular. Towards a solution for the footprint problem, first the scattering of isolated grating targets with decreasing target size will be investigated. Then it will be shown that the scattering signal of grating targets can be selected by aligning the incident beam to the grating. Finally, I will design and measure a sample comprising rotated metrology targets in surroundings resembling those found in logic manufacturing, showing that GISAXS measurements of grating targets with an area down to 4 µm × 4 µm are possible using conventional non-focused X-ray sources.

Most of what I present in this chapter has already been published in the conference paper "Selective Measurement of Small Metrology Targets Using CD-GISAXS" (Pflüger, Soltwisch, Scholze, and Krumrey, 2017), the peer-reviewed paper "Grazing-Incidence Small-Angle X-Ray Scattering (GISAXS) on Small Periodic Targets Using Large Beams" (Pflüger, Soltwisch, Probst, Scholze, and Krumrey, 2017), and the German patent "Verfahren Zur Qualitätssicherung Einer Belichtungsmaske, Substrat Und Belichtungsmaske" (Soltwisch and Pflüger, 2018).

6.1 Application

For a typical GISAXS incidence angle of $\alpha_i \approx 0.5°$, the footprint on the sample is approximately 100 times longer than the incident beam height. For a moderately small beam of a synchrotron radiation beamline (height ≈ 500 µm), the length of the footprint on the sample is thus several centimetres. To achieve shorter beam footprints, the beam height needs to be reduced. The smallest beam height of about 300 nm used in GISAXS experiments so far (Roth et al. 2007), has led to a footprint on the sample of about 30 µm, but requires specialized X-ray optics, presents large technical challenges in aligning the sample to the beam, and suffers from dealignment by thermal drift. Therefore, GISAXS has so far been routinely used only on samples which are at least several millimetres long.

This large footprint is acceptable or even desirable in semiconductor applications with large homogeneous sample structures such as memory manufacturing (Hagihara, Taniguchi, Yamanaka,

Omote, et al. 2017; Hagihara, Taniguchi, Yamanaka, Hirano, et al. 2019). However, in other applications such as logic manufacturing, the sample structures are not homogeneous.

For optical scatterometry, homogeneous metrology targets that are approximately 40 µm × 40 µm in size and consist of grating lines that are representative for the structures in the circuit are printed in spare areas of the wafer (Thony 2003). Since these metrology targets are not functional in the finished product, their size must be kept as small as possible. Therefore, the large beam footprints in GISAXS would lead to large metrology targets with prohibitive cost. Indeed, Bunday (2016) identified the problem of the large beam footprint as one of the key challenges for the use of GISAXS as a metrology tool in semiconductor production (compare also table 5.2).

6.2 Scattering off small measurement targets

To test the lower limits of target sizes in GISAXS, I measured a series of isolated grating targets with decreasing target length.

6.2.1 Sample description

The sample consisted of multiple grating targets on a single silicon wafer, with each target consisting of 40 grooves of differing line length L, forming a grating with pitch $d = 100\,\text{nm}$. The targets were produced by Jürgen Probst at the HZB. He fabricated them by electron beam lithography on a Vistec EBPG5000+ using positive resist ZEP520A on silicon substrates, followed by reactive ion etching with SF_6 and C_4F_8 and resist stripping with an oxygen plasma treatment (Senn et al. 2011). In total, 11 targets were produced in this length series, one "infinitely" long target with $L = 2500\,\mu\text{m}$ and 10 targets with lengths ranging from $L = 50\,\mu\text{m}$ down to $4\,\mu\text{m}$. For all targets, the target width is $4\,\mu\text{m}$, the individual line width is $w_l = 55\,\text{nm}$ and the nominal line height is $h_l = 45\,\text{nm}$. The targets were placed at a distance of 3.04 mm from their nearest neighbour to ensure that in non-coplanar mounting only one target is hit by the beam.

6.2.2 GISAXS measurements

For the measurement of the very small targets in GISAXS, it is necessary to consider how much of the incoming X-ray beam can interact with the measured target. Due to the shallow incidence angle, the beam footprint on the sample is enlarged by $1/\sin(\alpha_i)$. With a beam size of about 0.5 mm × 0.5 mm and an incidence angle of $\alpha_i = 0.6°$, this yields a beam footprint on the sample of about 0.5 mm × 50 mm. The largest target covers an area of 4 µm × 2500 µm on the substrate, so only $\approx 4 \cdot 10^{-4}$ of the incident beam interacts with the largest target, and for the smallest target (4 µm × 4 µm), only $\approx 6 \cdot 10^{-7}$ of the beam hits the target. It is therefore necessary to suppress parasitic signals as much as possible. For this purpose, I used low-scatter beam-defining pinholes and a scatter guard as described in section 3.1. In this configuration, I measured a photon flux of approximately $8 \cdot 10^9/\text{s}$, which means that for the smallest target, less than 5000 photons interact with the target grating per second.

Measurements for all targets were taken at $E_{\text{ph}} = 6\,\text{keV}$ with an incidence angle of $\alpha_i \approx 0.6°$ in non-coplanar mounting. Using suitably long exposure times of $t = 1\,\text{h}$ with the hybrid pixel photon counting detector, I could collect scattering patterns. The scattering from the targets is extraordinarily weak and incoherently superimposed with the scattering from the surrounding substrate; however, the scattering from the targets is recorded clearly and even the signal of the smallest grating target shows grating diffraction peaks, see figure 6.1a.

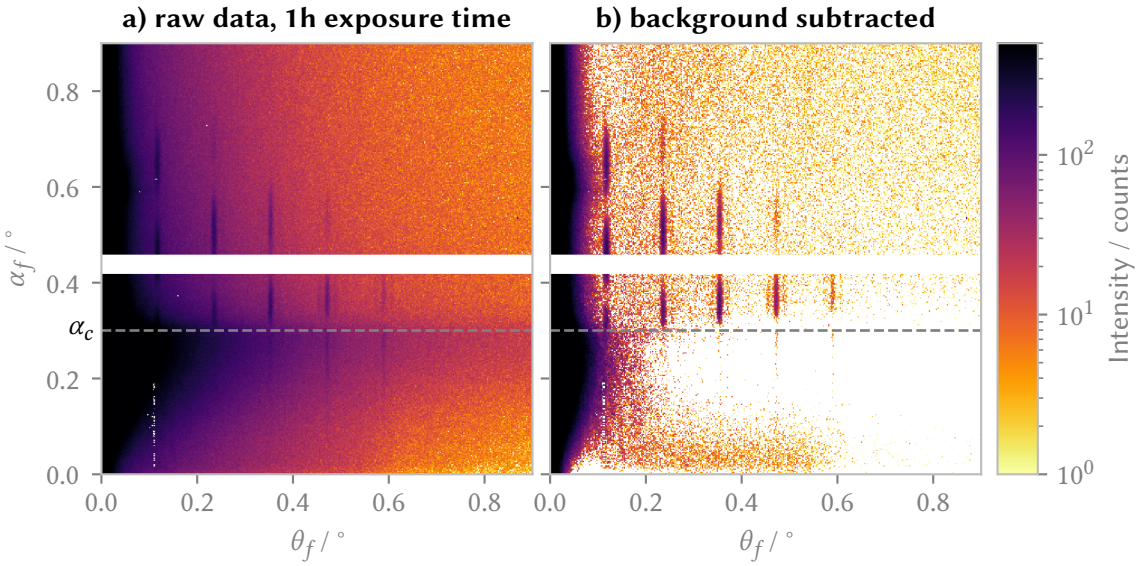

Figure 6.1: GISAXS pattern of the smallest target before and after background subtraction. a) Shown is the scattering of the 4 µm × 4 µm target. **b)** After background subtraction, the signal is visible more clearly. The background subtraction works well above the critical angle of the substrate α_c, but fails below α_c and very close to the specular axis at $\theta_f = 0$.

In order to extract the scattering of the targets only, I fitted the background I_B which stems from the scattering of the surrounding substrate for each measurement with the exception of the longest $L = 2500$ µm grating. I assumed that the background I_B can be factorized to $I_B(\alpha_f, \theta_f) = A(\alpha_f) \cdot T(\theta_f)$. For the function $A(\alpha_f)$, I used a smooth B-spline approximation of degree 2 to closely follow the scattering of the background around the critical angle of total external reflection α_c of the substrate. In order to only fit the substrate contribution, I took a cut along α_f between the first and second grating diffraction orders. For the function $T(\theta_f)$, I fitted a polynomial of degree 4 to a cut along θ_f at $\alpha_f > 0.8°$, i.e. above the sample scattering features. The resulting smooth background was subtracted from the GISAXS measurement, yielding the scattering from the target only (figure 6.1b).

6.2.3 Results

While the scattering from the longest grating (figure 6.2a) shows sharp diffraction orders on a semi-circle similar to the scattering patterns of infinitely long gratings, a shorter grating shows elongated diffraction orders (figure 6.2b) and the shortest grating (figure 6.2c) produces a scattering pattern which has lost the circle-like interference pattern almost completely. The changes in the form of the first diffraction order are shown in detail in figures 6.2d and 6.2e. For the small ($L \leq 50$ µm) gratings, side lobes above and below the grating diffraction order are visible, and with decreasing length, the diffraction orders as well as the side lobes elongate in the vertical direction and the side lobes move further away from the main peak. The width of the peaks in the horizontal direction does not change with line length L and is due to the size and divergence of the incoming X-ray beam.

To explain the changes in the scattering patterns for gratings with finite length, we need to consider the changes in reciprocal space when the grating is finite in the x-direction. The finite length enlarges the grating truncation rods in k_x, leading to grating truncation sheets. The intersection

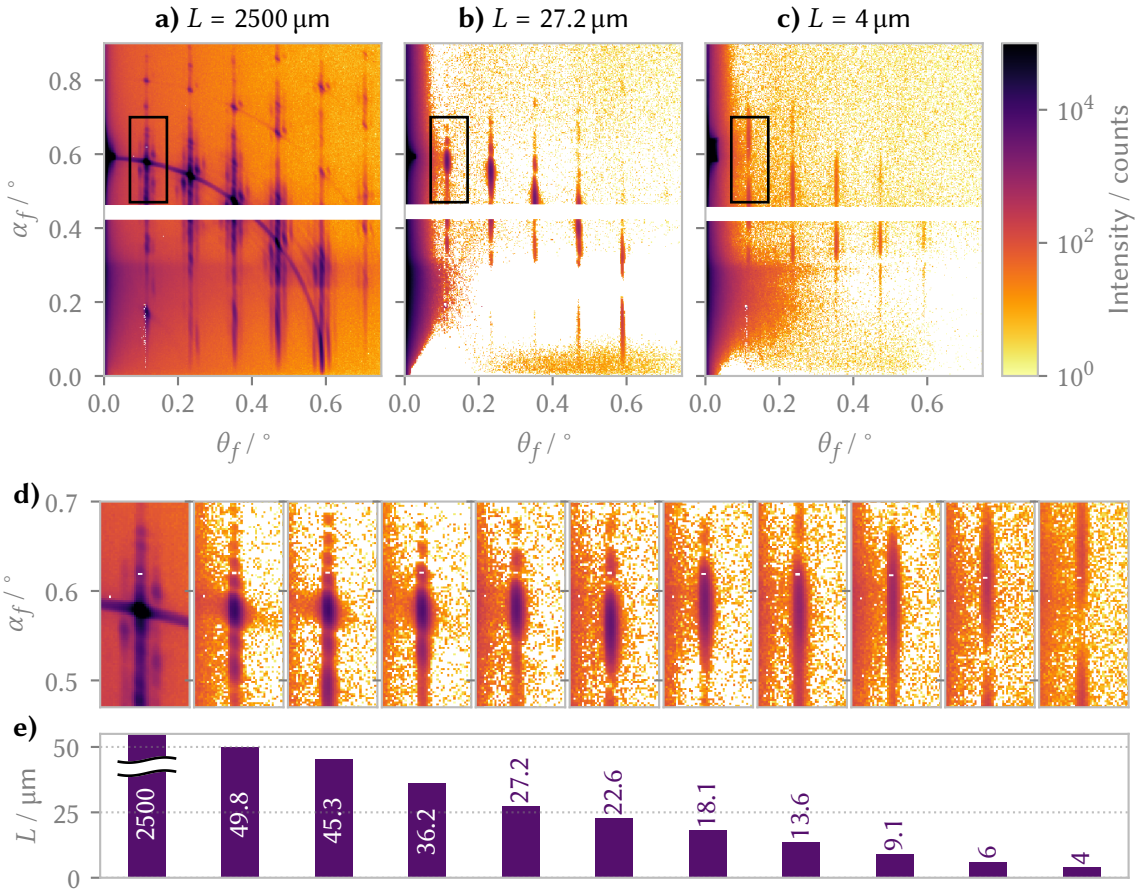

Figure 6.2: Changes in the GISAXS pattern by target length. **a)** In the GISAXS pattern of the 2500 µm long grating, diffraction orders on a semi-circle are visible. **b)** The diffraction orders of the 27.2 µm long grating are slightly elongated and show satellite orders above and below. **c)** The shortest grating shows long diffraction orders with intensity oscillations along the orders. **d)** A detailed view of the first diffraction order of all gratings shows the elongation of the first diffraction order with decreasing grating length, which is shown in part **e)**. For comparability, all measurements were taken with the same exposure time $t = 1\,\mathrm{h}$, which leads to overexposure for the 2500 µm long grating.

of the grating truncation sheets with the Ewald sphere then leads to elongated diffraction orders (see figure 6.3).

For a quantitative description of the intensity profile along the diffraction orders, I will extend the description of non-coplanar grating scattering in the framework of the BA that I explained in subsection 3.2.1 to gratings with finite length. The Fourier transform $\hat{V}_{sg}$ of a grating comprising lines with length L is:

$$\hat{V}_{sg}(L, \boldsymbol{k}) = L\,\mathrm{sinc}(k_x L/2) \cdot \hat{V}_{sg,y}(k_y) \tag{6.2.1}$$

$$\text{with } \hat{V}_{sg,y}(k_y) = \begin{cases} 1 & \text{if } k_y = k_0 p\lambda/d \\ 0 & \text{otherwise}\,, \end{cases} \tag{6.2.2}$$

with the unnormalized cardinal sine function

$$\mathrm{sinc}(x) = \begin{cases} 1 & \text{if x=0} \\ \sin(x)/x & \text{otherwise}\,. \end{cases} \tag{6.2.3}$$

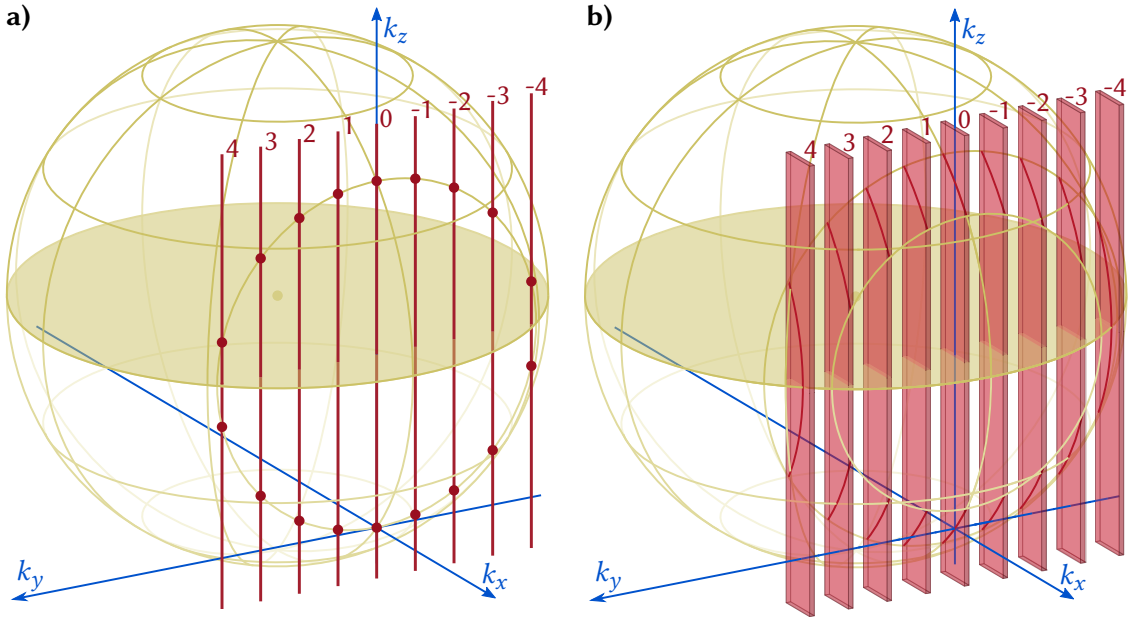

Figure 6.3: Reciprocal space construction of GISAXS from short gratings. a) For an infinitely long grating, the Fourier transform comprises grating truncation rods (red) and the intersection with the Ewald sphere (yellow) leads to sharp grating diffraction orders (red dots). **b)** For a short (i.e. finitely long) grating, the Fourier transform is not delta shaped along k_x any more. Instead, it has an extent in k_x, which I have represented qualitatively as a grating truncation sheet (pink). The intersection of the grating truncation sheets and the Ewald sphere leads to elongated diffraction orders (red).

It only differs from the infinitely long grating in k_x. The intersection with the Ewald sphere at $\boldsymbol{q}$ then yields

$$\hat{V}_{sg}(L, \boldsymbol{q}) = \begin{cases} L\,\mathrm{sinc}(q_x L/2) = L\,\mathrm{sinc}\left(k_0(\cos\alpha_f\cos\theta_f - \cos\alpha_i)L/2\right) & \text{if } q_y = k_0 p\lambda/d \\ 0 & \text{otherwise.} \end{cases} \tag{6.2.4}$$

The scattered intensity I is then in Born approximation

$$I_{sg}(\alpha_f, \theta_f) \propto |E_{sg}(\alpha_f, \theta_f)|^2 \propto |\hat{V}_{sg}(\alpha_f, \theta_f)|^2 \propto \mathrm{sinc}^2\left(k_0(\cos\alpha_f\cos\theta_f - \cos\alpha_i)L/2\right) \tag{6.2.5}$$

along the diffraction orders. The calculated scattered intensity is compared to measurements for different line lengths L in figure 6.4a.

For easy comparison of all measurements with the experimental data, I solved equation (6.2.5) numerically for α_f at $I(\alpha_f) = I_{\max}/2$ to compute the full width at half maximum

$$\Delta\alpha_{f,\mathrm{fwhm}} = \alpha_f^+(I_{\max}/2) - \alpha_f^-(I_{\max}/2) = \arccos\left(\frac{\cos\alpha_i + 0.443\lambda/L}{\cos\theta_f}\right) - \arccos\left(\frac{\cos\alpha_i - 0.443\lambda/L}{\cos\theta_f}\right). \tag{6.2.6}$$

I extracted the peak width $\Delta\alpha_{f,\mathrm{fwhm}}$ as shown in figure 6.4a from the measurements for all grating targets. The result is compared to calculated values in figure 6.4b.

As can be seen, the peak width and the magnitude of the side lobes as well as the frequency of the oscillation is described well by the calculation. This shows that the scattering of short grating targets can be described adequately within the framework of the Born approximation

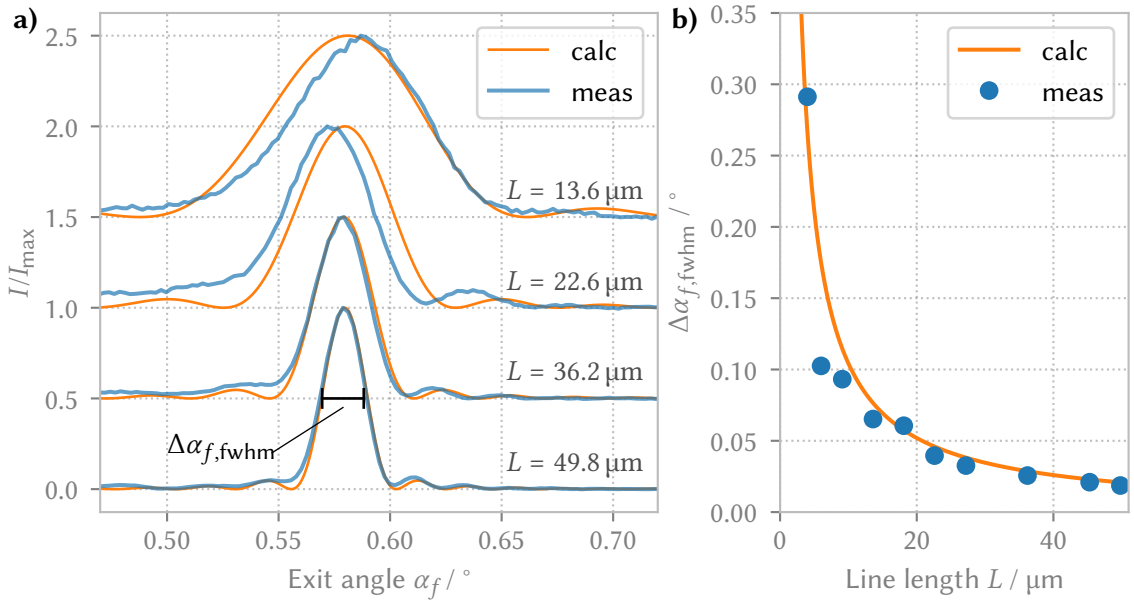

Figure 6.4: Scattering of short gratings. **a)** Shown is a cut along the first diffraction order of the scattering of grating targets with differing length. The calculation according to equation (6.2.5) is compared to the corresponding measurement. Lines are shifted vertically for visibility. **b)** Shown is the comparison between the measured $\Delta\alpha_{f,\mathrm{fwhm}}$ extracted from the GISAXS patterns for the length series and the $\Delta\alpha_{f,\mathrm{fwhm}}$ calculated from the line length L.

using only the line length as an additional parameter. However, for the shortest gratings with $L < 10\,\mu\mathrm{m}$, there are larger discrepancies. In particular, the deviation between calculated and measured $\Delta\alpha_{f,\mathrm{fwhm}}$ is substantial for $L = 6\,\mu\mathrm{m}$ (see figure 6.4b).

To describe the shortest gratings, also the changes in the scattering due to the finite line height have to be considered. Due to the curvature of the Ewald sphere, not only k_x, but also k_z changes along the elongated diffraction orders. So far, I used a model of the grating lines where the height of the line h_l was infinitesimal, leading to a uniform Fourier transform in k_z. This is a valid approximation as long as the projected length of the lines is much greater than the height of the lines. Then the frequency of the oscillations in the scattering due to the line length is much greater than the frequency of the oscillations due to the line height, and the line height can be neglected. For the shortest gratings, this is not the case anymore. Including the line height in the description, the scattered intensity becomes

$$I_{sgh}(\alpha_f, \theta_f) \propto \mathrm{sinc}^2\left(q_x L/2\right) \mathrm{sinc}^2\left(q_z h_l/2\right) \tag{6.2.7}$$

$$= \mathrm{sinc}^2\left(k_0(\cos\alpha_f \cos\theta_f - \cos\alpha_i)L/2\right) \mathrm{sinc}^2\left(k_0(\sin\alpha_f + \sin\theta_f)h_l/2\right) \quad . \tag{6.2.8}$$

Calculations using the simple description with L as the only parameter using equation (6.2.5) and calculations that include h_l using equation (6.2.8) are compared with measured values in figure 6.5. While the simple description does not fit the data at all, the calculation including h_l closely follows the measured data. The only major deviations are at small exit angles close to the angle of total external reflection $\alpha_c \approx 0.3°$. At these small exit angles, multiple scattering is much more likely than at large exit angles, so that the description in the framework of the BA that I used here is not adequate to describe the scattering quantitatively.

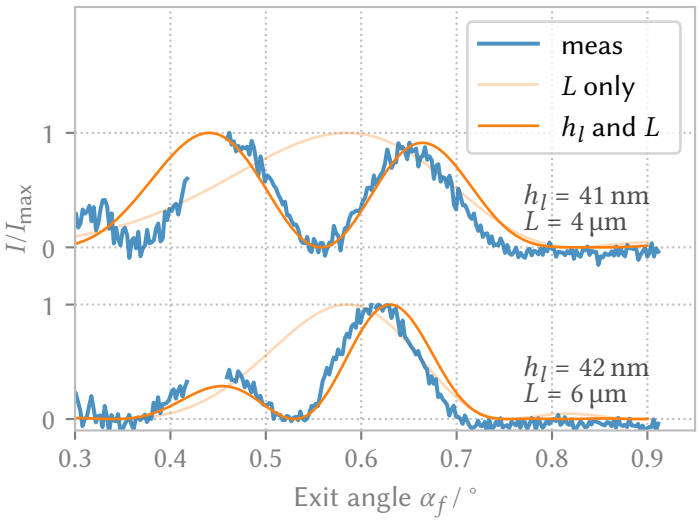

Figure 6.5: Scattering of short gratings with finite line height. The calculation that includes a description of h_l fits the experimental data. The line height was chosen close to the nominal one, but varied slightly to match the measured peak positions.

6.2.4 Discussion

In this section I have shown that very small grating targets can be measured using GISAXS, and the scattering can be understood using extensions of the reciprocal space construction that I described in subsection 3.2.1. To measure the signal of very small targets, it is necessary to suppress parasitic scattering as much as possible, and long integration times have to be used. Here, it was only possible to measure the very weak signals because the gratings were isolated on a blank silicon wafer, and the background scattering of the wafer could be fitted and subtracted relatively easily.

6.3 Selecting measurement targets in reciprocal space

In most cases, small targets are not isolated on a blank wafer. Therefore, it is essential to separate the parasitic scattering of the surroundings from the scattering of the target structure. If both the target and the surroundings are oriented internally, their scattering can be separated using a variation of the dominant length scale (for gratings, the pitch d) of the target with respect to the surroundings. This would lead to a separation in θ_f, as seen in chapter 5. However, the sensitivity of θ_f to changes in d is not very high and for surroundings with multiple dominant length scales, it might be difficult to find a suitable d for the target. Therefore, it could be advantageous to rotate the target in the sample plane with respect to the surroundings, which leads to a separation of the scattering in α_f. If the surroundings and the target can be described in good approximation as gratings, this effect can be quantified using equation (3.2.29) from subsection 3.2.1.

For a first test of this idea, I measured a sample which was already available. The sample consists of 40 µm × 40 µm area grating targets with pitch d = 250 nm. A total of 1360 grating targets are arranged in a field on an 80 µm grid (compare figure 6.6). The gratings are rotated in-plane by an angle φ_{target}, ranging from $\varphi_{\text{target}} = 0°$ to $\varphi_{\text{target}} = 180°$ in steps of 6°, resulting in $\varphi_{\text{target}} = m\,6°$ with m integer. In the field there are only 3 grating targets for each even m, while for odd m there are about 90 targets each.

I measured the sample using a fixed incidence angle $\alpha_i = 0.55°$ and $E_{\text{ph}} = 6$ keV at different sample rotations φ in order to align the incident beam to targets with different φ_{target}. With the beam width of about 0.5 mm and the field width of about 3 mm, the beam illuminates about 15 % of the field at once, corresponding to about 200 targets. Figure 6.7 shows measurements with the

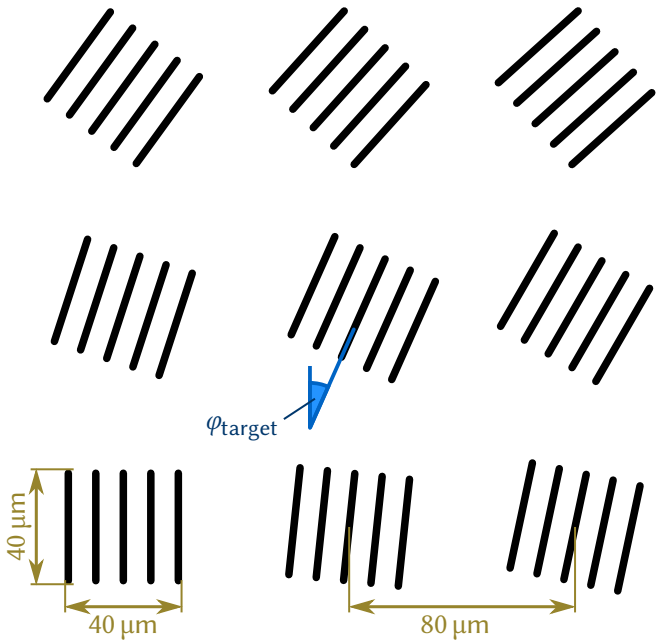

Figure 6.6: Sketch of the sample. Shown is a top view. Grating targets of the size 40 µm × 40 µm are arranged on an 80 µm grid. The targets are rotated in the sample plane by the angle φ_{target}. Note that the grating period is not to scale, in reality each grating target consists of 160 lines.

incident beam aligned to about 15 targets in a field at once with $\varphi = \varphi_{\text{target}} = 6°$ (a) and aligned to only 3 targets in a field with $\varphi = \varphi_{\text{target}} = 0°$ (b). As expected, the scattering of the aligned targets is on the semi-circle, while the scattering of all other targets is confined to an area close to the specular axis. For the higher grating diffraction orders, the scattering of the aligned targets is therefore well-separated from the signal of all other targets. Thus, the weak signal of the three targets per field with $\varphi_{\text{target}} = 0°$ can be separated from the scattering of the other about 200 illuminated targets with $\varphi_{\text{target}} \neq 0°$ per field. This shows that the rotation of metrology targets with respect to their surroundings is a viable strategy to solve the footprint problem in GISAXS.

6.4 Small targets in surroundings like logical circuits

In applications like logic manufacturing, only a small part of the wafer is dedicated to grating targets that can be used for metrology purposes. The rest of the wafer area is filled with the structures that will result in the functional device. In modern production processes, these structures consist of gratings, where the individual lines are cut at specific positions according to the intended functionality. The gratings are all oriented in one direction or perpendicular to it, i.e. at $\varphi_{\text{target}} = 0°$ or $\varphi_{\text{target}} = 90°$ (Seo et al. 2014).

6.4.1 Sample description

To show that GISAXS measurements of small rotated targets are possible in these conditions as well, I designed a sample comprising small grating targets surrounded by ordered but randomized structures, with the grating orientation rotated by 10° with respect to the orientation of the surroundings. In the sample design, the surroundings are covered by boxes with a randomized length between 0.2 µm and 3 µm and a direction of $\varphi_{\text{target}} = 0°$ or $\varphi_{\text{target}} = 90°$. To keep the production cost reasonable, the surroundings have a size of 100 µm × 100 µm. At the center of the surroundings, a metrology target consisting of a grating with pitch $d = 100$ nm and a size of

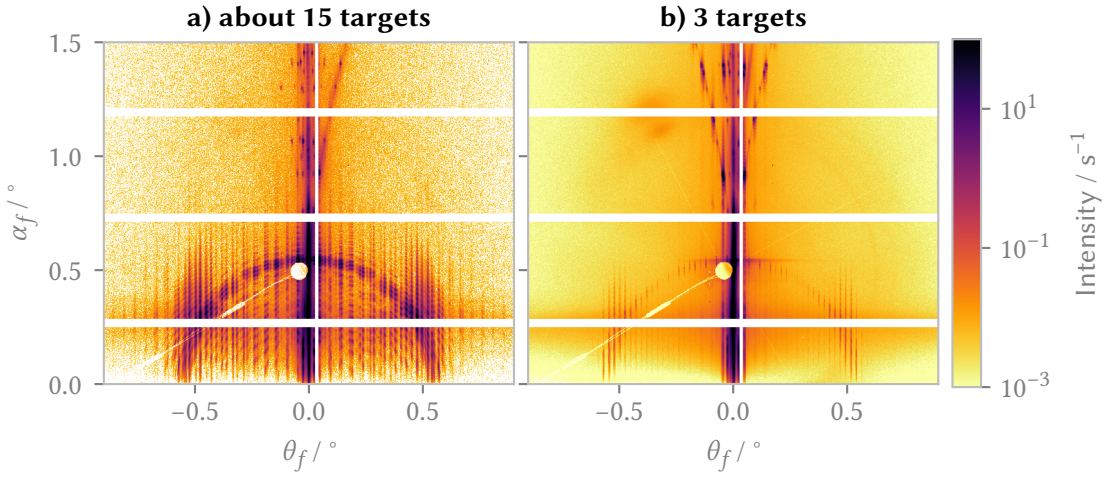

Figure 6.7: Selectively measuring targets using GISAXS. a) The measurement was taken at $\varphi = 6°$, with about 15 different targets per field with $\varphi_{\text{target}} = 6°$ aligned with the incident X-ray beam. The grating semi-circle shows a lot of overlapping signals, and extraction of meaningful details is impossible. **b)** This measurement has only 3 uniform targets per field with $\varphi_{\text{target}} = 0°$ aligned with the incident X-ray beam. The faint signal of three 40 µm × 40 µm grating targets on the grating semi-circle is clearly separated from the signals of gratings with $\varphi_{\text{target}} = \pm 6°$ which are confined near the specular axis.

15 µm × 15 µm is placed. The metrology target is rotated with respect to the surroundings, such that the lines are at $\varphi_{\text{target}} = 10°$ (see figure 6.8). To explore the sensitivity of GISAXS measurements of small grating targets to changes in the target line profile, I designed two different samples. Both have the same surroundings, but the grating targets differ in the line width w_l. For surrounded field 1, the line width is $w_l = 45$ nm, and for surrounded field 2 it is $w_l = 55$ nm. For both samples, the nominal line height is $h_l = 100$ nm, but small differences in actual line height are expected due to the differing line width. Both samples were manufactured on a single wafer by Jürgen Probst at HZB using the same process as the samples in section 6.2.

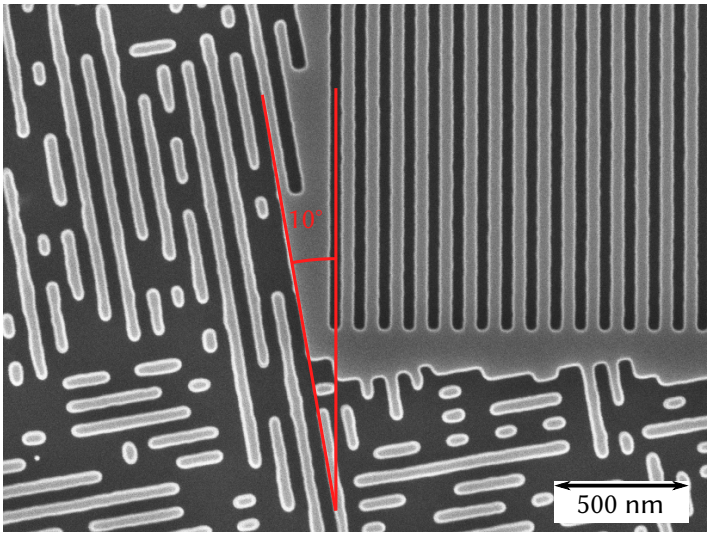

Figure 6.8: Top view SEM image of surrounded field 1. Shown is the corner of the small grating field (top right) and the surroundings. Darker areas correspond to etched grooves, lighter areas to mesas. The orientations of the small grating field and the surroundings, at 10° rotation, are in red. Measurement courtesy of Jürgen Probst at HZB.

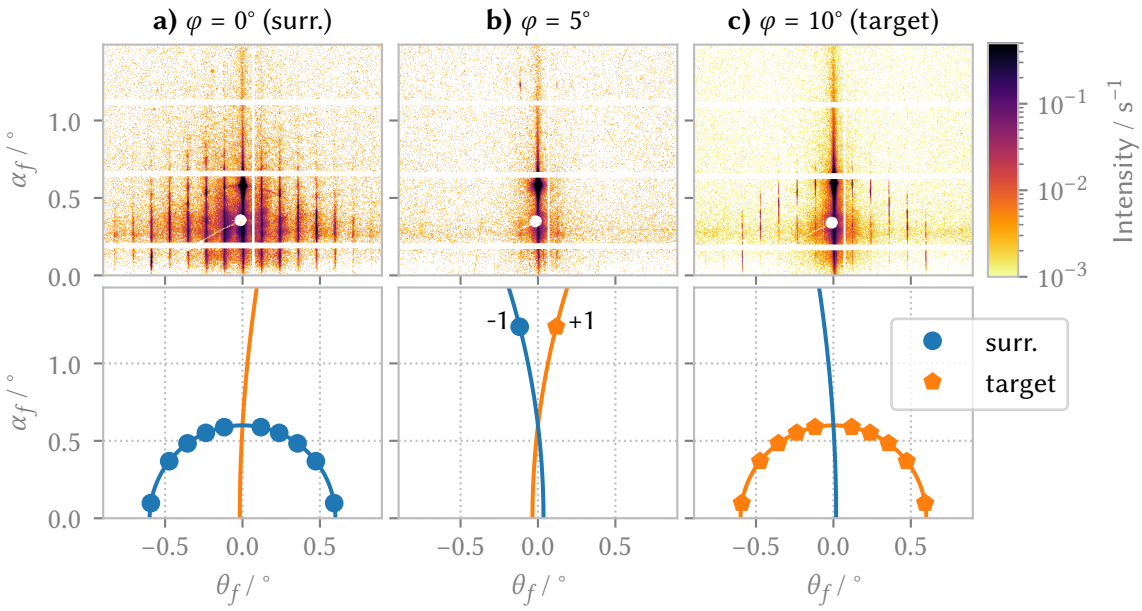

Figure 6.9: GISAXS measurements versus theoretical expectation of the position of grating diffraction orders. Shown are measurements (top row) and corresponding theoretical expectation (bottom row) of surrounded field 1 at different rotation angles φ. **a)** At $\varphi = 0°$ the X-ray beam is oriented along the surrounding structure, showing the scattering orders of the surroundings and a rich diffuse background. **b)** At $\varphi = 5°$ the X-ray beam is equally misaligned to the surroundings and the grating target, with only the minus or plus first diffraction order visible at $\alpha_f \approx 1.2°$ for the surroundings and the target, respectively. **c)** With the X-ray beam aligned to the target ($\varphi = 10°$), only the scattering of the target is visible on the detector. An animated sequence showing scattering patterns from $\varphi = 0°$ to $\varphi = 10°$ in steps of $\Delta\varphi = 0.1°$ is available as Figure S2 in the electronic supplementary information at `https://doi.org/10.18452/21660`.

6.4.2 Signal separation

I took GISAXS measurements of the surrounded fields using the small pinhole as described in section 3.1, resulting in a beam size of 0.15 mm × 0.15 mm, such that the width of the X-ray beam is close to the width of the surroundings. I took measurements at different sample rotations φ; the results for surrounded field 1 are shown in figure 6.9. When the X-ray beam is aligned to the surroundings at $\varphi = 0°$ (see figure 6.9a), grating diffraction orders as well as diffuse scattering of the surroundings can be seen. At $\varphi = 10°$ (see figure 6.9c), the signal from the measurement target becomes visible. This signal is much weaker and would be buried if superimposed with the signal of the surroundings seen at $\varphi = 0°$. However, the exit angle α_f is highly sensitive to small deviations in the rotation φ, as can be seen from the measurement at $\varphi = 5°$ (see figure 6.9b). Even at $\varphi = 5°$, only the $p = -1$ diffraction order of the surroundings is scattered onto the detector, and the background signal from the surroundings is completely suppressed, with the exception of scattering onto the specular axis. This follows the theoretical expectation for scattering of misaligned gratings from equation (3.2.29), showing that the diffuse scattering of the surroundings is caused by scattering at the grating-like structures in the surroundings. At $\varphi = 10°$, the scattering of the surroundings is thus fully outside of the detector and the signal of the target is measured without contributions from the surroundings even though the target only covers about 2.3 % of the structured area.

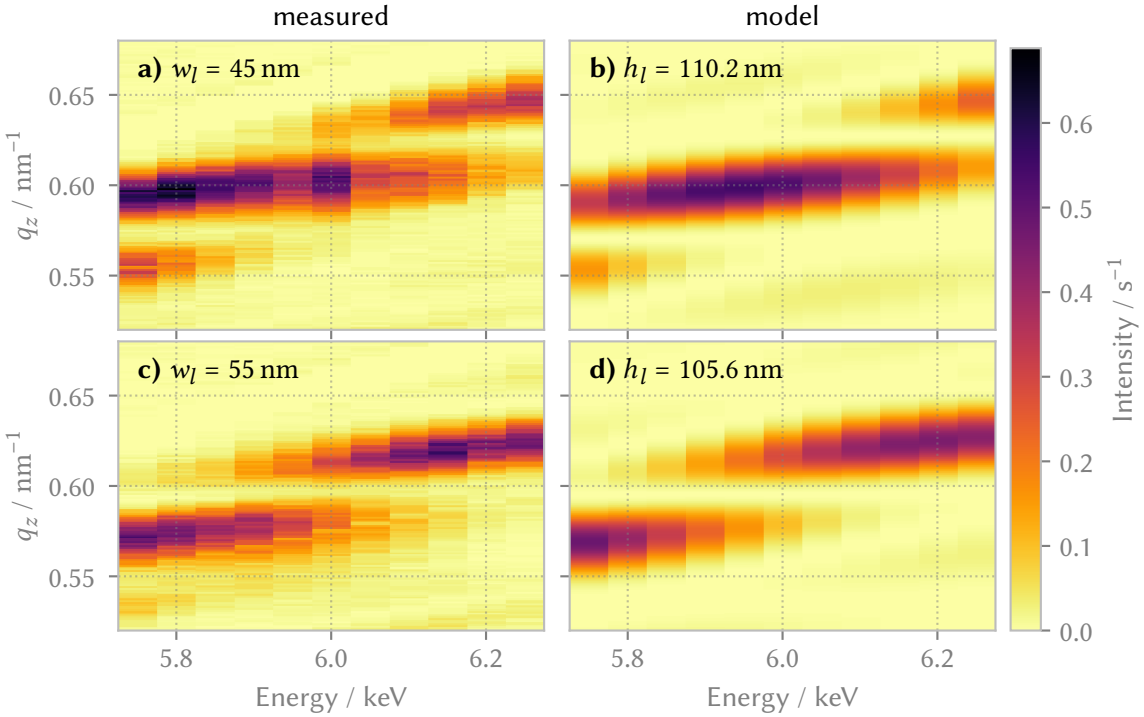

Figure 6.10: Comparison of GISAXS measurement and model of small grating targets with differing line width. Shown are vertical cuts through the second diffraction order of the GISAXS patterns collected at different photon energies. **a-b)** Shown are the measurement (a) and fit (b) for surrounded field 1. **c-d)** Shown are the measurement (c) and fit (d) for surrounded field 2. The fitted line height h_l is indicated for each model. Since detector quantum efficiency and photon flux change with the photon energy, absolute intensities are not comparable between different photon energies.

6.4.3 Comparison of different grating targets

I measured target GISAXS patterns ($\varphi = 10°$) at photon energies from $E_{\mathrm{ph}} = 5750\,\mathrm{eV}$ up to $E_{\mathrm{ph}} = 6250\,\mathrm{eV}$ for both surrounded field 1 (line width $w_l = 45\,\mathrm{nm}$) and surrounded field 2 ($w_l = 55\,\mathrm{nm}$). Vertical cuts through the second diffraction order for both targets and all energies are shown in figure 6.10.

Unfortunately, I was not able to use the FEM framework presented in chapter 5 to simulate the GISAXS measurements. This is mainly because the samples can not be accurately modeled using a two-dimensional unit cell due to the finite length of the gratings. Instead, a three-dimensional unit cell with a length of 15 µm has to be used, which leads to an unfeasible number of finite elements.

Instead, the measurements can be described qualitatively in terms of the reciprocal space construction for gratings with a finite height and width. Within this framework, changing the photon energy alters the radius of the Ewald sphere and consequently the position of the intersection between the Ewald sphere and the grating truncation sheets. Effectively, we measure a different part of the grating truncation sheets at each energy. The grating truncation sheets themselves have a modulation in intensity due to the finite height, as described by equation (6.2.8). To verify that the measurement data can be explained by the model, I fitted the model to the data using the known length $L = 15\,\mu\mathrm{m}$ and a variable line height h_l for each grating target (see figure 6.10). I used the local optimizer `scipy.optimize.minimize` from the `SciPy` software package for the fit.

While relative intensities are not fully represented, the models fit peak positions very well, showing that the intensity profile can be described using equation (6.2.8). The fitted line heights h_l are reasonably close to the nominal value of $h_l = 100\,\text{nm}$, and the deviation between the two targets of $\Delta h_l \approx 5\,\text{nm}$ is plausible considering the differing line widths. Note however that the result of the fit is not unique, the shown result is just one local minimum.

6.5 Discussion

In this chapter, I have discussed the footprint problem in GISAXS and have shown a solution to it for an important class of applications in semiconductor metrology. Conventionally, GISAXS can only be used for measurements of large targets. This was identified as a major obstacle for the use of GISAXS in semiconductor metrology, which could preclude the use of GISAXS in metrology for logic manufacturing (Bunday 2016). Using X-ray beams with a smaller focus to measure smaller measurement targets is possible, but technologically very demanding and therefore impractical for industrial applications. I have shown that for the important class of small grating-like measurement targets, GISAXS measurements are possible with existing X-ray beams with a large focus using metrology targets with a modified layout.

First, I have shown that the signal of targets with a size down to $4\,\mu\text{m} \times 4\,\mu\text{m}$ can be measured, which is one order of magnitude smaller than the smallest micro-beam footprints which have been used in GISAXS experiments so far (Roth et al. 2007). However, to separate the weak signal of the metrology targets from background signals caused by the remaining illuminated surface, it was necessary to isolate the measurement targets on an otherwise blank wafer. This does not solve the problem for semiconductor metrology, where the wafers are densely packed with structures. Therefore, it is necessary to separate the target signals with a different method. I have shown that the target signals can be separated very efficiently by manufacturing the metrology targets rotated in the sample plane. If the X-ray beam is then aligned to the direction of the grating lines, the target signal is clearly visible while other signals are efficiently suppressed. This enables GISAXS measurements for applications where GISAXS was previously dismissed due to the footprint problem.

My comparison of the scattering of two small grating targets with different line widths and heights shows that GISAXS measurements of small targets are sensitive to the grating line profile. The measured signals can be explained qualitatively using an extended reciprocal space construction in the Born approximation. However, a quantitative reconstruction of the line profiles from the GISAXS measurements was not possible, because three-dimensional FEM simulations at X-ray wavelengths are infeasible. The development of theoretical methods to quantitatively describe GISAXS measurements of inherently three-dimensional samples would therefore be of high interest.

7 Conclusion and Outlook

In my thesis, I extended the applications for quantitative GISAXS measurements, in particular for dimensional metrology of semiconductor devices. The challenges here are two-fold. On the one hand, the nanostructures that can be produced today in science and industry are considerably smaller and more complex than what is measured routinely using GISAXS. On the other hand, due to the use of X-rays and the GISAXS measurement geometry, samples have to fulfill high requirements to be measurable at all. With the presented studies I contributed to solutions for both of these challenges.

7.1 Better parameter reconstruction

Towards a solution of the first challenge, I extended and improved the existing metrology approaches for the reconstruction of line grating profiles using GISAXS measurements. Line gratings have applications in many areas of science and technology; consequently, investigations of line gratings using GISAXS had already drawn interest and studies on simple line gratings were already published in the literature. In particular, uncertainties had been evaluated for measurements of the grating period of relatively simple line gratings (Wernecke, Krumrey, et al. 2014). However, the line gratings that form the building blocks of modern semiconductor devices have smaller periods, more complex line profiles, and more diverse material compositions than the line gratings that had previously been studied. Additionally, traceable measurements with associated uncertainties are required not only for the pitch, but also for the full line profile including key parameters like line width and line height. In contrast to measurements of the grating pitch, no direct measurement formula can be given for the full line profile; instead, reconstruction of the line profile is an inverse problem which has to be solved by optimizing a model to fit the measured data. Therefore, statistical approaches beyond Gaussian uncertainty propagation are needed for the evaluation of the uncertainty of the results.

As a case study for an advanced line grating reconstruction, I showed GISAXS measurements of grating samples with a pitch of 32 nm which were produced in a multi-patterning process similar to the one in use in modern high-volume semiconductor manufacturing. To reconstruct the line profile, I used a differential evolution optimization algorithm to fit a scattering model based on solving Maxwell's equations using FEM. For the evaluation of uncertainties of the full line profile, I applied Bayesian statistics, in particular affine-invariant MCMC. A great advantage of this approach is that it allows the introduction of additional parameters and corrections into the simulation with relatively low effort. I used this to include into the simulation a model for the errors of the simulation due to the necessarily incomplete description of the experiment. This allowed me to estimate these errors from the mismatch between measurement data and optimized model results. I found that this simulation error is significant, and therefore must not be neglected in an uncertainty analysis.

The results of my analysis showed that GISAXS can be employed to reconstruct the line profile of complex grating samples and to establish the uncertainty of the result, but evaluating the uncertainties using the MCMC method needed almost 10^6 evaluations of the scattering model;

therefore, it was not feasible to conduct this analysis for more than one grating. To measure a series of grating targets with an intentionally introduced lithographic defect, I therefore assumed that they all shared the same line shape, and only the pitchwalk varied between them. With this approximation, it was possible to measure the pitchwalk of the six gratings in the series and derive the uncertainty of the measurement from the standard deviation of multiple measurements in different geometries. This shows that based on prior knowledge like the undisturbed line shape, data evaluation can be simplified considerably, albeit using a rather coarse approximation.

I compared my results for the line profile and the pitchwalk of the disturbed sample series to previously published SAXS measurements of the same samples. The SAXS measurements were available because the sample is unusually thin and therefore its structured surface is accessible in transmission geometry, which enabled the direct comparison of SAXS and GISAXS on the same sample. I found that both methods agree in the form of the lines, with differences between the reconstructed line shapes smaller than 2 nm. However, the GISAXS results show larger uncertainties and a larger line height and line width, with differences exceeding the combined uncertainties. I could not determine with certainty which of the results is correct, but I discussed possible reasons for an excess of material in the GISAXS results and inferred opportunities to enhance the simulation. In particular, the simulation can be improved by including a variation of the density of the material that forms the grating lines, calculating the effects of divergence of the incident X-ray beam, introducing a more detailed description of the multi layer under the grating, and modeling roughness of the grating lines and the multi layer.

For the pitchwalk measurements, I found that the GISAXS results are compatible with the SAXS results. While both measurements agree within the combined uncertainties, the GISAXS uncertainties are considerably higher and the GISAXS measurements show a trend towards systematically higher pitchwalks. I attributed both effects to the rough approximation of unchanged line shapes that I used in the GISAXS analysis. This shows that GISAXS reconstructions of line gratings would tremendously profit from simulation methods which are faster than solving Maxwell's equations using finite elements. For this purpose, I evaluated the DWBA, which is widely used for GISAXS simulations, but found that it only yielded the position of the grating diffraction orders correctly, and failed to simulate their relative intensity. I attribute this to the inherent limitation of the DWBA that it does not consider multiple scattering at the grating lines, so that it does not capture the formation of standing waves within the grating lines. Therefore, it is usable only for the measurement of the grating pitch and the orientation of the grating with respect to the incident beam, but not for the reconstruction of grating line profiles.

My study has shown that the traceable measurement of complex grating line shapes is possible using GISAXS, which would be very welcome due to the high signal intensities in reflection geometry even for arbitrarily thick samples. But my study has also shown the areas in which further progress is needed for the GISAXS method to be used to full effect. In particular, the theoretical description is not yet fully adequate, which is the most probable reason why the results are not in full agreement with SAXS results. At the same time, the theoretical description is already relatively slow to compute, so that the presented statistical methods for the evaluation of uncertainties can not be used to their full effect. Therefore, the best opportunities to further improve GISAXS for dimensional nanometrology in semiconductor applications can in my view be found by either improving the theoretical modeling for more accurate and faster evaluation, or by introducing other statistical methods to evaluate uncertainties more efficiently.

Toward more efficient modeling, it would be desirable to extend the multi beam dynamical diffraction theory that was recently shown to be effective in grazing-incidence X-ray fluorescence analysis of grating structures (Nikolaev et al. 2020) to the analysis of GISAXS measurements of gratings. For certain configurations, this approach was shown to be about 3 orders of magnitude

faster than an FEM analysis while delivering the same results, which is very promising. Regarding statistical approaches for reconstruction and uncertainty evaluation of geometrical parameters, many methods that are applied in optical scatterometry could probably be translated to GISAXS measurements as well; here, I would consider the use of virtual reference methods (Kagalwala et al. 2016) and the use of surrogate models (Farchmin et al. 2020) as promising candidates. In particular, we have already shown that a surrogate model based on a polynomial chaos expansion can be used to explore parameter sensitivities of GISAXS reconstructions (Casfor Zapata, Farchmin, Pflüger, Nikolaev, Soltwisch, Heidenreich, Laubis, Kolbe, and Scholze, 2020), and potentially offers much faster reconstruction. To determine the limits of validity of this approach, further research is needed.

In research, GISAXS is mainly employed for the characterization of samples which are less strictly ordered than gratings, such as hetero-junction solar cells (Coric, Saxena, Pflüger, Müller-Buschbaum, Krumrey, and Herzig, 2018; Müller-Buschbaum, 2009) and mesoporous films (Zhou et al. 2017). I have shown that for optical crystals with a small amount of disorder, the distortions of the crystal orientation can be quantified with GISAXS measurements using an analysis based on the reciprocal space construction for gratings. However, to enable the measurement of samples with even more disorder and other dimensional parameters, simulation methods have to be introduced which explicitly consider the effects of disorder and dispersity to enable traceable measurements.

Due to the relatively high signal intensities in GISAXS compared to SAXS, GISAXS is also used for fast in-situ measurements of processes such as film formation during spray coating (Su et al. 2017). Here, protocols for traceable measurements with rigorously evaluated uncertainties would aid in comparisons between measurements conducted by different groups and help in correlating geometrical form and chemical or electrical function. For this, additional experimental facilities are needed, which combine traceable measurements of photon energy and incident and scattered photon flux with flexible in-situ capabilities.

7.2 New applications for GISAXS

Scattering methods are ensemble methods that deliver information about the average properties of relatively large sample volumes. For GISAXS in particular, the shallow incidence angle leads to a centimetre long beam footprint on the sample, so that the scattering signal stems from a large surface area compared to the nanometre-sized structures that are investigated. For many applications, the ability to investigate average properties of a large number of scatterers in a single measurement is very valuable. In my study of defects in light harvesting nanostructures I have gained information in a large area of about 1 mm × 20 mm with a single measurement, showing the high statistical power of GISAXS. But not in all applications homogeneously structured surface areas with a size of at least 1 mm × 20 mm are available or interesting to measure, which limits the applicability of GISAXS. Bunday (2016) even identified this footprint problem as the most important challenge for the use of GISAXS as a tool for metrology for high-volume semiconductor manufacturing.

The only method to circumvent this problem which was published in the literature so far is to minimize the height of the X-ray beam, which naturally also minimizes the length of the beam footprint. Unfortunately, to achieve beam footprints of less than 40 µm, a beam height of less than 500 nm is necessary, which presents large technical challenges (Roth et al. 2007).

I have shown that for some samples, GISAXS measurements of small target areas are possible using conventional large X-ray beams. Using a sample comprising a series of grating targets with

varying lengths, I have shown that the scattering signal of very small targets can be collected. I explained the scattering signal of small grating targets qualitatively with a reciprocal space construction. The Fourier transformation directly yields that the grating diffraction orders widen vertically, which matched the experimental observation.

When the measurement target is much smaller than the beam footprint, the main problem is to reach an acceptable ratio of target signal to noise. The noise is caused by scattering of the illuminated surface surrounding the measurement target, and by air and optical components in the X-ray beam path. To measure the smallest targets, I therefore used an optimized beam line setup consisting of pinholes and optical slits selected for lowest scatter before the sample, and no optical elements or windows between sample and detector. Additionally, the whole beam path was evacuated, completely avoiding air scattering. This setup allowed GISAXS measurements of the smallest grating target with a size of only 4 µm × 4 µm, where the signal in the grating diffraction orders could clearly be picked up from the background caused by scattering at the surrounding blank substrate.

This shows that GISAXS can also be used on nanostructured samples that are either inherently limited in their size or too costly to produce on large areas. Small samples with a size on the order of 500 µm × 500 µm are relatively easy to measure, and with an optimized beam line setup measurements of samples with a size down to 4 µm × 4 µm are possible. However, it is crucial to suppress the noise due to scattering at the surrounding structures that are also illuminated. In particular for applications in semiconductor logic manufacturing, metrology targets are typically surrounded by other nanostructured area. Because the metrology targets are used for process control of the manufacturing process which is based on grating structures, the metrology targets and their surroundings consist of gratings with identical pitch. Therefore, the GISAXS signal of the target is buried by the signal of the surroundings.

For this application, I presented a method to separate the target signal from the signal of the surroundings, significantly enhancing the signal-to-noise ratio. By manufacturing the metrology targets rotated in the sample plane with respect to their surroundings, the target diffraction orders are shifted to other exit angles than the scattering of the surroundings. I tested this method by designing a rotated metrology target surrounded by randomized grating-like structures resembling semiconductor logic structures. In GISAXS measurements of these metrology targets, I found that the signal-to-noise ratio was excellent. This method has the potential to enable GISAXS to be used in semiconductor logic manufacturing metrology.

This novel method also opens new questions which warrant further studies. It would be interesting to quantify the differences between rotated metrology targets and normal metrology targets that are aligned with the actual functional structures. At the moment, it is not yet known if the rotated targets are actually representative of the process under study, which is of course imperative for process quality control. Additionally, a theory which accurately describes GISAXS scattering of finite, and therefore necessarily three-dimensional, gratings with acceptable numerical effort is of high interest. Due to the small area of the grating targets, edge effects can not be neglected, and the grating can not be approximated as extending periodically into infinity. Here, good simulation methods are a prerequisite to develop traceable reconstructions of important dimensional parameters.

An interesting avenue for further research would be to use the widening of the diffraction orders at shorter grating lengths to collect more information in a single measurement. The idea here is that the wider diffraction orders contain scattering information for a range of q vectors; therefore, information that traditionally can only be collected by taking multiple measurements at different incident photon energies or incident angles can be obtained in a single measurement. In my study I have already shown that the difference in line height of two metrology targets can indeed be

seen in a single measurement. Possibly, this could be used to offset the longer measurement times that are needed due to the small scattering signals of small measurement targets.

The technological progress in semiconductor manufacturing continues at a high speed, and therefore the demands for semiconductor metrology also grow continuously. In this thesis I have shown GISAXS measurements of structures produced with processes very similar to those in high-volume manufacturing today; however, these production processes evidently don't employ GISAXS, and the requirements of future production processes will be different from today's requirements. Some future requirements are already known. It is expected that future semiconductor processes will employ even more complex three-dimensional geometries such as gate-all-around designs, where the drain is formed by a nano wire which is fully surrounded by the gate (Orji et al. 2018). Here, it will likely be necessary to integrate different metrology methods that yield orthogonal information, such as GISAXS, X-ray fluorescence, optical scatterometry, and imaging methods into a hybrid metrology package. Therefore, there will be a need for statistical methods to evaluate uncertainties when linking multiple measurement methods with possibly very different error models.

Acknowledgements

Many people have helped me in the course of my thesis. In particular, I would like to thank Prof. Kurt Busch and Prof. Mathias Richter for supervising my thesis, as well as 奥田 浩司 / Prof. Hiroshi Okuda for his willingness to act as the external reviewer for my thesis. Further, I am grateful to Michael Krumrey and Christian Gollwitzer for providing me the opportunity of working in their working group at PTB's synchrotron radiation laboratory, and to Victor Soltwisch for being my mentor.

During beamtimes in the laboratory as well as during the data evaluation between beamtimes, I worked with many colleagues from PTB and collaborators from outside, in particular I would like to thank Alexander Schavkan, Analía Fernández Herrero, Anna Andrle, Anton Haase, Christian Laubis, Dieter Skroblin, Enrico Hauser, Evelyn Handick, Frank Scholze, Gilad Kaplan, Hans Kirschner, Jan Wernecke, Jérôme Deumer, Jürgen Probst, Karl Wiese, Konstantin Nikolaev, Layla Riemann, Levent Cibik, Maren Casfor Zapata, Martin Hammerschmidt, Michael Sintschuk, Mihael Coric, Nando Farchmin, Nitin Saxena, Peter Müller, Philipp Hönicke, Qais Saadeh, R. Joseph Kline, Raül García Diez, René Sachse, Richard Ciesielski, Sebastian Heidenreich, Sina Jaroslawzew, Stefanie Handreck, Swenja Schreiber, and Ulf Knoll. Finally, I would like to acknowledge Alexandra Elbakyan for help in literature research.

Bibliography

Abbe, Ernst (Dec. 1, 1873). "Beiträge zur Theorie des Mikroskops und der mikroskopischen Wahrnehmung". In: *Archiv für mikroskopische Anatomie* 9.1, pp. 413–468. ISSN: 0176-7364. DOI: 10.1007/BF02956173.

Alem, Nasim, Rolf Erni, Christian Kisielowski, Marta D. Rossell, Will Gannett, and A. Zettl (Oct. 12, 2009). "Atomically Thin Hexagonal Boron Nitride Probed by Ultrahigh-Resolution Transmission Electron Microscopy". In: *Physical Review B* 80.15, p. 155425. DOI: 10.1103/PhysRevB.80.155425.

Andor (Dec. 20, 2016). *iKon-M/L SO Series - DIRECT DETECTION IMAGING*. URL: https://andor.oxinst.com/products/high-energy-detection/ikon-l-so (visited on 11/18/2019).

Andor (Jan. 29, 2019). *Andor High Energy Detection Brochure*. URL: https://andor.oxinst.com/assets/uploads/Andor_High_Energy_Detection_Brochure.pdf.

Attwood, David (1999). *Soft X-Rays and Extreme Ultraviolet Radiation : Principles and Applications*. Cambridge: Cambridge University Press. ISBN: 0-521-65214-6.

Auger, Pierre (July 16, 1923). "Sur les rayons β - secondaires produits dans un gaz par des rayons X". In: Séances de l'Académie des sciences. Vol. 3. Paris, pp. 169–171. URL: https://gallica.bnf.fr/ark:/12148/bpt6k3130n/f187.image.langFR (visited on 11/06/2019).

Auth, Chris, A. Aliyarukunju, M. Asoro, D. Bergstrom, V. Bhagwat, J. Birdsall, N. Bisnik, M. Buehler, V. Chikarmane, G. Ding, Q. Fu, H. Gomez, W. Han, D. Hanken, M. Haran, M. Hattendorf, R. Heussner, H. Hiramatsu, B. Ho, S. Jaloviar, I. Jin, S. Joshi, S. Kirby, S. Kosaraju, H. Kothari, G. Leatherman, K. Lee, J. Leib, A. Madhavan, K. Marla, H. Meyer, T. Mule, C. Parker, S. Parthasarathy, C. Pelto, L. Pipes, I. Post, M. Prince, A. Rahman, S. Rajamani, A. Saha, J. Dacuna Santos, M. Sharma, V. Sharma, J. Shin, P. Sinha, P. Smith, M. Sprinkle, A. St. Amour, C. Staus, R. Suri, D. Towner, A. Tripathi, A. Tura, C. Ward, and A. Yeoh (Dec. 2017). "A 10nm High Performance and Low-Power CMOS Technology Featuring 3rd Generation FinFET Transistors, Self-Aligned Quad Patterning, Contact over Active Gate and Cobalt Local Interconnects". In: 2017 IEEE International Electron Devices Meeting (IEDM), pp. 29.1.1–29.1.4. DOI: 10.1109/IEDM.2017.8268472.

Babonneau, David, S. Camelio, D. Lantiat, Lionel Simonot, and A. Michel (Oct. 23, 2009). "Waveguiding and Correlated Roughness Effects in Layered Nanocomposite Thin Films Studied by Grazing-Incidence Small-Angle x-Ray Scattering". In: *Physical Review B* 80.15, p. 155446. DOI: 10.1103/PhysRevB.80.155446.

Bahrdt, Johannes (2016). "Shaping Photon Beams with Undulators and Wigglers". In: *Synchrotron Light Sources and Free-Electron Lasers: Accelerator Physics, Instrumentation and Science Applications*. Ed. by Eberhard J. Jaeschke, Shaukat Khan, Jochen R. Schneider, and Jerome B. Hastings. Springer International Publishing, pp. 751–819. ISBN: 978-3-319-14394-1. DOI: 10.1007/978-3-319-14394-1_16.

Bakker, R.J. (Mar. 1999). "Status and Commissioning-Results of BESSY II". In: Proceedings of the 1999 Particle Accelerator Conference (Cat. No.99CH36366). Vol. 1, 197–199 vol.1. DOI: 10.1109/PAC.1999.795662.

Barkla, Charles G. (Sept. 1911). "The Spectra of the Fluorescent Röntgen Radiations". In: *The London, Edinburgh, and Dublin Philosophical Magazine and Journal of Science* 22.129, pp. 396–412. ISSN: 1941-5982, 1941-5990. DOI: 10.1080/14786440908637137.

Bayes, Thomas (Jan. 1, 1763). "An Essay towards Solving a Problem in the Doctrine of Chances. By the Late Rev. Mr. Bayes, F. R. S. Communicated by Mr. Price, in a Letter to John Canton, A. M. F. R. S". In: *Philosophical Transactions of the Royal Society of London* 53, pp. 370–418. DOI: 10.1098/rstl.1763.0053.

Becker, Christiane, Daniel Amkreutz, Tobias Sontheimer, Veit Preidel, Daniel Lockau, Jan Haschke, Lisa Jogschies, Carola Klimm, Janis J. Merkel, Paul Plocica, Simon Steffens, and Bernd Rech (Dec. 1, 2013). "Polycrystalline Silicon Thin-Film Solar Cells: Status and Perspectives". In: *Solar Energy Materials and Solar Cells*. Thin-Film Photovoltaic Solar Cells 119 (Supplement C), pp. 112–123. ISSN: 0927-0248. DOI: 10.1016/j.solmat.2013.05.043.

Beckhoff, Burkhard, Alexander Gottwald, Roman Klein, Michael Krumrey, Ralph Müller, Mathias Richter, Frank Scholze, Reiner Thornagel, and Gerhard Ulm (July 1, 2009). "A Quarter-Century of Metrology Using Synchrotron Radiation by PTB in Berlin". In: *physica status solidi (b)* 246.7, pp. 1415–1434. ISSN: 1521-3951. DOI: 10.1002/pssb.200945162.

Beckhoff, Burkhard, Birgit Kanngießer, Norbert Langhoff, Reiner Wedell, and Helmut Wolff, eds. (2006). *Handbook of Practical X-Ray Fluorescence Analysis*. Berlin Heidelberg: Springer. 863 pp. ISBN: 978-3-540-28603-5.

Bhandari, Khagendra P., Jennifer M. Collier, Randy J. Ellingson, and Defne S. Apul (July 1, 2015). "Energy Payback Time (EPBT) and Energy Return on Energy Invested (EROI) of Solar Photovoltaic Systems: A Systematic Review and Meta-Analysis". In: *Renewable and Sustainable Energy Reviews* 47 (Supplement C), pp. 133–141. ISSN: 1364-0321. DOI: 10.1016/j.rser.2015.02.057.

Binnig, Gerd, Calvin Forrest Quate, and Christian Gerber (Mar. 3, 1986). "Atomic Force Microscope". In: *Physical Review Letters* 56.9, pp. 930–933. DOI: 10.1103/PhysRevLett.56.930.

Binnig, Gerd, Heinrich Rohrer, Christoph Gerber, and Edi Weibel (July 5, 1982). "Surface Studies by Scanning Tunneling Microscopy". In: *Physical Review Letters* 49.1, pp. 57–61. DOI: 10.1103/PhysRevLett.49.57.

Blumenstock, Gerry M., Christine Meinert, Nigel R. Farrar, and Anthony Yen (Jan. 27, 2005). "Evolution of Light Source Technology to Support Immersion and EUV Lithography". In: Advanced Microlithography Technologies. Vol. 5645. SPIE, pp. 188–195. DOI: 10.1117/12.577587.

Boldon, Lauren, Fallon Laliberte, and Li Liu (Jan. 1, 2015). "Review of the Fundamental Theories behind Small Angle X-Ray Scattering, Molecular Dynamics Simulations, and Relevant Integrated Application". In: *Nano Reviews* 6.1, p. 25661. DOI: 10.3402/nano.v6.25661.

Boyle, Michael (2019). *Quaternion Version 2019.12.11.22.25.52 Documentation*. URL: https://quaternion.readthedocs.io/en/latest/ (visited on 06/07/2020).

Bragg, William Henry and William Lawrence Bragg (July 1, 1913). "The Reflection of X-Rays by Crystals". In: *Proceedings of the Royal Society of London. Series A, Containing Papers of a Mathematical and Physical Character* 88.605, pp. 428–438. DOI: 10.1098/rspa.1913.0040.

Brent, Richard P (1973). "Chapter 3 and 4". In: *Algorithms for Minimization without Derivatives*. NJ, USA: Prentice-Hall Englewood Cliffs. ISBN: 978-0-486-41998-5. URL: https://store.doverpublications.com/0486419983.html.

Broennimann, Christoph, E. F. Eikenberry, B. Henrich, R. Horisberger, G. Huelsen, E. Pohl, B. Schmitt, C. Schulze-Briese, M. Suzuki, T. Tomizaki, H. Toyokawa, and A. Wagner (Mar. 1, 2006). "The PILATUS 1M Detector". In: *Journal of Synchrotron Radiation* 13.2, pp. 120–130. ISSN: 0909-0495. DOI: 10.1107/S0909049505038665.

Bunday, Benjamin (Mar. 24, 2016). "HVM Metrology Challenges towards the 5nm Node". In: *Proc. SPIE* 9778. Ed. by Martha I. Sanchez and Vladimir A. Ukraintsev, 97780E-97780E–34. DOI: 10.1117/12.2218375.

Bunday, Benjamin, Abner Bello, Eric Solecky, and Alok Vaid (Mar. 22, 2018). "7/5nm Logic Manufacturing Capabilities and Requirements of Metrology". In: Metrology, Inspection, and Process

Control for Microlithography XXXII. Ed. by Ofer Adan and Vladimir A. Ukraintsev. San Jose, United States: SPIE, p. 17. DOI: 10.1117/12.2296679.

Bureau International des Poids et Mesures (2019). *SI Brochure*. 9th ed. Paris. ISBN: 978-92-822-2272-0. URL: https://www.bipm.org/en/publications/si-brochure/ (visited on 10/09/2019).

Burger, Bruno, Klaus Kiefer, Christoph Kost, Sebastian Nold, Simon Philipps, Ralf Preu, Jochen Rentsch, Thomas Schlegl, Gerhard Stryi-Hipp, Harry Wirth, and Werner Warmuth (Nov. 14, 2019). *Photovoltaics Report*. Freiburg, p. 49. URL: https://www.ise.fraunhofer.de/content/dam/ise/de/documents/publications/studies/Photovoltaics-Report.pdf.

Burle, Jan, Céline Durniak, Jonathan M. Fisher, Marina Ganeva, Gennady Pospelov, Walter Van Herck, and Joachim Wuttke (Dec. 5, 2016). *Born Again Manual*. Version 1.7.1. URL: http://apps.jcns.fz-juelich.de/src/BornAgain/BornAgainManual-1.7.1.pdf (visited on 06/12/2018).

Busch, P., M. Rauscher, Detlef-M. Smilgies, D. Posselt, and C. M. Papadakis (June 1, 2006). "Grazing-Incidence Small-Angle X-Ray Scattering from Thin Polymer Films with Lamellar Structures – the Scattering Cross Section in the Distorted-Wave Born Approximation". In: *Journal of Applied Crystallography* 39.3, pp. 433–442. ISSN: 0021-8898. DOI: 10.1107/S0021889806012337.

Casfor Zapata, Maren, Nando Farchmin, Mika Pflüger, Konstantin V. Nikolaev, Victor Soltwisch, Sebastian Heidenreich, Christian Laubis, Michael Kolbe, and Frank Scholze (Mar. 20, 2020). "Sensitivity Analysis for the Detection of Pitchwalk in Self-Aligned Quadruple Patterning by GISAXS". In: Metrology, Inspection, and Process Control for Microlithography XXXIV. Vol. 11325. SPIE, p. 113251D. DOI: 10.1117/12.2552037.

Chao, Robin, Mary Breton, Benoit L'herron, Brock Mendoza, Raja Muthinti, Florence Nelson, Abraham De La Pena, Fee li Le, Eric Miller, Stuart Sieg, James Demarest, Peter Gin, Matthew Wormington, Aron Cepler, Cornel Bozdog, Matthew Sendelbach, Shay Wolfling, Tom Cardinal, Sivananda Kanakasabapathy, John Gaudiello, and Nelson Felix (Mar. 30, 2016). "Advanced In-Line Metrology Strategy for Self-Aligned Quadruple Patterning". In: Metrology, Inspection, and Process Control for Microlithography XXX. Vol. 9778. SPIE, p. 977813. DOI: 10.1117/12.2220601.

Chawla, Jasmeet S., K. J. Singh, A. Myers, D. J. Michalak, R. Schenker, C. Jezewski, B. Krist, F. Gstrein, T. K. Indukuri, and H. J. Yoo (Mar. 28, 2014). "Patterning Challenges in the Fabrication of 12 Nm Half-Pitch Dual Damascene Copper Ultra Low-k Interconnects". In: Advanced Etch Technology for Nanopatterning III. Vol. 9054. SPIE, p. 905404. DOI: 10.1117/12.2048599.

Chou, Stephen Y., Peter R. Krauss, and Preston J. Renstrom (Apr. 5, 1996). "Imprint Lithography with 25-Nanometer Resolution". In: *Science* 272.5258, pp. 85–87. ISSN: 0036-8075, 1095-9203. DOI: 10.1126/science.272.5258.85.

Compton, Arthur H. (May 1, 1923a). "A Quantum Theory of the Scattering of X-Rays by Light Elements". In: *Physical Review* 21.5, pp. 483–502. DOI: 10.1103/PhysRev.21.483.

Compton, Arthur H. (June 1923b). "The Total Reflexion of X-Rays". In: *The London, Edinburgh, and Dublin Philosophical Magazine and Journal of Science* 45.270, pp. 1121–1131. ISSN: 1941-5982, 1941-5990. DOI: 10.1080/14786442308634208.

Coric, Mihael, Nitin Saxena, Mika Pflüger, Peter Müller-Buschbaum, Michael Krumrey, and Eva M. Herzig (June 7, 2018). "Resonant Grazing-Incidence Small-Angle X-Ray Scattering at the Sulfur K-Edge for Material-Specific Investigation of Thin-Film Nanostructures". In: *The Journal of Physical Chemistry Letters* 9.11, pp. 3081–3086. ISSN: 1948-7185. DOI: 10.1021/acs.jpclett.8b01111.

Crookes, William (1898). "Address of the President Before the British Association for the Advancement of Science, Bristol, 1898". In: *Science* 8.200. Crookes' speech is mostly nationalistic and racist rhetoric; however, his call to develop a solution to the emerging Guano shortage is widely regarded to have spurred the development of nitrogen fixation., pp. 561–575. ISSN: 00368075, 10959203. JSTOR: 1627238.

Daillant, Jean and Alain Gibaud, eds. (2009). *X-Ray and Neutron Reflectivity*. Red. by Wolf Beiglböck, Jürgen Ehlers, Klaus Hepp, Hans A. Weidenmüller, Robert Beig, Wolfgang Domcke, Berthold-Georg Englert, Uriel Frisch, Peter Hänggi, Günther Hasinger, Wolfgang Hillebrandt, Robert L. Jaffe, Wolfhard Janke, H. von Löhneysen, Michelangelo Mangano, Jean-Michel Raimond, Didier Sornette, Stefan Theisen, Wolfram Weise, Johannes Zittartz, Francisco Guinea, and Dieter Vollhardt. Vol. 770. Lecture Notes in Physics. Berlin, Heidelberg: Springer Berlin Heidelberg. ISBN: 978-3-540-88588-7. URL: http://link.springer.com/10.1007/978-3-540-88588-7 (visited on 11/04/2014).

Dalesio, L. R., A. J. Kozubal, and M. R. Kraimer (Jan. 1, 1991). *EPICS Architecture*. LA-UR-91-3543; CONF-911116-9. Los Alamos National Lab., NM (United States). URL: https://www.osti.gov/biblio/6110347 (visited on 06/07/2020).

Davisson, C. J. and L. H. Germer (Apr. 1, 1928). "Reflection of Electrons by a Crystal of Nickel". In: *Proceedings of the National Academy of Sciences* 14.4, pp. 317–322. ISSN: 0027-8424, 1091-6490. DOI: 10.1073/pnas.14.4.317. pmid: 16587341.

De Broglie, Louis (1924). "Recherches sur la théorie des Quanta". Paris. URL: https://tel.archives-ouvertes.fr/tel-00006807 (visited on 10/11/2019).

DECTRIS (Apr. 27, 2016). *PILATUS3 S and X Series*. URL: https://www.dectris.com/products/pilatus3/pilatus3-x-for-synchrotron (visited on 11/18/2019).

Diebold, Alain C., Andy Antonelli, and Nick Keller (May 1, 2018). "Perspective: Optical Measurement of Feature Dimensions and Shapes by Scatterometry". In: *APL Materials* 6.5, p. 058201. DOI: 10.1063/1.5018310.

Dietrich, S. and H. Wagner (Oct. 17, 1983). "Critical Surface Scattering of X Rays and Neutrons at Grazing Angles". In: *Physical Review Letters* 51.16, pp. 1469–1471. ISSN: 0031-9007. DOI: 10.1103/PhysRevLett.51.1469.

Dietrich, S. and H. Wagner (Sept. 1984). "Critical Surface Scattering of X-Rays at Grazing Angles". In: *Zeitschrift für Physik B Condensed Matter* 56.3, pp. 207–215. ISSN: 0722-3277, 1434-6036. DOI: 10.1007/BF01304174.

Dirac, Paul Adrien Maurice (Mar. 1, 1927). "The Quantum Theory of the Emission and Absorption of Radiation". In: *Proceedings of the Royal Society of London. Series A* 114, p. 23. DOI: 10.1098/rspa.1927.0039.

Dixit, Dhairya J., Vimal Kamineni, Richard Farrell, Erik R. Hosler, Moshe Preil, Joseph Race, Brennan Peterson, and Alain C. Diebold (Apr. 2015). "Metrology for Block Copolymer Directed Self-Assembly Structures Using Mueller Matrix-Based Scatterometry". In: *Journal of Micro/Nanolithography, MEMS, and MOEMS* 14.2, p. 021102. ISSN: 1932-5150, 1932-5134. DOI: 10.1117/1.JMM.14.2.021102.

Downey, Allen B. (2013). *Think Bayes - Bayesian Statistics Made Simple*. 1.0.9. Needham, Massachusetts: Green Tea Press. ISBN: 978-1-4493-7078-7. URL: https://greenteapress.com/wp/think-bayes/.

Durniak, Céline, Marina Ganeva, Walter Van Herck, Gennady Pospelov, and Joachim Wuttke (2014). *GISAS Data Analysis with Born Again*. FZJ-2014-03382. Streumethoden, Neutronenstreuung , JCNS-FRM-II, JARA-FIT. URL: http://juser.fz-juelich.de/record/153925/ (visited on 08/23/2015).

Eisenhauer, David, Beatrix Pollakowski, Jonas Baumann, Veit Preidel, Daniel Amkreutz, Bernd Rech, Franziska Back, Eveline Rudigier-Voigt, Burkhard Beckhoff, Birgit Kanngie β er, and Christiane Becker (Mar. 1, 2015). "Grazing Incidence X-Ray Fluorescence Analysis of Buried Interfaces in Periodically Structured Crystalline Silicon Thin-Film Solar Cells". In: *physica status solidi (a)* 212.3, pp. 529–534. ISSN: 1862-6319. DOI: 10.1002/pssa.201400112.

Ertl, G, D Prigge, R Schloegl, and M Weiss (Feb. 1983). "Surface Characterization of Ammonia Synthesis Catalysts". In: *Journal of Catalysis* 79.2, pp. 359–377. ISSN: 00219517. DOI: 10.1016/0021-9517(83)90330-5.

Ewald, Paul Peter (June 1, 1913). "Zur Theorie Der Interferenzen Der Röntgenstrahlen". In: *Physikalische Zeitschrift* 14.11, pp. 465–472.

Fahlman, A., K. Hamrin, R. Nordberg, C. Nordling, and K. Siegbahn (Feb. 1966). "Chemical Shift in Auger Spectra". In: *Physics Letters* 20.2, pp. 159–160. ISSN: 00319163. DOI: 10.1016/0031-9163(66)90917-6.

Falta, Jens and Thomas Möller (Nov. 3, 2010). *Forschung Mit Synchrotronstrahlung*. Springer-Verlag. ISBN: 978-3-519-00357-1.

Farchmin, Nando, Martin Hammerschmidt, Philipp-Immanuel Schneider, Matthias Wurm, Bernd Bodermann, Markus Bär, and Sebastian Heidenreich (May 2020). "Efficient Bayesian Inversion for Shape Reconstruction of Lithography Masks". In: *Journal of Micro/Nanolithography, MEMS, and MOEMS* 19.2, p. 024001. ISSN: 1932-5150, 1932-5134. DOI: 10.1117/1.JMM.19.2.024001.

Fermi, Enrico (1974). *Nuclear Physics*. In collab. with Jay Orear, Arthur H. Rosenfeld, and Robert Schluter. Midway Reprints. Chicago: University of Chicago Press. 258 pp. ISBN: 978-0-226-24365-8. URL: https://www.press.uchicago.edu/ucp/books/book/chicago/N/bo3631242.html.

Fernández Herrero, Analía, Mika Pflüger, Jürgen Probst, Frank Scholze, and Victor Soltwisch (Oct. 28, 2019). "Applicability of the Debye-Waller Damping Factor for the Determination of the Line-Edge Roughness of Lamellar Gratings". In: *Optics Express* 27.22, pp. 32490–32507. ISSN: 1094-4087. DOI: 10.1364/OE.27.032490.

Foreman-Mackey, Daniel, David W. Hogg, Dustin Lang, and Jonathan Goodman (Mar. 2013). "Emcee: The MCMC Hammer". In: *Publications of the Astronomical Society of the Pacific* 125.925, pp. 306–312. ISSN: 00046280, 15383873. DOI: 10.1086/670067. arXiv: 1202.3665.

Franklin, Rosalind E. and R. G. Gosling (Apr. 1953). "Molecular Configuration in Sodium Thymonucleate". In: *Nature* 171.4356, pp. 740–741. ISSN: 1476-4687. DOI: 10.1038/171740a0.

Friedrich, Walter, Paul Knipping, and Max Laue (1913). "Interferenzerscheinungen bei Röntgenstrahlen". In: *Annalen der Physik* 346.10, pp. 971–988. ISSN: 00033804, 15213889. DOI: 10.1002/andp.19133461004.

Fuchs, D., Michael Krumrey, Peter Müller, Frank Scholze, and Gerhard Ulm (Feb. 1, 1995). "High Precision Soft X-Ray Reflectometer". In: *Review of Scientific Instruments* 66.2, pp. 2248–2250. ISSN: 0034-6748, 1089-7623. DOI: 10.1063/1.1145720.

Glatter, O and O Kratky, eds. (1982). *Small Angle X-Ray Scattering*. London: Academic Press. ISBN: 0-12-286280-5. URL: https://web.archive.org/web/20080421213544/http://physchem.kfunigraz.ac.at/sm/Software.htm (visited on 10/11/2019).

Gleber, Gudrun, Levent Cibik, S. Haas, Arne Hoell, Peter Müller, and Michael Krumrey (Oct. 1, 2010). "Traceable Size Determination of PMMA Nanoparticles Based on Small Angle X-Ray Scattering (SAXS)". In: *Journal of Physics: Conference Series* 247, p. 012027. ISSN: 1742-6596. DOI: 10.1088/1742-6596/247/1/012027.

Gollmer, D. A., F. Walter, C. Lorch, J. Novák, R. Banerjee, J. Dieterle, G. Santoro, F. Schreiber, D. P. Kern, and M. Fleischer (May 1, 2014). "Fabrication and Characterization of Combined Metallic Nanogratings and ITO Electrodes for Organic Photovoltaic Cells". In: *Microelectronic Engineering*. Micro/Nano Devices and Systems 2013 119, pp. 122–126. ISSN: 0167-9317. DOI: 10.1016/j.mee.2014.03.042.

Goodman, Jonathan and Jonathan Weare (Jan. 31, 2010). "Ensemble Samplers with Affine Invariance". In: *Communications in Applied Mathematics and Computational Science* 5.1, pp. 65–80. ISSN: 2157-5452, 1559-3940. DOI: 10.2140/camcos.2010.5.65.

Gottwald, Alexander, Udo Kroth, Michael Krumrey, Mathias Richter, Frank Scholze, and Gerhard Ulm (Mar. 2006). "The PTB High-Accuracy Spectral Responsivity Scale in the VUV and x-Ray Range". In: *Metrologia* 43.2, S125–S129. ISSN: 0026-1394. DOI: 10.1088/0026-1394/43/2/S25.

Graafsma, Heinz and Thierry Martin (Mar. 20, 2008). "Detectors for Synchrotron Tomography". In: *Advanced Tomographic Methods in Materials Research and Engineering*. Ed. by John Banhart.

Oxford University Press, pp. 277–302. ISBN: 978-0-19-921324-5. DOI: 10.1093/acprof:oso/9780199213245.003.0010.

Green, Martin A. (Oct. 1, 2007). "Thin-Film Solar Cells: Review of Materials, Technologies and Commercial Status". In: *Journal of Materials Science: Materials in Electronics* 18.1, pp. 15–19. ISSN: 1573-482X. DOI: 10.1007/s10854-007-9177-9.

Gu, Yu, Cheng Wang, and Thomas P. Russell (June 1, 2012). "Multi-Length-Scale Morphologies in PCPDTBT/PCBM Bulk-Heterojunction Solar Cells". In: *Advanced Energy Materials* 2.6, pp. 683–690. ISSN: 1614-6840. DOI: 10.1002/aenm.201100726.

Haber, Fritz and G van Oordt (Jan. 1, 1905). "Über Die Bildung von Ammoniak Aus Den Elementen". In: *Zeitschrift für anorganische Chemie* 44.1, pp. 341–378. ISSN: 0863-1778. DOI: 10.1002/zaac.19050440122.

Hagihara, Kazuki, Rikiya Taniguchi, Eiji Yamanaka, Takashi Hirano, Kazuhiko Omote, Yoshiyasu Ito, Kiyoshi Ogata, and Naoya Hayashi (Apr. 19, 2019). "Throughput Improvement Method for Cross-Sectional Profile Measurement of Hole Patterns in Nanoimprint Templates". In: Photomask Technology 2018. Vol. 10810. SPIE, p. 1081010. DOI: 10.1117/12.2503252.

Hagihara, Kazuki, Rikiya Taniguchi, Eiji Yamanaka, Kazuhiko Omote, Yoshiyasu Ito, Kiyoshi Ogata, and Naoya Hayashi (Oct. 16, 2017). "The Capability of Measuring Cross-Sectional Profile for Hole Patterns in Nanoimprint Templates Using Small-Angle x-Ray Scattering". In: Photomask Technology. Vol. 10451. SPIE, 104510H. DOI: 10.1117/12.2284761.

Hamamatsu (Sept. 2014). "X-Ray Detectors". In: *Opto-Semiconductor Handbook*. Hamamatsu. URL: https://www.hamamatsu.com/sp/ssd/doc_en.html.

Hannon, Adam F., Daniel F. Sunday, Donald Windover, and R. Joseph Kline (2016). "Advancing X-Ray Scattering Metrology Using Inverse Genetic Algorithms". In: *Journal of Micro/Nanolithography, MEMS, and MOEMS* 15.3, pp. 034001–034001. ISSN: 1932-5150. DOI: 10.1117/1.JMM.15.3.034001.

Hastings, W. K. (Apr. 1, 1970). "Monte Carlo Sampling Methods Using Markov Chains and Their Applications". In: *Biometrika* 57.1, pp. 97–109. ISSN: 0006-3444. DOI: 10.1093/biomet/57.1.97.

Hazelton, Andrew J., Shinji Wakamoto, Shigeru Hirukawa, Martin McCallum, Nobutaka Magome, Jun Ishikawa, Céline Lapeyre, Isabelle Guilmeau, Sébastien Barnola, and Stéphanie Gaugiran (Jan. 1, 2009). "Double-Patterning Requirements for Optical Lithography and Prospects for Optical Extension without Double Patterning". In: *Journal of Micro/Nanolithography, MEMS, and MOEMS* 8.1, p. 011003. ISSN: 1932-5150. DOI: 10.1117/1.3023077.

Hemberg, O., M. Otendal, and H. M. Hertz (Aug. 12, 2003). "Liquid-Metal-Jet Anode Electron-Impact x-Ray Source". In: *Applied Physics Letters* 83.7, pp. 1483–1485. ISSN: 0003-6951. DOI: 10.1063/1.1602157.

Henke, B. L., E. M. Gullikson, and J. C. Davis (July 1993). "X-Ray Interactions: Photoabsorption, Scattering, Transmission, and Reflection at E=50-30000 eV, Z=1-92". In: *Atomic Data and Nuclear Data Tables* 254.2, pp. 181–342. DOI: 10.1006/adnd.1993.1013.

Hexemer, Alexander and Peter Müller-Buschbaum (Jan. 1, 2015). "Advanced Grazing-Incidence Techniques for Modern Soft-Matter Materials Analysis". In: *IUCrJ* 2.1, pp. 106–125. ISSN: 2052-2525. DOI: 10.1107/S2052252514024178.

Hlaing, Htay, Xinhui Lu, Tommy Hofmann, Kevin G. Yager, Charles T. Black, and Benjamin M. Ocko (Sept. 27, 2011). "Nanoimprint-Induced Molecular Orientation in Semiconducting Polymer Nanostructures". In: *ACS Nano* 5.9, pp. 7532–7538. ISSN: 1936-0851, 1936-086X. DOI: 10.1021/nn202515z.

Hofmann, Albert (2004). *The Physics of Synchrotron Radiation*. Cambridge Monographs of Particle Physics, Nuclear Physics, and Cosmology 20. Cambridge: Cambridge University Press. ISBN: 978-0-511-19416-0. DOI: 10.1017/CBO9780511534973.

Hofmann, Tommy, E. Dobisz, and Benjamin M. Ocko (2009). "Grazing Incident Small Angle X-Ray Scattering: A Metrology to Probe Nanopatterned Surfaces". In: *Journal of Vacuum Science &*

Technology B: Microelectronics and Nanometer Structures 27.6, p. 3238. ISSN: 10711023. DOI: 10.1116/1.3253608.

Holý, V. and T. Baumbach (Apr. 15, 1994). "Nonspecular X-Ray Reflection from Rough Multilayers". In: *Physical Review B* 49.15, pp. 10668–10676. DOI: 10.1103/PhysRevB.49.10668.

Holý, V., J. Kuběna, I. Ohlídal, K. Lischka, and W. Plotz (June 15, 1993). "X-Ray Reflection from Rough Layered Systems". In: *Physical Review B* 47.23, pp. 15896–15903. DOI: 10.1103/PhysRevB.47.15896.

HZB (2020a). *Free-Electron Lasers*. URL: https://www.helmholtz-berlin.de/forschung/oe/fg/mi-synchrotron-radiation/synchrotron/photons/x-ray-pulses/free-electron-lasers_en.html (visited on 06/07/2020).

HZB (2020b). *Zahlen und Fakten*. URL: https://www.helmholtz-berlin.de/forschung/quellen/bessy/bessy-in-zahlen_de.html (visited on 06/06/2020).

IUCr (June 7, 2018). *Quasicrystal - Online Dictionary of Crystallography*. URL: http://reference.iucr.org/dictionary/Quasicrystal (visited on 06/07/2018).

James, R. W. (1962). *The Optical Principles of the Diffraction of X-Rays*. Vol. 2. The Crystalline State. London: G. Bell and Sons Ltd. URL: https://archive.org/details/opticalprinciple031059mbp.

JCGM (Sept. 2008). *Guide to the Expression of Uncertainty in Measurement - JCGM 100:2008 (GUM 1995 with Minor Corrections)*. Bureau International des Poids et Mesures. URL: https://www.bipm.org/en/publications/guides/#gum (visited on 06/13/2019).

Jergel, M., P. Mikulík, E. Majková, Š Luby, R. Senderák, E. Pinčík, M. Brunel, P. Hudek, I. Kostič, and A. Konečníková (Jan. 15, 1999). "Structural Characterization of a Lamellar W/Si Multilayer Grating". In: *Journal of Applied Physics* 85.2, pp. 1225–1227. ISSN: 0021-8979, 1089-7550. DOI: 10.1063/1.369346.

Jiang, Zhang, Dong Ryeol Lee, Suresh Narayanan, Jin Wang, and Sunil K. Sinha (Aug. 2011). "Waveguide-Enhanced Grazing-Incidence Small-Angle x-Ray Scattering of Buried Nanostructures in Thin Films". In: *Physical Review B* 84.7, p. 075440. DOI: 10.1103/PhysRevB.84.075440.

Johnson, I., A. Bergamaschi, H. Billich, S. Cartier, R. Dinapoli, D. Greiffenberg, M. Guizar-Sicairos, B. Henrich, J. Jungmann, D. Mezza, A. Mozzanica, B. Schmitt, X. Shi, and G. Tinti (May 2014). "Eiger: A Single-Photon Counting x-Ray Detector". In: *Journal of Instrumentation* 9.05, pp. C05032–C05032. ISSN: 1748-0221. DOI: 10.1088/1748-0221/9/05/C05032.

Jones, Ronald L., Tengjiao Hu, Eric K. Lin, Wen-Li Wu, Rainer Kolb, Diego M. Casa, Patrick J. Bolton, and George G. Barclay (Nov. 3, 2003). "Small Angle X-Ray Scattering for Sub-100 Nm Pattern Characterization". In: *Applied Physics Letters* 83.19, pp. 4059–4061. ISSN: 0003-6951. DOI: 10.1063/1.1622793.

Jung, Woo-Yung, Choi-Dong Kim, Jae-Doo Eom, Sung-Yoon Cho, Sung-Min Jeon, Jong-Hoon Kim, Jae-In Moon, Byung-Seok Lee, and Sung-Ki Park (Mar. 10, 2006). "Patterning with Spacer for Expanding the Resolution Limit of Current Lithography Tool". In: SPIE 31st International Symposium on Advanced Lithography. San Jose, CA, 61561J. DOI: 10.1117/12.650991.

Kagalwala, Taher, Alok Vaid, Sridhar Mahendrakar, Michael Lenahan, Fang Fang, Paul Isbester, Michael Shifrin, Yoav Etzioni, Aron Cepler, Naren Yellai, Prasad Dasari, and Cornel Bozdog (Oct. 2016). "Measuring Self-Aligned Quadruple Patterning Pitch Walking with Scatterometry-Based Metrology Utilizing Virtual Reference". In: *Journal of Micro/Nanolithography, MEMS, and MOEMS* 15.4, p. 044004. ISSN: 1932-5150, 1932-5134. DOI: 10.1117/1.JMM.15.4.044004.

KETEK (Nov. 18, 2019). *VITUS H7 - Silicon Drift Detector (SDD)*. URL: https://www.ketek.net/sdd/vitus-sdd-modules/vitus-h7/ (visited on 11/18/2019).

Khaira, Gurdaman, Manolis Doxastakis, Alec Bowen, Jiaxing Ren, Hyo Seon Suh, Tamar Segal-Peretz, Xuanxuan Chen, Chun Zhou, Adam F. Hannon, Nicola J. Ferrier, Venkatram Vishwanath, Daniel F. Sunday, Roel Gronheid, R. Joseph Kline, Juan J. de Pablo, and Paul F. Nealey (Oct. 10, 2017). "Derivation of Multiple Covarying Material and Process Parameters

Using Physics-Based Modeling of X-Ray Data". In: *Macromolecules* 50.19, pp. 7783–7793. ISSN: 0024-9297. DOI: 10.1021/acs.macromol.7b00691.

Khan, Hassan N., David A. Hounshell, and Erica R. H. Fuchs (Jan. 2018). "Science and Research Policy at the End of Moore' s Law". In: *Nature Electronics* 1.1, pp. 14–21. ISSN: 2520-1131. DOI: 10.1038/s41928-017-0005-9.

Kim, Kwang-Je (May 15, 1986). "Angular Distribution of Undulator Power for an Arbitrary Deflection Parameter K". In: *Nuclear Instruments and Methods in Physics Research Section A: Accelerators, Spectrometers, Detectors and Associated Equipment* 246.1, pp. 67–70. ISSN: 0168-9002. DOI: 10.1016/0168-9002(86)90047-1.

Kincaid, Brian M. (July 1, 1977). "A Short ‐ period Helical Wiggler as an Improved Source of Synchrotron Radiation". In: *Journal of Applied Physics* 48.7, pp. 2684–2691. ISSN: 0021-8979. DOI: 10.1063/1.324138.

Kissel, Lynn, R. H. Pratt, and S. C. Roy (Nov. 1, 1980). "Rayleigh Scattering by Neutral Atoms, 100 eV to 10 MeV". In: *Physical Review A* 22.5, pp. 1970–2004. DOI: 10.1103/PhysRevA.22.1970.

Klein, Roman, Guido Brandt, Rolf Fliegauf, Arne Hoehl, Ralph Müller, Reiner Thornagel, Gerhard Ulm, Michael Abo-Bakr, Jörg Feikes, Michael v. Hartrott, Karsten Holldack, and Godehard Wüstefeld (Nov. 20, 2008). "Operation of the Metrology Light Source as a Primary Radiation Source Standard". In: *Physical Review Special Topics - Accelerators and Beams* 11.11, p. 110701. DOI: 10.1103/PhysRevSTAB.11.110701.

Knoll, M. and E. Ruska (May 1, 1932). "Das Elektronenmikroskop". In: *Zeitschrift für Physik* 78.5, pp. 318–339. ISSN: 0044-3328. DOI: 10.1007/BF01342199.

Koch, Michel H. J., Patrice Vachette, and Dmitri I. Svergun (May 2003). "Small-Angle Scattering: A View on the Properties, Structures and Structural Changes of Biological Macromolecules in Solution". In: *Quarterly Reviews of Biophysics* 36.2, pp. 147–227. ISSN: 1469-8994, 0033-5835. DOI: 10.1017/S0033583503003871.

Krishnamurti, P. (1930). "Studies in X-Ray Diffraction : Part II - Some Colloidal Solutions and Liquid Mixtures". In: *Indian Journal of physics* 5, p. 489. ISSN: 0973-1458. URL: http://hdl.handle.net/10821/573.

Krumrey, Michael, Erich Tegeler, Jochen Barth, Michael Krisch, Franz Schäfers, and Reinhard Wolf (Oct. 15, 1988). "Schottky Type Photodiodes as Detectors in the VUV and Soft X-Ray Range". In: *Applied Optics* 27.20, pp. 4336–4341. ISSN: 2155-3165. DOI: 10.1364/AO.27.004336.

Krumrey, Michael and Gerhard Ulm (2001). "High-Accuracy Detector Calibration at the PTB Four-Crystal Monochromator Beamline". In: *Nuclear Instruments and Methods in Physics Research Section A: Accelerators, Spectrometers, Detectors and Associated Equipment* 467, pp. 1175–1178. DOI: 10.1016/S0168-9002(01)00598-8.

Kumar, N., K. Kennedy, K. Gildersleeve, R. Abelson, C. M. Mastrangelo, and D. C. Montgomery (Dec. 2006). "A Review of Yield Modelling Techniques for Semiconductor Manufacturing". In: *International Journal of Production Research* 44.23, pp. 5019–5036. ISSN: 0020-7543, 1366-588X. DOI: 10.1080/00207540600596874.

Kuske, P., M. Abo-Bakr, W. Anders, T. Birke, K. B. Buerkmann-Gehrlein, M. Dirsat, O. Dressler, V. Duerr, F. Falkenstern, W. Gericke, R. Goergen, F. Hoffmann, T. Kamps, and J. Kuszynski (2008). "Preparations of BESSY for Top Up Operation". In: EPAC08. Genoa, Italy, p. 3. URL: http://accelconf.web.cern.ch/e08/papers/wepc037.pdf.

Lairson, B. M., A. P. Payne, S. Brennan, N. M. Rensing, B. J. Daniels, and B. M. Clemens (Oct. 1, 1995). "In Situ X ‐ ray Measurements of the Initial Epitaxy of Fe(001) Films on MgO(001)". In: *Journal of Applied Physics* 78.7, pp. 4449–4455. ISSN: 0021-8979. DOI: 10.1063/1.359853.

Lam, Siu Kwan, Antoine Pitrou, and Stanley Seibert (2015). "Numba: A LLVM-Based Python JIT Compiler". In: *Proceedings of the Second Workshop on the LLVM Compiler Infrastructure in HPC*. LLVM '15. New York, NY, USA: ACM, 7:1–7:6. ISBN: 978-1-4503-4005-2. DOI: 10.1145/2833157.2833162.

Lane, Nick (Apr. 19, 2015). "The Unseen World: Reflections on Leeuwenhoek (1677) 'Concerning Little Animals' ". In: *Philosophical Transactions of the Royal Society B: Biological Sciences* 370.1666, p. 20140344. DOI: 10.1098/rstb.2014.0344.

Larmor, J. (Dec. 1897). "On the Theory of the Magnetic Influence on Spectra; and on the Radiation from Moving Ions". In: *The London, Edinburgh, and Dublin Philosophical Magazine and Journal of Science* 44.271, pp. 503–512. ISSN: 1941-5982, 1941-5990. DOI: 10.1080/14786449708621095.

Lazzari, Rémi (Aug. 1, 2002). "IsGISAXS: A Program for Grazing-Incidence Small-Angle X-Ray Scattering Analysis of Supported Islands". In: *Journal of Applied Crystallography* 35.4, pp. 406–421. ISSN: 0021-8898. DOI: 10.1107/S0021889802006088.

Lee, Byeongdu, Insun Park, Jinhwan Yoon, Soojin Park, Jehan Kim, Kwang-Woo Kim, Taihyun Chang, and Moonhor Ree (May 2005). "Structural Analysis of Block Copolymer Thin Films with Grazing Incidence Small-Angle X-Ray Scattering". In: *Macromolecules* 38.10, pp. 4311–4323. ISSN: 0024-9297, 1520-5835. DOI: 10.1021/ma047562d.

Leeuwenhoek, Antoni Van (Mar. 25, 1677). "Observations, Communicated to the Publisher by Mr. Antony van Leewenhoeck, in a Dutch Letter of the 9th Octob. 1676. Here English'd: Concerning Little Animals by Him Observed in Rain-Well-Sea- and Snow Water; as Also in Water Wherein Pepper Had Lain Infused". In: *Philosophical Transactions of the Royal Society of London* 12.133, pp. 821–831. DOI: 10.1098/rstl.1677.0003.

Levine, J. R., J. B. Cohen, Y. W. Chung, and P. Georgopoulos (Dec. 1, 1989). "Grazing-Incidence Small-Angle X-Ray Scattering: New Tool for Studying Thin Film Growth". In: *Journal of Applied Crystallography* 22.6, pp. 528–532. ISSN: 00218898. DOI: 10.1107/S002188988900717X.

Lim, Chang-Moon, Seo-Min Kim, Young-Sun Hwang, Jae-Seung Choi, Keun-Do Ban, Sung-Yoon Cho, Jin-Ki Jung, Eung-Kil Kang, Hee-Youl Lim, Hyeong-Soo Kim, and Seung-Chan Moon (Mar. 10, 2006). "Positive and Negative Tone Double Patterning Lithography for 50nm Flash Memory". In: SPIE 31st International Symposium on Advanced Lithography. Ed. by Donis G. Flagello. San Jose, CA, p. 615410. DOI: 10.1117/12.656187.

Mack, Chris (May 2011). "Fifty Years of Moore's Law". In: *IEEE Transactions on Semiconductor Manufacturing* 24.2, pp. 202–207. DOI: 10.1109/TSM.2010.2096437.

MacKay, David J. C. (Mar. 28, 2005). *Information Theory, Inference and Learning Algorithms*. 5th ed. Cambridge: Cambridge University Press. 694 pp. ISBN: 978-0-521-64298-9. URL: https://www.inference.org.uk/itila/.

Martin, J. E., N. P. Fox, and P. J. Key (Jan. 1985). "A Cryogenic Radiometer for Absolute Radiometric Measurements". In: *Metrologia* 21.3, pp. 147–155. ISSN: 0026-1394. DOI: 10.1088/0026-1394/21/3/007.

marXperts (Nov. 18, 2019). *marXperts - SX-165 CCD Detector*. URL: https://www.marxperts.com/products/x-ray-detectors/sx-165 (visited on 11/18/2019).

Meier, Robert, Hsin-Yin Chiang, Matthias A. Ruderer, Shuai Guo, Volker Körstgens, Jan Perlich, and Peter Müller-Buschbaum (May 1, 2012). "In Situ Film Characterization of Thermally Treated Microstructured Conducting Polymer Films". In: *Journal of Polymer Science Part B: Polymer Physics* 50.9, pp. 631–641. ISSN: 1099-0488. DOI: 10.1002/polb.23048.

Meitner, Lise (Dec. 1, 1922). "Über die Entstehung der β -Strahl-Spektren radioaktiver Substanzen". In: *Zeitschrift für Physik* 9.1, pp. 131–144. ISSN: 0044-3328. DOI: 10.1007/BF01326962.

Meschede, Dieter (2015a). "Die Elemente und die Chemie". In: *Gerthsen Physik*. Springer-Lehrbuch. Berlin, Heidelberg: Springer Berlin Heidelberg, pp. 819–852. ISBN: 978-3-662-45977-5. DOI: 10.1007/978-3-662-45977-5_18.

Meschede, Dieter (2015b). "Elektrodynamik". In: *Gerthsen Physik*. Springer-Lehrbuch. Berlin, Heidelberg: Springer Berlin Heidelberg, pp. 391–459. ISBN: 978-3-662-45977-5. DOI: 10.1007/978-3-662-45977-5_9.

Meschede, Dieter (2015c). "Festkörperphysik". In: *Gerthsen Physik*. Springer-Lehrbuch. Berlin, Heidelberg: Springer Berlin Heidelberg, pp. 853–926. ISBN: 978-3-662-45977-5. DOI: 10.1007/978-3-662-45977-5_19.

Meschede, Dieter (2015d). "Physik der Atome und ihre Anwendungen". In: *Gerthsen Physik*. Springer-Lehrbuch. Berlin, Heidelberg: Springer Berlin Heidelberg, pp. 715–792. ISBN: 978-3-662-45977-5. DOI: 10.1007/978-3-662-45977-5_16.

Meschede, Dieter (2015e). "Strahlungsfelder". In: *Gerthsen Physik*. Springer-Lehrbuch. Berlin, Heidelberg: Springer Berlin Heidelberg, pp. 585–615. ISBN: 978-3-662-45977-5. DOI: 10.1007/978-3-662-45977-5_13.

Metropolis, Nicholas, Arianna W. Rosenbluth, Marshall N. Rosenbluth, Augusta H. Teller, and Edward Teller (June 1, 1953). "Equation of State Calculations by Fast Computing Machines". In: *The Journal of Chemical Physics* 21.6, pp. 1087–1092. ISSN: 0021-9606. DOI: 10.1063/1.1699114.

Metzger, T. H., K. Haj-Yahya, J. Peisl, M. Wendel, H. Lorenz, J. P. Kotthaus, and G. S. Cargill Iii (Feb. 1, 1997). "Nanometer Surface Gratings on Si(100) Characterized by x-Ray Scattering under Grazing Incidence and Atomic Force Microscopy". In: *Journal of Applied Physics* 81.3, pp. 1212–1216. ISSN: 0021-8979, 1089-7550. DOI: 10.1063/1.363864.

Mikulík, Petr and T. Baumbach (Mar. 15, 1999). "X-Ray Reflection by Rough Multilayer Gratings: Dynamical and Kinematical Scattering". In: *Physical Review B* 59.11, pp. 7632–7643. DOI: 10.1103/PhysRevB.59.7632.

Mikulík, Petr, M. Jergel, T. Baumbach, E. Majková, E. Pincik, S. Luby, L. Ortega, R. Tucoulou, P. Hudek, and I. Kostic (2001). "Coplanar and Non-Coplanar x-Ray Reflectivity Characterization of Lateral W/Si Multilayer Gratings". In: *Journal of Physics D: Applied Physics* 34 (10A), A188. DOI: 10.1088/0022-3727/34/10A/339.

Millman, K. J. and M. Aivazis (Mar. 2011). "Python for Scientists and Engineers". In: *Computing in Science Engineering* 13.2, pp. 9–12. ISSN: 1521-9615. DOI: 10.1109/MCSE.2011.36.

Minato, Osamu, Toshiaki Masuhara, Toshio Sasaki, Yoshio Sakai, Tetsuya Hayashida, Kouichi Nagasawa, Kotaro Nishimura, and Tokumasa Yasui (Oct. 1982). "A Hi-CMOSll 8K x 8 Bit Static RAM". In: *IEEE Journal of Solid-State Circuits* SC-17.5, pp. 793–798. DOI: 10.1109/JSSC.1982.1051820.

Mittasch, Alwin and Carl Bosch (Dec. 3, 1912). "Verfahren Zur Herstellung von Ammoniak Aus Seinen Elementen Mit Hilfe von Katalysatoren". German pat. 254437. URL: https://worldwide.espacenet.com/publicationDetails/biblio?CC=DE&NR=254437C&KC=C# (visited on 09/25/2019).

Mochalin, Vadym N., Olga Shenderova, Dean Ho, and Yury Gogotsi (Jan. 2012). "The Properties and Applications of Nanodiamonds". In: *Nature Nanotechnology* 7.1, pp. 11–23. ISSN: 1748-3395. DOI: 10.1038/nnano.2011.209.

Monk, Peter and Yangwen Zhang (Oct. 22, 2019). "Finite Element Methods for Maxwell's Equations". In: arXiv: 1910.10069 [cs, math]. URL: http://arxiv.org/abs/1910.10069 (visited on 05/06/2020).

Moore, Gordon Earle (1965). "Cramming More Components Onto Integrated Circuits". In: *Electronics* 38.8, pp. 114–117. DOI: 10.1109/JPROC.1998.658762.

Moore, Samuel K. (June 2019). "Another Step toward the End of Moore's Law: Samsung and TSMC Move to 5-Nanometer Manufacturing - [News]". In: *IEEE Spectrum* 56.6, pp. 9–10. ISSN: 1939-9340. DOI: 10.1109/MSPEC.2019.8727133.

Müller, R., T. Birke, F. Falkenstern, K. Holldack, P. Kuske, A Schälicke, and D. Schüler (2016). "BESSY II Supports an Extensive Suite of Timing Experiments". In: IPAC 2016. Busan, Korea, p. 4. DOI: 10.18429/JACoW-IPAC2016-WEPOW011.

Müller-Buschbaum, Peter (2003). "Grazing Incidence Small-Angle X-Ray Scattering: An Advanced Scattering Technique for the Investigation of Nanostructured Polymer Films". In: *Analytical and bioanalytical chemistry* 376.1, pp. 3–10. DOI: 10.1007/s00216-003-1869-2.

Müller-Buschbaum, Peter (2009). "A Basic Introduction to Grazing Incidence Small-Angle X-Ray Scattering". In: *Applications of Synchrotron Light to Scattering and Diffraction in Materials and Life Sciences*. Ed. by Marian Gomez, Aurora Nogales, Mari Cruz Garcia-Gutierrez, and T. A. Ezquerra. Lecture Notes in Physics 776. Springer Berlin Heidelberg, pp. 61–89. ISBN: 978-3-540-95967-0. DOI: 10.1007/978-3-540-95968-7_3.

Müller-Buschbaum, Peter (Dec. 2014). "The Active Layer Morphology of Organic Solar Cells Probed with Grazing Incidence Scattering Techniques". In: *Advanced Materials* 26.46, pp. 7692–7709. ISSN: 09359648. DOI: 10.1002/adma.201304187.

Natarajan, S., M. Agostinelli, S. Akbar, M. Bost, A. Bowonder, V. Chikarmane, S. Chouksey, A. Dasgupta, K. Fischer, Q. Fu, T. Ghani, M. Giles, S. Govindaraju, R. Grover, W. Han, D. Hanken, E. Haralson, M. Haran, M. Heckscher, R. Heussner, P. Jain, R. James, R. Jhaveri, I. Jin, H. Kam, E. Karl, C. Kenyon, M. Liu, Y. Luo, R. Mehandru, S. Morarka, L. Neiberg, P. Packan, A. Paliwal, C. Parker, P. Patel, R. Patel, C. Pelto, L. Pipes, P. Plekhanov, M. Prince, S. Rajamani, J. Sandford, B. Sell, S. Sivakumar, P. Smith, B. Song, K. Tone, T. Troeger, J. Wiedemer, M. Yang, and K. Zhang (Dec. 15, 2014). "A 14nm Logic Technology Featuring 2nd-Generation FinFET, Air-Gapped Interconnects, Self-Aligned Double Patterning and a 0.0588μm² SRAM Cell Size". In: 2014 IEEE International Electron Devices Meeting. San Francisco, CA, USA, p. 3. ISBN: 978-1-4799-8001-7. DOI: 10.1109/IEDM.2014.7046976.

Nedelec, J. C. (Sept. 1, 1980). "Mixed Finite Elements in R^3". In: *Numerische Mathematik* 35.3, pp. 315–341. ISSN: 0945-3245. DOI: 10.1007/BF01396415.

Nikolaev, Konstantin V., Victor Soltwisch, Philipp Hönicke, Frank Scholze, J. de la Rie, S. N. Yakunin, I. A. Makhotkin, R. W. E. van de Kruijs, and F. Bijkerk (Mar. 1, 2020). "A Semi-Analytical Approach for the Characterization of Ordered 3D Nanostructures Using Grazing-Incidence X-Ray Fluorescence". In: *Journal of Synchrotron Radiation* 27.2 (2), pp. 386–395. ISSN: 1600-5775. DOI: 10.1107/S1600577519016345.

Novikova, Tatiana, Antonello De Martino, Sami Ben Hatit, and Bernard Drévillon (June 1, 2006). "Application of Mueller Polarimetry in Conical Diffraction for Critical Dimension Measurements in Microelectronics". In: *Applied Optics* 45.16, p. 3688. ISSN: 0003-6935, 1539-4522. DOI: 10.1364/AO.45.003688.

Noyce, Robert N. (Apr. 25, 1961). "Semiconductor Device-and-Lead Structure". U.S. pat. 2981877A. Fairchild Semiconductor Corp. URL: https://patents.google.com/patent/US2981877A/en (visited on 01/30/2020).

Orji, N. G., M. Badaroglu, B. M. Barnes, C. Beitia, Benjamin Bunday, U. Celano, R. Joseph Kline, M. Neisser, Y. Obeng, and A. E. Vladar (Oct. 2018). "Metrology for the next Generation of Semiconductor Devices". In: *Nature Electronics* 1.10, pp. 532–547. ISSN: 2520-1131. DOI: 10.1038/s41928-018-0150-9.

Pflüger, Mika, R. Joseph Kline, Analía Fernández Herrero, Martin Hammerschmidt, Victor Soltwisch, and Michael Krumrey (Jan. 28, 2020). "Extracting Dimensional Parameters of Gratings Produced with Self-Aligned Multiple Patterning Using Grazing-Incidence Small-Angle x-Ray Scattering". In: *Journal of Micro/Nanolithography, MEMS, and MOEMS* 19.01, p. 1. ISSN: 1932-5150. DOI: 10.1117/1.JMM.19.1.014001.

Pflüger, Mika, Victor Soltwisch, Jürgen Probst, Frank Scholze, and Michael Krumrey (July 1, 2017). "Grazing-Incidence Small-Angle X-Ray Scattering (GISAXS) on Small Periodic Targets Using Large Beams". In: *IUCrJ* 4.4, pp. 431–438. ISSN: 2052-2525. DOI: 10.1107/S2052252517006297.

Pflüger, Mika, Victor Soltwisch, Frank Scholze, and Michael Krumrey (Oct. 16, 2017). "Selective Measurement of Small Metrology Targets Using CD-GISAXS". In: Photomask Technology. Vol. 10451. SPIE, p. 1045110. DOI: 10.1117/12.2280455.

Pflüger, Mika, Victor Soltwisch, Jolly Xavier, Jürgen Probst, Frank Scholze, Christiane Becker, and Michael Krumrey (Apr. 1, 2019). "Distortion Analysis of Crystalline and Locally Quasicrys-

talline 2D Photonic Structures with Grazing-Incidence Small-Angle X-Ray Scattering". In: *Journal of Applied Crystallography* 52.2. ISSN: 1600-5767. DOI: 10.1107/S1600576719001080.

Planck, Max (1900). "Zur Theorie Des Gesetzes Der Energieverteilung Im Normalspectrum". In: *Physikalische Blätter* 4.4. Nachdruck 1948, pp. 146–151. ISSN: 1521-3722. DOI: 10.1002/phbl.19480040404.

Pomplun, Jan, Sven Burger, Lin Zschiedrich, and Frank Schmidt (2007). "Adaptive Finite Element Method for Simulation of Optical Nano Structures". In: *physica status solidi (b)* 244.10, pp. 3419–3434. ISSN: 1521-3951. DOI: 10.1002/pssb.200743192.

Popov, Evgeny, ed. (2014). *Gratings: Theory and Numeric Applications, Second Revisited Edition*. ISBN: 978-2-85399-943-4. URL: http://www.fresnel.fr/numerical-grating-book-2.

Priolo, Francesco, Matteo Galli, Thomas F. Krauss, and Tom Gregorkiewicz (Jan. 2014). "Silicon Nanostructures for Photonics and Photovoltaics". In: *Nature Nanotechnology* 9.1, p. 19. ISSN: 1748-3395. DOI: 10.1038/nnano.2013.271.

Pröller, Stephan, Feng Liu, Chenhui Zhu, Cheng Wang, Thomas P. Russell, Alexander Hexemer, Peter Müller-Buschbaum, and Eva M. Herzig (Jan. 1, 2016). "Following the Morphology Formation In Situ in Printed Active Layers for Organic Solar Cells". In: *Advanced Energy Materials* 6.1, n/a–n/a. ISSN: 1614-6840. DOI: 10.1002/aenm.201501580.

Quaschning, Volker (2010). *Renewable Energy and Climate Change*. Trans. by Hedy Jourdan. Chichester: John Wiley & Sons, Ltd. ISBN: 978-0-470-74707-0. URL: https://www.volker-quaschning.de/publis/klimaschutz_e/index_e.php.

Rabus, H., V. Persch, and Gerhard Ulm (Aug. 1, 1997). "Synchrotron-Radiation-Operated Cryogenic Electrical-Substitution Radiometer as the High-Accuracy Primary Detector Standard in the Ultraviolet, Vacuum-Ultraviolet, and Soft-x-Ray Spectral Ranges". In: *Applied Optics* 36.22, pp. 5421–5440. ISSN: 2155-3165. DOI: 10.1364/AO.36.005421.

Rauscher, M., T. Salditt, and H. Spohn (Dec. 15, 1995). "Small-Angle x-Ray Scattering under Grazing Incidence: The Cross Section in the Distorted-Wave Born Approximation". In: *Physical Review B* 52.23, pp. 16855–16863. ISSN: 0163-1829, 1095-3795. DOI: 10.1103/PhysRevB.52.16855.

Renaud, Gilles, M Ducruet, Olivier Ulrich, and Rémi Lazzari (Aug. 2004). "Apparatus for Real Time in Situ Quantitative Studies of Growing Nanoparticles by Grazing Incidence Small Angle X-Ray Scattering and Surface Differential Reflectance Spectroscopy". In: *Nuclear Instruments and Methods in Physics Research Section B: Beam Interactions with Materials and Atoms* 222.3-4, pp. 667–680. ISSN: 0168583X. DOI: 10.1016/j.nimb.2004.04.158.

Renaud, Gilles, Rémi Lazzari, and Frédéric Leroy (Aug. 2009). "Probing Surface and Interface Morphology with Grazing Incidence Small Angle X-Ray Scattering". In: *Surface Science Reports* 64.8, pp. 255–380. ISSN: 01675729. DOI: 10.1016/j.surfrep.2009.07.002.

Renaud, Gilles, Rémi Lazzari, Christine Revenant, Antoine Barbier, Marion Noblet, Olivier Ulrich, Frédéric Leroy, Jacques Jupille, Yves Borensztein, Claude R. Henry, Jean-Paul Deville, Fabrice Scheurer, Jeannot Mane-Mane, and Olivier Fruchart (May 30, 2003). "Real-Time Monitoring of Growing Nanoparticles". In: *Science* 300.5624, pp. 1416–1419. ISSN: 0036-8075, 1095-9203. DOI: 10.1126/science.1082146. pmid: 12775836.

Richter, Mathias and Gerhard Ulm (2019). "Metrology with Synchrotron Radiation". In: *Synchrotron Light Sources and Free-Electron Lasers: Accelerator Physics, Instrumentation and Science Applications*. Ed. by Eberhard Jaeschke, Shaukat Khan, Jochen R. Schneider, and Jerome B. Hastings. Cham: Springer International Publishing, pp. 1–35. ISBN: 978-3-319-04507-8. DOI: 10.1007/978-3-319-04507-8_63-1.

Richtmyer, F. K. (July 1, 1921). "The Laws of Absorption of X-Rays." In: *Physical Review* 18.1, pp. 13–30. ISSN: 0031-899X. DOI: 10.1103/PhysRev.18.13.

Röntgen, Wilhelm Conrad (1895). "Ueber Eine Neue Art von Strahlen (Vorläufige Mittheilung.)" In: *Aus Den Sitzungsberichten Der Würzburger Physik.-Medic. Gesellschaft*. Würzburg: Verlag der Stahel' schen k. Hof- u. Univers.-Buch- u. Kunsthandlung in Würzburg. URL: https:

//de.wikisource.org/wiki/Ueber_eine_neue_Art_von_Strahlen_%28Vorl%C3%A4ufige_Mittheilung%29 (visited on 11/08/2019).

Röntgen, Wilhelm Conrad (1898). "Ueber Eine Neue Art von Strahlen". In: *Annalen der Physik* 300.1, pp. 1–11. ISSN: 1521-3889. DOI: 10.1002/andp.18983000102.

Rossander, Lea H., Natalia K. Zawacka, Henrik F. Dam, Frederik C. Krebs, and Jens W. Andreasen (Aug. 1, 2014). "In Situ Monitoring of Structure Formation in the Active Layer of Polymer Solar Cells during Roll-to-Roll Coating". In: *AIP Advances* 4.8, p. 087105. ISSN: 2158-3226. DOI: 10.1063/1.4892526.

Roth, Stephan V., T. Autenrieth, G. Grübel, C. Riekel, M. Burghammer, R. Hengstler, L. Schulz, and Peter Müller-Buschbaum (Aug. 27, 2007). "In Situ Observation of Nanoparticle Ordering at the Air-Water-Substrate Boundary in Colloidal Solutions Using x-Ray Nanobeams". In: *Applied Physics Letters* 91.9, p. 091915. ISSN: 0003-6951. DOI: 10.1063/1.2776850.

Rueda, D. R., I. Martín-Fabiani, M. Soccio, N. Alayo, F. Pérez-Murano, E. Rebollar, M. C. García-Gutiérrez, M. Castillejo, and T. A. Ezquerra (Oct. 1, 2012). "Grazing-Incidence Small-Angle X-Ray Scattering of Soft and Hard Nanofabricated Gratings". In: *Journal of Applied Crystallography* 45.5, pp. 1038–1045. ISSN: 0021-8898, 1600-5767. DOI: 10.1107/S0021889812030415.

Sasaki, Shigemi, Kazunori Kakuno, Takeo Takada, Taihei Shimada, Ken-ichi Yanagida, and Yoshikazu Miyahara (July 1, 1993). "Design of a New Type of Planar Undulator for Generating Variably Polarized Radiation". In: *Nuclear Instruments and Methods in Physics Research Section A: Accelerators, Spectrometers, Detectors and Associated Equipment* 331.1, pp. 763–767. ISSN: 0168-9002. DOI: 10.1016/0168-9002(93)90153-9.

Schmüser, Peter, Martin Dohlus, Jörg Rossbach, and Christopher Behrens (2014). *Free-Electron Lasers in the Ultraviolet and X-Ray Regime*. Vol. 258. Springer Tracts in Modern Physics. Cham: Springer International Publishing. ISBN: 978-3-319-04081-3. DOI: 10.1007/978-3-319-04081-3.

Schneidmiller, E A and M V Yurkov (Sept. 2011). *Photon Beam Properties at the European XFEL (December 2010 Revision)*. XFEL.EU TR-2011-006. Hamburg: Deutsches Elektronen-Synchrotron (DESY), p. 127. URL: https://docs.xfel.eu/alfresco/d/a/workspace/SpacesStore/32150a06-3b16-4c44-8ea5-b1741220cdc2/TR-2011-006_Photon_Beam_Properties.pdf (visited on 11/04/2019).

Schor, David (2020). *Process Technology History - Intel*. URL: https://en.wikichip.org/wiki/intel/process (visited on 01/30/2020).

Schwinger, Julian (Sept. 19, 1946). "Electron Radiation in High Energy Accelerators". In: *Physical Review*. Minutes of the Meeting of the American Physical Society of September 19-21, 1946. Vol. 70. New York, pp. 784–800. DOI: 10.1103/PhysRev.70.784.2.

Schwinger, Julian (June 15, 1949). "On the Classical Radiation of Accelerated Electrons". In: *Physical Review* 75.12, pp. 1912–1925. DOI: 10.1103/PhysRev.75.1912.

Senn, T., J. Bischoff, N. Nüsse, M. Schoengen, and B. Löchel (July 2011). "Fabrication of Photonic Crystals for Applications in the Visible Range by Nanoimprint Lithography". In: *Photonics and Nanostructures - Fundamentals and Applications* 9.3, pp. 248–254. ISSN: 1569-4410. DOI: 10.1016/j.photonics.2011.04.007.

Seo, K. -I., B. Haran, D. Gupta, D. Guo, T. Standaert, R. Xie, H. Shang, E. Alptekin, D. -I. Bae, G. Bae, C. Boye, H. Cai, D. Chanemougame, R. Chao, K. Cheng, J. Cho, K. Choi, B. Hamieh, J. G. Hong, T. Hook, L. Jang, J. Jung, R. Jung, D. Lee, B. Lherron, R. Kambhampati, B. Kim, H. Kim, K. Kim, T. S. Kim, S.-B. Ko, F. L. Lie, D. Liu, H. Mallela, E. Mclellan, S. Mehta, P. Montanini, M. Mottura, J. Nam, S. Nam, F. Nelson, I. Ok, C. Park, Y. Park, A. Paul, C. Prindle, R. Ramachandran, M. Sankarapandian, V. Sardesai, A. Scholze, S. -C Seo, J. Shearer, R. Southwick, R. Sreenivasan, S. Stieg, J. Strane, X. Sun, M. G. Sung, C. Surisetty, G. Tsutsui, N. Tripathi, R. Vega, C. Waskiewicz, M. Weybright, C.-C. Yeh, H. Bu, S. Burns, D. Canaperi, M. Celik, M. Colburn, H. Jagannathan, S. Kanakasabaphthy, W. Kleemeier, L. Liebmann, D. Mcherron, P. Oldiges, V. Paruchuri, T. Spooner, J. Stathis, R. Divakaruni, T. Gow, J. Iacoponi, J. Jenq,

R. Sampson, and M. Khare (June 2014). "A 10nm Platform Technology for Low Power and High Performance Application Featuring FINFET Devices with Multi Workfunction Gate Stack on Bulk and SOI". In: 2014 IEEE Symposium on VLSI Technology. Honolulu, HI, USA: IEEE, pp. 1–2. DOI: 10.1109/VLSIT.2014.6894342.

Shechtman, D., I. Blech, D. Gratias, and J. W. Cahn (Nov. 12, 1984). "Metallic Phase with Long-Range Orientational Order and No Translational Symmetry". In: *Physical Review Letters* 53.20, pp. 1951–1953. DOI: 10.1103/PhysRevLett.53.1951.

Sinha, S. K., E. B. Sirota, S. Garoff, and H. B. Stanley (Aug. 1, 1988). "X-Ray and Neutron Scattering from Rough Surfaces". In: *Physical Review B* 38.4, pp. 2297–2311. DOI: 10.1103/PhysRevB.38.2297.

Sinkó, Katalin, Viktoria Torma, and Attila Kovács (Dec. 2008). "SAXS Investigation of Porous Nanostructures". In: *Journal of Non-Crystalline Solids* 354.52-54, pp. 5466–5474. ISSN: 00223093. DOI: 10.1016/j.jnoncrysol.2008.08.021.

Skroblin, Dieter, Alexander Schavkan, Mika Pflüger, Nicolas Pilet, Benjamin Lüthi, and Michael Krumrey (Feb. 1, 2020). "Vacuum-Compatible Photon-Counting Hybrid Pixel Detector for Wide-Angle x-Ray Scattering, x-Ray Diffraction, and x-Ray Reflectometry in the Tender x-Ray Range". In: *Review of Scientific Instruments* 91.2, p. 023102. ISSN: 0034-6748. DOI: 10.1063/1.5128487.

Soccio, M., D. R. Rueda, M. C. García-Gutiérrez, N. Alayo, F. Pérez-Murano, N. Lotti, A. Munari, and T. A. Ezquerra (Mar. 20, 2015). "Morphology of Poly(Propylene Azelate) Gratings Prepared by Nanoimprint Lithography as Revealed by Atomic Force Microscopy and Grazing Incidence X-Ray Scattering". In: *Polymer* 61, pp. 61–67. ISSN: 0032-3861. DOI: 10.1016/j.polymer.2015.01.066.

Soltwisch, Victor, Analía Fernández Herrero, Mika Pflüger, Anton Haase, Jürgen Probst, Christian Laubis, Michael Krumrey, and Frank Scholze (Oct. 1, 2017). "Reconstructing Detailed Line Profiles of Lamellar Gratings from GISAXS Patterns with a Maxwell Solver". In: *Journal of Applied Crystallography* 50.5, pp. 1524–1532. ISSN: 1600-5767. DOI: 10.1107/S1600576717012742.

Soltwisch, Victor and Mika Pflüger (Mar. 1, 2018). "Verfahren Zur Qualitätssicherung Einer Belichtungsmaske, Substrat Und Belichtungsmaske". Pat. 10 2017 100 273.1 (Deutschland). Bundesrepublik Deutschland, vertreten durch das Bundesministerium für Wirtschaft und Energie, dieses vertreten durch den Präsidenten der Physikalisch-Technischen Bundesanstalt. URL: https://register.dpma.de/DPMAregister/pat/register?AKZ=1020171002731.

Storn, Rainer and Kenneth Price (Dec. 1, 1997). "Differential Evolution – A Simple and Efficient Heuristic for Global Optimization over Continuous Spaces". In: *Journal of Global Optimization* 11.4, pp. 341–359. ISSN: 0925-5001, 1573-2916. DOI: 10.1023/A:1008202821328.

Stribeck, Norbert (2007). *X-Ray Scattering of Soft Matter*. Springer Laboratory. Berlin, Heidelberg: Springer Berlin Heidelberg. ISBN: 978-3-540-69855-5. URL: http://link.springer.com/10.1007/978-3-540-69856-2 (visited on 11/04/2014).

Strutt, J.W. (Feb. 1871). "On the Light from the Sky, Its Polarization and Colour". In: *The London, Edinburgh, and Dublin Philosophical Magazine and Journal of Science* 41.271, pp. 107–120. ISSN: 1941-5982, 1941-5990. DOI: 10.1080/14786447108640452.

Su, Bo, Herbert A. Caller-Guzman, Volker Körstgens, Yichuan Rui, Yuan Yao, Nitin Saxena, Gonzalo Santoro, Stephan V. Roth, and Peter Müller-Buschbaum (Dec. 20, 2017). "Macroscale and Nanoscale Morphology Evolution during in Situ Spray Coating of Titania Films for Perovskite Solar Cells". In: *ACS Applied Materials & Interfaces* 9.50, pp. 43724–43732. ISSN: 1944-8244. DOI: 10.1021/acsami.7b14850.

Suck, Jens-Boie, M. Schreiber, and P. Häussler (July 23, 2002). *Quasicrystals: An Introduction to Structure, Physical Properties and Applications*. Berlin Heidelberg New York: Springer Verlag. 592 pp. ISBN: 978-3-540-64224-4. Google Books: a0_F4CiHevkC. URL: https://www.springer.com/de/book/9783540642244.

Suh, H. S., X. Chen, P. A. Rincon-Delgadillo, Z. Jiang, J. Strzalka, J. Wang, W. Chen, R. Gronheid, J. J. de Pablo, N. Ferrier, M. Doxastakis, and P. F. Nealey (June 1, 2016). "Characterization of the Shape and Line-Edge Roughness of Polymer Gratings with Grazing Incidence Small-Angle X-Ray Scattering and Atomic Force Microscopy". In: *Journal of Applied Crystallography* 49.3, pp. 823–834. ISSN: 1600-5767. DOI: 10.1107/S1600576716004453.

Sunday, Daniel F., Scott List, Jasmeet S. Chawla, and R. Joseph Kline (Oct. 1, 2015). "Determining the Shape and Periodicity of Nanostructures Using Small-Angle X-Ray Scattering". In: *Journal of Applied Crystallography* 48.5, pp. 1355–1363. ISSN: 1600-5767. DOI: 10.1107/S1600576715013369.

Sunday, Daniel F., Scott List, Jasmeet S. Chawla, and R. Joseph Kline (2016). "Evaluation of the Effect of Data Quality on the Profile Uncertainty of Critical Dimension Small Angle X-Ray Scattering". In: *Journal of Micro/Nanolithography, MEMS, and MOEMS* 15.1, pp. 014001–014001. ISSN: 1932-5150. DOI: 10.1117/1.JMM.15.1.014001.

Thompson, Albert, Ingolf Landau, David Attwood, Yanwei Liu, Eric Gullikson, Piero Pianetta, Malcolm Howells, Arthur Robinson, Kwang-Je Kim, James Scofield, Janos Kirz, James Underwood, Jeffrey Kortright, Gwyn Williams, and Herman Winick (Oct. 2009). *X-Ray Data Booklet*. Berkely: Lawrence Berkeley National Laboratory. 176 pp. URL: http://xdb.lbl.gov (visited on 10/14/2019).

Thony, Philippe (2003). "Review Of CD Measurement And Scatterometry". In: *AIP Conference Proceedings*. International Conference on Characterization and Metrology for ULSI Technology. Vol. 683. Austin, Texas (USA): AIP, pp. 381–388. DOI: 10.1063/1.1622499.

Tolan, M., W. Press, F. Brinkop, and J. P. Kotthaus (1995). "X-Ray Diffraction from Laterally Structured Surfaces: Total External Reflection". In: *Physical Review B* 51.4, p. 2239. DOI: 10.1103/PhysRevB.51.2239.

Vaid, Alok, Givantha Iddawela, Jamie Tsai, Gilad Wainreb, Paul Isbester, Byung Cheol (Charles) Kang, Michael Klots, Yinon Katz, Cornel Bozdog, and Matt Sendelbach (Mar. 19, 2015). "Improved Scatterometry Time-to-Solution Using Virtual Reference". In: Metrology, Inspection, and Process Control for Microlithography XXIX. Vol. 9424. SPIE, p. 94240X. DOI: 10.1117/12.2087232.

Van Veenhuizen, M., G. Allen, M. Harmes, T. Indukuri, C. Jezewski, B. Krist, H. Lang, A. Myers, R. Schenker, K. J. Singh, R. Turkot, and H.J. Yoo (June 2012). "Demonstration of an Electrically Functional 34nm Metal Pitch Interconnect in Ultralow-k ILD Using Spacer-Based Pitch Quartering". In: *2012 IEEE International Interconnect Technology Conference*, pp. 1–3. DOI: 10.1109/IITC.2012.6251665.

Verschuuren, Marc and Hans Van Sprang (2007). "3D Photonic Structures by Sol-Gel Imprint Lithography". In: *MRS Online Proceedings Library Archive* 1002, 1002-N03–05. ISSN: 1946-4274, 0272-9172. DOI: 10.1557/PROC-1002-N03-05.

Villarrubia, J.S., A.E. Vladár, B. Ming, R. Joseph Kline, Daniel F. Sunday, Jasmeet S. Chawla, and S. List (July 2015). "Scanning Electron Microscope Measurement of Width and Shape of 10 Nm Patterned Lines Using a JMONSEL-Modeled Library". In: *Ultramicroscopy* 154, pp. 15–28. ISSN: 03043991. DOI: 10.1016/j.ultramic.2015.01.004.

Vineyard, George H. (Oct. 1982). "Grazing-Incidence Diffraction and the Distorted-Wave Approximation for the Study of Surfaces". In: *Physical Review B* 26.8, pp. 4146–4159. DOI: 10.1103/PhysRevB.26.4146.

Virtanen, Pauli, Ralf Gommers, Travis E. Oliphant, Matt Haberland, Tyler Reddy, David Cournapeau, Evgeni Burovski, Pearu Peterson, Warren Weckesser, Jonathan Bright, Stéfan J. van der Walt, Matthew Brett, Joshua Wilson, K. Jarrod Millman, Nikolay Mayorov, Andrew R. J. Nelson, Eric Jones, Robert Kern, Eric Larson, C. J. Carey, İlhan Polat, Yu Feng, Eric W. Moore, Jake VanderPlas, Denis Laxalde, Josef Perktold, Robert Cimrman, Ian Henriksen, E. A. Quintero, Charles R. Harris, Anne M. Archibald, Antônio H. Ribeiro, Fabian Pedregosa, and Paul van

Mulbregt (Feb. 3, 2020). "SciPy 1.0: Fundamental Algorithms for Scientific Computing in Python". In: *Nature Methods*, pp. 1–12. ISSN: 1548-7105. DOI: 10.1038/s41592-019-0686-2.

Von Ardenne, Manfred (Sept. 1, 1938). "Das Elektronen-Rastermikroskop". In: *Zeitschrift für Physik* 109.9, pp. 553–572. ISSN: 0044-3328. DOI: 10.1007/BF01341584.

Wang, Xiaoqiang (2020). *PCASpy Version 0.7.2 Documentation*. URL: https://pcaspy.readthedocs.io/en/latest/ (visited on 06/07/2020).

Wansleben, Malte, Claudia Zech, Cornelia Streeck, Jan Weser, Christoph Genzel, Burkhard Beckhoff, and Roland Mainz (2019). "Photon Flux Determination of a Liquid-Metal Jet X-Ray Source by Means of Photon Scattering". In: *Journal of Analytical Atomic Spectrometry* 34.7, pp. 1497–1502. ISSN: 0267-9477, 1364-5544. DOI: 10.1039/C9JA00127A.

Warren, B. E. and J. Biscce (1938). "The Structure of Silica Glass by X-Ray Diffraction Studies". In: *Journal of the American Ceramic Society* 21.2, pp. 49–54. ISSN: 1551-2916. DOI: 10.1111/j.1151-2916.1938.tb15742.x.

Watson, J. D. and F. H. C. Crick (Apr. 1953). "Molecular Structure of Nucleic Acids: A Structure for Deoxyribose Nucleic Acid". In: *Nature* 171.4356, pp. 737–738. ISSN: 1476-4687. DOI: 10.1038/171737a0.

Wernecke, Jan, Christian Gollwitzer, Peter Müller, and Michael Krumrey (May 1, 2014). "Characterization of an In-Vacuum PILATUS 1M Detector". In: *Journal of Synchrotron Radiation* 21.3, pp. 529–536. ISSN: 1600-5775. DOI: 10.1107/S160057751400294X.

Wernecke, Jan, Michael Krumrey, Armin Hoell, R. Joseph Kline, Hung-Kung Liu, and Wen-Li Wu (Dec. 1, 2014). "Traceable GISAXS Measurements for Pitch Determination of a 25 Nm Self-Assembled Polymer Grating". In: *Journal of Applied Crystallography* 47.6, pp. 1912–1920. ISSN: 1600-5767. DOI: 10.1107/S1600576714021050.

Wernecke, Jan, Hiroshi Okuda, Hiroki Ogawa, Frank Siewert, and Michael Krumrey (Aug. 26, 2014). "Depth-Dependent Structural Changes in PS-*b*-P2VP Thin Films Induced by Annealing". In: *Macromolecules* 47.16, pp. 5719–5727. ISSN: 0024-9297, 1520-5835. DOI: 10.1021/ma500642d.

Wernecke, Jan, Frank Scholze, and Michael Krumrey (2012). "Direct Structural Characterisation of Line Gratings with Grazing Incidence Small-Angle x-Ray Scattering". In: *Review of Scientific Instruments* 83.10, p. 103906. ISSN: 00346748. DOI: 10.1063/1.4758283.

Wilkins, M. H. F., A. R. Stokes, and H. R. Wilson (Apr. 1953). "Molecular Structure of Nucleic Acids: Molecular Structure of Deoxypentose Nucleic Acids". In: *Nature* 171.4356, pp. 738–740. ISSN: 1476-4687. DOI: 10.1038/171738a0.

Winick, Herman (May 1, 1998). "Synchrotron Radiation Sources – Present Capabilities and Future Directions". In: *Journal of Synchrotron Radiation* 5.3, pp. 168–175. ISSN: 0909-0495. DOI: 10.1107/S0909049597018761.

Winick, Herman and S. St. Lorant (1975). *Stanford Synchrotron Radiation Project Report SSRP*. 75/06. (unpublished). Stanford.

Wormington, Matthew, Charles Panaccione, Kevin M. Matney, and D. Keith Bowen (Oct. 1, 1999). "Characterization of Structures from X-Ray Scattering Data Using Genetic Algorithms". In: *Philosophical Transactions of the Royal Society of London. Series A: Mathematical, Physical and Engineering Sciences* 357.1761, pp. 2827–2848. DOI: 10.1098/rsta.1999.0469.

Wuttke, Joachim (Mar. 1, 2017). "Form Factor (Fourier Shape Transform) of Polygon and Polyhedron". In: arXiv: 1703.00255 [math-ph]. URL: http://arxiv.org/abs/1703.00255 (visited on 02/28/2018).

Xavier, Jolly, Martin Boguslawski, Patrick Rose, Joby Joseph, and Cornelia Denz (Jan. 19, 2010). "Reconfigurable Optically Induced Quasicrystallographic Three-Dimensional Complex Nonlinear Photonic Lattice Structures". In: *Advanced Materials* 22.3, pp. 356–360. ISSN: 1521-4095. DOI: 10.1002/adma.200901792.

Xavier, Jolly, Jürgen Probst, Franziska Back, Philippe Wyss, David Eisenhauer, Bernd Löchel, Eveline Rudigier-Voigt, and Christiane Becker (Nov. 1, 2014). "Quasicrystalline-Structured Light

Harvesting Nanophotonic Silicon Films on Nanoimprinted Glass for Ultra-Thin Photovoltaics". In: *Optical Materials Express* 4.11, pp. 2290–2299. ISSN: 2159-3930. DOI: 10.1364/OME.4.002290.

Xavier, Jolly, Jürgen Probst, and Christiane Becker (Dec. 12, 2016). "Deterministic Composite Nanophotonic Lattices in Large Area for Broadband Applications". In: *Scientific Reports* 6, p. 38744. ISSN: 2045-2322. DOI: 10.1038/srep38744.

Yamanaka, Eiji, Rikiya Taniguchi, Masamitsu Itoh, Kazuhiko Omote, Yoshiyasu Ito, Kiyoshi Ogata, and Naoya Hayashi (May 18, 2016). "The Measurement Capabilities of Cross-Sectional Profile of Nanoimprint Template Pattern Using Small Angle x-Ray Scattering". In: Photomask Japan 2016: XXIII Symposium on Photomask and Next-Generation Lithography Mask Technology. Vol. 9984. SPIE, p. 99840V. DOI: 10.1117/12.2246570.

Yan, Minhao and Alain Gibaud (Dec. 1, 2007). "On the Intersection of Grating Truncation Rods with the Ewald Sphere Studied by Grazing-Incidence Small-Angle X-Ray Scattering". In: *Journal of Applied Crystallography* 40.6, pp. 1050–1055. ISSN: 0021-8898. DOI: 10.1107/S0021889807044482.

Yeoh, A., A. Madhavan, N. Kybert, S. Anand, J. Shin, M. Asoro, S. Samarajeewa, J. Steigerwald, C. Ganpule, M. Buehler, A. Tripathi, V. Souw, M. Haran, S. Nigam, V. Chikarmane, P. Yashar, T. Mule, Y-H. Wu, K-S. Lee, M. Aykol, K. Marla, P. Sinha, S. Kirby, H. Hiramatsu, W. Han, M. Mori, M. Sharma, H. Jeedigunta, M. Sprinkle, C. Pelto, M. Tanniru, G. Leatherman, K. Fischer, I. Post, and C. Auth (June 2018). "Interconnect Stack Using Self-Aligned Quad and Double Patterning for 10nm High Volume Manufacturing". In: 2018 IEEE International Interconnect Technology Conference (IITC). Santa Clara, CA, USA: IEEE, pp. 144–147. ISBN: 978-1-5386-4337-2. DOI: 10.1109/IITC.2018.8430489.

Zhou, Chun, Tamar Segal-Peretz, Muhammed Enes Oruc, Hyo Seon Suh, Guangpeng Wu, and Paul F. Nealey (July 24, 2017). "Fabrication of Nanoporous Alumina Ultrafiltration Membrane with Tunable Pore Size Using Block Copolymer Templates". In: *Advanced Functional Materials* 27.34, p. 1701756. ISSN: 1616-3028. DOI: 10.1002/adfm.201701756.

Zschornack, Günter (2006). *Handbook of X-Ray Data*. Berlin Heidelberg New York: Springer. 967 pp. ISBN: 978-3-540-28618-9. DOI: 10.1007/978-3-540-28619-6.